Transition to turbulence in planar shear flows

Sébastien Gomé

To cite this version:

Sébastien Gomé. Transition to turbulence in planar shear flows. Fluid mechanics [physics.class-ph]. Sorbonne Université, 2022. English. NNT : 2022SORUS351 . tel-03935299

HAL Id: tel-03935299
https://theses.hal.science/tel-03935299v1

Submitted on 11 Jan 2023

Transition to turbulence in planar shear flows

Sébastien Gomé

Thèse de doctorat de Sorbonne Université
Spécialité: Mécanique des Fluides

Préparée au laboratoire de Physique et Mécanique des Milieux Hétérogènes
Ecole Doctorale SMAER (ED391)

Composition du jury:

Rapporteur : Alexandros Alexakis, ENS Paris
Rapporteur : Yohann Duguet, Université Paris-Saclay
Examinateur : Freddy Bouchet, ENS Lyon
Examinateur : Yongyun Hwang, Imperial College London
Examinatrice : Elena Marensi, University of Sheffield
Examinatrice : Taraneh Sayadi, Sorbonne Université
Directrice de thèse : Laurette Tuckerman, ESPCI Paris
Directeur de thèse : Dwight Barkley, University of Warwick

To my mother.

Ackowledgements

First and foremost, I would like to thank my advisors Laurette Tuckerman and Dwight Barkley. I should not linger much on their kindness, generosity and support, nor on their incredible scientific input, because this would be an endless effort. Instead, I should point their particular sense of scientific rigour: in asking the right questions, follow the good directions, and drawing the right interpretations. Although each one of them has its own way of thinking and interacting, they make a very unique kind of scientific entity. I could feel part of a scientific family, and I thank them for that.

Next, I would like to warmly thank Yohann Duguet and Alexandros Alexakis for accepting to be my reporters and for reading this manuscript in the middle of August. I would also like to thank Freddy Bouchet, Elena Marensi, Yongyun Hwang and Taraneh Sayadi for accepting to be members of my jury.

In undertaking such an intense journey as a PhD thesis, I had the chance to meet many people who hugely influenced and guided me. I am particularly grateful to Francois Gallaire, Camille Duprat, Yacine Bengana, Tobias Grafke, Anna Frishman and Aliénor Rivière.

Fortunately, doing a PhD is not a lonely task. For that, PMMH was the perfect place, for both intellectual and non-intellectual reasons. There is here a spirit that is very hard to describe. PMMH is a very incentive place for research, and I would especially acknowledge Damien Vandembroucq, Jose-Eduardo Wesfreid, Laurent Duchemin, Sylvain Patinet, Stéphane Perrard, Benoît Semin, Ramiro Godoy-Diana and Tao Liu. Each one of them was particularly insightful at some point of my thesis. I also thank Juan Cruz for his insightful work on our side, along with Jean-Gabriel Thiriet. I am particularly grateful to Stéphane for having moved from one side of the Montage Sainte-Geneviève to the other (and for bringing Aliénor with him); I particularly enjoyed the turbulent discussions.

However, not all PMMH life happens inside the lab. A major part of it actually happens 200 meters away, in a sanctified institution called *Les Arènes.* I thank Chloé Dupuis, Saurabh Nath, Magdalena Kopec, Pierre-Henri Delville, Manon L'Estimé, Manon Quiros, Maïka Saint-Jean, Juan Pimienta, Baptiste Lafoux, Tristan Auregan, Joseph Vermeil, Anumita Jawahar, Renaud Baillou, Samantha Kucher, Adrian Koźluk, Adam Anglart, Roméo Antier, Gaspard Junot, Jean Cappello, Pierre-Brice Bintein, Martyna Goral, Hector Ignacio, Xavier Mousset, Aditya Jha, Lars Kool, Armand Barbot, Valentin Laplaud; and the many others who made me come there.

I have some special thoughts to Matthias Lerbinger, who was a pillar of this friendly assemblage and unfortunately passed away in 2022.

Part of this thesis was written during summer 2022 in Boulder (Colorado) and in Boston (Massachusetts). This might explain some mess in part of the manuscript, and I apologise for that in advance. For the good time and fruitful discussions I had during this period, I thank Yves-Marie Ducimetière, Adrian Van Kaan, Xueying Wang, Pratik Aghor, Egor Kiselev and all the other participants of the Boulder 2022 summer school, along with (again) Saurabh Nath for motivating me back in Boston. Santiago Benavides is also warmly thanked for his corrections to some of my chapters.

I am very thankful to all my friends who supported me during this thesis. Amongst them, Mathilda, Louis, Kevin, Sara, Antonin, Jean-Baptiste, Adrien, Eduardo, Hortense, Baptiste, Matthieu... and many others that I apologise for not mentioning.

As a large part of my free time during this PhD was devoted to music, I would like to thank anyone I met during this joyful period of my life. Of course, my viola teachers, Anne Rihoit and Claudine Christophe, but also my companions from the conservatory, especially Inès, Prune and Mathilde. Then come all my friends from my most-beloved orchestra, that I met back in Saclay and with whom I had adventurous musical *échappées*: Christophe, Marie, Louise, Delphine, Pierre, Clara, Noé, Simon, Antoine, Antoine, Alice, Abel, Camille, David, Léo, Marie, Robin, Marianne, Mathieu, Sébastien, Thomas, Thomas, Valentin...

Last, but not least, I thank my father who has always been there for me, and for his love and everyday support.

Contents

General introduction

Turbulence is the chaotic motion of a fluid, whose velocity and pressure evolve in a seemingly random manner. This flow motion can be very easily observed in our everyday life: water in a river, smoke out of a chimney, blowing wind, etc. Turbulent flow contrasts with laminar flow, a state in which the fluid motion occurs in parallel layers, which are not disturbing one another. Understanding the conditions in which turbulence appears out of quiescent flow is both a fundamental and fascinating topic of research, that has driven physicists for centuries.

1 Some perspectives on transition to turbulence

In the late 19th century, Osborne Reynolds was the first to systematically investigate how turbulence arises. A flow of water was continuously injected into a long pipe, in such a way that the flow rate was controlled (or the speed of the fluid at the inlet). Reynolds instilled colored water at the inlet of the pipe, via a dye located in the center of the pipe section. Various sketches from Reynolds (1883) are reproduced on Figure 1. By varying the diameter or the flow speed at the inlet, Reynolds observed that the injected colored water presented various behaviours: it could align in a regular stripe (Fig. 1a), or sometimes show swirls at different locations within the pipe (Fig. 1b-d). Reynolds found that at fixed diameter and viscosity of the fluid, the flow transits from an ordered laminar state to a disordered turbulent state when the flow rate was increased. This led to the definition of a single non-dimensional parameter governing the transition, since referred to as the Reynolds number:

$$Re = \frac{Ud}{\nu}$$

Here, U is the characteristic velocity inside the pipe, d is the pipe diameter, and ν is the viscosity of the fluid.

In the first observations of Reynolds, a particular regime was found within an intermediate range of flow speeds. In this regime, the flow is neither fully laminar nor fully

(a) Laminar

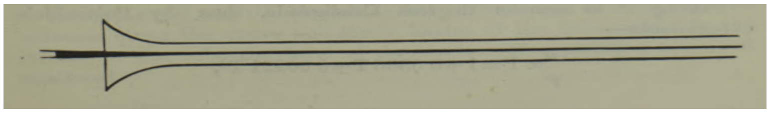

(b, c) Intermittent

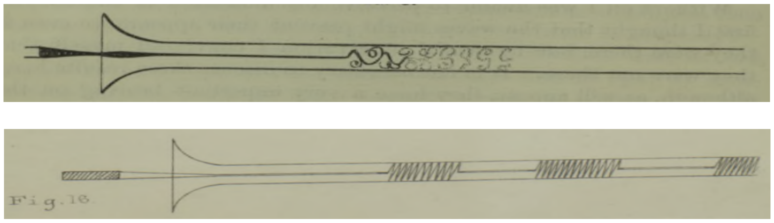

(d) Turbulent

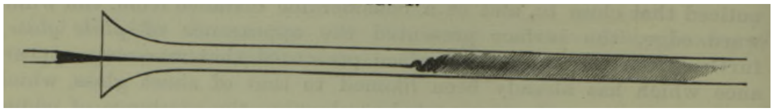

Figure 1: Visualisation of the different regimes found by Reynolds (1883). The flow is from left to right. At low flow speeds (a), the flow is laminar, as visible by the straight colored streakline, injected at the pipe inlet. With increasing flow speed, the flow shows incoherent and irregular motions. These propagate gradually throughout the pipe, with a transitional regime at intermediate flow speeds, where turbulent motions are intermittent (b, c). Once the flow speed is large enough (d), these swirling motions appear at a short distance from the pipe inlet, and are present up to the pipe outlet. The sketches are those drawn by Reynolds (1883).

turbulent, but shows localised turbulent zones, evolving both in space and time. These are illustrated on Figure 1b and c. One shall bear this regime in mind, since it will be the main discussion of this thesis. But first, I shall take a few important detours.

The flow within the pipe is a simple experiment of an out-of-equilibrium system: energy is injected by pressure difference between pipe extemities or imposed flow rate, and is constantly dissipated by tangential viscous shear. The laminar state is a stationary solution of this system: it instantaneously dissipates the work due to pressure difference. This is not true for the turbulent state: the eddies fluctuate in time, and, as a result, their kinetic energy is not stationary, and dissipation and external work do not instantaneously compensate.

Following Reynolds experiment, important theories were established so as to explain how turbulent flows dissipate energy. They involve a hierarchy of turbulent eddies of different scales, and a cascade of energy between these scales. Major understandings were achieved by Richardson, Kolmogorov, Kraichnan... among others. These theories were based on a particular set of equations describing the conservation laws of fluid motions: the Navier-Stokes equations.

However, these descriptions of *developed turbulence* do not explain how turbulence arises in an initially quiescent flow. This problem is a challenge in many aspects: for physicists, the rise of turbulence breaks space and time symmetries in multiple ways. For mechanicians, turbulence enhances mixing but increases dissipation. Knowing when it appears is a fundamental problem. Lowering or suppressing turbulence is another fundamental problem. As for mathematicians, they can view the equations of flow motion as a dynamical system, whose number of solutions grows infinitely with Reynolds number. This led to the theory of chaos; and this is an important part of the story.

In the decades following Reynolds experiments, many attempted to find the onset of turbulence from a direct analysis of the Navier-Stokes equations: Orr, Sommerfeld, Heisenberg... Their main tool was that of linear stability analysis: under which conditions does a set of infinitesimal perturbations of the laminar flow becomes unstable? Taylor (1923) conducted experiments on the flow between concentric rotating cylinders, now commonly called Taylor–Couette flow. He carried out a linear stability analysis that was in outstanding agreement with his experimental results. Later, with the insights of Landau (1944) and Stuart (1958), the influence of non-linearities on the stability of flow equations led to the development of *bifurcation theory*: not only the flow can undergo an initial primary instability, but secondary instabilities can perturb the resulting flow state, via a series of bifurcations.

A fundamental improvement of bifurcation theory happened with the works of Ruelle & Takens (1971) and Feigenbaum (1978) on chaos. Chaos theory explained how a finite number of instabilities could generate complex non-periodic dynamics. This route to turbulence was confirmed in corotating Taylor-Couette flow by Gollub & Swinney (1975). Bifurcation theory then became a sanctuarised cornerstone of fluid dynamics.

However, linear stability analysis and bifurcation theory fail in explaining the onset of turbulence in the pipe experiment. It does so in many other wall-bounded shear flows. The reason is that transition to turbulence in these flows is *subcritical*: turbulence exists in regimes of Re where the laminar flow is linearly stable. This is the case for the regimes observed by Reynolds (1883) (see Fig. 1) and later by Wygnanski & Champagne (1973), where Re was typically of order $O(10^3)$, while it is known from numerical computations that laminar pipe flow is linearly stable up to $Re \sim 10^7$ (Meseguer & Trefethen, 2003).

In other canonical shear flows such as plane Couette (two parallel plates moving at opposite speeds) or plane Poiseuille flow (two fixed parallel plates subject to a pressure difference), the laminar base flow is also stable in the range in Re where turbulence emerges. In these planar geometries, the route to turbulence is not quite the same as in pipe flow: once initiated, intermittent turbulence takes the form of laminar-turbulent structures, which are oblique with respect to the streamwise direction. These oblique

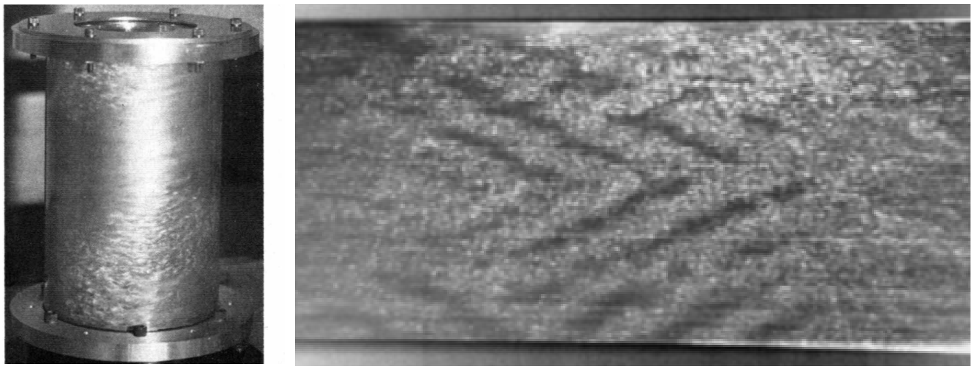

(a) Taylor-Couette flow

(b) Plane Couette flow

Figure 2: (a) Turbulent spiral in a Taylor–Couette flow experiment (Coles & van Atta, 1966). (b) Turbulent–laminar pattern in a plane Couette flow experiment at $Re = 358$ (Prigent *et al.*, 2003).

structures were first observed by Coles & Von Atta (Coles, 1965; Van Atta, 1966; Coles & van Atta, 1966) in counter-rotating Taylor-Couette flow (Figure 2a), and by Prigent *et al.* (2003) in planar Couette flow (Figure 2b), where they were shown to form patterns. The emergence of these patterns in plane shear flows, and the nature of the coexistence of laminar and turbulent phases, will be the subject of this thesis.

The coexistence of both laminar and turbulent states at the same value of the control parameter, Re, suggests that one can trigger turbulence by perturbing laminar flow with some finite-amplitude kick. The reason for this is called *non-normality*: although any modal perturbation to the laminar flow would exponentially decay, these modes might be non-orthogonal, and a combination of them can be amplified. This amplification might be enough to lead to a nonlinear regime, that might itself develop into turbulence (Butler & Farrell, 1992; Trefethen *et al.*, 1993). But this is another story.

Let us go back to pipe flow. If the flow is perturbed at some specific location in space, turbulence will develop locally, and might or might not propagate within the pipe. Wygnanski & Champagne (1973) carried out such an experiment, and their observations are summarised on Figure 3 (issued from Barkley (2016)). If Re is low enough, the initial turbulent patch decays with time, after propagating downstream because of the advection of laminar flow. Once Re increases above a certain threshold, the localised turbulent patch is both advected downstream, and extends, finally contaminating all the downstream part of the pipe.

A very insightful analogy was drawn by Pomeau (1986) in terms of reaction-diffusion

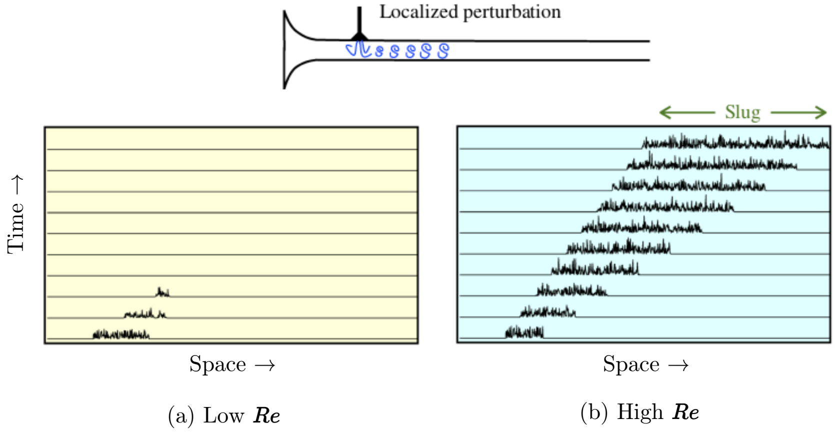

(a) Low ***Re*** (b) High ***Re***

Figure 3: Effect of a localised perturbation in pipe flow. At low Re (a), turbulence is locally triggered but finally decay, after being advected downstream. At high enough Re, the initial turbulent patch both travels downstream and increases in size. This is called a *slug*.

processes. If two possible states of a generic system are coexisting in space, and separated by a boundary, this boundary might move with a constant mean speed. The relative stability of each state can be simply deduced from the value and sign of this velocity: the stable phase contaminates the metastable one, and with changing the control parameter, the stable phase might become metastable, so the contamination process is reversed. Having in mind recent discoveries on spatio-temporal intermittency (Pomeau & Manneville, 1989), Pomeau envisioned one phase as a collection of non-coherent oscillators, each one showing a time-intermittent behaviour. Each of these oscillators could then either relax to its quiescent state or contaminate its neighbours. The turbulent phase would be the collection of intermittent oscillators, while the laminar phase is the state of relaxed oscillators. The contamination of turbulence into laminar flow was therefore assumed to be a contact process in the class of *Directed Percolation* (Hinrichsen, 2000). The reason for this assumption is that Directed Percolation (DP) is a universal class for non-equilibrium absorbing processes[1]. Following Pomeau (1986), simple models exhibiting spatio-temporal chaos were investigated and entered this universality class (Chaté & Manneville, 1987; Kaneko, 1985).

It is only in the 2010's that the vision of Pomeau was experimentally and numerically confirmed in transition to turbulence (Barkley, 2011; Lemoult *et al.*, 2016; Chantry *et al.*, 2017; Klotz *et al.*, 2022). However, although Pomeau's insight was visionary, one has to

---

[1] This will be briefly discussed in the next section.

deviate from his initial analogy to understand how localised turbulence organises close to the critical point of DP. Barkley (2011, 2016) enlarged the vision of Pomeau with help of a different analogy, that of excitable media. This resulted in a model which proved to reproduce the quintessence of transition to turbulence in pipe flow.

2 A brief introduction of phase transition

In the following section, I will shortly introduce the concept of phase transition, that lies behind Directed Percolation. I will introduce basic concepts that are not essential for understanding the transition to turbulence, but that will remotely accompany us throughout this manuscript.

Phase transition is a cooperative phenomenon: a system with many constituents interacting one with another, might exhibit such a collective behavior. When undergoing a phase transition, a new property or structure is acquired by the system (Kubo *et al.*, 2012). For example, a gas condenses to the liquid state by compression or cooling, and a paramagnetic substance becomes ferromagnetic by cooling below some temperature. It is natural to wonder about the link with transition to turbulence, but the answer to this question is highly non-trivial. I will very briefly address this here and in part of the thesis, but this is an active research topic (Barkley, 2016; Goldenfeld & Shih, 2017).

Let us spend a few time on the well-known example of ferromagnets, because it is particularly illustrative. Ferromagnets are bar magnets and can be found on refrigerator doors holding up notes. These are permanent magnets. Unlike ferromagnets, paramagnets are magnetized only in the presence of an externally applied magnetic field. Otherwise, they do not show spontaneous magnetism, because of the effect of thermal motion that randomizes the spin orientations of the atoms inside the solid.

When the temperature increases beyond a certain point, called the Curie temperature T_c, a ferromagnet can no longer maintain its spontaneous magnetization because of these thermal effects, although it can still respond to an external field. This transition between ferromagnetic and paramagnetic phases with varying temperature is an example of a *second-order phase transition*. If now temperature is kept fixed below T_c, and an external magnetic field H is applied, the spins will align with H. If H continuously changes from positive to negative, the sign and value of the magnetisation will change abruptly. This change is discontinuous, and is an example of a *first-order transition*.

Both concepts are more formally defined in the thermodynamic limit of an infinite number of elements in the system (like atoms, particles, or any individual object in the system, interacting with its neighbours on a short range). A generic definition of first and second-order phase transition, illustrated on Figure 4, is the following (Goldenfeld, 2018; Yeomans, 1992):

- In a **second-order (or continuous) phase transition**, an initially stable state

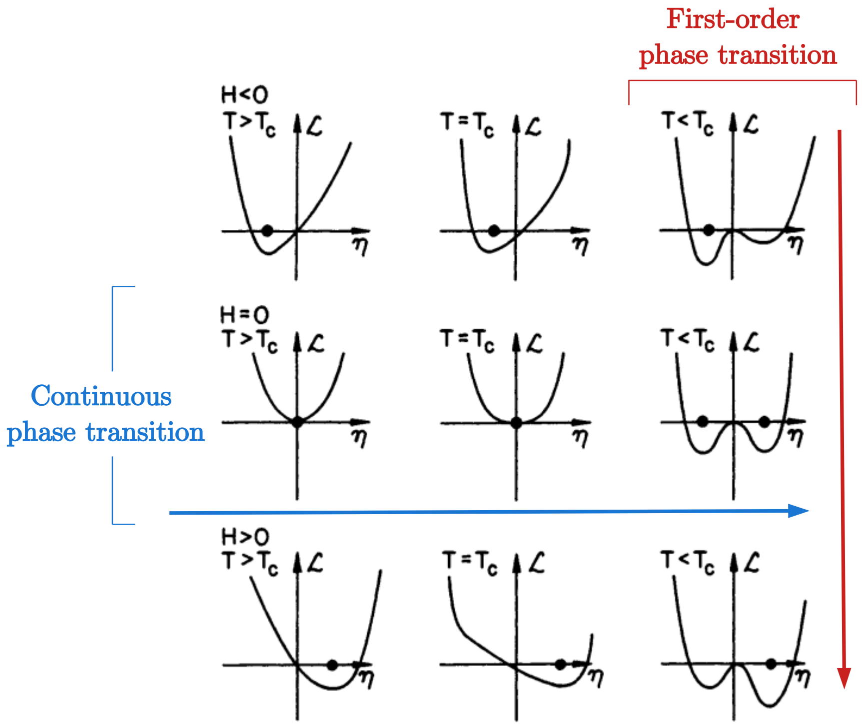

Figure 4: Evolution of the free energy (or any relevant thermodynamic potential) for various values of temperature T and applied magnetic field H, in the magnetic phase transition. η is the total magnetisation of the system (the order parameter). T decreases from left to right, H increases from top to bottom. The $\bullet$ indicate the values of η that minimize the potential. The transition in the right-most column is of first-order, while that in the central row is of second-order. Figure issued from (Goldenfeld, 2018, p. 143).

loses its stability, and typically divides into multiple stable states, different from the original one (Fig. 4, blue horizontal arrow). The order parameter (typically the total magnetisation in the spin system) varies continuously at the transition. The correlation length, which describes the spatial extent of the fluctuations of the (local) order parameter about its average, diverges algebraically near the transition point. The transition point is called a *critical point*, and the system at this point is very sensitive to any infinitesimal change in the control parameter: the response function associated with the order parameter diverges.

- In a **first-order phase transition**, an initially stable state becomes metastable when changing the control parameter (Fig. 4, red vertical arrow). The order parameter is discontinuous at the transition. The correlation length is always finite. Close

> to the transition point, the system is usually driven by nucleation of the new stable phase within the old metastable one: the system attempts to nucleate one or more bubbles of the stable phase until some of them reach some critical size and then quickly grow, invading all the old phase.

In thermodynamics and equilibrium statistical mechanics, phase transitions correspond to nonanalytical behaviours in the free energy, as a function of one or more of its thermodynamic variables. But in non-equilibrium mechanics, the situation is more rich. There, second-order phase transitions can take the form of **absorbing phase transitions** (Henkel *et al.*, 2008): one goes from a fluctuating state to a so-called absorbing state, which can never be left. Absorbing phase transitions exhibit universal behaviours, independent of the microscopic details of the system. These are determined by symmetries and conservation laws, and can be segregated into universality classes.

Directed Percolation is one of such classes. It directly comes from the picture of water percolating throughout a porous medium, like a piece of cloth or sand. If you imagine a water filter, fluid infiltrates this piece of cloth and is cleaned of impurities. However, at some point, the impurities in the water accumulate and clog the pores, so that water cannot penetrate anymore. This transition from percolation to a state of bottleneck is the core of Directed Percolation models (Obukhov, 1980; Grassberger, 1981; Janssen, 1981; Henkel *et al.*, 2008; Täuber, 2014).

Models usually use sites of a lattice to represent the pores of the filter: adjacent sites are connected by bonds, which are open or closed with a probability p. The value of p controls the macroscopic permeability of the filter. The connection to intermittent turbulence is illustrated on Figure 5, issued from the experimental investigation of Lemoult *et al.* (2016): turbulence contaminates the absorbing laminar state, and the value of Reynolds number controls the probability of contamination. Below a certain value Re_c (or below some value p_c of the propagation probability) the contamination stops after a sufficiently long time, and the flow fully laminarises. This is the critical point of the second-order phase transition.

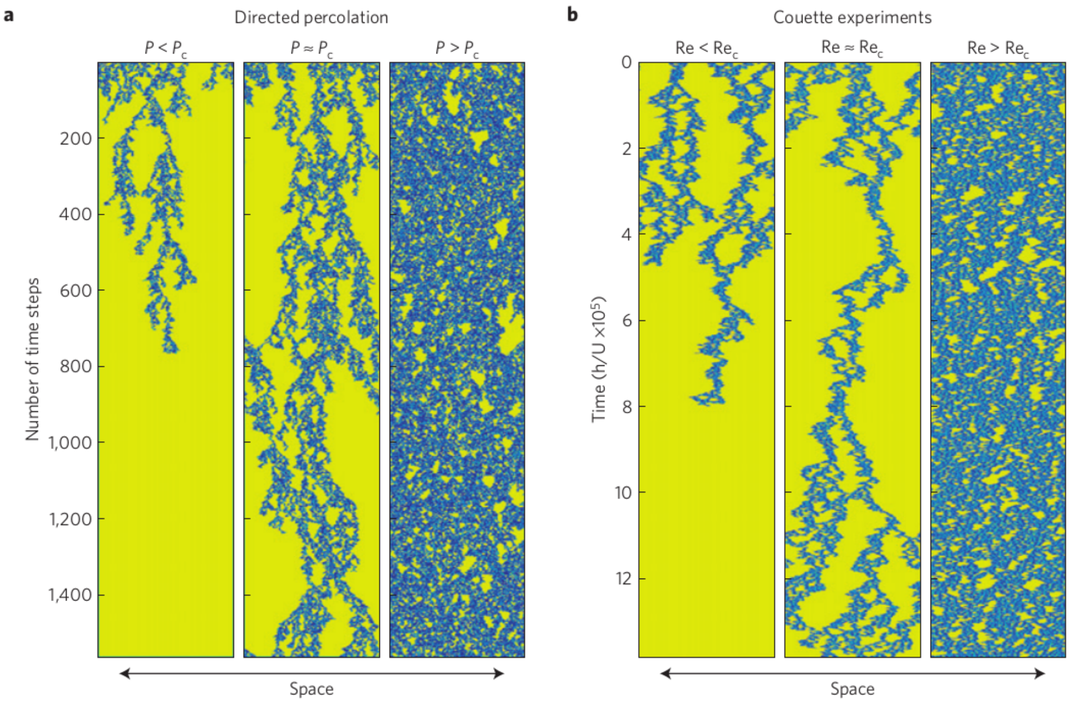

Figure 5: Spatio-temporal dynamics in Directed Percolation (a) and in plane Couette flow (b). The active sites are shown in blue and the absorbing/laminar state is shown in yellow. Three cases, below, at and above p_c are shown. Below the critical point all sites finally enter the absorbing/laminar state (left panel). Close to the critical point (mid panel), active sites (turbulence) persist but coexist with large laminar regions. For $p > p_c$ (right panel), active sites fill a large fraction of the domain.

3 Overview of the thesis

This thesis is organised as follows:

Chapters 1 and 2 are devoted to the transitional regime of plane channel flow. Numerical simulations of Navier-Stokes equations are used to study the coexistence of laminar and turbulent structures near the critical point. The lifetimes of these structures are computed, by classical Monte-Carlo method (Chapter 1) or by a novel rare-event approach (Chapter 2). Turbulent structures either decay and laminarise, or propagate via self-replication (a process called splitting). An onset Reynolds number is defined when these processes balance: above it, turbulence statistically propagates. This value of Re is close to the critical point of Directed Percolation. The time-scale at which turbulence decays or splits evolves super-exponentially with Re, and a probabilistic description explaining this tendency is developed in Chapter 2.

Chapters 3 and 4 focus on the emergence of laminar-turbulent patterns out of uniform plane Couette flow. In Chapter 3, we understand the mechanisms by which turbulent eddies energise patterns, and more particularly their associated large-scale circulation. We show that this large-scale flow is strongly advective, and this contributes to extracting energy from the mean shear. In Chapter 4, this energy cycle clarifies the way in which a pattern wavelength is selected. Via simulations in large domains, we find a transition from the uniform turbulent state to a regime in which turbulence is punctuated by isolated intermittent laminar pockets or *gaps*, whose lifetimes increase with decreasing Re. These laminar gaps eventually form patterns because of their associated large-scale flow, which is best energised at some preferred wavelength.

Finally, Chapter 5 proposes a control experiment which suppresses the large-scale circulation associated to laminar-turbulent interfaces in plane Couette flow. As a result, the flow does not present regular structures, and the transition scenario follows a contamination process, similar to Pomeau's vision.

Chapter 1

Statistical transition to turbulence in plane channel flow

Intermittent turbulent-laminar patterns characterize the transition to turbulence in pipe, plane Couette and plane channel flows. In this first chapter, we study the time evolution of turbulent-laminar bands in plane channel flow via direct numerical simulations using the parallel pseudospectral code ChannelFlow. Simulations are carried out in a narrow computational domain tilted by 24° with respect to the streamwise direction. This specific numerical domain will be of large importance throughout this manuscript, and is introduced in Section 1.2. In this numerical configuration, mutual interactions between bands are studied through their propagation velocities. Energy profiles show that the flow surrounding isolated turbulent bands returns to the laminar base flow over large distances. Depending on the Reynolds number, a turbulent band can either decay to laminar flow or split into two bands. As with past studies of other wall-bounded shear flows, in most cases survival probabilities are found to be consistent with exponential distributions for both decay and splitting, indicating that the processes are memoryless. Statistically estimated mean lifetimes for decay and splitting are plotted as a function of the Reynolds number and lead to the estimation of a critical Reynolds number $Re_{\mathrm{cross}} \simeq 965$, where decay and splitting lifetimes cross at greater than 10^6 advective time units. The processes of splitting and decay are also examined through analysis of their Fourier spectra. The dynamics of large-scale spectral components seem to statistically follow the same pathway during the splitting of a turbulent band and may be considered as precursors of splitting.

This chapter is extracted from the article *"Statistical transition to turbulence in plane channel flow"*, published in *Physical Review Fluids* (2020).

1.1 Introduction

The route to turbulence in many wall-bounded shear flows involves intermittent laminar-turbulent patterns that evolve on vast space and time scales ((Tuckerman *et al.*, 2020) and references therein). These states have received much attention over the years, both because of their intrinsic fascination and also because of their fundamental connection to critical phenomena associated with the onset of sustained turbulence in subcritical shear flows. Below a critical Reynolds number, intermittent turbulence exists only transiently – inevitably reverting to laminar flow, possibly after some very long time. Just above the critical Reynolds number, turbulence can become sustained in the form of intermittent laminar-turbulent patterns.

Flow geometry, specifically the number of unconstrained directions, plays an important role in these patterns. In flows with one unconstrained direction, large-scale turbulent-laminar intermittency can manifest itself only in that direction. Pipe flow is the classic example of such a system (Reynolds, 1883), but other examples are variants such as duct flow (Takeishi *et al.*, 2015) and annular pipe flow (Ishida *et al.*, 2016), and also constrained Couette flow between circular cylinders where the height and gap are both much smaller than the circumference (Lemoult *et al.*, 2016). In terms of large-scale phenomena, these systems are viewed as one dimensional. Turbulent-laminar intermittency takes the comparatively simple form of localized turbulent patches, commonly referred to as puffs, interspersed within laminar flow (Darbyshire & Mullin, 1995; Nishi *et al.*, 2008; van Doorne & Westerweel, 2009). In this case much progress has been made in understanding the localization of puffs and the critical phenomena associated with them (Hof *et al.*, 2010; Samanta *et al.*, 2011; Avila *et al.*, 2011; Barkley, 2016; Barkley *et al.*, 2015), including the scaling associated with one-dimensional directed percolation (Lemoult *et al.*, 2016).

In flow geometries with one confined and two extended directions, turbulent-laminar intermittency takes a more complex form that is dominated by turbulent bands which are oriented obliquely to the flow direction. Examples of such flows are Taylor-Couette flow (Coles & van Atta, 1966; Andereck *et al.*, 1986; Dong, 2009; Meseguer *et al.*, 2009; Kanazawa, 2018; Berghout *et al.*, 2020; Prigent *et al.*, 2002), plane Couette flow (Prigent *et al.*, 2002; Duguet *et al.*, 2010), plane channel flow (Tsukahara *et al.*, 2005*a*; Brethouwer *et al.*, 2012; Fukudome & Iida, 2012), and a free-slip version of plane Couette flow called Waleffe flow (Waleffe, 1997; Chantry *et al.*, 2016). In terms of large-scale phenomena, one views these systems as two dimensional. Understanding the transition scenario in these systems is complicated by the increased richness of the phenomena they exhibit and also by the experimental and computational challenges involved in studying systems with two directions substantially larger than the wall separation. So large are the required dimensions that only for a truncated model of Waleffe flow has it thus far been possible to verify that the transition to turbulence is of the universality class of two-dimensional directed percolation (Chantry *et al.*, 2017).

Between the one-dimensional and fully two-dimensional cases are the numerically obtainable restrictions of planar flows to long, but narrow, periodic domains tilted with respect to the flow direction (Barkley & Tuckerman, 2005). These domains restrict turbulent bands to a specified angle. They have only one long spatial direction, thereby limiting the allowed large-scale variation to one dimension, but they permit flow in the narrow (band-parallel) direction, flow that is necessary for supporting turbulent bands in planar shear flows. Such computational domains were originally proposed as minimal computational units to capture and understand the oblique turbulent bands observed in planar flows (Barkley & Tuckerman, 2005). Tilted computational domains have subsequently been used in numerous studies of transitional wall-bounded flows, notably plane Couette flow(Barkley & Tuckerman, 2007; Tuckerman & Barkley, 2011; Shi *et al.*, 2013; Lemoult *et al.*, 2016; Reetz *et al.*, 2019) and plane channel flow (Tuckerman *et al.*, 2014; Paranjape *et al.*, 2020). Lemoult *et al.* (Lemoult *et al.*, 2016) showed that in tilted domains plane Couette flow exhibits a transition to sustained turbulence in the directed percolation universality class. Reetz, Kreilos & Schneider (Reetz *et al.*, 2019) computed a state resembling a periodic turbulent band in plane Couette flow while Paranjape, Duguet & Hof (Paranjape *et al.*, 2020) computed localized traveling waves in plane channel flow as a function of the Reynolds number and the tilt angle. Shi, Avila & Hof (Shi *et al.*, 2013) used simulations in a tilted domain to measure decay and splitting lifetimes in plane Couette flow and it is this approach that we apply here to plane channel flow.

We mention two important points concerning the relevance of turbulent bands in narrow tilted domains to those in plane channel flow in large domains. The first is that a regime in transitional channel flow has been discovered at Reynolds numbers lower than those studied here in which turbulent bands elongate at their downstream end while they retract from their upstream end (Xiong *et al.*, 2015; Kanazawa, 2018; Tao *et al.*, 2018; Xiao & Song, 2020; Shimizu & Manneville, 2019). Such bands of long but finite length are excluded in narrow tilted domains. In full two-dimensional domains and at lower Reynolds numbers, this one-sided regime takes precedence over the transition processes that we will describe here. The second point is that critical Reynolds numbers obtained in narrow tilted domains (Shi *et al.*, 2013; Chantry, 2020) have been found to agree closely with transition thresholds found in the full planar setting (Bottin & Chaté, 1998; Bottin *et al.*, 1998; Duguet *et al.*, 2010; Chantry *et al.*, 2017) in both plane Couette flow and in stress-free Waleffe flow. We will return to both of these points in Sec. 1.6.

Here we study the onset of turbulent channel flow in narrow tilted domains. We follow closely the work of Shi, Avila & Hof (Shi *et al.*, 2013) on plane Couette flow. We are particularly focused on establishing the time scales and Reynolds numbers associated with the splitting and decay processes.

1.2 Numerical procedure and choice of dimensions

Plane channel flow is generated by imposing a mean or bulk velocity U_{bulk} on flow between two parallel rigid plates. The length scales are nondimensionalized by the half-gap h between the plates. Authors differ on the choice of velocity scales for nondimensionalizing channel flow, but one standard choice, that we adopt here, is to use $3U_{\text{bulk}}/2$. This is equal to the centerline velocity U_{cl} of the corresponding laminar parabolic flow since

$$U_{\text{bulk}} = \frac{1}{2}\int_{-1}^{+1} U_{\text{cl}}(1-y^2)dy = \frac{2}{3}U_{\text{cl}} \tag{1.1}$$

The Reynolds number is then defined to be $Re = U_{\text{cl}}h/\nu = 3U_{\text{bulk}}h/(2\nu)$.

The computational domain used in this study is tilted with respect to the streamwise direction, as illustrated in Fig. 1.1(b). Its wall-parallel projection is a narrow doubly-periodic rectangle with the narrow dimension (labelled by the x coordinate) aligned along the turbulent band. The long dimension of the domain (labelled by the z coordinate) is orthogonal to the bands, i.e. it is aligned with the pattern wavevector. The relationship between streamwise-spanwise coordinates and (x, z) coordinates is:

$$\mathbf{e}_{\text{streamwise}} = \quad \cos\theta\,\mathbf{e}_x + \sin\theta\,\mathbf{e}_z \tag{1.2a}$$

$$\mathbf{e}_{\text{spanwise}} = \; - \; \sin\theta\,\mathbf{e}_x + \cos\theta\,\mathbf{e}_z \tag{1.2b}$$

The wall-normal coordinate is denoted y and is independent of the tilt.

The angle in this study is fixed at $\theta = 24°$, as has been used extensively in the past. The tilt angle of the domain imposes a fixed angle on turbulent bands. (Turbulent bands at larger angles have also been observed in large or tilted domains.) The narrowness of the computational domain in the x direction prohibits any large-scale variation along turbulent bands, effectively simulating infinitely long bands. These restrictions of a tilted domain have both advantages and disadvantages for simulations of transitional turbulence. We return to this in the discussion.

We have carried out direct numerical simulations (DNS) using the parallelized pseudospectral C++-code ChannelFlow (Gibson, 2012). This code simulates the incompressible Navier-Stokes equations in a periodic channel by employing a Fourier-Chebychev spatial discretization, fourth-order semi-implicit backwards-differentiation time stepping, and an influence matrix method with Chebyshev tau correction to impose incompressibility in the primitive-variable formulation. The velocity field is decomposed into a parabolic base flow and a deviation, $\mathbf{U} = \mathbf{U}_{\text{base}} + \mathbf{u}$, where the deviation field $\mathbf{u}$ has zero flux. Simulating in the tilted domain gives velocity components $\mathbf{u} = (u, v, w)$ aligned with the oblique coordinates (x, y, z). All kinetic energies reported here are those of the deviation from laminar flow $\frac{1}{2}\int(u^2 + v^2 + w^2)$, rather than the turbulent kinetic energy (defined to be that of the deviation from the mean velocity).

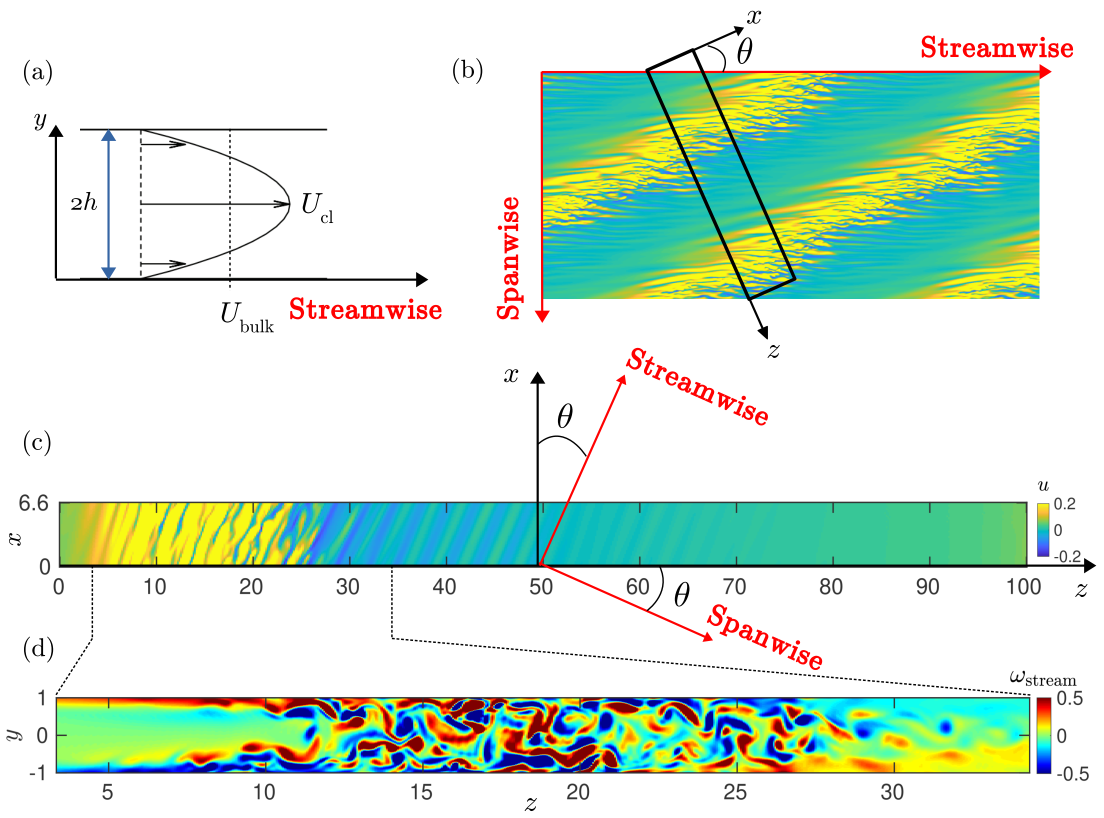

Figure 1.1: (a) Sketch of the laminar profile. (b) Visualization of turbulent bands in a 240 × 108 streamwise-spanwise domain at $Re = 1000$. Colors indicate the streamwise velocity in the $y = -0.8$ plane. A superimposed black box illustrates a long-narrow computational domain, tilted with an angle θ relative to the streamwise direction. (c) and (d) Structure of a turbulent-laminar pattern computed in a tilted domain at $Re = 1200$. Plot (c) shows the x component of the velocity in the (x, z) plane at $y = -0.8$. The streamwise and spanwise directions are indicated in red. Plot (d) shows streamwise vorticity in a (y, z) plane with the vertical y scale stretched by a factor of 2. Only the portion of the computational domain containing the turbulent region is shown in (d). As seen in (c), on the downstream side of the turbulent region the flow exhibits weak straight streaks, oriented in the streamwise direction, that slowly diminish as the flow returns laminar.

Most of the simulations presented have been carried out in a domain with dimensions $(L_x, L_y, L_z) = (6.6, 2, 100)$. The numerical resolution is $(N_x, N_y, N_z) = (84, 64, 1250)$, which both ensures that $\Delta x = \Delta z \simeq 0.08$ and that Δy varies from $\Delta y = \cos(31\pi/64) = 0.05$ at $y = 0$ to $\Delta y = 1 - \cos(\pi/64) = 0.001$ at $y = \pm 1$. This resolution has been shown to be sufficient to simulate small turbulent scales at low Reynolds numbers (Kim *et al.* (Kim *et al.*, 1987), Tsukahara *et al.* for $Re = 1370$ (Tsukahara *et al.*, 2005*a*)).

In the Fourier-Chebychev discretization the deviation velocity is expressed as:

$$\mathbf{u} = \sum_{-N_x/2+1}^{N_x/2} \sum_{-N_z/2+1}^{N_z/2} \sum_{0}^{N_y} \hat{\mathbf{u}}_{m_x,m_y,m_z} e^{i(k_x m_x x + k_z m_z z)} T_{m_y}(y) \tag{1.3}$$

where $k_x = 2\pi/L_x$, $k_z = 2\pi/L_z$, $\hat{\mathbf{u}}_{m_x,m_y,m_z}$ are the Fourier-Chebyshev coefficients, and $T_{m_y}(y)$ are the Chebychev polynomials. For brevity, we will refer to m_x and m_z (rather than $m_x k_x$, $m_z k_z$) as wavenumbers.

The structure of a typical turbulent band in this domain is shown on Fig. 1.1. A series of straight periodic streaks is visible downstream of the turbulent band, whereas the upstream laminar-turbulent interface is much sharper. Streaks are visible here as streamwise velocity modulated along the spanwise direction. They are wavy in the core of the turbulent zone, in accordance with the self-sustaining process of transitional turbulence (Waleffe, 1997).

Our choice for the standard domain dimensions, $(L_x, L_y, L_z) = (6.6, 2, 100)$, is dictated as follows: $L_y = 2$ is fixed by non-dimensionalization. The choice of the short dimension L_x is dictated by the natural streak wavenumber. In plane Couette flow, this was found to be approximately $L_{x,\text{Couette}} = 10 = 4/\sin 24°$ (Hamilton *et al.*, 1995), and widely used since (Barkley & Tuckerman, 2005; Shi *et al.*, 2013). Chantry *et al.* showed that the correspondence between length scales in plane Couette and plane channel flows is $h_{\text{Poiseuille}} \simeq 1.5 h_{\text{Couette}}$ (by doubling the Couette height and subtracting the resulting spurious mid-gap boundary layer (Chantry *et al.*, 2016)). This leads to an optimal short dimension in a 24° box of $L_{x,\text{Poiseuille}} = 6.6$. ($L_x = 6.6$ has also been used in (Paranjape *et al.*, 2020), whereas $L_x = 10$ was used in (Tuckerman *et al.*, 2014).) $L_z = 100$ is chosen to be sufficiently large that periodicity in the z-direction does not have a significant effect on the turbulent band dynamics, as we will see in the next section.

1.3 Band velocity and interaction length

As in pipe flow (Hof *et al.*, 2010; Samanta *et al.*, 2011; Barkley, 2016), bands in channel flow interact when sufficiently close and this can affect the quantities we seek to measure. For example, in a one-dimensional directed percolation model (Shih, 2017, p. 167), the time scales observed for decay and splitting increase strongly with the inter-band distance, while the critical point increases weakly. We wish to choose the length L_z of our domain to be the minimal distance above which bands can be considered to be isolated.

Unlike their counterparts in plane Couette flow, turbulent bands in plane channel flow are not stationary relative to the bulk velocity U_{bulk}. As in pipe flow (Avila *et al.*, 2011; Barkley *et al.*, 2015), bands move either faster or slower than the bulk velocity, depending on the Reynolds number (Tuckerman *et al.*, 2014). One important way in which the interaction between bands manifests itself is by a change in propagation speed.

Figure 1.2 illustrates some of the key issues via spatio-temporal plots of turbulent bands in a reference frame moving at the bulk velocity. Note that the imposition of periodic boundary conditions in z leads to interaction across the boundary. Figure 1.2a illustrates a typical long-lived turbulent band at $Re \lesssim 1000$. The band moves slowly in the positive z direction, *i.e* downstream relative to the bulk velocity, and then decays, i.e. the flow relaminarizes.

Figure 1.2b illustrates a typical band splitting at $Re = 1100$, for which bands move upstream relative to the bulk velocity. At $t \simeq 13\,000$ a daughter band emerges from the downstream side of the parent band, very much like puff splitting observed in pipe flow (Avila *et al.*, 2011; Shimizu *et al.*, 2014). Following the split, the distance between bands decreases (from $L_z = 100$ to $L_z/2 = 50$), thereby increasing the band interaction, as can be seen by a change in the propagation velocity following the split. The time range in Fig. 1.2b is very long and this visually accentuates the speed change. The absolute speed change following the split is approximately 1% of the bulk velocity. Figure 1.2c presents a band splitting in a box of size $L_z = 50$ at $Re = 1200$ and shows a more pronounced difference in propagation velocities between the single band and its two offspring. The quasi-laminar gap separating the two offspring bands is quite narrow and hence the bands can be assumed to strongly interact. The spatio-temporal diagrams of Fig. 1.2 also show that the size of turbulent bands increases slightly with Re, and moreover that fluctuations in the size and propagation speed become greater. Fluctuations are more pronounced on the downstream side of bands. More quantitatively, we have measured the propagation speed, U_{band}, of single turbulent bands over a range of Re in domains of different lengths L_z, as shown in Fig. 1.3. Periodic boundary conditions in z set the center-to-center interaction distance between bands to the domain length L_z. Single bands were simulated for up to a total of 70000 time units. Error bars (only shown in case $L_z = 100$ for clarity) represent normal-approximated confidence intervals for time-weighted velocity measurements over the multiple simulations comprising the total simulation time. Care was taken to discard pushing effects due to missed splittings or decays that may deviate the band from its average velocity. An initial time $t_0 > 0$ was subtracted to eliminate the effect of the initial conditions (see Sec. 1.4 and 1.5).

We find that the band speed becomes independent of L_z for $L_z \gtrsim 100$. The speeds vary approximately linearly with Re, over the range studied, and remain close to the bulk velocity: $|U_{\text{band}} - U_{\text{bulk}}|$ is less than 2% of U_{bulk}. For values of $L_z < 100$, speeds are shifted

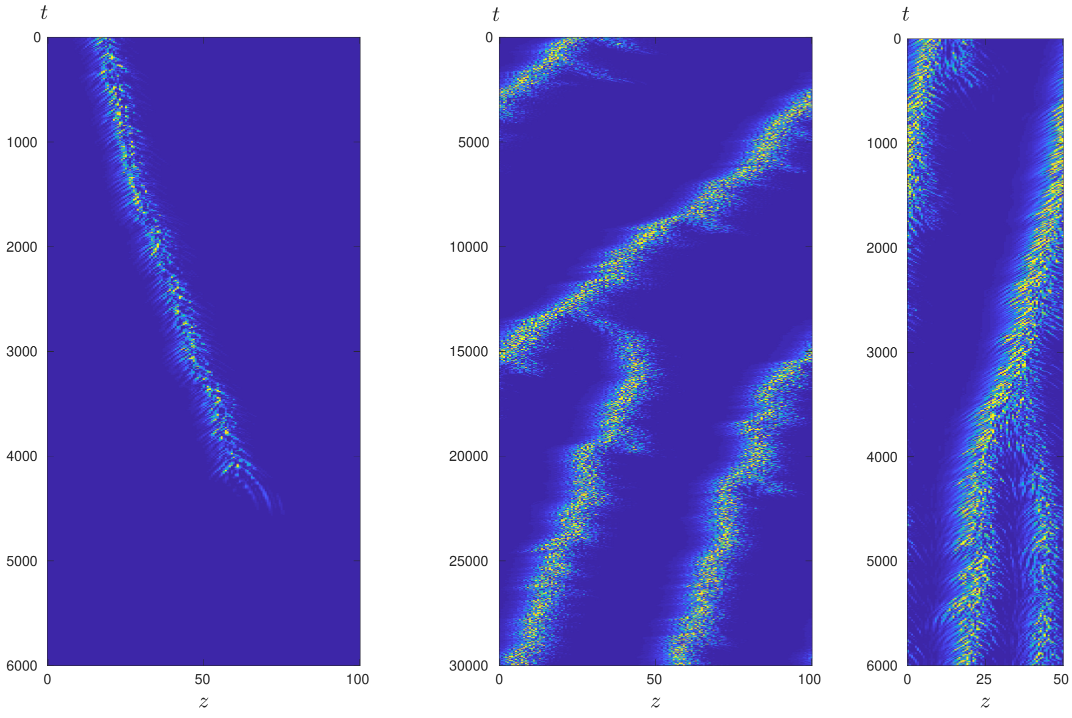

(a) **(b)** **(c)**

Figure 1.2: Space-time diagrams of turbulent bands in a frame moving at the bulk velocity, U_{bulk}, with (a) $Re = 830$, $L_z = 100$, (b) $Re = 1100$, $L_z = 100$, (c) $Re = 1200$, $L_z = 50$. Colors show the perturbation energy $E = \frac{1}{2}(u^2 + v^2 + w^2)$ as a function of z and t, sampled in the $y = -0.8$ plane at a arbitrary value of x (yellow: $E = 0.1$, blue: $E = 0$). Average band propagation velocities, relative to U_{bulk}, and the degree of fluctuations can be discerned from diagrams. Case (a) is an example of a band moving downstream relative to U_{bulk}, which occurs for $Re \lesssim 1000$, and then decaying. In case (b), a single band in a domain with $L_z = 100$ splits into two bands, resulting in a pair of bands separated in z by distance $50 = L_z/2$. The change in velocity resulting from a decrease in interaction distance is evident. Note, however, that the time range covered in the plot is large, which visually accentuates the effect. Case (c) shows band splitting in a domain of size $L_z = 50$. The resulting bands are closely spaced and interact strongly.

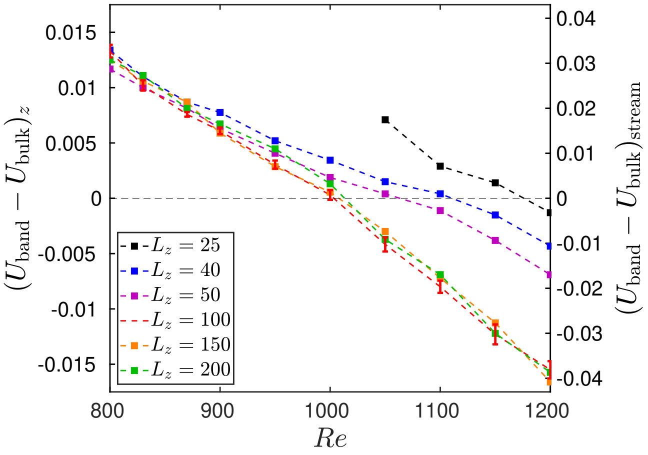

Figure 1.3: Dependence of the band propagation velocity on the Reynolds number and on the inter-band distance L_z (left axis: z velocity, right axis: streamwise velocity). Normal-approximated error bars are shown for $L_z = 100$.

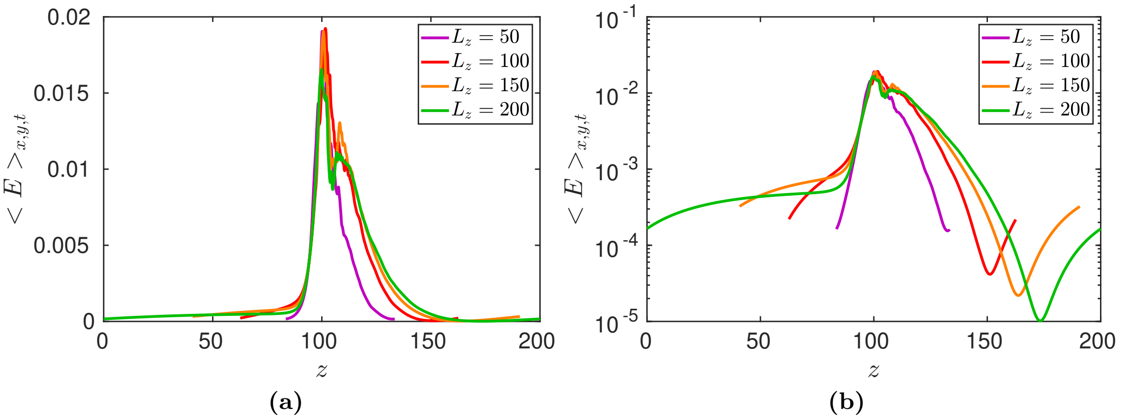

(a) **(b)**

Figure 1.4: Energy averaged over x, y and t as a function of z, for different L_z, in (a) linear and (b) logarithmic scales, for a one-band state at $Re = 1000$

upwards, and their slopes vary from the slope at higher L_z. Note that bands at $L_z = 25$ are not sustained for $Re \lesssim 1050$. Values at $L_z = 40$ are similar to those reported in a domain of the same size in (Tuckerman *et al.*, 2014); Figure 1.3 shows that this inter-band separation is too small to be in the asymptotic regime. (In addition, here the streamwise velocity is defined as $v_z/\sin\theta$, i.e. such that its projection in the z direction is the z velocity, whereas in (Tuckerman *et al.*, 2014) it is defined to be $v_z \sin\theta$, i.e. the projection of the z velocity along the streamwise direction.)

The streamwise band speeds observed here compare with what is known for puff speeds in pipe flow. For Reynolds numbers near where the puff speed equals the bulk velocity, the speed is given by $U_\mathrm{p} - \bar{U} \simeq -2.4 \times 10^{-4}(Re - 1995)$, where U_p is the nondimensional puff speed and $\bar{U} = 1$ is the nondimensional bulk velocity for pipe flow. (This expression comes from the data given in supplemental material for Ref. (Avila *et al.*, 2011).) Making a linear approximation to the data in Fig. 1.3, the streamwise band speeds can be approximated by $(U_\mathrm{band} - U_\mathrm{bulk})_\mathrm{stream} \simeq -1.7 \times 10^{-4}(Re - 1000)$. Thus we find that variation of speed with Reynolds number is of the same magnitude in the two cases, that is the coefficients -2.4×10^{-4} and -1.7×10^{-4} are comparable. Both coefficients are negative reflecting that the downstream speed decreases as Reynolds number increases. (The reason for this is discussed at length for pipe flow in (Barkley *et al.*, 2015; Barkley, 2016).) If one uses $2h$ for the length scale and bulk velocity for the velocity scale in channel flow, the coefficient for channel flow changes slightly to become -1.9×10^{-4}. Detailed comparisons beyond this are not obviously meaningful without a precise way to map the Reynolds numbers between the two flows.

We also compare the kinetic energy profile in z of stationary single bands at $Re = 1000$, calculated in domains with L_z between 50 and 200. Figure 1.4a shows the kinetic energy, i.e. the deviation from laminar flow, averaged over x, y, and $\Delta T = 1000$, as a function of z, centered at $z = 100$. We see a strong peak and width that, except for $L_z = 50$, are nearly independent of L_z. The logarithmic representation of Fig. 1.4b highlights the weak tails of the turbulent bands. Except for $L_z = 50$, all have an upstream ”shoulder”, i.e. a change in curvature followed by a plateau. All have a downstream minimum, whose position depends on L_z: for $L_z = 50$ and 100, it is located halfway from the peak to its periodic repetition; for $L_z > 100$ the ratio of this distance to L_z decreases with increasing L_z. We doubled the resolution in the z direction, and observed very little effect ($< 2\%$) on the localization of the minimum.

Localized turbulent regions have been studied in other realizations of wall-bounded shear flows. For exact computed solutions of plane channel flow, the downstream spatial decay is observed to be more rapid than the upstream decay (Zammert & Eckhardt, 2014, 2016; Paranjape *et al.*, 2020), as in our case. In plane Couette flow (Barkley & Tuckerman, 2005; Brand & Gibson, 2014), the upstream and downstream spatial decay rates are equal, by virtue of symmetry, while those of pipe flow show a strong dependence of the upstream decay rate on Reynolds number (Ritter *et al.*, 2018). Asymmetry between upstream and downstream spatial decay rates is also seen in turbulent spots in boundary layer flow

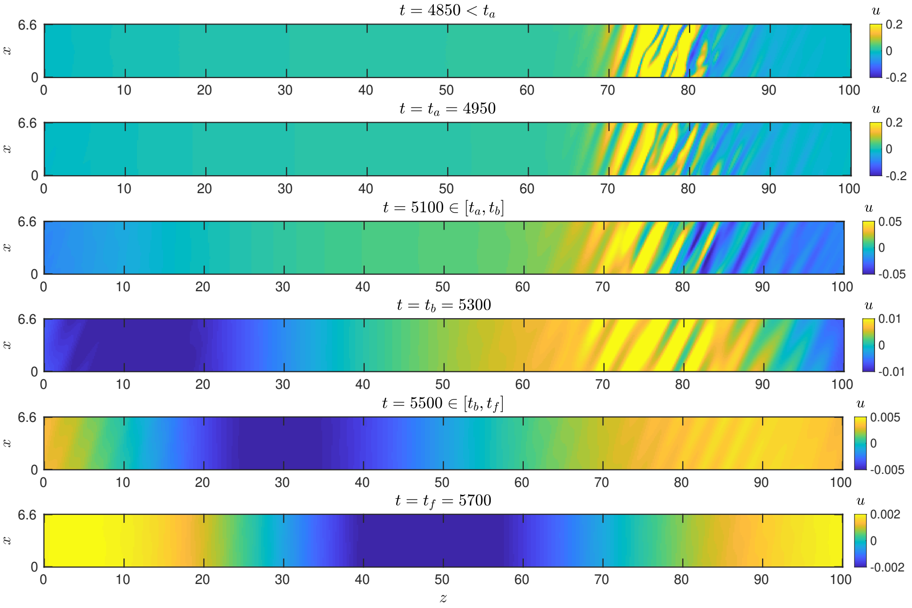

Figure 1.5: Band decay at $Re = 830$. Plotted is the x velocity in (x, y) planes at $y = -0.8$. For clarity the color scale changes over time.

(Marxen & Zaki, 2019) and in Poiseuille-Couette flow (Klotz *et al.*, 2017).

Notwithstanding the long-range weak tails in Fig. 1.4b, we believe that turbulent bands in domains of at least $L_z = 100$ can be considered as isolated: the quasi-laminar gap is sufficiently wide that one band does not substantially affect its neighbor and modify its velocity.

1.4 Analysis of decay and splitting

1.4.1 Decay

We now focus on the decay and splitting events. Figure 1.5 illustrates a typical decay event, a turbulent band at $Re = 830$ that persists as a long-lived metastable state before abruptly decaying to laminar flow. A visualisation of the x velocity is shown in the $y = -0.8$ plane, approximately where the streaks are most intense, at representative times during the final decay to laminar flow.

States can be quantitatively characterized via their instantaneous (x, z) Fourier spectra. Figure 1.6 shows an example of such a 2D Fourier spectrum of the x velocity at $y = -0.8$, $Re = 830$, corresponding to the snapshot $t = 4850$ on Figure 1.5. We observe that the amplitudes along horizontal lines $m_x = 0$ and $m_x = \pm 1$ are much larger than the

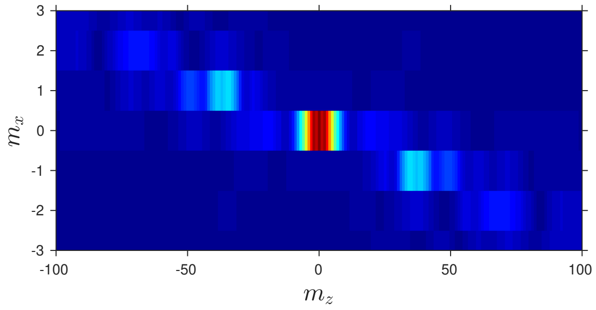

Figure 1.6: Example of a (x, z) Fourier spectrum of the x velocity u in the $y = -0.8$ plane, for a turbulent band at $Re = 830$. Colors show the modulus of spectral coefficients, spanning from 0 (blue) to 0.02 (red). The modulus of components $(m_x, -m_z)$ and $(-m_x, m_z)$ are equal since the velocity is real.

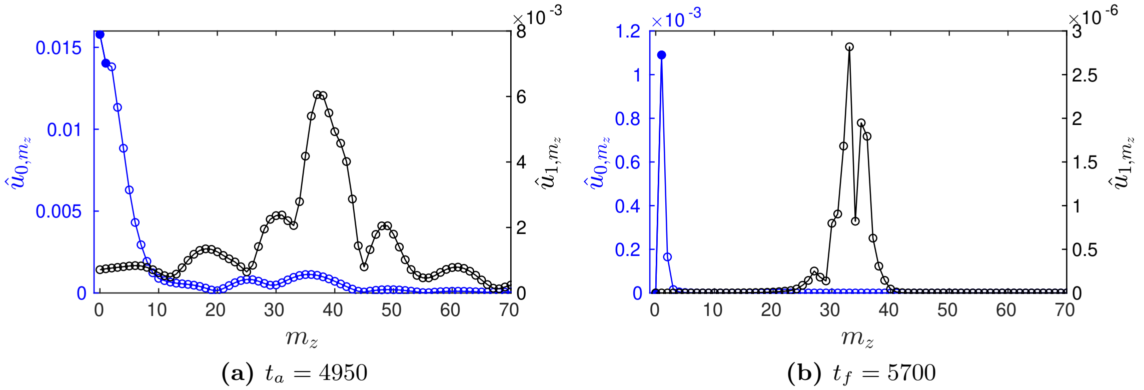

(a) $t_a = 4950$ **(b)** $t_f = 5700$

Figure 1.7: Illustrative Fourier spectra $\hat{u}_{0,m_z}$ and $\hat{u}_{1,m_z}$ (a) before band decay and (b) in the final relaxation to laminar flow. $Re = 830$. The black symbols $\hat{u}_{1,m_z}$ with m_z surrounding 35 correspond to streaks while the blue symbols $\hat{u}_{0,m_z}$ at low m_z correspond to large-scale structures. Filled symbols indicate $\hat{u}_{0,1}$ and $\hat{u}_{0,2}$.

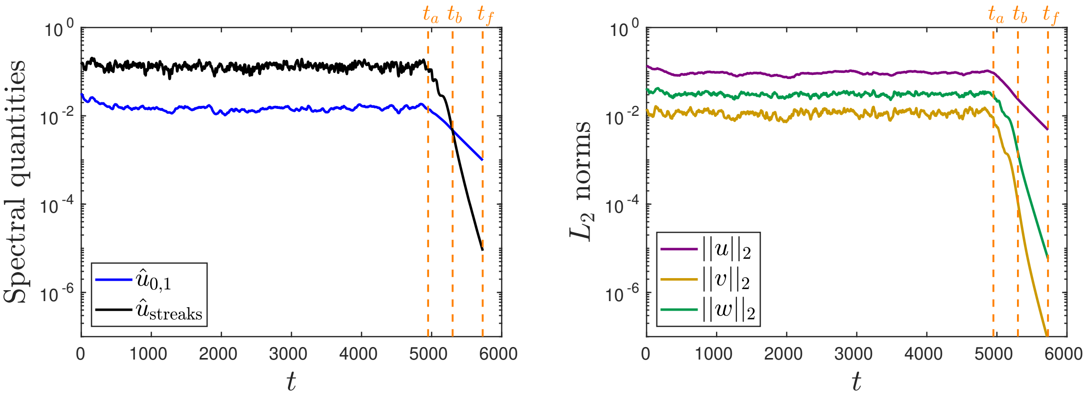

Figure 1.8: Time evolution of (a) spectral quantities $\hat{u}_{0,1}$ and $\hat{u}_{\text{streaks}}$, (b) L_2 norms $||u||_2$, $||v||_2$ and $||w||_2$ for a decay event at $Re = 830$. Times t_a, t_b and t_f refer to slices shown on Fig. 1.5. The band starts to decay at t_a, $\hat{u}_{0,1} = \hat{u}_{\text{streaks}}$ at t_b, and the relaminarization is considered as complete at t_f.

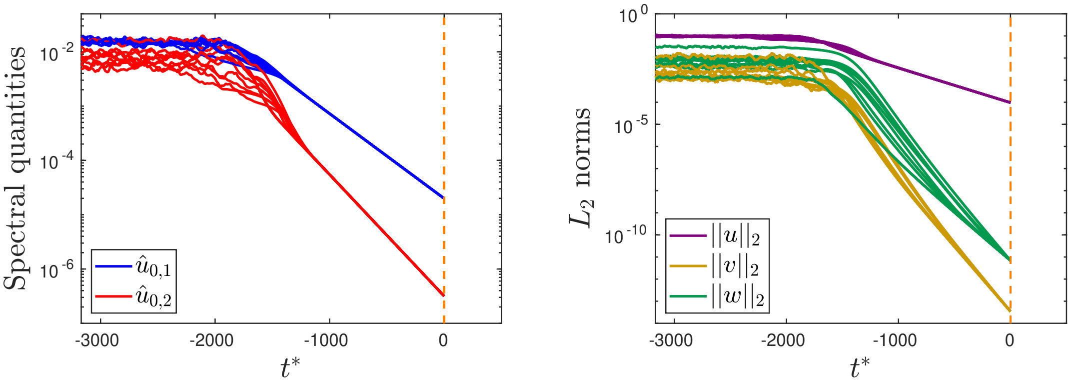

Figure 1.9: Time evolution of (a) $\hat{u}_{0,1}$ and $\hat{u}_{0,2}$ and of (b) $||u||_2$, $||v||_2$ and $||w||_2$ during ten realizations of decay events at $Re = 830$. Time t^* and vertical quantities are respectively translated and scaled to obtain the same final value for each realization. Final decay rates for $\hat{u}_{0,1}$ and $\hat{u}_{0,2}$ (a) are -3.6×10^{-3} and -5.2×10^{-3}, respectively.

others. For brevity, we use $\hat{u}_{m_x,m_z}$ to denote the modulus of the 2D Fourier component $(\pm m_x, \mp m_z)$ of the x velocity evaluated at $y = -0.8$. We recall from Eq. (1.3) that $m_x = 1$ corresponds to a wavelength of $L_x = 6.6$, while $m_z = 1$ corresponds to a wavelength of $L_z = 100$. The large-scale pattern for a single band is characterized by the x-constant and z-trigonometric Fourier coefficient $\hat{u}_{0,1}$. Streaks are the small-scale spanwise variation of the streamwise velocity. Here we use the x-trigonometric Fourier coefficients of the x-velocity as a proxy for streak amplitude:

$$\hat{u}_{\text{streaks}} = \sum_{m_z=0}^{100} \hat{u}_{1,m_z}$$

While the x direction of the tilted domain does not correspond to the spanwise direction, it is clear from Fig. 1.5 that the streaks correspond to x-wavenumber $m_x = 1$. The velocity in the x direction is not the streamwise velocity, but it has a large projection in the streamwise direction.

Figure 1.7 illustrates the spectra before decay ($t_a = 4950$) and near at the end of the decay process ($t_f = 5700$). The final stages of the flow field as it returns to laminar flow is almost exclusively contained in the $\hat{u}_{0,1}$ coefficient corresponding to no x dependence and trigonometric z dependence on the scale of the simulation domain. Weak streaks are still discernible, but their amplitudes are 10^{-3} that of the large-scale flow $\hat{u}_{0,1}$. (Note right-hand scale in Fig. 1.7(b).) This shows that the decay from a turbulent band to the laminar state results in a large-scale flow structure aligned with, and moving parallel to, the band. This large-scale flow, although weak and declining during laminarization, dominates the streak patterns characterizing turbulence.

Figure 1.8 plots the time evolution of spectral quantities and velocity norms. The life of the band is characterized by small random fluctuations in the spectral quantities and the velocity norms, especially $\hat{u}_{\text{streaks}}$, which shows the strongest variability. After time $t = t_a = 4950$, all the signals suddenly undergo exponential decay, with $||u||_2$ and $\hat{u}_{0,1}$ decaying more slowly than $||w||_2$, $||v||_2$ and $\hat{u}_{\text{streaks}}$. Small-scale streaks and rolls have been shown to have different temporal decay rates in a Couette-Poiseuille quenching experiment (Liu *et al.*, 2020).

After the decay process begins, the averaged absolute level of the streaks $\hat{u}_{\text{streaks}}$ decays more rapidly than the large-scale component $\hat{u}_{0,1}$, resulting in the crossing of $\hat{u}_{\text{streaks}}$ and $\hat{u}_{0,1}$ at time $t = t_b = 5300$ in Fig. 1.8a. From this point, the one-band structure becomes prominent in comparison with the streaks. One sees indeed on the physical slices of Fig. 1.5 that the remaining weak flow consists primarily of an L_z-periodic structure, constant over x, and moving parallel to the previous band. Band-orthogonal and cross-channel velocities w and v are negligible in comparison to u, and only show a remaining streaky pattern.

We now consider how these quantities vary for different decay events. Figure 1.9

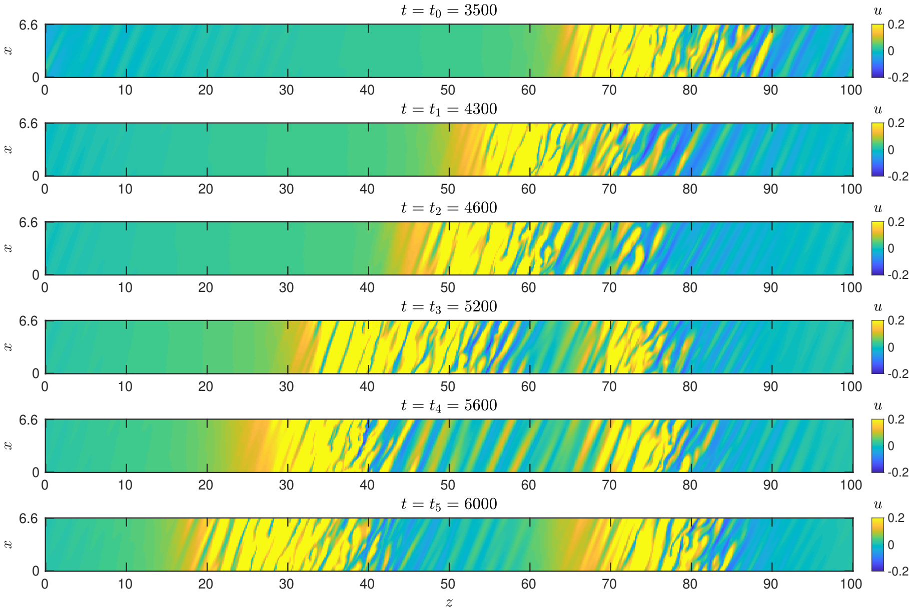

Figure 1.10: Band splitting at $Re = 1200$. Plotted is the x velocity in (x, y) planes at $y = -0.8$.

presents the evolution of spectral quantities and velocity field norms for 10 decay events. For each realization i, time is translated, $t^* = t - t_{f,i}$, so that all realizations end at the same time: $t^* = 0$. Quantities are also normalized to obtain the same final value: $q^* = \min(q_{f,i}) \times q_i/q_{f,i}$. Note that the final time for the simulation t_f is dictated by the criterion $||u||_2 < 5 \times 10^{-3}$ and that $||u||_2$ is dominated by $\hat{u}_{0,1}$, which is why both signals terminate with the same final value for each realization.

The evolution of the spectral component $\hat{u}_{0,1}(t)$ for the different realizations all eventually collapse onto a single curve. The same is true, slightly later, for $\hat{u}_{0,2}(t)$. These final phases of the evolution correspond to viscous diffusion; $\hat{u}_{0,1}(t)$ and $\hat{u}_{0,2}(t)$ evolve towards eigenvectors of laminar plane channel flow. The difference between their decay rates (eigenvalues) is due to differences in their cross-channel dependence.

The norm $||u||_2$ also behaves in this way, since it is dominated by $\hat{u}_{0,1}$, but $||v||_2$ and $||w||_2$ do not. These are sums over different spectral components each with its own decay rate, and the levels of these components differ from one realization to the next, thereby leading to different decay rates for each realization.

1.4.2 Splitting

A splitting event at $Re = 1200$ is shown in Fig. 1.10 via the evolution of (x, z) slices of u, at times from t_0 (initial band) to t_5. The turbulent band at $t_1 = 4300$ is wider

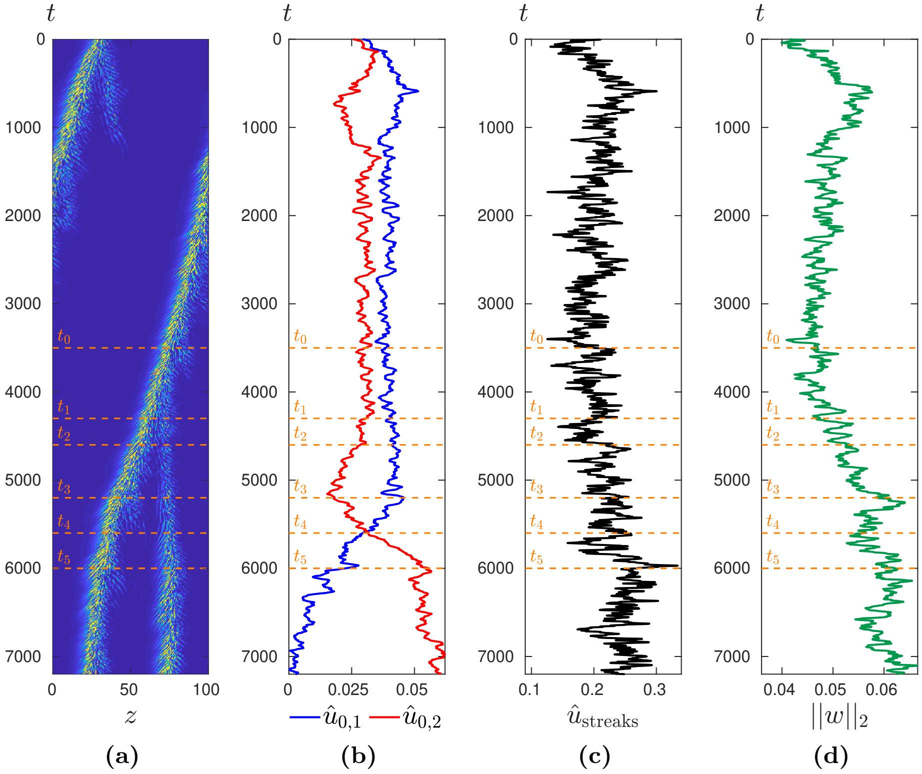

Figure 1.11: Evolution of a band while it splits at $Re = 1200$. (a) Spatiotemporal diagram of the band. Colors show the turbulent perturbation energy E between 0 (blue) and 0.1 (yellow). (b, c, d) Time evolution of spectral quantities $\hat{u}_{0,1}$ and $\hat{u}_{0,2}$ (b), $\hat{u}_{\text{streaks}}$ (c) and the L_2-norm $||w||_2$ (d).

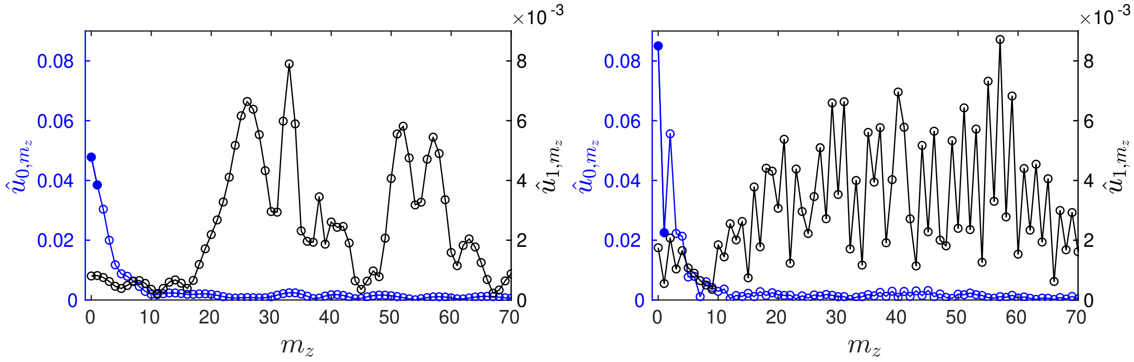

(a) $t_0 = 3500$ **(b)** $t_5 = 6000$

Figure 1.12: Illustrative Fourier spectra $\hat{u}_{0,m_z}$ and $\hat{u}_{1,m_z}$ (a) before and (b) after band splitting at $Re = 1200$. The black symbols $\hat{u}_{1,m_z}$ with m_z surrounding 35 correspond to streaks while the blue symbols $\hat{u}_{0,m_z}$ at low m_z correspond to large-scale structures. Filled symbols indicate $\hat{u}_{0,1}$ and $\hat{u}_{0,2}$.

than it is at $t_0 = 3500$. At $t_2 = 4600$ one sees the appearance of a gap in the turbulent region corresponding to the birth of the second band. The parent band continues to move towards lower z while the child band remains at its position and intensifies from t_2 to t_5, smoothly acquiring all the characteristics of the parent band.

Figure 1.11 presents a spatio(z)-temporal diagram of the perturbation energy and traces the evolution of spectral quantities $\hat{u}_{0,1}$ and $\hat{u}_{0,2}$ at $y = -0.8$, which represent a single or a double banded pattern. The evolution of $\hat{u}_{\text{streaks}}$ and of the L_2-norm $||w||_2$ are also shown. A slight initial drop in the two-band coefficient $\hat{u}_{0,2}$ is seen from $t = t_1 = 4300$, which coincides with the appearance of the second band. A laminar gap opens between the initial band and its offspring at $t = t_2 = 4600$. Then $\hat{u}_{0,2}$ starts to increase whereas $\hat{u}_{0,1}$ decreases, from $t = t_3 = 5200$. The two quantities cross at $t = t_4 = 5600$ and finally reach plateaus at $t = t_5 = 6000$. This is the time from which the energy of the second band reaches approximately the same level as that of the first band, as seen from the spatio-temporal diagram (Fig. 1.11a). The other quantities, $\hat{u}_{\text{streaks}}$ and $||w||_2$, follow slightly different trends from those of the spectral coefficients, as shown on Fig. 1.11c and 1.11d. Oscillations in $\hat{u}_{\text{streaks}}$ are strong and it is difficult to distinguish trends corresponding to the band evolution. However, there is a relatively strong increase in the streak intensity just before t_5, when the second band is fully developed. In addition, $||w||_2$ increases from t_1 to t_3 and then reaches a plateau of around 0.06.

The evolution before the splitting shows a missed splitting event between $t = 200$ and 1000. A weakly turbulent patch detaches from the initial stripe, and quantities $\hat{u}_{0,1}$, $\hat{u}_{0,2}$, $\hat{u}_{\text{streaks}}$, and $||w||_2$ all follow a trend between $t = 200$ and 600 similar to that between t_2 and t_3. The birth ceases after $t = 1000$: $\hat{u}_{0,2}$ does not increase sufficiently to cross $\hat{u}_{0,1}$, and $\hat{u}_{\mathrm{streaks}}$ and $||w||_2$ drop to their previous levels.

Figure 1.12 shows a comparison between Fourier spectra $\hat{u}_{0,m_z}$ and $\hat{u}_{1,m_z}$ before and after splitting. The decrease in $\hat{u}_{0,1}$ and increase in $\hat{u}_{0,2}$, already seen in Fig. 1.11b, appears clearly. In addition, the two-band streak spectrum $\hat{u}_{1,m}$ shows conspicuous small-scale oscillations due to the fact that a perfectly $L_z/2$-periodic field would contain only even modes.

We now carry out simulations, still at $Re = 1200$, in a shorter tilted domain of length $L_z = 50$ to avoid secondary splittings which would lead to a three-band state. All realizations of the formation of the second band follow the same sequence of events previously described. Meanwhile, the three-band component $\hat{u}_{0,3}$ can also be monitored to analyze the interactions between modes 1 and 2 during the splitting.

This evolution is represented in a phase portrait $(\hat{u}_{0,1}, \hat{u}_{0,2}, \hat{u}_{0,3})$ in Fig. 1.13. The one-band state is characterized here by an average segment around which the spectral components show noisy oscillations (state 1) because of the proportionality between the components. Because the two-band state selects the even components (see Fig. 1.12b), $\hat{u}_{0,1}$ and $\hat{u}_{0,3}$ have low values and show no correlation with the prominent $\hat{u}_{0,2}$. This representation shows that large-scale spectral components statistically follow the same transition path from one to two turbulent bands. This common transition path can be seen as a low-dimensional projection of the dynamics of band splitting. Such a statistical pathway for configuration changes in a turbulent fluid system was observed in the case of barotropic jet nucleation (Bouchet *et al.*, 2019).

1.5 Statistics of band decay and splitting

We now investigate the decay and splitting statistics of single turbulent bands over a range of Reynolds numbers. The mean lifetime of decay increases with Re, that of splitting decreases with Re, and hence these lifetimes are equal at some Reynolds number. The primary goal here is to determine at which Reynolds number value this occurs. The domain size is fixed at $L_z = 100$. Since decay and splitting events are effectively statistical, many realisations are necessary to determine the mean decay and splitting times. Regarding the evolution of band interactions with L_z (Section 1.3), $L_z = 100$ was chosen as a compromise between mitigating the potential effect of interactions on decay and splitting probabilities and the numerical cost of a statistical study. The effect of inter-band distance on mean decay and especially on splitting times still remains an open question. To generate large numbers of initial conditions for these realisations, we start from featureless turbulent flow at $Re = 1500$ and reduce Re to an intermediate value in [900, 1050], where a single band then forms. We continue these simulations and extract snapshots, that are then used as initial conditions for simulations with $Re \in$ [700, 1350].

Each simulation is run with a predefined maximum cut-off time $t_{\mathrm{f}} = 10^5$. If a decay or

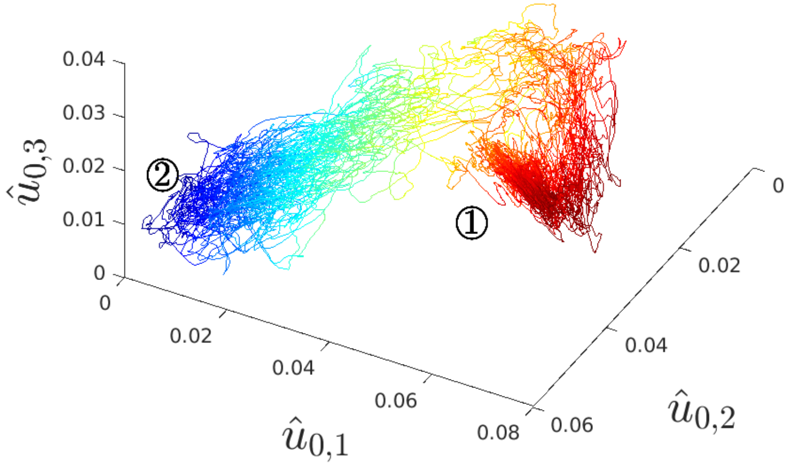

Figure 1.13: Evolution of spectral quantities during 10 splittings at $Re = 1200$, in a domain of length $L_z = 50$. Each curve represents one simulation, and is colored by $\hat{u}_{0,1}$ to illustrate the transition between a one-band (1) to a two-band state (2).

splitting event occurs before t_f, the run is automatically terminated after the event and the time is recorded. For a decay, the termination criterion is $||\mathbf{u}||_{L_2} < 0.005$, meaning that the flow has nearly reached the laminar base flow. For splitting, termination occurs when two (or more) well-defined turbulent zones (whose x and short-time averaged turbulent energy exceed 0.005) coexist over more than 2000 time units. We can then estimate the real time at which the splitting event occurs, defined as the time at which a second laminar gap appears from the initial band, through careful observations of space-time diagrams.

For a given value of Re, let N^d, N^s, and N be the number of decay events, splitting events, and the total number of runs, respectively. Thus $N - N^d - N^s$ is the number of runs reaching the cut-off time t_f without having decayed or split.

We consider first the decay statistics. (The splitting statistics follow similarly.) The analysis closely follows previous work; see especially (Avila *et al.*, 2010, 2011; Shi *et al.*, 2013). The decay times at a given Re are sorted in increasing order, giving the sequence $\{t_i^d\}_{1\leq i\leq N^d}$. The survival probability that a band has not decayed by time t_i^d is then approximated by:

$$P(t_i^d) = P(\text{decay at } t \geq t_i^d) = 1 - (i-1)/N. \tag{1.4}$$

The survival distributions for decay events over a range of Re are plotted on semi-log axes in Fig. 1.14. The data support exponential form $P(t_i^d) = \exp(-(t_i^d - t_0^d)/\tau^d(Re))$, where $\tau^d(Re)$ is the Reynolds-number-dependent mean lifetime (characteristic time) for decay and t_0^d is an offset time, for $Re \geq 750$. (The case $Re = 730$ exhibits deviations from

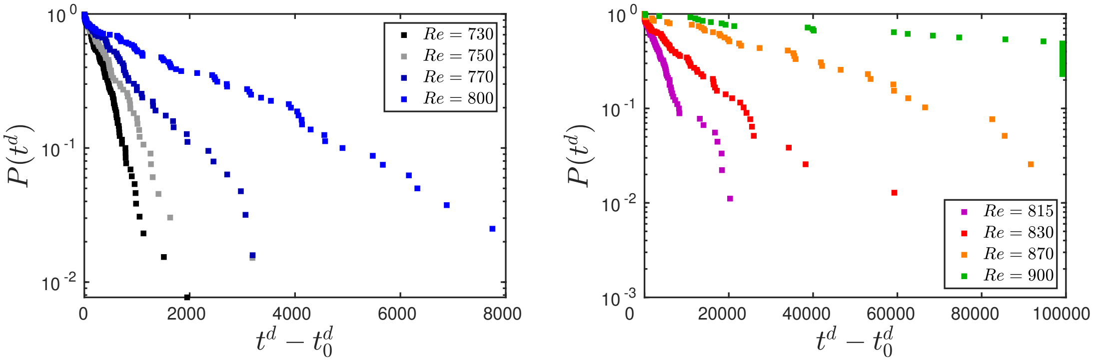

Figure 1.14: Survival probability distributions for the decay of a turbulent band, $Re \in [730, 900]$.

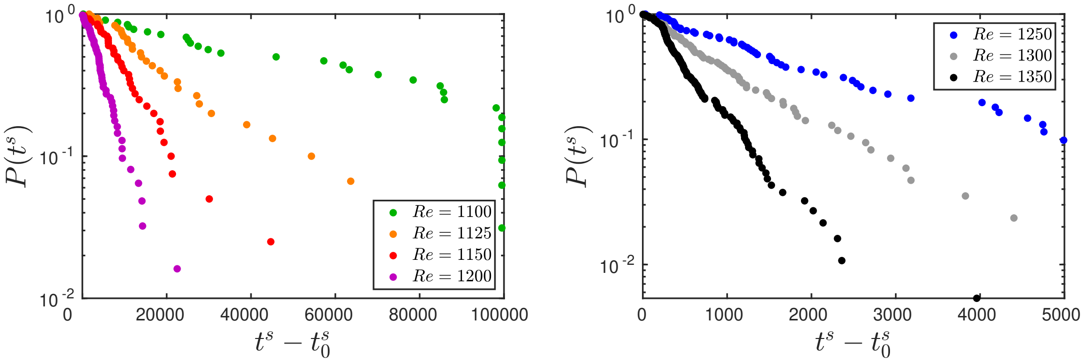

Figure 1.15: Survival probability distributions for the splitting of a turbulent band, $Re \in [1100, 1350]$.

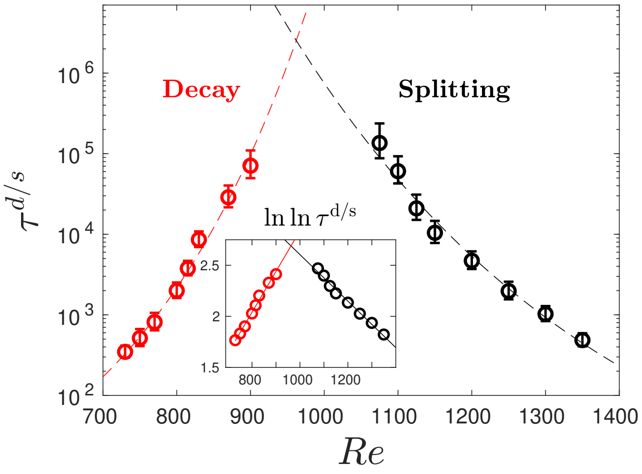

Figure 1.16: Variation of mean decay times (red) and splitting times (black) with Reynolds number Re. The error bars correspond to 95% confidence intervals. Inset: $\ln \ln \tau^{s/d}$ versus Re and associated linear fits. The crossing point is at $Re_{\text{cross}} \approx 965$, $\tau \approx 3 \times 10^6$.

an exponential distribution very similar to those observed in pipe flow at $Re = 1700$ (Avila *et al.*, 2010)). These exponential survival distributions are indicative of an effectively memoryless process, as has been frequently observed for turbulent decay in transitional flows (Darbyshire & Mullin, 1995; Faisst & Eckhardt, 2004; Hof *et al.*, 2006; Peixinho & Mullin, 2006; Willis & Kerswell, 2007; Avila *et al.*, 2010).

Quantitatively, the characteristic time $\tau^d(Re)$ is obtained by the following Maximum Likelihood Estimator (Avila *et al.*, 2010):

$$\tau^d \simeq \frac{1}{N'^d}\Big(\sum_{t_i^d > t_0^d} (t_i^d - t_0^d) + (N - N^d)(t_{\text{f}} - t_0^d)\Big) \tag{1.5}$$

where N'^d is the number of decay events taking place after t_0^d. The offset time t_0^d is included to account for the time necessary for the flow to equilibrate following a change in Re associated with the initial condition, and also the fixed time it takes for the flow to achieve the termination condition after it commences decay (as seen in Fig. 1.8b). As in (Avila *et al.*, 2010), we determine the value of t_0^d by varying it in Eq. (1.5), monitoring the resulting characteristic time τ^d, and choosing t_0^d to be the minimal time for which the estimate τ^d no longer depends significantly on t_0^d. We find $t_0^d = 850$ is a good value over the range of Re investigated.

The same procedure has been applied to the splitting events. The splitting times are denoted $\{t_i^s\}_{1\leq i\leq N^s}$, the estimated mean lifetimes are denoted τ^s, and the offset time is denoted t_0^s. In the case of splitting we find the offset time to be $t_0^s = 500$, except for $Re = 1350$, the largest value studied, where $t_0^s = 800$. It should be noted that obtaining splitting times becomes delicate at $Re = 1350$ because turbulence spreads in less distinct bands. The survival distributions for various Re are plotted in Fig. 1.15. As with decay, these data are again consistent with exponential distributions.

At $Re = 900$ and $Re = 1100$, some of the runs reach the cut-off time $t_\mathrm{f} = 10^5$. From a total simulation time of about 10^6 time units, we registered only 10 decay events at $Re = 900$ and 25 splitting events at $Re = 1100$, immediately showing that the characteristic lifetimes at these values of Re are on the order of 10^5 for $Re = 900$ and 6×10^4 for $Re = 1100$. Investigations at $Re = 950$, 1000 and 1050 were performed, but no events occurred before 10^5 time units. Due to the high numerical cost of sampling at these longer time scales, we did not attempt further investigation between $Re = 900$ and $Re = 1100$. As a result, we observed no case in which both splitting and decay events occurred at the same Reynolds number, unlike for plane Couette flow (Shi *et al.*, 2013) and pipe flow (Avila *et al.*, 2011).

Figure 1.16 shows the estimated mean lifetimes τ^d and τ^s as a function of Reynolds number. For simplicity, the error bars correspond to confidence intervals for censored data of type II (Lawless, 2002). The decay lifetimes increase rapidly as a function of Re, while the splitting times decrease rapidly as a function of Re. It is clear from the main semi-log plot that both dependencies are faster than exponential. While it is not possible to determine with certainty the functional form of the dependence on Re, the data are consistent with a double-exponential form, as shown in the inset where the double log of the lifetimes are plotted as a function of Re. The linear fits indicated in the inset are plotted as dashed curves in the main figure. From these curves one can estimate the crossing point to be $Re_\mathrm{cross} \simeq 965$ with a corresponding time-scale of about 3×10^6. The extrapolation of the data means that these values are only approximate. Nevertheless, we can be sure that the timescale of the crossing in our case is significantly above the crossing timescale of about 2×10^4 found in a similar study of plane Couette flow (Shi *et al.*, 2013), and it appears to be about a factor of 10 less than the value 2×10^7 found for pipe flow (Avila *et al.*, 2011).

1.6 Discussion and conclusion

We have studied the behavior of oblique turbulent bands in plane channel flow using narrow tilted computational domains. Bands in such domains have fixed angle with respect to the streamwise direction and are effectively infinitely long, with no large-scale variation along the band. We have measured the propagation velocity of these bands as a function of Reynolds number and inter-band spacing and found that band speed is affected by band spacing at distances greater than previously assumed (Tuckerman *et al.*, 2014).

After long times, bands either decay to laminar flow or else split into two bands. Survival distributions obtained from many realizations of these events confirm that both processes are effectively memoryless, with characteristic lifetimes $\tau^d(Re)$ and $\tau^s(Re)$, respectively. The dependence of these lifetimes on Re is super-exponential and consistent with a double-exponential scaling. Fitting the data with double-exponential forms, we estimate that the lifetimes cross at $Re_{\text{cross}} \simeq 965$, at about 3×10^6 advective time units. Below Re_{cross}, isolated bands decay at a faster rate than they split, while above Re_{cross}, isolated bands split at a faster rate than they decay. Hence Re_{cross} is very close to the critical point above which turbulence would be sustained in the tilted computational domain. Double-exponential scaling is consistent with what has been observed in pipe flow (Avila *et al.*, 2011). Such scaling is thought to be connected to extreme-value statistics, as first proposed by Goldenfeld *et al.* (Goldenfeld *et al.*, 2010) and recently examined quantitatively for puff decay in pipe flow by Nemoto & Alexakis (Nemoto & Alexakis, 2018, 2021).

The characteristic times $\tau^d(Re)$ and $\tau^s(Re)$ in plane channel flow are considerably larger than those for plane Couette flow in a similar computational domain by Shi *et al.* (Shi *et al.*, 2013), who found that splitting and decay lifetimes cross at about 2×10^4 advective time units. Time scales in plane channel flow are closer to those in pipe flow, where Avila *et al.* (Avila *et al.*, 2011) found that lifetimes cross at about 2×10^7 advective time units. The higher crossing times in plane channel flow and pipe flow pose a challenge for determining the exact crossing point. A practical consequence of this higher crossing time is that near the crossing Reynolds number, the flow has a greater tendency to appear to be at equilibrium, with neither decay nor splitting events observed over long times.

We also note that turbulent puffs in both pipe flow (Barkley *et al.*, 2015; Song *et al.*, 2017) and channel flow move slightly faster than the bulk flow for low Re and slightly slower for high Re; in both flows, the propagation speed becomes equal to U_{bulk} at a Reynolds number close to the critical point. It is possible that an explanation will be found that relates the propagation speed with the critical point.

Our crossover Reynolds number $Re_{\text{cross}} \simeq 965$ is close to what Shimizu & Manneville (Shimizu & Manneville, 2019) called a plausible 2D-DP threshold. These authors carried out channel flow simulations in a large domain and used the 2D-DP power law to extrapolate the turbulent fraction to zero, leading to a threshold of $Re_{\text{DP}} = 905$ or 984, depending on how the pressure-driven Reynolds number is converted to a bulk Reynolds number. (They did not, however, attempt to verify the other critical exponents associated with 2D-DP since they were unable to extend their data sufficiently close to Re_{DP}; see paragraph below.) This agreement between the lifetime crossing point obtained in our narrow tilted domain and the transition threshold obtained in the full planar setting for plane channel flow corroborates similar findings for plane Couette flow and stress-free Waleffe flow. Specifically, the decay-splitting lifetime crossing in tilted plane Couette flow was found by Shi *et al.* (Shi *et al.*, 2013) to occur at $Re \simeq 325$. The transition point in the planar case is not known precisely, but it has been estimated by Bottin *et al.* (Bottin

& Chaté, 1998; Bottin *et al.*, 1998) and Duguet *et al.* (Duguet *et al.*, 2010) to be close to this value. In a truncated model of Waleffe flow, tilted domain simulations indicate (Chantry, 2020) that the lifetime crossing point is at $Re_c \simeq 174$. The critical point in a very large domain was computed accurately by Chantry *et al.* (Chantry *et al.*, 2017) to be $Re_c = 173.80$. Heuristically some agreement between the two types of domains could be expected on the grounds that the onset of sustained turbulence is associated with its stabilization in a modified shear profile (Barkley, 2011, 2016; Song *et al.*, 2017) and a narrow tilted domain quantitatively captures this process. Nevertheless, the very close agreement between the thresholds in tilted and planar domains in several flows is not completely understood.

Shimizu & Manneville (Shimizu & Manneville, 2019) were prevented from approaching their estimate of Re_{DP} when lowering Re by a transition to what they called the one-sided regime. Flows in this regime contain bands of long but finite length which grow via the production of streaks at their stronger downstream heads (Xiong *et al.*, 2015; Kanazawa, 2018; Tao *et al.*, 2018; Xiao & Song, 2020). This regime thus shows a strong asymmetry between the upstream and downstream directions and therefore has no counterpart in plane Couette flow; isolated bands in plane Couette flow are transient (Manneville, 2011; Chantry *et al.*, 2017; Lu *et al.*, 2019). In the one-sided regime, bands eventually all have the same orientation of about 45° from the streamwise direction and do not form a regular pattern. Since an essential feature of this regime is the long but finite length of the bands, it cannot be simulated using narrow tilted domains. This can be viewed as a shortcoming of the tilted domain in capturing the full dynamics of channel flow, but it also has the advantage of allowing us to study channel flow with the one-sided regime excluded.

We have described the evolution of a band in a narrow tilted domain during a decay or a splitting event via Fourier spectral decomposition. During a band decay, small-scale structures, streaks and rolls, are damped more quickly, increasing the relative prominence of the large-scale flow parallel to (Coles & van Atta, 1966; Barkley & Tuckerman, 2007; Chantry *et al.*, 2016; Shimizu & Manneville, 2019; Xiao & Song, 2020) or around (Lemoult *et al.*, 2014; Shimizu & Manneville, 2019; Xiao & Song, 2020; Klotz *et al.*, 2020) a turbulent patch or band. All of our realizations have the same exponential decay rate at the end of the process.

Fourier analyses show that large-scale spectral components are correlated throughout the life of a band, but undergo opposite trends during a splitting event, due to one- and two-band interactions. By examining several realizations of band splitting, we find that the first three z-Fourier modes follow approximately the same path during the transition from one band to two bands. This characterization of the splitting pathway resembles transitions in other turbulent fluid systems for which rare-event algorithms have been applied to assess long time scales associated with infrequent events. This has been carried out in (Bouchet *et al.*, 2019) for barotropic jet dynamics in the atmosphere and in (Rolland, 2018) for a stochastic two-variable model that reproduces transitional turbulence (Barkley, 2016). This strategy will be explored in Chapter 2.

Chapter 2

Extreme events in transitional turbulence

Transitional localised turbulence in shear flows in general, and in channel flow in particular, is known to either decay to an absorbing laminar state or to proliferate via splitting. In Chapter 1, the average passage times from one state to the other was computed with brute Monte-Carlo method, and was shown to depend super-exponentially on the Reynolds number. In this chapter, we apply a rare event algorithm, the Adaptative Multilevel Splitting (AMS), to the deterministic Navier-Stokes equations to study transition paths and estimate large passage times in channel flow more efficiently than direct simulations. With help of this strategy, we build a probabilistic description of the decay and replication of localised turbulence. We especially establish a connection with extreme value distributions and show that transition between states is mediated by a regime that is self-similar with the Reynolds number. The super-exponential variation of the passage times is linked to the Reynolds-number dependence of the parameters of the extreme value distribution. Finally, motivated by instantons from Large Deviation Theory, we show that decay or splitting events approach a most-probable pathway.

This chapter is extracted from the article *"Extreme events in transitional shear flow"*, published in the *Transactions of the Royal Society A* (2022) (Gomé *et al.*, 2022).

2.1 Introduction

The route to turbulence in many wall-bounded shear flows is a spatiotemporal process that results from the interplay between the tendency for turbulence to decay or for it to proliferate. Individual decay and proliferation events occur extremely rarely near the critical Reynolds number for the onset of sustained turbulence, and this makes measuring, let alone understanding the onset of turbulence in these flows both fascinating and challenging. In this chapter we investigate these rare events.

Figure 2.1 illustrates individual decay and proliferation (splitting) events of interest. These have been obtained from numerical simulations of pressure-driven flow in a channel. The spatio-temporal diagrams of figure 2.1 display the evolution of such localised turbulent bands at two Reynolds numbers. Simulations begin after some initial equilibration time. It can be seen that the one-band state is metastable – it persists for significant time before transitioning to another state, either laminar flow, as in the upper panel, or a two-band state, as in the lower one. The corresponding phase-space picture for the governing Navier-Stokes equations is sketched in figure 2.2. Trajectories spend a significant time in a region of phase space associated with a single turbulent band, $\mathcal{A}$, before exiting the region and going to laminar flow or to the two-band state. Repeated simulations starting from one-band states (in the region $\mathcal{A}$) show that the exit times are distributed exponentially, so that decay and splitting events are effectively governed by a memoryless, Poisson process. See (Faisst & Eckhardt, 2004; Eckhardt *et al.*, 2007; Avila *et al.*, 2010, 2011; Shi *et al.*, 2013; Gomé *et al.*, 2020) and references therein.

A typical study consists of the following. For each value of the Reynolds number, Re, a large number of events is generated, from which the mean lifetime is determined by averaging the lifetimes observed in the sample events. This is the Monte Carlo approach. The process is repeated for a range of Re to obtain the mean lifetimes to decay $\tau_d(Re)$ and to split $\tau_s(Re)$. These lifetimes are observed to depend super-exponentially on Reynolds number as sketched in figure 2.2(b), and are approximated by a double exponential form: $\tau_d(Re) \sim \exp(\exp(a_d Re + b_d))$ and similarly for $\tau_s(Re)$. (Figure 2.7 discussed below contains actual measured mean lifetimes for channel flow.) The timescales cross at a critical value Re_c. Below Re_c decay events occur more frequently, while above Re_c splitting events occur more frequently. The crossover between these cases is a key mechanism in the onset of sustained turbulence in wall-bounded shear flow. This crossing point is not, however, the focus of the present study.

The present study focuses instead on two key issues associated with the rare events themselves. The first is the efficient numerical computation of mean lifetimes. In shear flows, τ_d and τ_s become extremely large near Re_c, making brute force Monte Carlo estimation of mean times exceedingly expensive. Hence we turn to a more sophisticated class of algorithms that sample rare events by advancing ensembles of trajectories, removing (pruning) unfavourable and duplicating (cloning) favourable ones. In particular, we will employ the Adaptative Multilevel Splitting (AMS) algorithm proposed by Cérou & Guyader (Cérou & Guyader, 2007; Cérou *et al.*, 2011, 2019). (This nomenclature of "splitting" in the algorithm is unrelated to the splitting of turbulent bands.) This algorithm impressively paved the way for quantitative study of low-dimensional stochastic systems, as pioneered by Rolland & Simonnet (Rolland & Simonnet, 2015), Rolland, Bouchet & Simonnet (Rolland *et al.*, 2016) or Lestang *et al.* (Lestang *et al.*, 2018). It was recently applied to large-dimensional fluid-dynamical systems such as atmospheric dynamics (Bouchet *et al.*, 2019; Simonnet *et al.*, 2021) and bluff-body flow (Lestang *et al.*, 2020). Rolland

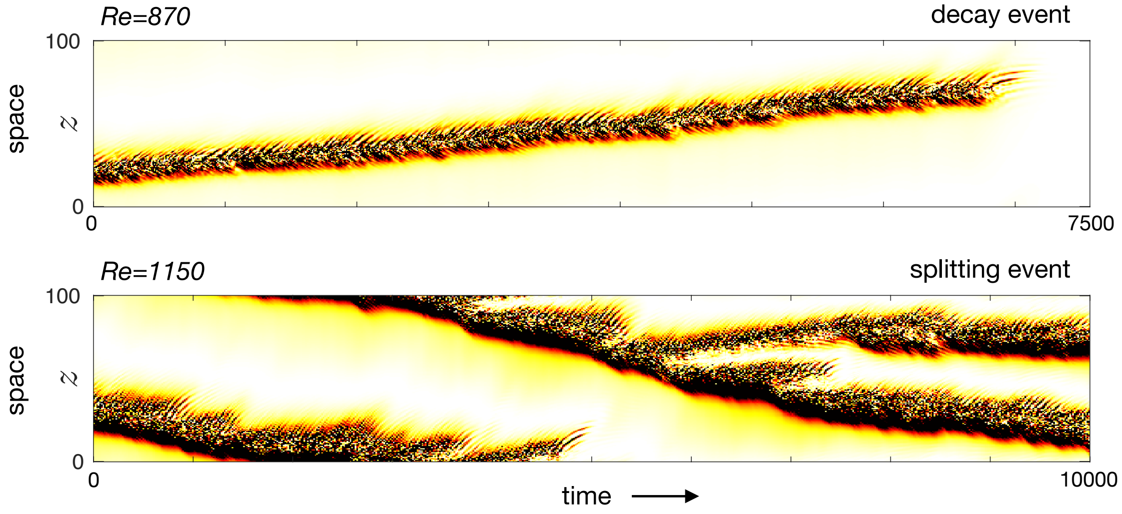

Figure 2.1: Evolution of turbulence in channel flow at two different Reynolds numbers. Turbulence is seen as black and is localised to only a portion of space. White corresponds to laminar (or nearly laminar) flow. The motion of the turbulent patch is seen in a frame of reference moving with the mean flow in the channel and the system is periodic in spatial coordinate z. At $Re = 870$ the localised band of turbulence maintains an approximately constant width and intensity for a considerable time and then abruptly transitions to laminar flow in a decay event. At $Re = 1150$ the localised turbulent band is wider and noticeably asymmetric. In this case the band splits into two bands. In the vicinity of $Re = 1000$, both of these key events become extremely rare and the mean exit time from the one-band state becomes very large. Results are obtained by a numerical simulation in an oblique domain represented in Figure 4.1.

(Rolland, 2018) extended the application of this rare-event technique to transitional turbulence, first for transition in a stochastic reduced-order model (Barkley, 2016) of pipe flow, and then for the collapse of homogeneous turbulence in plane Couette flow (Rolland, 2022).

The second main focus of our study is the origin of the super-exponential dependence of mean lifetimes on Reynolds number, and in particular the connection to extreme values of fluctuations within the one-band state. Goldenfeld, Gutenberg & Gioia (Goldenfeld *et al.*, 2010) proposed a mechanism to account for the super-exponential dependence of decay lifetimes of Reynolds number. The essential insight is that the decay process is governed by extreme values and that a linear variation of Reynolds number translates via extreme value distributions to a super-exponential variation in lifetimes. This mechanism was investigated and refined by Nemoto & Alexakis (Nemoto & Alexakis, 2018, 2021) in a numerical study of decay events in pipe flow. We will follow a similar analysis applied

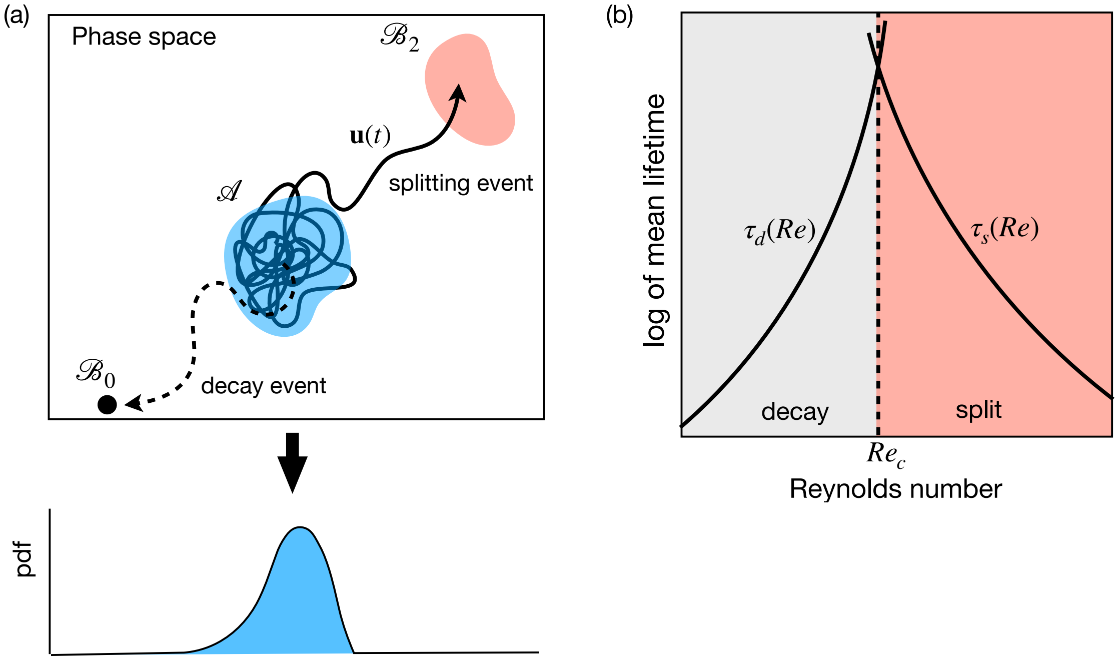

Figure 2.2: (a) Illustration of the phase space of the Navier-Stokes equations. Time evolving flow fields $\mathbf{u}(t)$ are seen as trajectories. The one-band state corresponds to a region $\mathcal{A}$ in the phase space in which trajectories $\mathbf{u}(t)$ spend considerable time before exiting and transitioning either to laminar flow $\mathcal{B}_0$ or to the two-band state $\mathcal{B}_2$. The fluctuations of observables, such as the turbulence fraction, are described by extreme value distributions. (b) Schematic showing the dependence of mean lifetimes on Reynolds number, Re. Lifetimes vary super-exponentially with Re, with τ_d increasing and τ_s decreasing with Re. The timescales cross at a critical value Re_c. Below Re_c, decay occurs more frequently while above Re_c, splitting occurs more frequently.

to both decay and splitting events in channel flow. Finally, the possible connection to the large deviation framework is considered through the computation of most-probable pathways and mean reactive times for rare events.

2.2 Methods

We will now describe two very different types of methods, first, those we use for solving the Navier-Stokes equations governing channel flow, and second, our implementation of the AMS algorithm for capturing rare events.

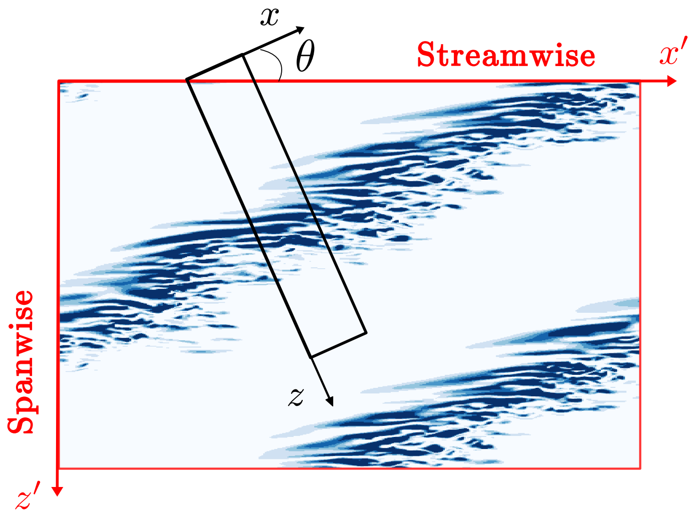

Figure 2.3: Visualisation of a turbulent band in a domain periodic in the streamwise and spanwise directions (red bounding box) at $Re = 1000$. Colors show transverse energy $\frac{1}{2}(v^2 + w'^2)$ in the plane $y = 0.8$, from our numerical simulation in a box of size $L_{x'} = 200$, $L_{z'} = 120$. Illustration of the associated tilted computational domain (black) at angle $\theta = 24°$.

2.2.1 Integration of Navier-Stokes equations in a transitional flow unit

The turbulent bands that are the subject of our study are illustrated in figure 4.1. We impose a mean velocity U_{bulk} on the flow between the two parallel rigid plates. Lengths are nondimensionalised by the half-gap h between the plates, velocities by $3U_{\text{bulk}}/2$ (which is the centerline velocity of the parabolic laminar flow with mean velocity U_{bulk}), and time by the ratio between them. The Reynolds number is defined to be $Re = 3U_{\text{bulk}}h/(2\nu)$. The non-dimensionalized equations that we simulate are the incompressible Navier-Stokes equations

$$\frac{\partial \mathbf{U}}{\partial t} + (\mathbf{U} \cdot \nabla) \mathbf{U} = -\nabla p + \frac{1}{Re} \nabla^2 \mathbf{U} \tag{2.1a}$$

$$\nabla \cdot \mathbf{U} = 0 \tag{2.1b}$$

Since the bands are found to be oriented obliquely with respect to the streamwise direction, we use a periodic numerical domain which is tilted with respect to the streamwise direction of the flow, shown as the black rectangle in figure 4.1. This is common in studying turbulent bands (Barkley & Tuckerman, 2005; Tuckerman *et al.*, 2020) and more specifically those in transitional plane channel flow (Tuckerman *et al.*, 2014; Gomé *et al.*, 2020; Paranjape *et al.*, 2020). The x direction is chosen to be aligned with a typical turbulent band and the z coordinate to be orthogonal to the band. The relationship between streamwise-spanwise coordinates (x', z') and tilted band-oriented (x, z) coordinates is:

$$\mathbf{e}_{x'} = \quad \cos\theta\, \mathbf{e}_x + \sin\theta\, \mathbf{e}_z \tag{2.2a}$$

$$\mathbf{e}_{z'} = -\sin\theta\, \mathbf{e}_x + \cos\theta\, \mathbf{e}_z \tag{2.2b}$$

The usual wall-normal coordinate is denoted by y. The field visualised in figure 4.1 comes from an additional simulation we carried out in a domain of size $(L_{x'}, L_y, L_{z'}) = (200, 2, 120)$ aligned with the streamwise-spanwise coordinates.

Equations (5.2) are completed by rigid boundary conditions in y, periodic boundary conditions in x and z, and imposed flux $2/3$ in the streamwise direction x' and zero in the spanwise direction z':

$$\mathbf{U}(x + L_x, y, z) = \mathbf{U}(x, y, z + L_z) = \mathbf{U}(x, y, z) \qquad \mathbf{U}(x, \pm 1, z) = 0 \tag{2.3a}$$

$$\frac{1}{2} \int_{-1}^{+1} dy\, \mathbf{U}(x, y, z) = \frac{2}{3} \mathbf{e}_{x'} = \frac{2}{3} \left(\cos\theta\, \mathbf{e}_x + \sin\theta\, \mathbf{e}_z \right) \tag{2.3b}$$

To integrate (5.2) with boundary conditions (2.3), we use the parallelised pseudospectral C++ code ChannelFlow (Gibson, 2012), which employs a Fourier-Chebychev spatial discretisation. The velocity field can be decomposed into the stationary laminar parabolic base flow $\mathbf{U}_{\text{base}} = (1 - y^2)\mathbf{e}_{x'}$ and the deviation $\mathbf{u} \equiv \mathbf{U} - \mathbf{U}_{\text{base}}$ which satisfies the same equations and boundary conditions as $\mathbf{U}$ but with zero flux instead of (2.3b). A Green's function method is used to impose the flux in each direction. More specifically, for each periodic direction, one computes and uses the pressure gradient such that the resulting flow field will have the desired bulk velocity, e.g. (Pugh & Saffman, 1988; Barkley, 1990). Throughout our study, we present the deviation $\mathbf{u} = (u, v, w)$ so as to highlight the difference with the dominant laminar flow $\mathbf{U}_{\text{base}}$ and the motion of flow features with respect to the bulk velocity.

The angle in this study is fixed at $\theta = 24°$, as has been used extensively in the past (Barkley & Tuckerman, 2005; Tuckerman *et al.*, 2014; Gomé *et al.*, 2020). The orientation of the domain imposes a fixed angle on turbulent bands, and choosing a short length for the x direction of the domain suppresses any large-scale variation along the bands. Thus, these simulations effectively capture the dynamics of infinitely long bands that only interact along their perpendicular direction, preventing complex 2D interactions that are possible for finite-length bands (Shimizu & Manneville, 2019; Xiao & Song, 2020). In this way, localised bands in the tilted channel geometry are similar to localised puffs in pipe flow.

Our domain Ω has dimensions $(L_x, L_y, L_z) = (6.6, 2, 100)$ and a numerical resolution of $(N_x, N_y, N_z) = (84, 64, 1250)$, exactly as in (Gomé *et al.*, 2020), thus allowing direct comparison with these prior results. The length $L_z = 100$ of our tilted domain corresponds to an inter-band distance above which a band is considered as isolated, while the domain width $L_x = 6.6$ is used because it corresponds to the natural spacing of streaks in channel flow in a 24° box (Chantry *et al.*, 2016; Gomé *et al.*, 2020). For puffs in pipe flow, which are similar in many respects to the isolated bands considered here, Nemoto & Alexakis (Nemoto & Alexakis, 2021) conducted extensive computations showing that domain length had some effect on mean decay timescales, with $L = 50$ and $L = 100$ giving quantitatively different, but qualitatively similar results. Domain length is expected to have a quantitative effect on the splitting timescale; our domain length $L_z = 100$ has been selected as a compromise between accuracy and computational cost.

A semi-implicit time-stepping scheme is used to progress from $\mathbf{u}(t)$ to $\mathbf{u}(u + dt)$, with time step $dt = 1/32 = 0.03125$. Trajectories and associated quantities such as turbulence fraction are sampled at time intervals $\delta t = 32dt = 1$. This sampling time is used throughout for collecting statistics and generating probability distributions. The computation of solutions of the Navier-Stokes equations discretised in space and time is called, as usual, direct numerical simulation or DNS.

2.2.2 The Adaptive Multilevel Splitting (AMS) algorithm

Here we present the essence of the AMS algorithm. We follow closely the method originally described in Cérou *et al.* (Cérou & Guyader, 2007), although here we consider a deterministic dynamical system, the Navier-Stokes equations (5.2), whereas Cérou *et al.* considered a stochastic process. The AMS algorithm has been applied recently to other deterministic fluid systems (Lestang *et al.*, 2018, 2020; Rolland, 2022). For the application of other rare-event algorithms to deterministic systems, see (Wouters & Bouchet, 2016) and references therein.

Symbol	Definition
$h_{\mathcal{A}}$	Hypersurface within $\mathcal{A}$, origin of trajectories, in practice one-band state
$h_{\mathcal{S}}$	Hypersurface $\mathcal{S}$ close to and surrounding $\mathcal{A}$
$h_{\mathcal{B}}$	Hypersurface within $\mathcal{B}$, destination of trajectories
$h_{\mathcal{B}_0}$	Threshold for decay events in AMS
$h_{\mathcal{B}_2}$	Threshold for splitting events in AMS
h_0	Entrance of the *collapse zone* for decays for all Re
h_2	Entrance of the *collapse zone* for splits for all Re
h_M	Maximal value of F_t at fixed Re
h_{left}	left endpoint of fit between PDF of F_t and Fisher-Tippett distribution
h_{right}	right endpoint of fit between PDF of F_t and Fisher-Tippett distribution

Table 2.1: Definitions of designated levels of a turbulent fraction or score function used throughout Chapter 2

Re	815	830	870	900	950	1000	1050	1100	1150	1200
$h_{\mathcal{A}}$	0.21	0.22	0.24	0.26	0.31	0.34	0.37	0.40	0.43	0.44
$h_{\mathcal{S}}$	0.17	0.18	0.21	0.23	0.27	0.375	0.41	0.44	0.46	0.47
$h_{\mathcal{B}_0}, h_{\mathcal{B}_2}$	0.0001	0.0001	0.0001	0.0001	0.0001	0.70	0.70	0.70	0.70	0.70
h_0, h_2	0.22	0.22	0.22	0.22	0.22	0.42	0.431	0.461	0.474	0.483
h_M	0.292	0.305	0.344	0.385	0.44	0.635	0.616	0.659	0.677	0.69
h_{left}	0.13	0.148	0.176	0.207	0.243	0.30	0.32	0.279	0.271	0.326
h_{right}	0.285	0.278	0.307	0.327	0.364	0.42	0.436	0.469	0.501	0.536

Table 2.2: Values of designated levels of a turbulent fraction or score function used throughout the chapter.

a) Setup

Let $\mathcal{A}$ and $\mathcal{B}$ be two states visited by trajectories of a dynamical system. More precisely, $\mathcal{A}$ and $\mathcal{B}$ are regions in phase space corresponding to particular flow states of interest. We commonly refer to $\mathcal{A}$ and $\mathcal{B}$ simply as states. The goal is to produce a large sample of the rare transitions from $\mathcal{A}$ to $\mathcal{B}$. In our case $\mathcal{A}$ will always be the one-band state, labelled as $\mathcal{A}$ in Figure 2.2, while $\mathcal{B}$ will be either the laminar flow, labelled as $\mathcal{B}_0$, or else the two-band state, labelled as $\mathcal{B}_2$ in figure 2.2.

Perhaps the most crucial piece of the AMS algorithm is the specification of a score function, or reaction coordinate, ϕ, that quantifies transitions from $\mathcal{A}$ to $\mathcal{B}$. The score function $\phi(\mathbf{u})$ is a real-valued function of the flow field whose gradient is non-zero (at least everywhere of interest), and such that there exist real values $h_{\mathcal{A}}$ and $h_{\mathcal{B}}$, with $h_{\mathcal{A}} < h_{\mathcal{B}}$, such that $\phi(\mathbf{u}) < h_{\mathcal{A}}$ implies $\mathbf{u} \in \mathcal{A}$ while $\phi(\mathbf{u}) > h_{\mathcal{B}}$ implies $\mathbf{u} \in \mathcal{B}$. Note that for decay, the laminar state is a single point in phase space, so we will take $\mathcal{B}$ to be a set within its basin of attraction. Tables 2.1 and 2.2 list the various thresholds of the score function that

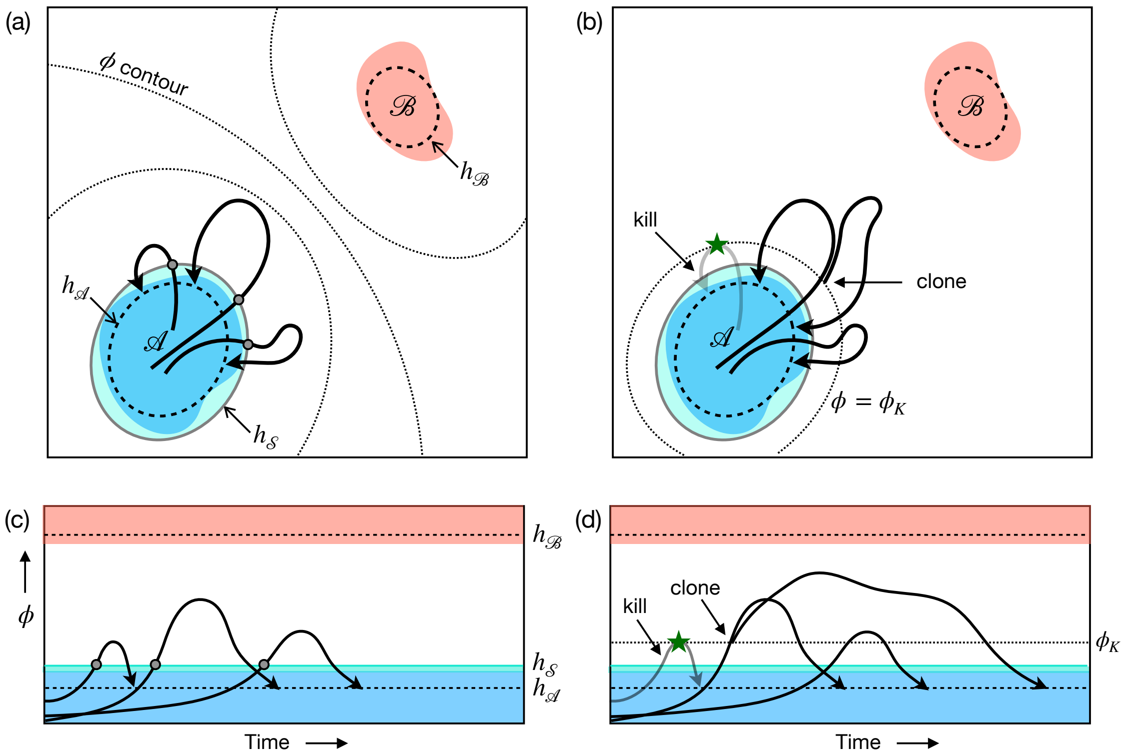

Figure 2.4: Schematic depiction of the AMS algorithm for a transition from $\mathcal{A}$ to $\mathcal{B}$. (a) The initialisation of the algorithm. Contours are shown for the score function $\phi(\mathbf{u})$ and a hypersurface $\mathcal{S}$ surrounding $\mathcal{A}$. N trajectories are computed starting from random initial conditions in $\mathcal{A}$ that cross $\mathcal{S}$ and then either return to $\mathcal{A}$ or go to $\mathcal{B}$. (Here $N = 3$ and no initial trajectories reach $\mathcal{B}$.) (b) First iteration of the algorithm. The trajectory attaining the smallest maximum score function (here ϕ_K with $K = 1$) is killed, and a new trajectory is cloned from another randomly selected trajectory, resulting in an improved set of trajectories. The process is then iterated until a sufficient number of trajectories reach $\mathcal{B}$. Time series (c) and (d) correspond to the trajectories in (a) and (b).

we will use throughout the chapter. The score function provides a smooth landscape for quantifying the progress of the transition between $\mathcal{A}$ and $\mathcal{B}$, as illustrated in figure 2.4(a). The algorithm also requires a value $h_{\mathcal{S}}$ and associated hypersurface $\mathcal{S}$, close to $\mathcal{A}$, given by

$$\mathcal{S} = \{\mathbf{u} \mid \phi(\mathbf{u}) = h_{\mathcal{S}}\}.$$

b) Initialisation

The initialisation step consists of generating a sample of N trajectories $\mathbf{u}_i(t)$, $i \in \{1, \ldots, N\}$, that start within $\mathcal{A}$, leave $\mathcal{A}$ at least as far as $\mathcal{S}$, and then either reach $\mathcal{B}$ or, more likely, return to $\mathcal{A}$. See figure 2.4(a). In practice the N initial conditions $\mathbf{u}_i(0)$ are obtained by taking N snapshots, equally spaced in time, from a single trajectory that remains in $\mathcal{A}$ over a long time and thus samples the natural measure of states within $\mathcal{A}$.

The role of the hypersurface $\mathcal{S}$ is to ensure that after initialisation, all trajectories in our sample have ventured from $\mathcal{A}$ at least as far as $\mathcal{S}$. Hence the maximum value of the score function obtained along each trajectory is at least $h_{\mathcal{S}}$. From the point of view of the score function, all trajectories in our initial sample have made some, possibly small, progress towards $\mathcal{B}$. Since $\mathcal{S}$ is chosen close to $\mathcal{A}$, the initialisation step is not computationally demanding.

For the initialisation and subsequent iterations, it is necessary to store the trajectories. In practice we store full flow fields $\mathbf{u}_i(t_j)$ for each trajectory $i \in \{1, \ldots, N\}$ at sparsely spaced times $t_j = j\ dT$, as a compromise between the large CPU times required for computing trajectories and the large memory needed to store them. The computations reported here all use a storage interval of $dT = 320\ dt = 10$, which is 10 times the sampling time δt used to collect statistics on trajectories.

c) Iteration

Iterative step m consists of discarding the K worst-performing trajectories and replacing them with trajectories obtained by cloning non-discarded trajectories. Specifically, we compute the maximal value $\phi_i^{(m)}$ of the score function along each trajectory and re-order the trajectories such that

$$\phi_1^{(m)} \leq \phi_2^{(m)} \leq \cdots \leq \phi_K^{(m)} \leq \cdots \leq \phi_N^{(m)}.$$

We discard the K trajectories whose maximal values are lowest, in practice a value $K^{(m)} \geq K$ because of possible equality of the maxima. Thus, in general we retain trajectories $\mathbf{u}_i$ such that $\phi_i^{(m)} > \phi_K^{(m)}$. We replace each discarded trajectory $\mathbf{u}_k(t)$ with a new trajectory constructed as follows:

1. Choose at random (uniformly) one of the trajectories $\mathbf{u}_l(t)$ from the set of $N - K^{(m)}$

retained trajectories. Overwrite the trajectory $\mathbf{u}_k(t)$ with the part of the trajectory $\mathbf{u}_l(t)$ up to time t^{clone} at which the score function along $\mathbf{u}_l(t)$ first reaches $\phi_K^{(m)}$, i.e. $\phi(\mathbf{u}_l(t^{\mathrm{clone}})) = \phi_K^{(m)}$. See figure 2.4(b). (Due to the discrete sampling of stored trajectories, in practice we copy trajectories until the score function first exceeds $\phi_K^{(m)}$.)

2. Modify $\mathbf{u}_l(t^{\mathrm{clone}})$ with a low-amplitude multiplicative spectral perturbation as follows. Let

$$\boldsymbol{\eta}(x,y,z) = \sum_{m_x}\sum_{m_z}\sum_{m_y} \tilde{\eta}_{m_x,m_y,m_z} s^{|m_x|+|m_y|+|m_z|} e^{i(m_x k_x x + m_z k_z z)} T_{m_y}(y)$$

where each $\tilde{\eta}_{m_x,m_y,m_z}$ is a vector whose components are uniform random complex numbers of modulus less than 1, s is a smoothing parameter such that $0 < s < 1$, and T_{m_y} is the Chebyshev polynomial of order m_y. Then the low-amplitude multiplicative perturbation at the cloning time is

$$\mathbf{u}_k(x,y,z,t^{\mathrm{clone}}) = (\boldsymbol{I} + \epsilon\boldsymbol{\eta}(x,y,z))\mathbf{u}_l(x,y,z,t^{\mathrm{clone}}) \tag{2.4}$$

where ϵ sets the size of the perturbation. The weak random perturbation is necessary to ensure that cloned trajectories do not exactly repeat the path of the trajectory from which they are cloned. Perturbations are always sufficiently weak that they leave the score function unchanged to at least four significant digits. Rolland (Rolland, 2022) uses a similar approach in applying AMS to turbulence collapse in Couette flow. The remainder of the trajectory $\mathbf{u}_k(t)$ for $t > t^{\mathrm{clone}}$ is obtained by simulating the new trajectory until it reaches $\mathcal{A}$ or $\mathcal{B}$ as before.

Once the $K^{(m)}$ discarded trajectories have been replaced (overwritten), we have a new set of N trajectories that are superior to the set at the start of the iteration, in the sense of being closer to reaching $\mathcal{B}$. Specifically, the maximum value of the score function for each of the new trajectories is now at least $\phi_K^{(m)}$. We increment m and repeat as necessary.

d) Stopping and post processing

Iterations end once the N samples have all reached $\mathcal{B}$. The final number of iterations is denoted by M. From the resulting trajectories and information gathered during the iteration process, we can construct estimators of relevant statistical quantities. Trajectories begin in $\mathcal{A}$, pass through $\mathcal{S}$ and terminate upon arrival at either $\mathcal{A}$ or $\mathcal{B}$. The estimator of the probability to go from $\mathcal{S}$ to $\mathcal{B}$ is given by (Cérou & Guyader, 2007):

$$\hat{p} = \prod_{m=1}^{M}\left(1 - \frac{K^{(m)}}{N}\right), \tag{2.5}$$

where $K^{(m)}$ is the number of trajectories eliminated at iteration m. The probability of going from $\mathcal{S}$ to $\mathcal{A}$ is $(1-\hat{p})$ and that of going from $\mathcal{A}$ to $\mathcal{S}$ is 1.

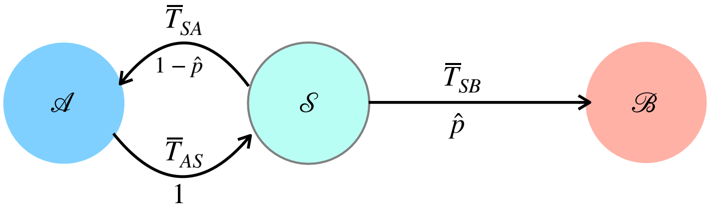

Figure 2.5: Schematic depiction of the data gathered via the AMS algorithm for a transition from $\mathcal{A}$ to $\mathcal{B}$ via $\mathcal{S}$. The probability $\hat{p}$ of transition from $\mathcal{S}$ to $\mathcal{B}$ is estimated, thus giving $1-\hat{p}$ as the probability for transition from $\mathcal{S}$ to $\mathcal{A}$. The sample mean times obtained for the two transitions are $\overline{T}_{\mathcal{SB}}$ and $\overline{T}_{\mathcal{SA}}$. From $\mathcal{A}$, all trajectories reach $\mathcal{S}$ (probability of one) and the sample mean time for this transition is $\overline{T}_{\mathcal{AS}}$. Trajectories begin at $\mathcal{A}$ and make some number of round trips between $\mathcal{S}$ and $\mathcal{A}$ before possibly reaching $\mathcal{B}$.

The main quantity of interest is the mean first passage time τ from state $\mathcal{A}$ to state $\mathcal{B}$. For this, we will require the sample mean times available from the computations (Cérou *et al.*, 2011). Let $T_{\mathcal{AS}} \equiv \inf\{t>0,\ \mathbf{u}(t)\in\mathcal{S} \mid \mathbf{u}(0)\in\mathcal{A}\}$ and let $\overline{T}_{\mathcal{AS}}$ denote its sample mean obtained from trajectories whose initial conditions $\mathbf{u}(0)$ are selected from a long simulation lying within $\mathcal{A}$. Because $\mathcal{S}$ is close to $\mathcal{A}$, $\overline{T}_{\mathcal{AS}}$ is easily obtained from DNS (or from the initialisation step of the AMS). Similarly, from the trajectories that cross $\mathcal{S}$ and return to $\mathcal{A}$ we can compute $\overline{T}_{\mathcal{SA}}$, the sample mean time to go from $\mathcal{S}$ to $\mathcal{A}$. Finally, from the N sample paths constructed as part of the AMS we can compute $\overline{T}_{\mathcal{SB}}$, the sample mean time to go from $\mathcal{S}$ to $\mathcal{B}$.

From these quantities, the estimator for the mean first passage time τ is constructed as illustrated in figure 2.5. A trajectory going from $\mathcal{A}$ to $\mathcal{B}$ does so by going from $\mathcal{A}$ to $\mathcal{S}$ and back some number of times, n, before finally transitioning from $\mathcal{A}$ to $\mathcal{S}$ to $\mathcal{B}$. The probability of such a trajectory is $(1-\hat{p})^n\,\hat{p}$ and the mean time for all such trajectories is $\left(\overline{T}_{\mathcal{AS}}+\overline{T}_{\mathcal{SA}}\right)n+\overline{T}_{\mathcal{AS}}+\overline{T}_{\mathcal{SB}}$. Summing over all possible n yields the estimator for τ:

$$\begin{aligned}\tau &= \sum_{n=0}^{\infty}(1-\hat{p})^n\hat{p}\left[\left(\overline{T}_{\mathcal{AS}}+\overline{T}_{\mathcal{SA}}\right)n+\overline{T}_{\mathcal{AS}}+\overline{T}_{\mathcal{SB}}\right]\\ &= \left(\overline{T}_{\mathcal{AS}}+\overline{T}_{\mathcal{SA}}\right)\frac{1-\hat{p}}{\hat{p}}+\left(\overline{T}_{\mathcal{AS}}+\overline{T}_{\mathcal{SB}}\right). \qquad (2.6)\end{aligned}$$

We do not use separate notation for the true mean first passage time and this estimator of it. In describing the transition dynamics in terms of a Markov chain in figure 2.5, we rely on standard assumptions of the AMS algorithm, stated by Cérou *et al.* (Cérou *et al.*, 2011, p. 12).

The time $\overline{T}_{\mathcal{AS}} + \overline{T}_{\mathcal{SA}}$ is the mean *non-reactive time*. This is the mean time for trajectories starting from within $\mathcal{A}$ to return to $\mathcal{A}$, conditioned on the fact that they reach $\mathcal{S}$. Similarly, $\overline{T}_{\mathcal{AS}} + \overline{T}_{\mathcal{SB}}$ is the mean *reactive time* for trajectories starting from within $\mathcal{A}$ to reach $\mathcal{B}$, conditioned on the fact that they do not return to $\mathcal{A}$. Neither the reactive time nor the non-reactive time is particularly large. What makes the mean first passage time large is that on average a trajectory will make many failed attempts to reach $\mathcal{B}$ so that the mean non-reactive time is multiplied by the large factor $(1-\hat{p})/\hat{p}$.

2.3 Computing mean passage times in channel flow

2.3.1 Choice of the score function for band decay and splitting

The choice of the score function is critical for the AMS algorithm. In our case we need functions that quantify the transition progress between the one-band state $\mathcal{A}$ and either the laminar state $\mathcal{B}_0$ (decay event) or the two-band state $\mathcal{B}_2$ (splitting event). We use slightly different score functions for decay and splitting.

We introduce the turbulent fraction, F_t, quantifying the proportion of the flow that is turbulent: $F_t = 0$ for laminar flow, while $F_t = 1$ for flow that is turbulent throughout the channel. For localised turbulent bands, the turbulent fraction is between zero and one. Specifically we define

$$e(z) \equiv \frac{1}{L_x L_y} \int_{-1}^{1} \int_{0}^{L_x} \frac{1}{2}(v^2 + w'^2)\, \mathrm{d}x\, \mathrm{d}y, \quad \text{and} \quad F_t \equiv \frac{1}{L_z} \int_0^{L_z} H(e(z) - e_{\text{thresh}})\, \mathrm{d}z \quad (2.7)$$

where H is the Heaviside function. These quantities use the energy contained in the cross-channel and spanwise velocity components v and w', which is zero for laminar flow. Its cross-sectional integral $e(z)$ provides a good characterisation of the turbulence as a function of z. We define the flow at location z to be turbulent if $e(z)$ exceeds the empirical threshold e_{thresh}, where $e_{\text{thresh}} = 1.1 \times 10^{-3}$. Figure 2.6a presents the typical life of a decaying band, repeated from figure 2.1, along with the corresponding time series of the turbulent fraction F_t. Local minima of F_t occur at local contractions of the band, which are themselves small detours towards the laminar state. Then F_t drops sharply to zero when the band transitions to the laminar state. In practice, we take $\phi = F_t$ and replace $<$ with $>$ (and max with min) as necessary in the algorithm. We define the system to be in $\mathcal{B}_0$ if $\phi < h_{\mathcal{B}_0} = 0.0001$ independently of Re, since all trajectories attaining this value of F_t are in the basin of attraction of the laminar state. The value $h_{\mathcal{A}}$ is taken as the most probable value of the score function from a long simulation of the one-band state. As a result, $h_{\mathcal{A}}$ depends on Reynolds number. The level $h_{\mathcal{S}}$ is chosen to be approximately $0.8\, h_{\mathcal{A}}$. (See also Tables 2.1 and 2.2 for definitions and values of all of these levels.)

We now consider the transition from one to two bands. Unlike for band decay, we have

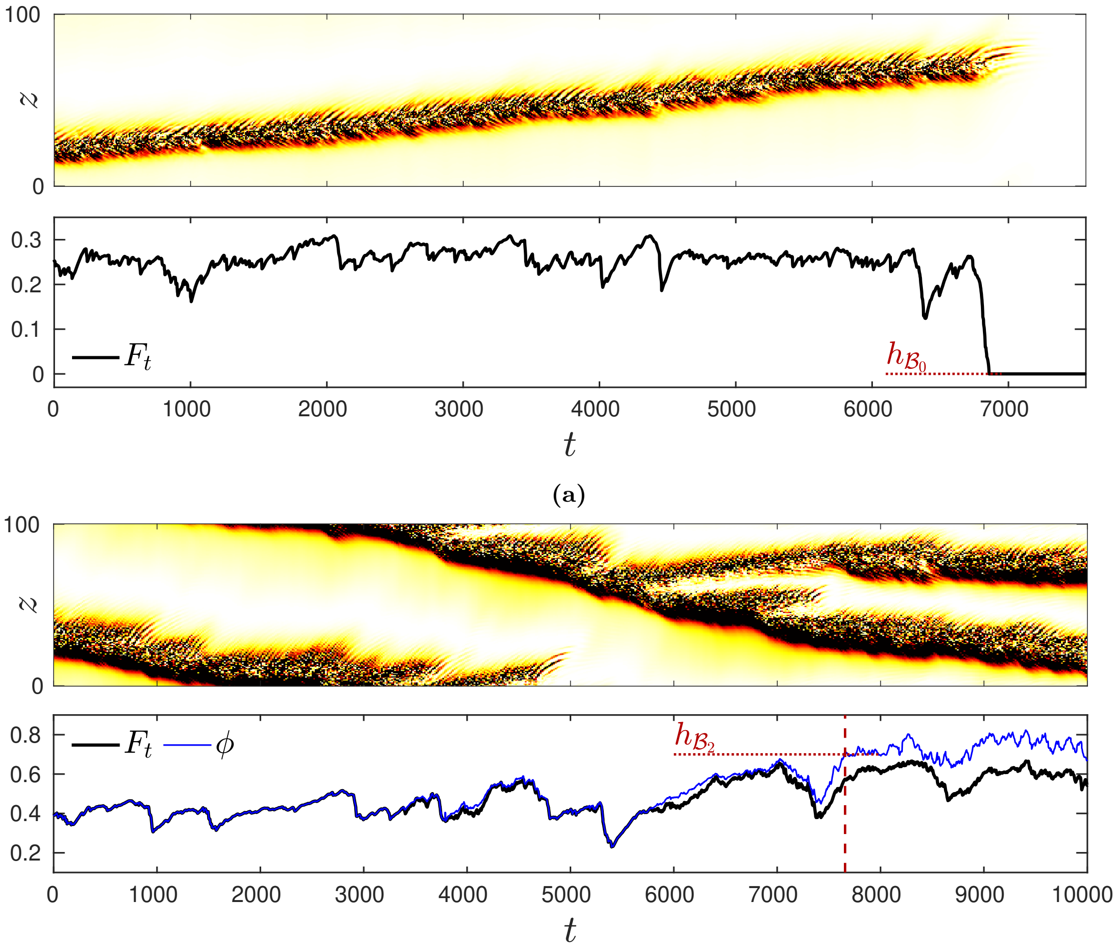

(a)

(b)

Figure 2.6: Evolution of the turbulent band during (a) a decay at $Re = 870$ and (b) a split at $Re = 1150$. Top: Spatio-temporal visualisation. Colors show $(v^2 + w'^2)/2$ at $(x = 3.3, y = 0.8)$ (white: 0, black: 0.001). Bottom: Evolution of the turbulent fraction F_t (black curves) and of score function ϕ (thin blue curve) defined for splits in (2.8).

found that the turbulent fraction is not an adequate score function for band splitting. Figure 2.6b illustrates the difficulty. We see that before attaining the two-band state, multiple attempts to split occur. These deviations from the one-band state are characterised by widening of the initial band, possibly leading to the opening of a laminar gap between two turbulent regions. The resulting downstream turbulent patch then either decays, leading to a one-band state, or gains in intensity, ultimately leading to a steady second turbulent band whose shape and energy level are comparable to those of the initial band. The problem with using F_t as a score function is that while it captures the widening of the single band, it does not select for the intensification of downstream patches that results in a persistent secondary band. In figure 2.6b, the branching which will eventually lead to a new band occurs at $t \approx 5400$, but it is only at $t \approx 7660$ that this band becomes wider and more intense, acquiring some permanence and stability. It is this latter event that we will define as the split.

We have constructed an empirical but successful score function ϕ that encompasses the entire process of band stretching, captured by F_t, as well as separation into multiple bands and subsequent intensification of downstream bands. As can be seen by comparing the blue and black curves in figure 2.6b, ϕ does not differ greatly from F_t, but the difference is crucial for the performance of the AMS algorithm. The score function is given as follows. Consider the flow to consist of n_b turbulent bands, i.e. n_b distinct regions in which $e(z) > e_{\text{thresh}}$, as defined in (2.7). We associate to each turbulent band its width W_i in z, the laminar gap length L_i upstream until the next turbulent band, and finally its average energy E_i. We consider the mother band to be the band whose upstream laminar gap is maximal. Its properties are labeled (W_1, L_1, E_1), and the other bands i are ordered by downstream distance from the mother band. We then define the following empirical score function for splits:

$$\phi = F_t + \sum_{i=1}^{n_b} \frac{l_i}{L_z} \left(\frac{E_i}{E_{\max}} \right)^{\alpha} = \frac{1}{L_z} \sum_{i=1}^{n_b} \left[W_i + l_i \left(\frac{E_i}{E_{\max}} \right)^{\alpha} \right] \tag{2.8}$$

Here, $E_{\max} \equiv \max\limits_{1 \le i \le n_b} E_i$ and $l_i \equiv \sum_{j=2}^{i} L_j$ is the total laminar gap between band i and the mother band, which can describe continuously the collapse or splits of multiple child bands. The exponent α is chosen empirically to balance energy localization and turbulence spreading. In practice, we use $\alpha = 0.5$, in order to counteract the decrease in turbulent fraction usually observed after a split, as shown on figure 2.6b at $t = 7\,500$. In this way, we have enhanced the turbulent fraction by adding a function of band intensity E_i and of the total laminar distance l_i to the mother band. In this study, the level $h_{\mathcal{B}_2} = 0.7$ is found to capture a successful split: the presence of a lasting secondary band whose profile and intensity are similar to those of the initial band. We take $h_{\mathcal{S}} \simeq 1.2 h_{\mathcal{A}}$, with $h_{\mathcal{A}}$ the most probable value of (2.8) in the one-band state.

We have introduced a number of numerical parameters that could affect the performance and the accuracy of the computations. Of these, the selection of $h_{\mathcal{B}_2}$ and ϵ require the most care. Referring to figure 2.6b one sees that the threshold $h_{\mathcal{B}_2}$ must correctly capture the completion of a splitting event. As with the difficulty in defining a good score function for splitting, this is a reflection of our lack of good understanding of the splitting process. As can be seen in figure 2.6a, this issue does not arise for decay since the score function of the laminar state is known to be zero. Concerning the perturbation size ϵ used in the cloning, equation (2.4), one would ideally choose this to be small and independent of Re. In practice we have found it necessary to vary ϵ with Re, and as discussed at the end of section 2.32.3.2, the current algorithm applied to decay events sometimes requires ϵ to be larger than desired. (See the Supplemental Material for further discussion of the perturbation size ϵ and also the sample size N.)

2.3.2 Simulating rare events with AMS

We have used the AMS algorithm to compute the mean decay and splitting times of an isolated turbulent band in a channel. These mean times are plotted as a function of Reynolds number in Figure 2.7, where we also include previous results obtained via standard Monte Carlo (MC) simulations (Gomé *et al.*, 2020). The AMS results overlap with the Monte Carlo data, but also substantially extend the range of accessible time scales. Both the AMS and Monte Carlo results use the same tilted computational domain, the same spatial resolution, and the same underlying time-stepping code, as described in section 2.2.2.2.1. This permits direct comparison of the two methods.

Figure 2.7 confirms the super-exponential dependence of the time scales found for decay and splitting events in wall-bounded shear flows (Avila *et al.*, 2010, 2011; Shi *et al.*, 2013; Gomé *et al.*, 2020). From fits with $\tau_d = \exp\left(\exp(a_d\ Re + b_d)\right)$ and $\tau_s = \exp\left(\exp(a_s\ Re + b_s)\right)$ in the decay and split regimes, we find $Re_c \simeq 980$ as an improved estimate of the crossing Reynolds number for this flow configuration. (Previous fits to the Monte Carlo data gave a crossing Reynolds number of 965.)

We recall a few details from the Monte Carlo computations in (Gomé *et al.*, 2020). The initial fields for the simulations are taken from snapshots of long-lasting bands simulated at $Re \in [900 - 1050]$. The Reynolds number is then changed to the desired value. Decay and splitting times from the start of the simulation are recorded. From these, the mean times and associated error bars are obtained (Gomé *et al.*, 2020). The Monte Carlo estimate of the transition probability $\hat{p}_{\mathrm{MC}}$ is computed from the multiple simulations by counting the number of decays or splits relative to the number of passages through $\mathcal{S}$. Typically $N = 40$ decay and splitting events are obtained at each Reynolds number. Fewer than $N = 40$ events were obtained by Monte Carlo at the largest values of τ. With such techniques, only time scales $\tau < 10^5$ are currently accessible in practice.

The AMS initial fields are created from long-lasting bands, as in the Monte Carlo method, except that each initial field is simulated for an additional relaxation time of 500 before commencing the AMS algorithm. The number of trajectories we seek to discard at each AMS iteration is $K = 1$. At each value of Re, the AMS algorithm is run N_{AMS} times, with each realisation computing a sample of N trajectories. Each realisation gives a value of τ calculated using (2.6), where $\overline{T}_{\mathcal{AS}} + \overline{T}_{\mathcal{SA}}$ is computed by DNS as part of the initialisation step, $\overline{T}_{\mathcal{AS}} + \overline{T}_{\mathcal{SB}}$ is obtained from the AMS trajectories, and $\hat{p}$ is obtained via (2.5). Then the final estimate of τ is obtained by averaging over the N_{AMS} independent realisations.

Table 2.3 compares estimates of the transition probability $\hat{p}$ from the Monte Carlo and

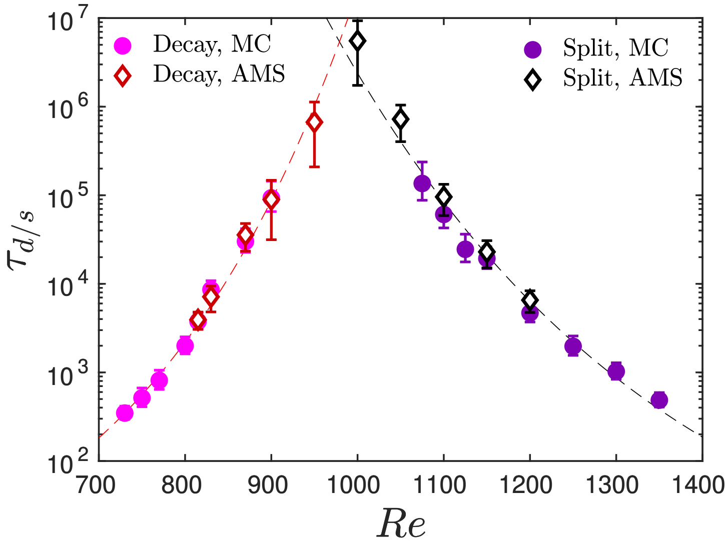

Figure 2.7: Mean decay times (red, magenta) and splitting times (black, purple) of turbulent bands as a function of Reynolds number, estimated with the Monte Carlo method (MC, circles) or with the Adaptative Multilevel Splitting (AMS, diamonds). Error bars give confidence intervals for MC and are computed from multiple realizations of the algorithm for AMS. Dashed lines are best fits to double exponential form using the combined AMS and MC data: $\tau_d \simeq \exp\left[\exp\left(3.9 \times 10^{-3}\ Re - 1.09\right)\right]$; $\tau_s \simeq \exp\left[\exp\left(-2.6 \times 10^{-3}\ Re + 5.27\right)\right]$.

AMS strategies. Both methods yield comparable estimates when Monte Carlo results can be obtained. We emphasise that lifetimes τ change by orders of magnitude over the range of Re of interest, so we do not seek more than about one digit of accuracy in their values. The overall gain in computational speed achieved by the AMS over Monte Carlo is measured by the total CPU time. One component of this cost is the CPU time per trajectory, for which the AMS shows a typical improvement of order $\mathcal{O}(10)$ and even $\mathcal{O}(100)$ for the low-transition-probability cases we considered; see $Re = 1000$ in Table 2.4. For higher-transition-probability cases, AMS does not outperform Monte Carlo because AMS requires N_{AMS} realisations to compensate for the variability in individual realisations. For low-transition-probability cases such as $Re = 1000$, only AMS is capable of inducing the very rare trajectories which are out of reach for the Monte Carlo method. (See Supplemental Material for further comparisons.)

The results from AMS show larger variability than those from Monte Carlo, especially for decay cases, as seen by the error bars on figure 2.7. It is known that the standard deviation of the estimated probability for AMS will decrease as $1/\sqrt{N}$ (at least in ideal cases) (Bréhier *et al.*, 2016; Rolland & Simonnet, 2015). For our high-dimensional system,

Re	Monte Carlo (MC)			Adaptive Multilevel Splitting (AMS)			
	N	$\hat{p}_{\text{MC}}$	τ_{MC}	ϵ	$N_{\text{AMS}} \times N$	$\hat{p}$	τ
870	40	0.081	3.0×10^4	5×10^{-4}	9×50	0.081	3.6×10^4
900	40	0.013	9.3×10^4	1×10^{-3}	7×50	0.015	8.9×10^4
1000	–	–	–	1×10^{-3}	3×50	0.00029	5.5×10^6
1150	40	0.047	2.1×10^4	1×10^{-5}	9×50	0.046	2.2×10^4

Table 2.3: Results of Monte Carlo (MC) and AMS (Adaptative Multilevel Splitting). N is the number of samples for MC or for a single realisation of AMS. For AMS, N_{AMS} is the number of realisations of the algorithm and ϵ is the perturbation amplitude used in cloning. The estimated transition probability and mean first passage time obtained by MC and AMS are $\hat{p}_{\text{MC}}$, τ_{MC} and $\hat{p}$, τ, respectively.

Re	Monte Carlo (MC)			Adaptive Multilevel Splitting (AMS)			
	N	CPU_{traj}	CPU_{tot}	ϵ	$N_{\text{AMS}} \times N$	CPU_{traj}	CPU_{tot}
870	40	2500	1×10^5	5×10^{-4}	9×50	360	1.6×10^5
900	40	7500	3×10^5	1×10^{-3}	7×50	330	1.2×10^5
1000*	40	4×10^5	2×10^7	1×10^{-3}	3×50	1000	1.5×10^5
1150	40	5000	2×10^5	1×10^{-5}	9×50	500	2.2×10^5

Table 2.4: Performance of Monte Carlo (MC) and AMS (Adaptative Multilevel Splitting). N is the number of samples for MC or for a single realisation of AMS. For AMS, N_{AMS} is the number of realisations of the algorithm and ϵ is the perturbation amplitude used in cloning. The estimated CPU time per successful trajectory is given, as well as the total CPU time (both in processor hours on an HPE SGI 8600 computer). *For $Re = 1000$, no estimator of the time scale could be achieved by Monte Carlo, so the CPU times are extrapolated from the AMS estimator τ.

N is restricted by computational costs. Using N larger than 100 is not practical and we typically use $N = 50$. We observe that the large variability between different realisations of the AMS algorithm is associated with variability in the initialisation, especially the extent to which the initial trajectories are a representative sample.

The amplitude ϵ of the perturbation that we use in cloning trajectories is chosen to promote separation of the trajectories. The only issue occurs for rare decay ($Re \in [900 - 950]$) where the amplitude must be increased ($\epsilon > 10^{-2}$ at $Re = 950$). In these cases, cloned trajectories resulting from small-amplitude perturbations separate from one another only after having reached their minimum F_t value. Hence they do not acquire an improved score function, causing the algorithm to stagnate. The reason for this is that the duration of the approach to the minimum of F_t is shorter than the Lyapunov time of the system. This limitation of our current procedure has been observed in other studies (Lestang *et al.*, 2020; Rolland, 2022) and has been addressed in (Rolland, 2022) by anticipating branching. This technique clones trajectories prior to where one would in the standard algorithm, thus promoting the separation of trajectories near the minimum of F_t.

2.4 Extreme value description of decay and splitting trajectories

The super-exponential dependence of lifetime of turbulence on Reynolds numbers seen in figure 2.7 is ubiquitous for decay and splitting events in wall-bounded shear flows, e.g. (Hof *et al.*, 2008; Avila *et al.*, 2010, 2011; Shi *et al.*, 2013; Gomé *et al.*, 2020). Goldenfeld, Gutenberg & Gioia (Goldenfeld *et al.*, 2010) have formulated a hypothesis explaining decays through extreme value theory. The main idea is to associate the decay of a turbulent patch to the statistical distribution of the largest fluctuation over some space-time interval. If the maximum amplitude of fluctuations becomes lower than some threshold, then the multiple fluctuations comprising a turbulent zone will all laminarise. This connects laminarisation to the distribution of extrema of a set of random variables. Just as the Central Limit Theorem states that under very general conditions the limit of the sum of independent and identically distributed random variables is a Gaussian, the Fisher-Tippett-Gnedenko theorem (Fisher & Tippett, 1928) states that the extrema of a set of n independent and identically distributed variables should follow a Fisher-Tippett distribution. Goldenfeld *et al.* assumed that the decay threshold depends on Re and approximated that dependence locally as linear. This linear dependence translates into a super-exponential dependence of the lifetimes on Re via properties of the Fisher-Tippett distribution.

In a study of the decay of turbulent puffs in pipe flow, Nemoto & Alexakis (Nemoto & Alexakis, 2021) found that the maximal vorticity over the domain followed a Fréchet distribution, a member of the Fisher-Tippett family. Moreover, they found that the parameters of this distribution depend linearly on Re over a range of 75 in Re near the critical value Re_c. Similar to the Goldenfeld *et al.* argument, this linear dependence on parameters translates to a super-exponential dependence of the lifetimes on Re. Thus, Nemoto & Alexakis were able to directly relate extreme values to the super-exponential evolution with Re of the puff decay times in pipe flow. Other quantities related to the distance to the laminar attractor have been shown to follow the extreme value law (Manneville, 2011; Shimizu *et al.*, 2019), particularly when a maximal or minimal value is extracted from a divided time series (Faranda *et al.*, 2014).

Here we explore these ideas for both the decay and splitting of turbulent bands in channel flow over a substantial range of Re. To do so, we must link the rare events (decay or split) with some observable that follows an extreme distribution. Rather than speculate on which variable or combination of variables are mechanistically responsible for driving decay and splitting events, we choose to focus on F_t for both transitions. Our reasoning is that turbulence fraction is a useful observable of general interest that is easily obtainable in computations and experiments. As we show below, the turbulent fluctuations and reaction pathways project onto F_t and allow us to analyse the connection between fluctuations and the rare events. As a practical matter, it is helpful to study distributions of a quantity that is (or is closely related to) the score function used to obtain rare events.

2.4.1 Probability densities of turbulent fraction

We begin by showing in figure 2.8 the probability density function (PDF) of the turbulent fraction $p(F_t)$ for a variety of Reynolds numbers. These PDFs have been constructed from Monte Carlo simulations that start, after initial equilibration time, from the one-band state $\mathcal{A}$ and terminate at the end of a decay or split. The distributions have a clear asymmetry about their maxima and they have broad tails that depend on Re: the low-F_t tails are present at lower Re while high-F_t tails are present at higher Re. To our knowledge, this is the first report of $p(F_t)$ in any transitional shear flow.

We find that the central portions of these PDFs are closely approximated by Fisher-Tippett distributions. The cumulative distribution function (CDF) of the Fisher-Tippett (also called Generalized Extreme Value) distribution that we will use is:

$$\mathbb{P}(X \leq h) = P_{FT}(h) \equiv 1 - e^{-(1+\xi(\mu-h)/\sigma)^{-1/\xi}} \tag{2.9}$$

where the location μ, scale σ, and shape ξ are fitting parameters. Equation (2.9) is the CDF for minima of a set of random variables, and it is this form that fits our data. We fit $p(F_t)$ with the Fisher-Tippett density $p_{FT}(h) = dP_{FT}/dh$ shown as dashed curves on figure 2.8. (The resemblance of the abbreviation FT for Fisher-Tippett and the notation F_t for turbulent fraction is coincidental.)

Figure 2.8 shows that the central region near the maximum of each PDF fits well with the Fisher-Tippett distribution inside a range spanning from h_{left} to h_{right}. As an example, these lower and upper bounds of the fit are indicated by colored and white circles for $Re = 830$. The quality of the fit is particularly good for $Re < 1000$ but shows some noticeable deviations at $Re = 1000$ and $Re = 1050$. The fitting parameter values as a function of the Reynolds number are plotted in figure 2.10a, which will be discussed below.

The turbulence fraction F_t defined in equation (2.7) is not a maximum of a set of independent quantities (although it includes a Heaviside function which, like the maximum, is a non-analytic operation). Hence, it is not obvious that F_t should be governed by an extreme value distribution. Even in the case of vorticity maxima, Nemoto & Alexakis noted that it is not possible to fully justify Fisher-Tippett distributions since vorticity is correlated in space and time and hence the maxima are not independent. At present we do not have a formal justification for the fits used in figure 2.8 other than that the distributions are clearly non-Gaussian and are fit reasonably well with the Fisher-Tippett form. We hypothesize that the strong spatiotemporal correlations within the localized turbulent bands play a significant role in the statistics, but we leave this for further investigation.

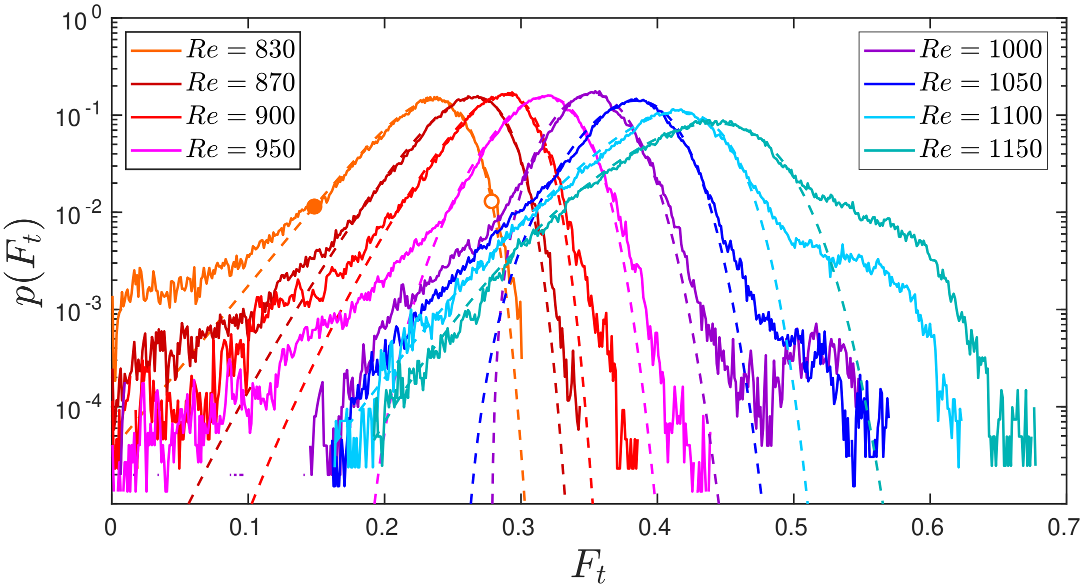

Figure 2.8: Probability density function of the turbulent fraction around the one-banded state $\mathcal{A}$. Dashed lines correspond to fits with a Fisher-Tippett probability density, the derivative of (2.9). Fits are carried out over intervals $[h_{\text{left}}, h_{\text{right}}]$, shown for the case $Re = 830$ by colored and white points. Values of h_{left} and h_{right} are given in table 2.2.

The only way the fits will enter into the analysis that follows is via their parameterisation. In this regard the fits give us a useful representation of the PDFs in terms of three parameters depending on Re. It is nevertheless possible that the distributions are of some other type.

The Nemoto & Alexakis approach requires many numerical simulations of rare events in order to obtain the tails of probability distributions. Here, the AMS approach is particularly useful as it produces large samples of the rare event trajectories that reach destination $\mathcal{B}$. From the AMS data one can reconstruct the CDF of any observable X depending on a field $\mathbf{u}$ as follows. Each point on a trajectory $\mathbf{u}(t)$ is known to be on a segment from $\mathcal{A}$ to $\mathcal{S}$, from $\mathcal{S}$ to $\mathcal{A}$, or from $\mathcal{S}$ to $\mathcal{B}$. (See figure 2.5.) Hence the CDF can be decomposed into a weighted sum of independent CDFs conditioned on the location of $\mathbf{u}$:

$$\mathbb{P}(X \le h) = \frac{\tau_{\mathcal{AS}}}{\tau}\,\mathbb{P}(X \le h \mid \mathcal{C}_{\mathcal{AS}}) + \frac{\tau_{\mathcal{S}A}}{\tau}\,\mathbb{P}(X \le h \mid \mathcal{C}_{\mathcal{SA}}) + \frac{\tau_{\mathcal{S}B}}{\tau}\,\mathbb{P}(X \le h \mid \mathcal{C}_{\mathcal{SB}}), \quad (2.10)$$

where $\mathcal{C}_{\mathcal{AS}}$ (resp. $\mathcal{C}_{\mathcal{SA}}$ and $\mathcal{C}_{\mathcal{SB}}$) is the conditional event that a field $\mathbf{u}$ lies on a trajectory that goes from $\mathcal{A}$ to $\mathcal{S}$ (resp. from $\mathcal{S}$ to $\mathcal{A}$ or to $\mathcal{B}$). The weights are the relative time spent in each segment, where

$$\begin{aligned}\tau &= \tau_{\mathcal{AS}} + \tau_{\mathcal{SA}} + \tau_{\mathcal{SB}} \\ &= \frac{1}{\hat{p}}\,\overline{T}_{\mathcal{AS}} + \frac{1-\hat{p}}{\hat{p}}\,\overline{T}_{\mathcal{SA}} + \overline{T}_{\mathcal{SB}}.\end{aligned}$$

We refer the reader back to equation (2.6) for the formula for τ in terms of $\overline{T}_{\mathcal{AS}}$, etc. The individual CDFs in (2.10) are obtained in the standard way by rank ordering the sample data and performing a cumulative summation followed by normalisation.

Figure 2.9a shows the CDF $P(h) = \mathbb{P}(F_t \leq h)$ for the low-Re decay cases and figure 2.9b shows its complement, the survival function $S(h) \equiv 1 - P(h) \equiv \mathbb{P}(F_t \geq h)$, for the high-$Re$ splitting cases. Results from the Monte Carlo simulations are shown as continuous curves, while those from AMS have been included as dotted curves. It can be seen that the distribution functions constructed from AMS improve the quality of the tails from Monte Carlo, particularly in the range $900 \leq Re \leq 1100$ where Monte Carlo systematically underestimates the tails associated with rare transitions. (We note, however, that even with the improvements from the AMS, there remain some sampling effects in the weak tails.) Dashed curves show the Fisher-Tippett CDFs obtained by fitting the PDFs of F_t shown in figure 2.8.

2.4.2 Timescales from extreme value distributions

We can now apply the Nemoto & Alexakis approach (Nemoto & Alexakis, 2021) to our decay and splitting data. The essential idea is to scale the CDFs and obtain forms that separate into approximately Re-independent portions and Re-dependent portions that can be fit to Fisher-Tippett distributions. From this it is possible to express the mean timescales for decay and splitting directly in terms of the parameters of the Fisher-Tippett distributions.

We will first describe the decay case and afterwards summarise the differences for the splitting case. Recall that in the decay case the score function for AMS is just the turbulence fraction and the boundary of the laminar state is $h_{\mathcal{B}_0} = 0.0001$, meaning that trajectories $\mathbf{u}(t)$ that reach the threshold $F_t(\mathbf{u}) = \phi(\mathbf{u}) = h_{\mathcal{B}_0}$ from above are considered to have undergone transition to the laminar state. As shown in figure 2.9c, by rescaling CDFs by their value at the threshold $P(h_{\mathcal{B}_0})$, the low-probability tails for different Re nearly collapse to a common curve. More specifically, we observe that below a value h_0, indicated on the plot, the ratio $P(h)/P(h_{\mathcal{B}_0})$ depends only weakly on Re. (Moreover, some of this dependence is likely due to sampling errors of the low-probability tails.) Flow fields $\mathbf{u}$ such that $F_t(\mathbf{u}) \in [h_{\mathcal{B}_0}, h_0]$, called the *collapse zone* in the following, are in an intermediate state that can either recover (missed decay) or die (successful decay). This process is not a strong function of Re. Above h_0, the rescaled CDFs depend strongly on Re, varying by over an order of magnitude over the Re range shown. Significantly,

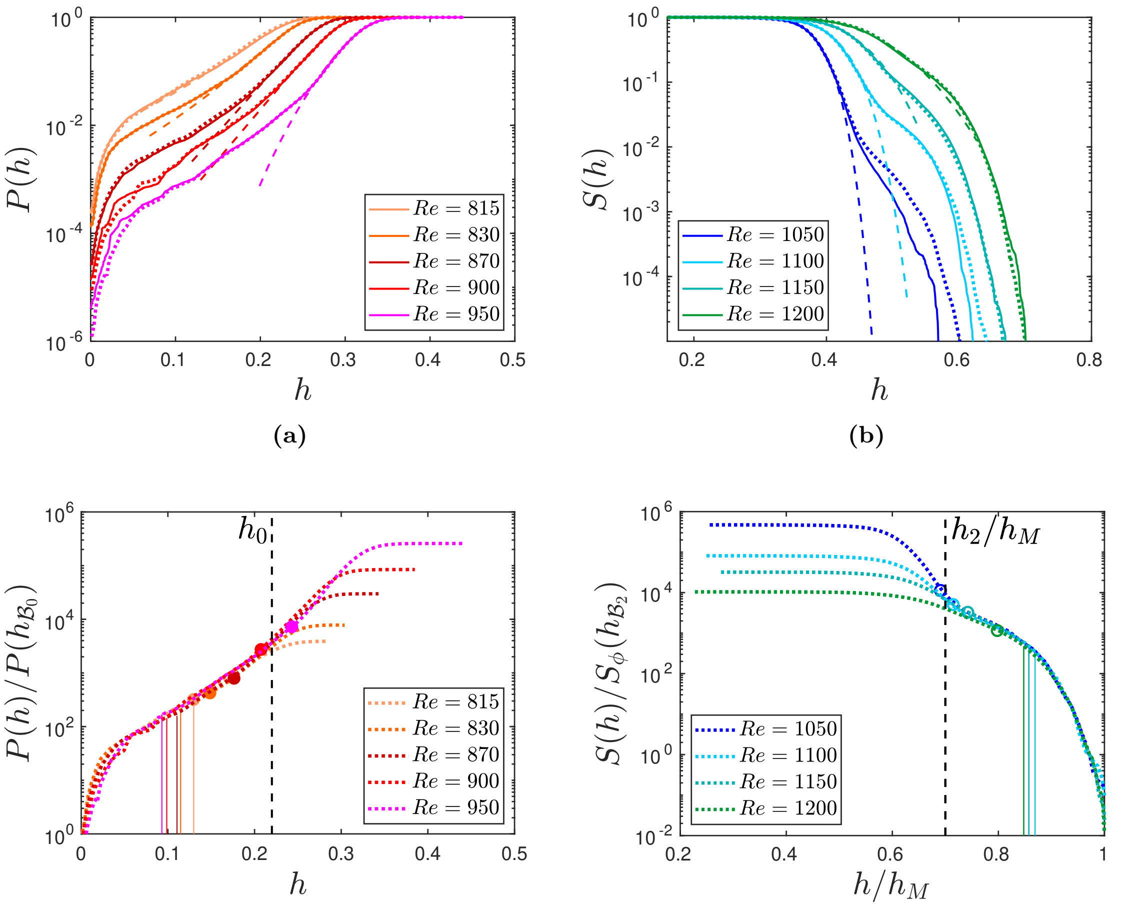

(a) (b)

(c) (d)

Figure 2.9: (a) Cumulative distribution function $P(h) = \mathbb{P}(F_t \leq h)$ for band decay and (b) survival function $S(h) \equiv 1 - P(h) \equiv \mathbb{P}(F_t \geq h)$ for band splitting at values of Re indicated in the legend. Continuous lines are obtained from Monte Carlo and dotted lines are from the AMS algorithm. Dashed lines correspond to fits to a Fisher-Tippett distribution (2.9). (c, d) Distributions from the AMS algorithm rescaled by $P(h_{\mathcal{B}_0})$ and $S_\phi(h_{\mathcal{B}_2}) \equiv 1 - P_\phi(h_{\mathcal{B}_2})$. In the splitting case (d), the range in F_t is rescaled by $h_M(Re) = \max(F_t)$. Coloured points in (c) show h_{left}, the lower bounds of the fit to the PDF with a Fisher-Tippett density function (see figure 2.8). Similarly the open points in (d) show the upper bounds h_{right}. Vertical lines show the break-even points defined in the text.

however, for almost all Re this portion of the CDFs lies within the region that is well fit by the Fisher-Tippett distribution. Concretely, the coloured points in figure 2.9c indicate the left-most values of h for each Re for which the Fisher-Tippett fits are good and in almost all cases, these points are below h_0, with the point for $Re = 950$ slightly above h_0.

Following Nemoto & Alexakis, we can connect the CDFs to decay lifetime τ_d. The algebraic statement is

$$\tau_d = \frac{\delta t}{P(h_{\mathcal{B}_0})} = \delta t \frac{P(h_0)}{P(h_{\mathcal{B}_0})} \frac{1}{P(h_0)} \simeq \underbrace{\delta t \frac{P(h_0)}{P(h_{\mathcal{B}_0})}}_{\Pi_d} \underbrace{\frac{1}{1 - e^{-(1+\xi(\mu - h_0)/\sigma)^{-1/\xi}}}}_{f_d(Re)}, \tag{2.11}$$

which we will explain in steps.

The first equality can be understood as follows (Nemoto & Alexakis, 2021). Consider estimating τ_d by Monte Carlo simulation with N_{decay} independent realisations of decay events. Then $\tau_d = T_{\text{total}}/N_{\text{decay}}$, where T_{total} is the total combined time to decay for all realisations. Further letting $T_{\text{total}} = \delta t \, N_{\text{total}}$, where N_{total} is the total number of sample points on all trajectories and δt is the sample time, we have $\tau_d = \delta t \, N_{\text{total}}/N_{\text{decay}}$. Finally, from N_{decay} simulations that terminate at $h_{\mathcal{B}_0}$, we have $P(h_{\mathcal{B}_0}) = N_{\text{decay}}/N_{\text{total}}$, since there are N_{decay} out of N_{total} sample points with $F_t \leq h_{\mathcal{B}_0}$. In practice we construct $P(h_{\mathcal{B}_0})$ from AMS simulations via (2.10) with a sampling time $\delta t = 1$.

The remainder of (2.11) consists of multiplying and dividing by $P(h_0)$ and then applying the previous observations about figure 2.9c to decompose (2.11) into a factor Π_d, that depends only weakly on Re, and $1/P(h_0)$, that depends strongly on Re. Furthermore, we approximate $P(h_0)$ by the Fisher-Tippett distribution evaluated at h_0. The Re-dependence of $f_d \simeq 1/P(h_0)$ is contained in the Re-dependence of the parameters μ, σ and ξ. We return to this after discussing the splitting case.

In almost all respects the splitting analysis is the same as that of the decay case. The only important differences comes from the fact that the score function ϕ for splitting (2.8) is not the turbulence fraction F_t. However, ϕ and F_t are closely related, both in terms of expression (2.8) and in terms of the values they take during band splitting in figure 2.6b. A split is deemed to have occurred when $\phi(\mathbf{u}(t))$ reaches $h_{\mathcal{B}_2}$ from below. Hence, analogously with (2.11), the time scale for splits is related to the survival function of ϕ evaluated at $h_{\mathcal{B}_2}$:

$$\tau_s = \frac{\delta t}{\mathbb{P}(\phi > h_{\mathcal{B}_2})} = \frac{\delta t}{S_\phi(h_{\mathcal{B}_2})}, \tag{2.12}$$

where S_ϕ is the survival function for ϕ. While one could analyse distributions of the score function ϕ, the turbulence fraction is ubiquitous in this field and the distributions in figures 2.8 and 2.9b are of general interest. Hence it is preferable to work with these distributions, even though it will be necessary to rescale the CDF in figure 2.9b using $S_\phi(h_{\mathcal{B}_2})$. This is not as awkward as it may seem since $S_\phi(h_{\mathcal{B}_2}) = N_{\text{split}}/N_{\text{total}}$, by the same argument as above for decay. Hence, while we write the normalisation in terms of S_ϕ, it is not necessary to have access to this CDF to know the normalisation, which is determined simply from the number of sample points and the number of splitting cases. To collapse the CDFs we must also rescale the horizontal axis of figure 2.9b. We rescale by h_M, the maximum value of F_t observed at each Re. This was unnecessary in the decay case because the minimum value of F_t is achieved at the Re-independent termination value $h_{\mathcal{B}_0}$.

Figure 2.9d shows the rescaled CDFs for band splitting. We observe that the low probability tails for different Re collapse well to a common curve $h \geq h_2$, while for $h < h_2$ the rescaled CDFs depend strongly on Re. Also shown as points in figure 2.9d are the upper limits for which the curves are well approximated by Fisher-Tippett distributions. These points are above, or nearly above h_2 in all cases. Hence, we can again exploit this to approximate the splitting time scale in terms of parameters of the Fisher-Tippett distributions. Starting from (2.12) the algebra is

$$\tau_s = \frac{\delta t}{S_\phi(h_{\mathcal{B}_2})} = \delta t\,\frac{S(h_2)}{S_\phi(h_{\mathcal{B}_2})}\frac{1}{S(h_2)} \simeq \underbrace{\delta t\,\frac{S(h_2)}{S_\phi(h_{\mathcal{B}_2})}}_{\Pi_s}\,\underbrace{e^{(1+\xi(\mu-h_2)/\sigma)^{-1/\xi}}}_{f_s(Re)}. \tag{2.13}$$

We thus obtain an approximation for τ_s as a product of a factor Π_s, weakly dependent on Re, and a factor $f_s(Re)$, strongly dependent on Re via the parameters μ, σ, ξ, as well as h_2. Note that h_2/h_M is constant at the start of the collapse zone, but h_M depends on Re, and hence so does h_2. Values of h_2 and h_M, as well as h_0, are given in table 2.2.

Finally, the vertical lines in figures 2.9c and 2.9d indicate the break-even point for transition events to take place. These have been determined from DNS trajectories that originate in $\mathcal{A}$ as follows. For a given value of h, we compute the fraction of trajectories attaining $F_t = h$ that successfully transition to $\mathcal{B}_0$ or $\mathcal{B}_2$, without returning to $\mathcal{A}$. The value of h for which this fraction is 1/2 is the break-even point. This is conceptually similar to finding where the *committor function* for a stochastic process (Vanden-Eijnden *et al.*, 2006) is equal to 1/2, but here we condition on values of the turbulence fraction and not points in phase space. At $Re = 1050$ we have not obtained a sufficient number of DNS trajectories undergoing transition to $\mathcal{B}_2$ to estimate the break-even point, and hence this case is not included in figure 2.9d. We provide context for these break-even points in the next section.

2.4.3 Super-exponential scaling

We now explore the connection between the observed super-exponential dependence of mean lifetimes on Re seen in figure 2.7 and the approximations to the mean lifetime given in (2.11) and (2.13). We have argued that the dominant dependence of mean lifetimes on Re is captured by the dependence of the functions f_d and f_s on Re. These functions depend on Re via the Fisher-Tippett parameters μ, σ, and ξ of (2.9) which are shown in figure 2.10a. The location parameter μ varies linearly with Re, a feature which can already be seen in the Re-dependence of the maxima in figure 2.8. The Re-dependence of the scale σ and the shape ξ is less clear; their fluctuations may be due to their sensitivity to the fitting procedure. Since the quality of the fits in figure 2.8 is not improved by the inclusion of more simulation data, the fluctuations may indicate that $p(F_t)$ is not exactly of Fisher-Tippett form even near its maximum.

The parameter ξ plays an essential role in the family of Fisher-Tippett distributions, dividing them into three categories. Those with $\xi > 0$ are the Fréchet distributions (also known as type II extreme value distributions), while $\xi < 0$ corresponds to Weibull (type III). Figure 2.10a shows that the central portions of most of the curves in figure 2.8 are best fit to Weibull distributions (ξ may be positive for $Re = 815$ and 830, but there is too much uncertainty in our fits to be sure). The limiting case $\xi = 0$ is the family of Gumbel distributions (type I), which will play a role in section 2.5.

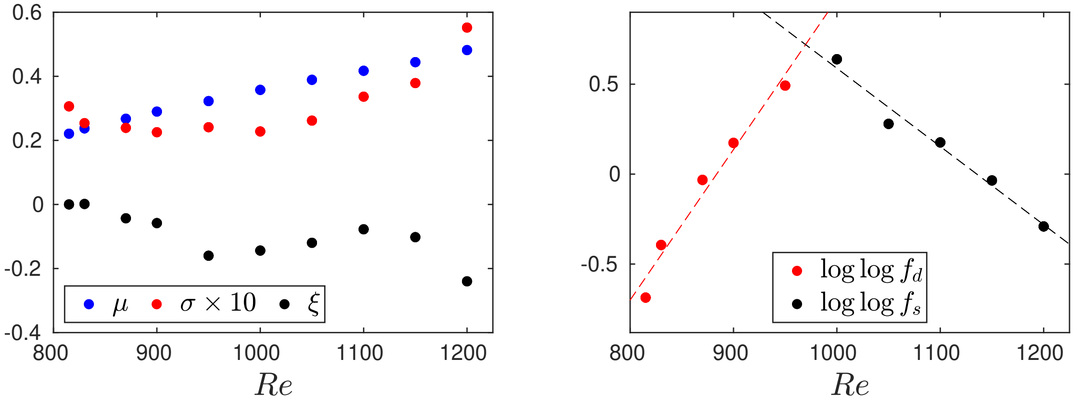

(a) **(b)**

Figure 2.10: (a) Dependence of the three Fisher-Tippett parameters on Re. These have been obtained by fitting Fisher-Tippett distributions to the numerical PDFs $p(F_t)$ over ranges $h_{\text{left}} \leq F_t \leq h_{\text{right}}$ as seen in figure 2.8. (b) Dependence of $\log\log f_d$ (2.11) and $\log\log f_s$ (2.13) on Re using the parameters from (a). Dashed lines show linear fits.

Figure 2.10b shows $\log\log f_d$ and $\log\log f_s$ from expressions (2.11) and (2.13) as a function of Re using the numerically obtained parameter values for each Re. Linear fits show that $\log\log f_d \simeq a_d\, Re + b_d$ and $\log\log f_s \simeq a_s\, Re + b_s$ over a range of nearly 200 in Re in each case. Hence both f_d and f_s depend super-exponentially on Re and are at least approximately of the form $[\exp(\exp(a\ Re + b))]$. Given the functional forms of f_d and f_s and the complicated dependence of the fitting parameters on Re, the double exponential dependence on Re is only an approximation. Nevertheless, we clearly observe a faster than exponential dependence on Re resulting from modest variation with Re of parameters of the Fisher-Tippett distribution characterising the fluctuations in the one-band state.

The interpretation of these results comes from the mechanism proposed by Goldenfeld et al. (Goldenfeld *et al.*, 2010) and subsequently refined by Nemoto and Alexakis (Nemoto & Alexakis, 2018, 2021). We focus on the decay case, but similar statements apply to the splitting case. The picture is that the statistics of strong turbulent fluctuations are governed by extreme value distributions and this gives rise to the strong Re dependence of the probability $P(h_0)$ of states being in the collapse zone $h \leq h_0$; see figure 2.9c. Note that most trajectories that enter the collapse zone do not decay directly, but instead return to the one-band state $\mathcal{A}$. Only when trajectories achieve values of F_t below the break-even points (shown as vertical lines in the figure) are trajectories more likely to decay than to return to $\mathcal{A}$. The probability of decay becomes one at $h_{\mathcal{B}_0}$, since this defines the boundary we have chosen for the laminar state $\mathcal{B}_0$, and the rate of ultimate decay is given by $P(h_{\mathcal{B}_0})$ which is much less than $P(h_0)$. However, the ratio $P(h_0)/P(h_{\mathcal{B}_0})$ is nearly independent of Reynolds number. Hence up to a Re-independent multiplicative factor, the decay rate is determined from probability $P(h_0)$. The reason why the CDFs for different Re collapse over a range of turbulence fractions, and why this occurs for both decay and splitting processes, remains unexplained.

We end this section with a few observations and caveats. We observe that PDFs of F_t are well fit near their maxima by Weibull distributions, at least for most of the Re range investigated. This is distinctly different from the Fréchet distributions observed by Nemoto & Alexakis for maximum vorticity in pipe flow (Nemoto & Alexakis, 2021). We note also that while F_t is a non-smooth function of the flow field, it is not given as an extremum over any feature of the field.

The purpose of decomposing the mean lifetimes (2.11), 2.13) and using the Fisher-Tippett parameter fits is not to obtain quantitatively accurate formulas for τ_d and τ_s, but to gain insight into the source of the super-exponential dependence on Re. In this regard we note that the biggest issue, both quantitative and conceptual, with this approach is that we rely on the existence of delimiters h_0 and h_2 that are simultaneously within the collapse zones and within the range in which the distributions are close to Fisher-Tippett form. As can be seen in figures 2.9c and 2.9d, this does not hold for $950 \lesssim Re \lesssim 1050$. This was also observed for puff decay in pipe flow: figure 10(a) in (Nemoto & Alexakis, 2021). This does not invalidate the connection between extreme value statistics and the super-exponential scaling, but it does mean that there is a gap in using the Fisher-Tippett approximation at large time scales that at present we do not see how to close.

2.5 Transition pathways

Extreme value theory not only relates the super-exponential scaling of mean lifetimes to the distribution of fluctuations of the one-band state, it also provides a framework for understanding the rare pathways from one state to another. In a previous publication (Gomé *et al.*, 2020) we observed that the dynamics of band splitting were concentrated around a most-probable pathway in the phase space of large-scale Fourier coefficients. This motivates us to explore connections with *instantons* in the framework of Large Deviation Theory for systems driven by weak random perturbations. See for example (Touchette, 2011; Grafke *et al.*, 2015; Grafke & Vanden-Eijnden, 2019) and references therein. The concept is easily illustrated with the following stochastic differential equation

$$\dot{X} = -\nabla V(X) + \sqrt{\varepsilon}\eta, \tag{2.14}$$

where $X \in \mathbb{R}^d$, V is a potential, ε is a perturbation strength and η is Gaussian white noise. We assume that V has two local minima $\mathcal{A}$ and $\mathcal{B}$ separated by a saddle point and we consider transitions from $\mathcal{A}$ to $\mathcal{B}$. In the weak-noise limit $\varepsilon \to 0$, transitions will be rare and the trajectories associated with these rare events will be concentrated around a most probable path that connects states $\mathcal{A}$ and $\mathcal{B}$. This is the *instanton*. The dynamics along the instanton is such as to climb uphill from $\mathcal{A}$ to the saddle point under the influence of weak noise, and then to fall deterministically from the saddle to $\mathcal{B}$.

Examples of instantons in fluid systems are found for shocks in Burgers equations (Grafke *et al.*, 2013, 2015), and have been predicted and experimentally observed in rogue waves (Dematteis *et al.*, 2019). The concentration of transition paths around an instanton in a high-dimensional fully turbulent system was first observed by Bouchet *et al.* (Bouchet *et al.*, 2019) in a 2D barotropic model of atmospheric dynamics. Schorlepp *et al.* (Schorlepp *et al.*, 2021) have used instanton calculus to investigate the most likely configurations to generate large vorticity or strain within turbulence in the 3D Navier-Stokes equations. This phenomenology can also apply to deterministic chaos, as in the solar system (Woillez & Bouchet, 2020). Rolland has discussed instantons specifically in relation to turbulent-laminar transition, both in a model system (Rolland, 2018) and in plane Couette flow (Rolland, 2022).

Rare transitions of the type considered here could exhibit instanton-type behaviour if turbulent fluctuations were to play the role of weak noise. A detailed investigation is outside the scope of this chapter, but the current interest in the topic and the capacity of AMS to generate large numbers of rare transitions motivates us to briefly present transition paths for decays and splits. Examples of each are shown in figure 2.11. By binning samples from 200 transition paths we construct PDFs and then render isosurfaces of these PDFs to reveal the reactive tubes where paths concentrate. We include only reactive trajectories that leave $\mathcal{A}$ and terminate at the boundary of $\mathcal{B}_0$ or $\mathcal{B}_2$ without returning to $\mathcal{A}$.

The coordinates used for the PDF are chosen separately for decay and splitting. For decay, we show the decay of energy associated with the three velocity components of the flow, E_x, E_y, E_z

$$E_{(x,y,z)} \equiv \frac{1}{L_x L_y L_z} \int_\Omega \frac{1}{2}(u^2, v^2, w^2)\mathrm{d}\mathbf{x}.$$

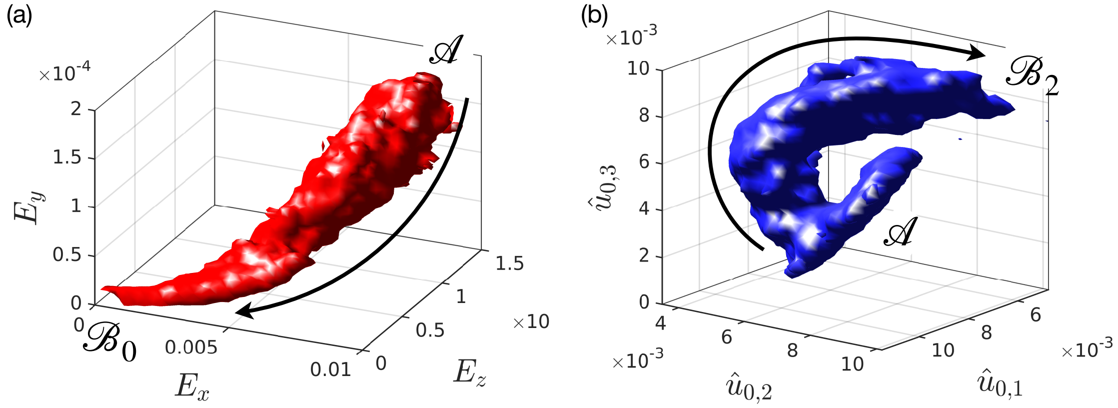

Figure 2.11: Joint probability density functions for reactive trajectories going from (a) $\mathcal{A}$ to $\mathcal{B}_0$ at $Re = 830$ (decay events) or (b) from $\mathcal{A}$ to $\mathcal{B}_2$ at Re $= 1150$ (splitting events). (a) Isosurface of $p(E_x, E_y, E_z)$ enclosing 90% of the total probability. (b) Isosurface of $p(\hat{u}_{0,1}, \hat{u}_{0,2}, \hat{u}_{0,3})$ enclosing 80% of the total probability. 200 trajectories are computed in each case.

Figure 2.11(a) shows that the reactive pathway from $\mathcal{A}$ to $\mathcal{B}_0$ is such that E_y decays most quickly, followed by E_z, followed by E_x so that the tube of reactive trajectories approaches $\mathcal{B}_0$ almost tangent to the E_x axis. This ordering of decay of energy components has been reported previously (Gomé *et al.*, 2020; Liu *et al.*, 2021); here the 90% probability isosurface shows that almost every successful decay trajectory follows a similar path.

For splits, we use coordinates similar to those in (Gomé *et al.*, 2020), the first three z Fourier components $\hat{u}_{0,1}, \hat{u}_{0,2}, \hat{u}_{0,3}$ of u, averaged in x and y:

$$\hat{u}_{0,n} = \frac{1}{L_x L_z} \int dy \left| \int dx \int dz \; u(x,y,z) e^{-2\pi i n z / L_z} \right| .$$

Figure 2.11(b) shows that the reactive pathway from $\mathcal{A}$ to $\mathcal{B}_2$ for the case of splits consists of a highly curved tube. This shape arises from the non-monotonicity of the splitting trajectories in these coordinates, as seen in (Gomé *et al.*, 2020). While a one-band state in $\mathcal{A}$ is characterized by high $\hat{u}_{0,1}$, the magnitude of $\hat{u}_{0,2}$ decreases at the beginning of a split before reaching its ultimate higher value in the two-band state in $\mathcal{B}_2$.

The transition pathways can also be described by the distribution of reactive times $T_{\mathcal{AB}}$. Reactive times have been characterised by Gumbel distributions

$$p_{\mathrm{Gum}}(T) = \beta e^{-\beta(T-\alpha)} \exp\left(-e^{-\beta(T-\alpha)}\right), \tag{2.15}$$

rigorously in simple stochastic ODEs in the weak noise limit (Cérou *et al.*, 2013), and observationally in one-dimensional stochastic PDEs (Rolland *et al.*, 2016; Rolland, 2018) and in the decay of uniform turbulence in the Navier-Stokes equations (Rolland, 2022). We find that the distributions of reactive times $T_{\mathcal{AB}_0}$ for decays and $T_{\mathcal{AB}_2}$ for splits are consistent with Gumbel distributions for each Re and hence also with instanton-like behaviour. Figure 2.12a illustrates this for $Re = 1150$, but the relatively small number of computed reaction trajectories (around 500 for this Re) precludes drawing more definite conclusions. The mean duration of reactive trajectories and their standard deviation as a function of Re are shown in figure 2.12b. The mean reactive times $\overline{T}_{\mathcal{AB}}$ vary only modestly with Re within each of the decay and the splitting regimes, as do the standard deviations (shown by the error bars).

The results presented in this section were motivated by interest in rare-event pathways and instantons in particular. We observe that reactive trajectories for both decays and splits concentrate around a reactive tube in phase space. This suggests that turbulent fluctuations are dominated by the collective behaviour of trajectories along a most-probable path, which may be an instanton. We observe mild contraction of pathways as we vary Re and events become rare. (See Supplementary Material.) Such contraction would be expected if the transitions exhibited instanton-like behavior. At the present time, even using the AMS algorithm, we have not produced sufficient numbers of independent reactive trajectories at very high transition times to draw definite conclusions and more work is needed to relate this behaviour to the Large Deviation theory.

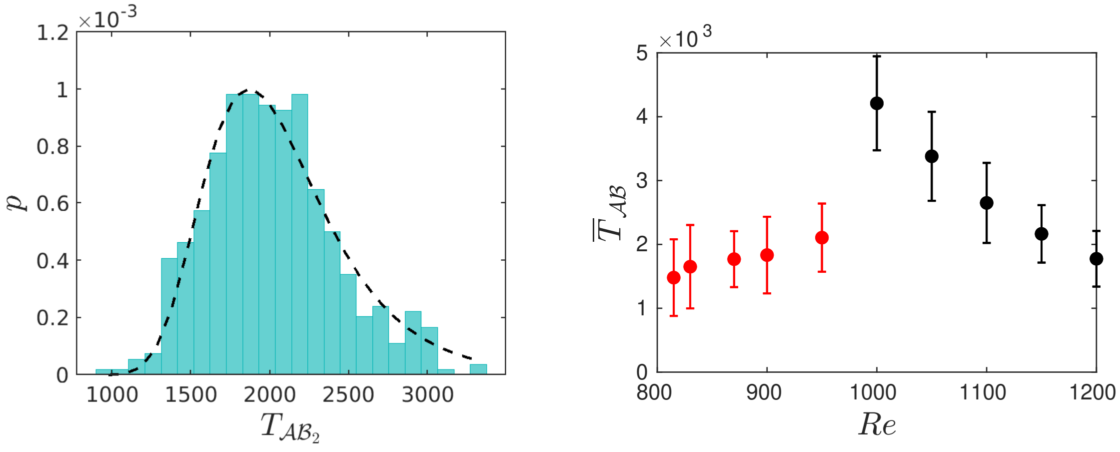

(a) **(b)**

Figure 2.12: (a) Histogram of the reactive times $T_{\mathcal{AB}_2}$ at $Re = 1150$, estimated with the AMS on $N = 500$ trajectories. Dashed lines show a fit with a Gumbel distribution (2.15) with $\alpha = 1.9 \times 10^3$ and $\beta = 2.7 \times 10^{-3}$. (b) Mean reactive times $\overline{T}_{\mathcal{AB}_0}$ and $\overline{T}_{\mathcal{AB}_2}$, for different Re, estimated with the AMS. Error bars indicated one standard deviation. Reactive times are measured from a random point in $\mathcal{A}$ to the boundary of $\mathcal{B}_0$ or $\mathcal{B}_2$.

2.6 Discussion

Determining – or even defining – the threshold for turbulence in wall-bounded shear flows has been an important question since Reynolds' 1883 article (Reynolds, 1883). Over time it has become clear that transitional turbulence is typically metastable and that transitions from metastable states play a crucial role in determining the onset of sustained turbulence (Pomeau, 1986; Bottin & Chaté, 1998; Bottin *et al.*, 1998; Peixinho & Mullin, 2006; Hof *et al.*, 2006; Willis & Kerswell, 2007). The culmination of this realization was the study of Avila *et al.* (Avila *et al.*, 2011) that determined the mean lifetimes for puff decay and puff splitting in pipe flow and showed that these lifetimes cross at a critical value of the Reynolds number Re_c. Although this work involved both numerical simulations and experiments, it was only through experiments that the very long lifetimes associated with Re_c were accessible. This has driven interest in capturing transitions from long-lived metastable states in wall-bounded flows via numerical simulations in order to obtain a clearer theoretical understanding of these events and of their Reynolds number dependence.

We have used the Adaptive Multilevel Splitting algorithm (Cérou & Guyader, 2007; Cérou *et al.*, 2011, 2019) to obtain rare events in plane channel flow. We have specifically analysed transitions from the metastable one-band state to either laminar flow (decay) or to a two-band state (splitting) in tilted-domain simulations of the 3D Navier-Stokes equations with 2×10^7 degrees of freedom. Using AMS on this large system we have been able to obtain mean lifetimes as large as 5×10^6 in advective time units with a gain in computational efficiency of a factor of up to 100 over the standard Monte Carlo approach. This has permitted us to access timescales near the lifetime crossing point for this flow. With the significant number of rare transitions we obtained, we have been able to construct weak tails in the probability distribution functions for the turbulence fraction. Exploiting ideas by Goldenfeld, Gutenberg & Gioia (Goldenfeld *et al.*, 2010) and Nemoto & Alexakis (Nemoto & Alexakis, 2018, 2021), we have been able to link directly the super-exponential variation of mean lifetimes with Re, for both decay and splitting, to the distribution of fluctuations in the one-band state. Finally, we have examined briefly the reaction pathways for decay and splitting.

Without conducting an extensive companion study in a large untilted domain, we cannot rule out effects of our narrow tilted domain on the transition rates and paths. However, we can cite comparisons of thresholds in the two types of domains. Shimizu & Manneville (Shimizu & Manneville, 2019) carried out channel flow simulations in large domains of size $L_{x'} \times L_{z'} = 500 \times 250$ or 1000×500 and obtained a threshold between $Re = 905$ and 984 for one of the two regimes they studied. This is quite close to the crossover at $Re \approx 980$ between the decay and splitting times that we have computed here in a narrow tilted domain via AMS. In plane Couette flow, the threshold for transition to turbulence was estimated to be $Re = 325$ by Shi *et al.* (Shi *et al.*, 2013) as the decay-splitting lifetime crossing in computations in a narrow tilted domain. This is the same as the value estimated experimentally by Bottin *et al.* (Bottin & Chaté, 1998; Bottin *et al.*, 1998) and numerically by Duguet *et al.* (Duguet *et al.*, 2010), in rectangular domains of size 380 × 70 and 800 × 356. An experiment in a much larger domain of size 3927 × 1500 by Klotz et al. (Klotz *et al.*, 2022) yields $Re = 330 \pm 0.5$ as the threshold .

Throughout this study we have focused on the turbulence fraction as a scalar observable of the state of the system, in large part because it is an easily obtainable quantity of general interest. While turbulence fraction is presumably not a mechanistic driver of either event, it is a very informative observable that is highly correlated to the distance to the targeted states. Our analysis of the super-exponential dependence of mean lifetimes on Re is probabilistic and relies heavily on the observed, but unexplained, collapse of rescaled distributions of F_t over what we call the collapse zone.

This approach is complementary to the dynamical-systems approach to turbulence (Eckhardt *et al.*, 2007; Kerswell, 2005; Kawahara *et al.*, 2012; Graham & Floryan, 2021). It would be useful to connect these approaches and to understand the mechanisms at work within the collapse zone. A particular question is the role played by saddle points or edge states (Eckhardt *et al.*, 2007; Schneider *et al.*, 2007; Duguet *et al.*, 2008; Chantry & Schneider, 2014; Paranjape *et al.*, 2020) in creating behaviour that can be rescaled and collapse to Re-independent form, because this is a key ingredient in how turbulent fluctuations are connected to decay and splitting events. While there is much previous work on decay from a dynamical-systems perspective, there is little to rely upon in the case of splitting.

Our investigation of reaction pathways demonstrates their concentration in phase space for both decay and splitting events. We have also observed a Gumbel distribution for the reaction times. The mild contraction of pathways that we have observed as the transition probability becomes very low resembles an instanton, but is inconclusive. To better support this picture, we would need to quantify the level of the fluctuations of the effective degrees of freedom in the system and how the fluctuation levels depend on the Reynolds number. Following this, we would need to compare the transition-rate dependence on the Reynolds number to what would be expected from the level of fluctuations within Large Deviation theory. This would require us to disentangle the effect of Re on turbulent fluctuations from its effect on the potential term, which itself strongly depends on Reynolds number as seen by the parameterisation of the PDFs within the one-band state (figures 2.8 and 2.10a). This approach would thus require the computation of the action minimizer in Large Deviation theory, which is out of the scope of the current study. This fundamental issue is related to the absence of a second parameter that would independently control the level of turbulent fluctuations and thereby allow an approach to a low-noise limit. We note that the states studied here are localised and insensitive to domain length. Hence domain size, the one parameter other than Re available in the numerical simulations, does not provide a means to influence the effect of fluctuations on the transitions. We refer the reader to the important studies of Rolland (Rolland, 2018, 2022) on rare events in transitional shear flows.

Finally, while we have succeeded in using the AMS algorithm to compute rare events in the 3D Navier-Stokes equations represented by $O(10^7)$ degrees of freedom, the experience has not been without difficulties. The most notable issues are: (1) the algorithm sometimes stagnates, making very slow progress toward obtaining trajectories reaching the target state and (2) the variance in the estimated mean lifetimes associated with the AMS realisations is large, thus requiring the costly step of running multiple realisations. The method used here could possibly be improved with the implementation of Anticipated AMS (Rolland, 2022). Most importantly, the score function is well known to be crucial to efficient performance of the algorithm. Finding a score function that targets successful splitting events has been particularly challenging. Although we have obtained a serviceable empirical score function based largely upon the turbulence fraction, a more far-ranging search for appropriate score functions is needed.

2.A Effect of perturbation level and sample size on AMS variance

Estimating rare events with the AMS (Adaptive Multilevel Splitting) algorithm for a high-dimensional system such as ours is a trade-off between accuracy of the estimate and computational cost. It is known from previous studies on low-dimensional systems (Rolland & Simonnet, 2015; Rolland, 2018) that the variance of the AMS scales with sample size N like $1/\sqrt{N}$, and that completely unbiased results depend, among other things, on the definition of the score function and the number of degrees of freedom. In (Rolland, 2018) it was shown empirically that $|\hat{p} - \hat{p}_{\mathrm{MC}}|/\hat{p}_{\mathrm{MC}}$ scales as $1/N$, where $\hat{p}$ and $\hat{p}_{\mathrm{MC}}$ are the transition probabilities estimated by the AMS and MC (Monte Carlo) methods, respectively

Although a large sample size N is desirable to produce low variance, sample sizes larger than $N = 100$ are challenging in terms of computational time and memory in our case. If smaller sample sizes are used, the accuracy of the estimator can be improved using multiple AMS realisations. We have verified the evolution of the AMS estimator $\hat{p}$ for different values of N and ϵ in Table 2.5 and find that good agreement with $\hat{p}_{\mathrm{MC}}$ was achieved at $N = 50$. We thus decide to take $N = 50$ for all Re, and we further average results over N_{AMS} realisations as listed in the main chapter.

Table 2.5 shows the dependence of the estimator of the transition probability $\hat{p}$ on ϵ for $Re = 1150$. We recall that $\hat{p}$ varies by orders of magnitude in the relevant range of Re and hence we seek only one digit of accuracy. By this criterion, $\hat{p}$ does not depend strongly on ϵ. We recall that the perturbation amplitude ϵ acts only at the cloning step of the AMS, through a multiplicative noise term. The choice of ϵ is governed by the following principles. If the perturbation is too small, the main risk is a low diversity of the clone samples and thus a stagnation of the iterative process. This issue arises particularly when the transition probability is very low. Stagnation is a potential explanation for what we observe in Table 2.5 for $\epsilon = 10^{-6}$, where the deviation from $\hat{p}_{\mathrm{MC}}$ slightly increases. The

ϵ	N	$\hat{p}$	$\lvert\hat{p}-\hat{p}_{\mathrm{MC}}\rvert/\hat{p}_{\mathrm{MC}}$	$\sigma(\hat{p})$
1×10^{-5}	30	0.0351	0.250	0.0365
1×10^{-5}	50	0.0456	0.021	0.0197
1×10^{-5}	100	0.0451	0.032	0.0137
5×10^{-6}	50	0.0455	0.022	0.0299
1×10^{-6}	50	0.0487	0.047	0.0085

Table 2.5: Dependence on N and on ϵ of the accuracy of the AMS estimator of the probability of transition $\hat{p}$ at $Re = 1150$, for which $\hat{p}_{\mathrm{MC}} = 0.047$ has been obtained from Monte Carlo simulations. $\sigma(\hat{p})$ is the standard deviation of $\hat{p}$ from at least $N_{\mathrm{AMS}} = 5$ AMS realisations.

reason for this stagnation is that the time of approach to the maximum of ϕ in each trajectory is shorter than the Lyapunov time of the system, causing all trajectories to be unmodified by noise at the maximum. In this case, all of the trajectories end up with the same values of the maximum, causing the iteration to stall. This could happen even if the average time to return to $\mathcal{A}$ or to reach $\mathcal{B}_2$ is larger than the Lyapunov time of the system. On the other hand, the perturbation should not be so large as to change the statistics of the trajectories compared to a fully deterministic strategy such as Monte Carlo. The score function must also remain unchanged at the cloning time, otherwise the trajectory selection could be altered. For each Re, ϵ is then chosen as the minimal stochastic input that promotes trajectory diversification and for which the algorithm does not stagnate.

2.B Evolution of reactive tubes with the Reynolds number

Figure 11 of the main chapter illustrates reactive tubes corresponding to decay (at $Re = 830$) and to splitting (at $Re = 1150$). The reactive tubes are isosurfaces of the probability density obtained from reactive trajectories going from $\mathcal{A}$ to $\mathcal{B}_0$ or $\mathcal{B}_2$. Here we investigate the effect of Re on these reactive tubes. Figures 2.13a and 2.13b compare trajectory concentration at different Re by showing the contours of the probability density obtained from reactive trajectories in the phase spaces (E_x, E_z) (for decays) and $(\hat{u}_{0,1}, \hat{u}_{0,2})$ (for splits). The contours surround 90% of the probability. These plots are 2D projections of Figure 11.

For decay cases, the reactive tubes seem to contract slightly during the final viscous phase of the decay process as Re is increased and decay becomes rarer. In the case of splits, portions of the reactive tubes contract as Re is decreased. These plots indicate that the reactive trajectories become slightly more concentrated as Re approaches Re_c. However, the range of Re under study is limited. It would be helpful to have data for decay events at $Re > Re_c$ and splits for $Re < Re_c$, both of which are still out of reach in our computations.

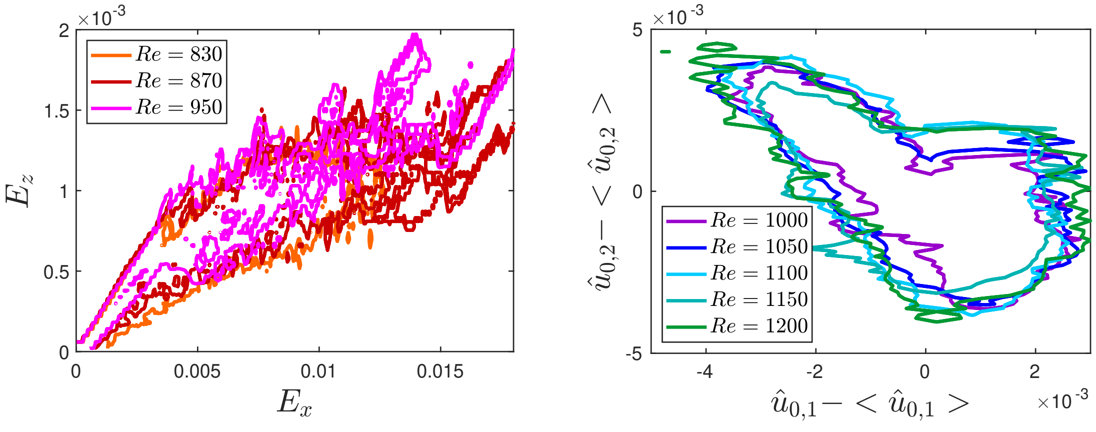

(a) **(b)**

Figure 2.13: Contours of joint PDFs at different Reynolds numbers (a) of (E_x, E_z) for trajectories going from $\mathcal{A}$ to $\mathcal{B}_0$ and (b) of $(\hat{u}_{0,1}, \hat{u}_{0,2})$ for trajectories going from $\mathcal{A}$ to $\mathcal{B}_2$. The temporal average during the transient trajectories is subtracted for better comparison, since sets $\mathcal{A}$ and $\mathcal{B}_2$ evolve with Re. Contours shown enclose 90% of the total probability of the joint PDFs.

2.C Approach to an edge state during decays

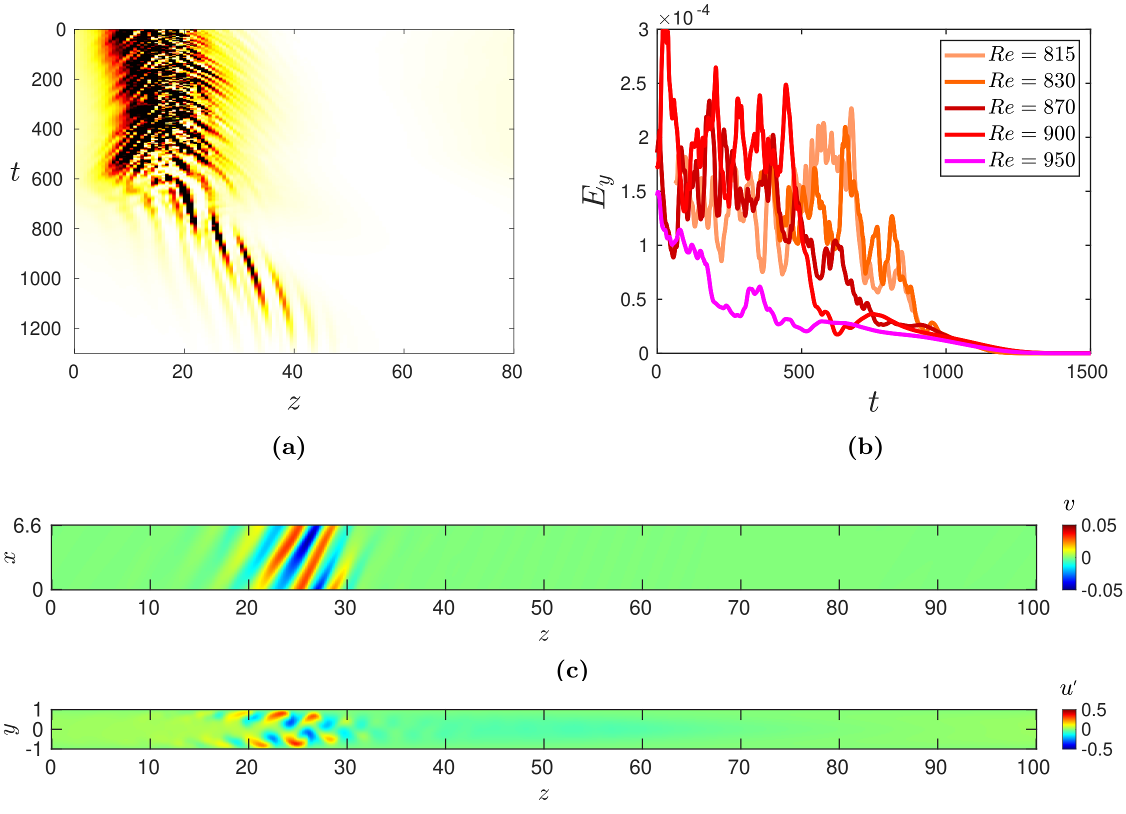

(a) **(b)**

(c)

(d)

Figure 2.14: Approach to the edge state of Paranjape *et al.* (Paranjape *et al.*, 2020): (a) Space-time diagram of the decay of a turbulent band at $Re = 900$. Colors (white: 0, black: 0.001) show the local deviation energy at $(x = 3.3, y = 0.8)$. (b) $E_y(t)$ for decay paths for different Re. Stagnation indicating proximity to an edge state is particularly noticeable at $Re = 900$ and 950. Trajectory at $Re = 900$ corresponds to (a). (c, d) Visualisation of possible edge state in the (z, x) plane (cross-flow velocity v) and the (z, y) plane (streamwise velocity u'), corresponding to $t = 800$ in the space-time plot.

The question of whether a saddle-point effectively separates the phase space between $\mathcal{A}$ and $\mathcal{B}_0$ or $\mathcal{B}_2$ can be answered by bisection techniques (Schneider *et al.*, 2007; Duguet *et al.*, 2008), as was done by Paranjape *et al.* (Paranjape *et al.*, 2020) between one band and the laminar state. The computation of multiple successful trajectories also helps to verify the presence of this edge state, that should be statistically approached by reactive trajectories. We show in Figure 2.14a a typical spatio-temporal diagram in the parameter range $Re \in [900, 950]$: during the decay of the band and before its full laminarisation, the trajectory approaches a state composed of weak straight streaks that differs from the one-band state. This state is visualised in Fig. 2.14c and 2.14d and resembles the edge state found by Paranjape *et al.*. As shown by Fig. 2.14a, this state moves at a velocity that differs from that of the initial turbulent band, and is approached within a time window of around 600 time units starting from $t = 600$. The presence of an edge state is supported by Figure 2.14b, which shows $E_y(t)$ for decaying trajectories.

Proximity to the edge state is seen for $Re = 900$ and $Re = 950$ as approximate stagnation before the viscous decay. The particular case of $Re = 900$ (red curve in Fig. 2.14b, and space-time diagram in Fig. 2.14a) exemplifies a characteristic three-step process: a first departure from the initial one-band state ($t \simeq 450$), followed by an approach to a plateau ($t \simeq 600$) correlated to the appearance of straight streaks (Fig. 2.14a), which eventually decay exponentially ($t \gtrsim 1000$). For $Re \leq 830$, the energy decays directly from the one-band state to the laminar state and the plateau does not appear. The stagnation phase, which differs from the subsequent exponential decay, confirms the nonlinear nature of the dynamics in this region, and suggests that we are near the edge state computed by Paranjape *et al.* (Paranjape *et al.*, 2020).

Our simulations support the established idea that pathways are statistically mediated by an underlying edge state when transiting from the one-band state to laminar flow, and that the system remains longer near the saddle point when the transition probability is lower (or Re increased: see the longer stagnation phase at $Re = 950$ than at $Re = 900$). The importance of the edge state at higher Re is consistent with the higher concentration observed on Fig. 2.13a and with the longer reactive times (Fig. 12b).

Chapter 3

Spectral analysis of transitional shear turbulence

Low Reynolds number turbulence in wall-bounded shear flows *en route* to laminar flow takes the form of localized turbulent structures. In plane shear flows, these appear as a regular alternation of turbulent and quasi-laminar flow. Both the physical and the spectral energy balance of a turbulent pattern are computed, and compared to those of uniform turbulence at low Re. These energy balances show the presence of robust negative production at large scales, appearing in both pattern and uniform regimes. The turbulent energy is spectrally redistributed via a strong energy transfer from small to large scales. In transitional patterns, the mean flow is strongly modulated and is fuelled by two mechanisms: the absorbing interaction with turbulent fluctuations (via negative production) and the nonlinear self-interaction of the mean flow. This energetic cycle is surveyed as uniform turbulence loses its stability, and conserved quantities are found from the uniform to the patterned state. Signatures of this mechanism fuelling large scales are also found in the uniform flow at low Re.

Low Reynolds number turbulence in wall-bounded shear flows *en route* to laminar flow takes the form of localised turbulent structures. In plane shear flows, these appear as a regular alternation of turbulent and quasi-laminar flow. Both the physical and the spectral energy balance of a turbulent-laminar pattern are computed and compared to those of uniform turbulence at low Re. In the patterned state, the mean flow is strongly modulated and is fuelled by two mechanisms: primarily, the nonlinear self-interaction of the mean flow (via mean advection), and, secondly, the extraction of energy from turbulent fluctuations (via negative production, associated to a strong energy transfer from small to large scales). These processes are surveyed as uniform turbulence loses its stability. Inverse energy transfers and negative production are also found in the uniformly turbulent state.

3.1 Introduction

Transitional patterns in plane shear flows arise naturally from uniform turbulence at sufficiently low Reynolds number. These patterns feature a selected orientation of around $\simeq 24°$ when they emerge (Prigent *et al.*, 2003; Tsukahara *et al.*, 2005*b*; Shimizu & Manneville, 2019; Kashyap *et al.*, 2020*b*). When the Reynolds number is further reduced, these spatio-temporally intermittent structures display important features of non-equilibrium phase transitions; both experimental and numerical studies have demonstrated their membership in the directed percolation universality class in the case of plane Couette flow (Lemoult *et al.*, 2016; Chantry *et al.*, 2017; Klotz *et al.*, 2022).

Oblique patterns consist of turbulent regions or bands alternating with (quasi-) laminar gaps. An inherent feature of the coexistence of these two phases in planar shear flows is the large-scale flow along the laminar-turbulent interface. This along-band flow has been observed in both experimental and numerical configurations (Coles & van Atta, 1966; Barkley & Tuckerman, 2007; Duguet & Schlatter, 2013; Couliou & Monchaux, 2015; Tuckerman *et al.*, 2020; Klotz *et al.*, 2021), and can be seen as a consequence of the breaking of spanwise symmetry and incompressibility (Duguet & Schlatter, 2013).

Transitional turbulence presents a separation of scales: flow along the laminar-turbulent interface paves the large scales, while the streaks and the rolls governed by the self-sustaining process of turbulence (Hamilton *et al.*, 1995; Waleffe, 1997) are the basic ingredients of the small-scale flow. In channel flow, the streak spacing is commonly found to be around $\lambda_z^+ \approx 100$ (Kim *et al.*, 1987), whereas it is found to be larger ($\lambda_z^+ \approx 132$) in plane Couette flow at low-enough Reynolds number (Komminaho *et al.*, 1996; Jiménez, 1998; Tsukahara *et al.*, 2006). In contrast, the wavelength of the large-scale patterns is much larger than that of the rolls and streaks, e.g. with a ratio on the order of 20 in patterned plane Couette flow. This scale separation is visible in the spectral analysis presented by several authors. We mention Tsukahara *et al.* (2005*b*) in channel flow, Tuckerman & Barkley (2011); Duguet & Schlatter (2013) in Couette flow and Ishida *et al.* (2017) in annular pipe flow. However, the exact contribution of the rolls and streaks in energising the large-scale patterns has never been thoroughly investigated.

In pipe flow, the energy distribution within turbulent structures was measured in the classic experiments of Wygnanski *et al.* (Wygnanski & Champagne, 1973; Wygnanski *et al.*, 1975) and later in numerical simulations by Song *et al.* (2017). For localised turbulent structures known as puffs, turbulent production P at the upstream side of a puff is larger than turbulent dissipation ϵ, whereas at the downstream side, dissipation dominates production, as it does throughout regions of quasi-laminar flow in general. No local balance between P and ϵ is found within the puff. In contrast, in expanding or retracting turbulent zones, known as slugs, the flow in the turbulent core is locally in equilibrium, with production balancing dissipation ($P \approx \epsilon$). Theoretical efforts to model turbulent-laminar structures in pipe flow are based on these properties of the turbulent production and dissipation (?Barkley, 2016).

Spectral energy budgets have been extensively used to quantify energy transfers and interactions between mean flow and turbulent kinetic energy (TKE) in high Reynolds number wall-bounded flows. This approach dates from Lumley (1964), who conjectured that energy is transferred from small to large scales in shear flows as distance from the wall increases. This concept of inverse energy transfer was later investigated by Domaradzki *et al.* (1994); Bolotnov *et al.* (2010); Lee & Moser (2015); Mizuno (2016); Cho *et al.* (2018); Lee & Moser (2019); Kawata & Tsukahara (2021) (and references therein). However, it is only recently that the spectral energy budget has been computed at low Re_τ, in particular by Symon *et al.* (2021) in a turbulent channel of minimal size at $Re_\tau = 180$ and in an exact coherent state of channel flow (Park & Graham, 2015). Currently, there is a lack of understanding of the spectral distribution of energy in transitional wall-bounded turbulence, especially regarding the role of energy transfers and triad interactions in the emergence of the large-scale flow.

This chapter is devoted to the relationship between the inhomogeneous mean flow and turbulent fluctuations in transitional plane Couette flow. These are investigated through the computation of both physical (§3.4) and spectral (§3.5) energy balances in the regime where patterns emerge from uniform turbulence. We will survey various energy transfers as a function of Re in §3.6. In §3.7, turbulent production and non-linear transfers are analysed at various wall-normal positions. The energy processes reported in this chapter will be further investigated as a function of the pattern wavelength in chapter 4, where we will discuss their role in selecting the pattern wavelength.

3.2 Numerical setup

Plane Couette Flow is driven by two parallel rigid plates moving at opposite velocities $\pm U_{\text{wall}}$. Lengths are nondimensionalised by the half-gap h between the plates, velocities by U_{wall}, and time by h/U_{wall}. The Reynolds number is defined to be $Re = U_{\text{wall}} h/\nu$. We will require one last dimensional quantity, the horizontal mean shear at the walls, which we denote by U'_{wall}. We will use non-dimensional variables throughout. We use the pseudospectral parallel code `Channelflow` (?) to simulate the incompressible Navier-Stokes equations

$$\frac{\partial \boldsymbol{u}}{\partial t} + (\boldsymbol{u} \cdot \nabla)\,\boldsymbol{u} = -\nabla p + \frac{1}{Re}\nabla^2 \boldsymbol{u} \tag{3.1a}$$

$$\nabla \cdot \boldsymbol{u} = 0 \tag{3.1b}$$

in a domain which is periodic in the x and z directions.

Since the bands are found to be oriented obliquely with respect to the streamwise direction, we use a periodic numerical domain which is tilted with respect to the streamwise direction of the flow, shown as the oblique rectangle in figure 4.1. This choice was introduced by Barkley & Tuckerman (2005) and has become common in studying turbulent bands (e.g., **?**Paranjape *et al.*, 2020; Tuckerman *et al.*, 2020). The x direction is chosen to be aligned with a typical turbulent band and the z direction to be orthogonal to the band. The relationship between streamwise-spanwise coordinates and tilted band-oriented (x, z) coordinates is:

$$\mathbf{e}_{\text{strm}} = \cos\theta\,\mathbf{e}_x + \sin\theta\,\mathbf{e}_z \tag{3.2a}$$

$$\mathbf{e}_{\text{span}} = -\sin\theta\,\mathbf{e}_x + \cos\theta\,\mathbf{e}_z \tag{3.2b}$$

The usual wall-normal coordinate is denoted by y and the corresponding velocity by v. The field visualised in figure 4.1 (black box) is obtained by concatenating four times a field resulting from a simulation in $L_{\text{strm}} = 200$, $L_{\text{span}} = 100$.

The tilted box effectively reduces the dimensionality of the system by discarding large-scale variations along the short x direction. This direction is considered homogeneous over large scales because it is only determined by small turbulent scales, and because the band is assumed to be infinite in x. The main underlying assumption is the angle of the pattern. In large non-tilted domains, plane Couette flow shows two statistical orientations that equilibrate (Prigent *et al.*, 2002; Duguet *et al.*, 2010; Klotz *et al.*, 2022) whereas only one orientation is permitted by our tilted box.

In our simulations, we fix the angle $\theta = 24°$, the x domain length $L_x = 10$, the x resolution $= L_x/N_x = 10/120$, and z resolution $\Delta z = L_z/N_z = 0.08$, (similar to that used by Tsukahara *et al.* (2006); Barkley & Tuckerman (2007)). We will make extensive use of two numerical domains, with different domain sizes L_z, shown in figure 4.1.

1. **Minimal Band Units**, shown as the red box in figure 4.1, which can accommodate a single turbulent band and associated quasi-laminar gap. This effectively restricts the flow to a perfectly periodic turbulent-laminar pattern of wavelength $\lambda = L_z$. The size L_z governing the periodicity of the pattern and can be modified. L_z is fixed to $L_z = 40$, which is an approximation of the natural spacing of bands observed experimentally and numerically. The effect of size L_z will be investigated in chapter 4.
2. **Long Slender Boxes**, which have a large L_z direction that allows for a large number of gaps and bands in the system. The blue box in figure 4.1 is an example of such a domain size with $L_z = 240$, but a larger size of $L_z = 800$ will be used throughout this chapter.

We furthermore introduce the friction Reynolds number:

$$Re_\tau = \frac{u_\tau h}{\nu}, \qquad \text{with } u_\tau^2 = \nu U'_{\text{wall}} = \frac{U_{\text{wall}}^2}{Re}\left\langle \frac{\partial u_{\text{strm}}}{\partial y}(y = \pm 1)\right\rangle_{x,z,t} \tag{3.3}$$

Note that $Re_\tau = \sqrt{Re}$ in the laminar state. Later we will need the wall-normal coordinate

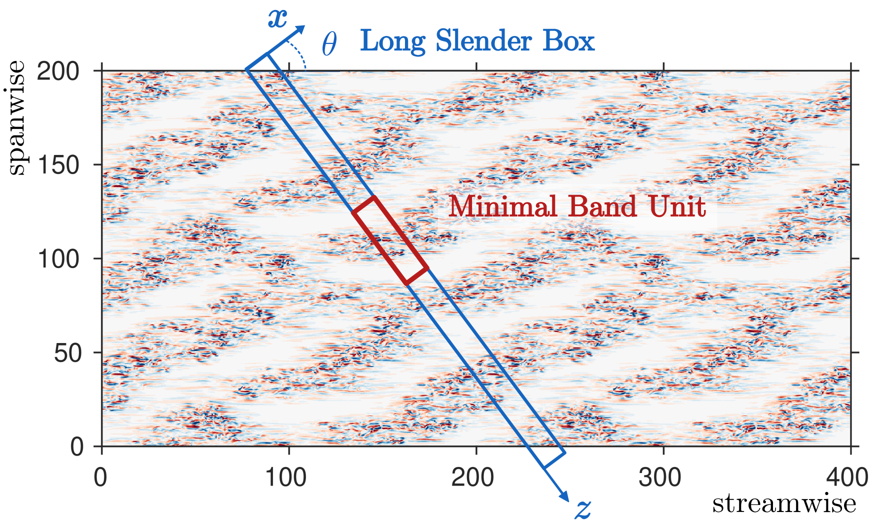

Figure 3.1: Visualisation of the numerically simulated flow at $Re = 360$ and of our numerical domains. Colors show y velocity at $y = 0$ (blue: -0.2, white: 0, red: 0.2) in a domain of size $L_{\text{strm}} = 400$, $L_{\text{span}} = 200$. Red and blue boxes show a Minimal Band Unit and a Long Slender Box, respectively.

in wall units $y^+ = (1-y)Re_\tau$, and similarly for other quantities. In a Minimal Band Unit at a transitional Reynolds number, the turbulence may be uniform or patterned during different time periods, i.e. it is temporally as well as spatially intermittent. For this reason, for each value of Re, we take the time average in (3.3) over a period during which the flow retains qualitatively the same state. This yields two slightly different values, Re_τ^u for a uniform state and Re_τ^p for a patterned state, as presented in table 3.1 for $L_z = 40$. In later nondimensionalisations, we will use either Re_τ^u or Re_τ^p, as appropriate for the flow state.

This procedure does not take into account the local variability of the wall shear stress due to spatial intermittency; for this, we would need to omit z-averaging in (3.3) to produce z-dependent values of Re_τ; see Kashyap *et al.* (2020*b*) for a thorough analysis of fluctuations of Re_τ within and outside of turbulent bands.

3.3 Spectra in different configurations

We carried out simulations in a Long Slender Box of size $L_z = 800$ for various Re, with the uniform state at $Re = 500$ as an initial condition. These simulations are shown via the spatio-temporal diagrams of figure 4.2 for $Re = 440$ and for $Re = 380$. With decreasing Re, the flow shows intermittent gaps (white spots on the figure) that emerge

Re	400	420	440	460	480	500	550	600	1000
Re_τ^p	29.68	31.09	32.82	34.61	35.90	37.33	-	-	-
Re_τ^u	30.65	32.24	33.69	35.08	36.42	37.67	40.66	43.62	66.42

Table 3.1: Values of Re_τ for various values of Re in a Minimal Band Unit of size $L_z = 40$. Re_τ^p and Re_τ^u are obtained by averaging over the patterned or uniform state, respectively. For $Re > 500$, the patterned state does not occur.

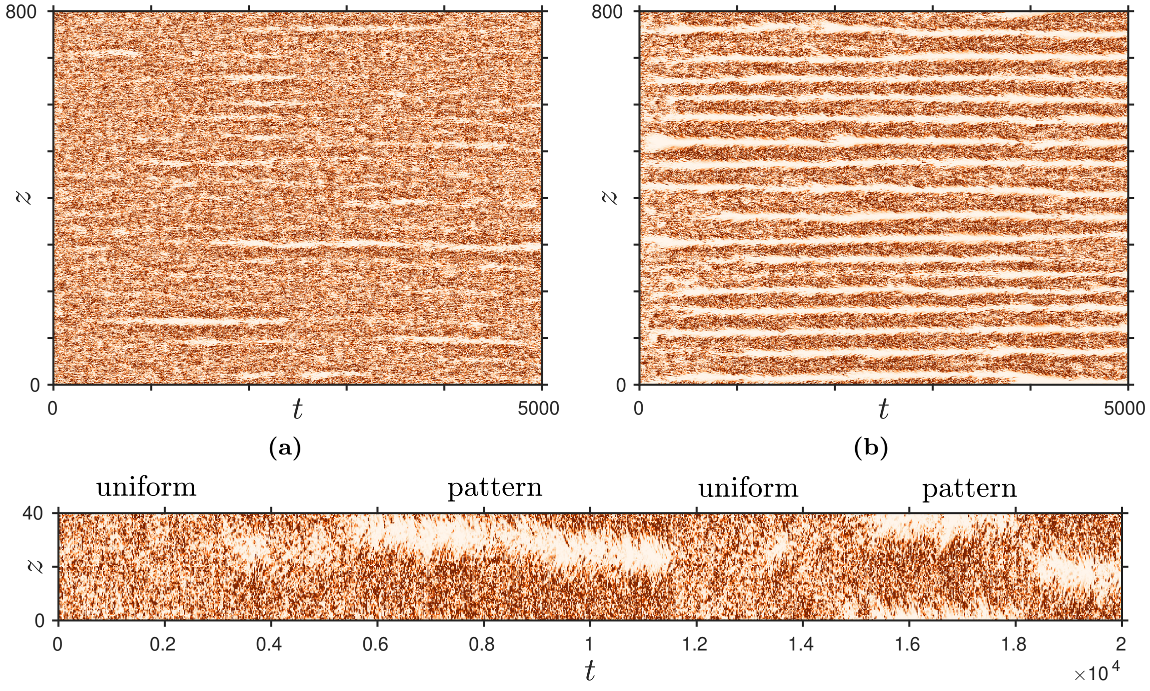

(a) **(b)**

(c)

Figure 3.2: Spatio-temporal visualisations of the emergence of gaps and patterns in a Long Slender Box with $L_z = 800$, for (a) $Re = 440$ and (b) 380. Flow at $t = 0$ is initiated from uniform turbulence at $Re = 500$. Colors show local cross-flow energy $(v^2 + u_{\text{span}}^2)/2$ at $x = L_x/2$, $y = 0$ (white: 0, dark orange: 0.02). (c) Intermittent alternation between uniform and patterned turbulence at $Re = 430$ in a Minimal Band Unit of $L_z = 40$.

from the turbulent field at seemingly random locations. A *gap* is defined as a weakened turbulent structure, or a quasi-laminar zone, surrounded by turbulent flow. A gap is the opposite of a *band*, which is a turbulent core surrounded by quasi-laminar flow. In plane Couette flow, bands are observed at $Re \in [300, 440]$ (Prigent *et al.*, 2003; Barkley & Tuckerman, 2007; Duguet *et al.*, 2010; Shi *et al.*, 2013). Gaps and bands self-organize into *patterns* as Re is decreased. This is the situation observed in a Long Slender Box in figure 3.2b ($Re = 380$), where a regular alternation of gaps and turbulent bands is visible. In a Minimal Band Unit, the system is constrained and the distinction between gaps and patterns is lost. While the system cannot exhibit the spatial intermittency seen in figure 3.2a, temporal intermittency is possible and is seen as alternations between uniform turbulence and patterns, as illustrated in figure 3.2c at $Re = 430$. chapter 4 investigate extensively the emergence of gap and patterns out of turbulent flow.

We define the total physical energy and total spectral energy of the flow as:

$$E(y, z) \equiv \frac{1}{2}\overline{\boldsymbol{u} \cdot \boldsymbol{u}} \quad \text{and} \quad \widehat{E}(y, k_z) \equiv \frac{1}{2}\overline{\hat{\boldsymbol{u}}^* \cdot \hat{\boldsymbol{u}}},$$

where $\overline{(.)}$ denotes the time and x average and the Fourier transform is taken in the band-orthogonal direction z:

$$\hat{\boldsymbol{u}}(x, y, k_z) = \frac{1}{L_z} \int_0^{L_z} \boldsymbol{u}(x, y, z) e^{-ik_z z} \mathrm{d}z. \tag{3.4}$$

Figure 3.3a shows $\widehat{E}(y = 0, k_z)$ for simulations in a Long Slender Box at different values of Re. Here, the average is carried out over a long period of time ($t \in [100, 5000]$). The total energy spectra show two prominent energy-containing scales: one at small wavenumbers (around $k_z = 0.15$, i.e. $\lambda_z \simeq 42$) corresponding to the alternation of turbulent bands and quasi-laminar gaps, and a second one at large wavenumbers ($k_z \simeq 1.41$, $\lambda_z \simeq 4.45$), which we will denote k_{rolls}. This small wavelength corresponds to a spanwise spacing of $\lambda_{\text{span}} = 2\pi \cos\theta / k_{\text{rolls}} = 4.06$, which is approximately the idealised periodicity of pairs of streaks and rolls in Couette flow (Waleffe, 1997), with individual rolls occupying the height $L_y = 2$ of the shear layer. In wall units, this peak corresponds to $\lambda^+_{\text{span}} = 130$ at $Re = 430$ ($Re_\tau = 31.9$). This is not far from the streak spacing of $\lambda^+_{\text{span}} = 136$ measured by Komminaho *et al.* (1996) in plane Couette flow at $Re_\tau = 52$. For $k_z > k_{\text{rolls}}$, the energy decreases with k_z up to the resolution scale. The scale separation between the large-scale gaps and bands and the small-scale streaks and rolls was already observed in the transitional regime by many authors (Tsukahara *et al.*, 2005*b*; Tuckerman & Barkley, 2011; Ishida *et al.*, 2016).

The spectrum varies with Reynolds number, but mostly at large scales (low k_z): the large-scale peak is barely visible at $Re = 500$ and grows in intensity with decreasing Re, becoming dominant for $Re < 440$. Meanwhile, the small-scale spectrum is only very weakly affected by the change in Re.

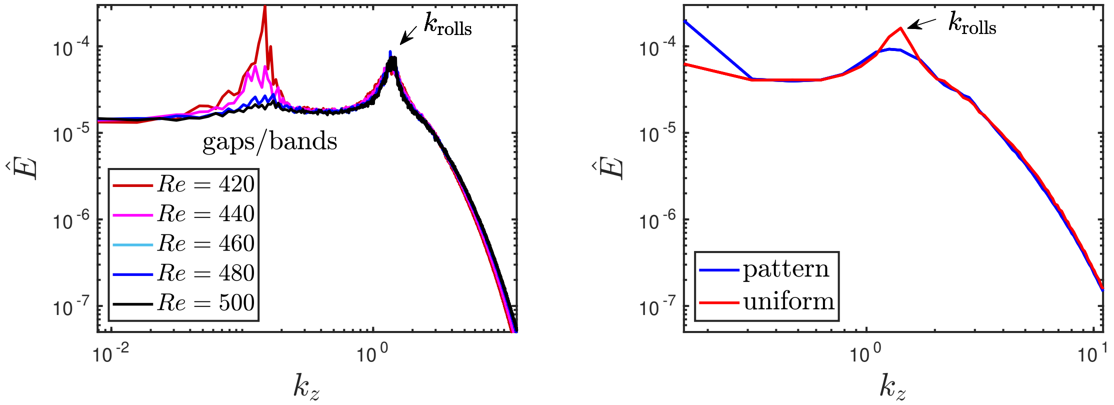

(a) Long Slender Box **(b)** Minimal Band Unit at $Re = 430$

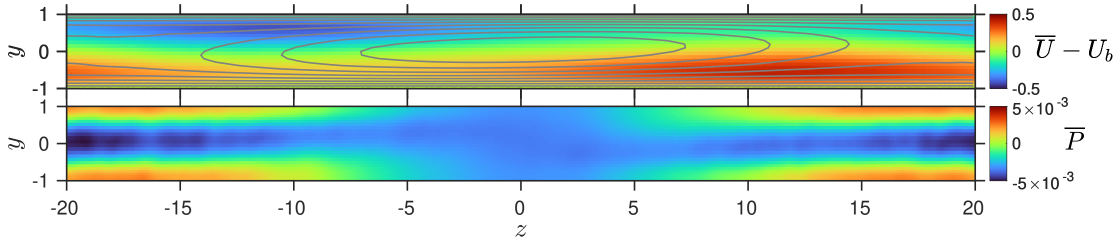

(c) Patterned mean flow in a Minimal Band Unit

Figure 3.3: (a) Total energy spectra in a large domain $L_z = 800$ (black line) at $y = 0$, for different Re. The spectra are averaged irrespective of the nature of the state (patterned or uniform). (b) Total energy spectra (continuous lines) in a Minimal Band Unit of size $L_z = 40$. The spectra are individually computed in the uniform turbulence (red) and patterned states (blue), at $Re = 430$. (c) Visualisation of the mean flow: colors show the deviation of the along-band velocity from the laminar base flow $\overline{U} - U_b$ (top) and the pressure $\overline{P}$ (bottom). Streamlines of the mean flow perpendicular to the bands are shown as grey curves.

We now turn to the Minimal Band Unit, which has exactly the periodicity of a single wavelength of the pattern. The flow in this configuration does not have localised gaps like those which appear in figure 3.2a. The system is instead fluctuates between patterned and uniform states as seen in figure 3.2c, and each of the two states can be distinguished and consequently analysed separately. In particular, we can take means for patterned and uniform states independently. For this reason, the remainder of this chapter will focus on the Minimal Band Unit with a fixed length of $L_z = 40$.

The total energy spectrum in a Minimal Band Unit at $Re = 430$ is presented in figure 3.3b. Contrary to figure 3.3a, where unconditional averaging mixes uniform turbulence and localised gaps in the spectrum, here we have conditionally computed the spectrum for the patterned state (blue line) and the uniform state (red line) separately. As expected, the spectrum for the uniform state lacks the peak at the pattern scale. The energy of the streak-roll structures $\widehat{E}(k_{\text{rolls}})$ is higher in the uniform case than in the patterned case. This hints at a redistribution of the energy from small scales (near k_{rolls}) to large scales ($\ll k_{\text{rolls}}$) when the flow changes from uniform to patterned turbulence. For $k_z > 2$, both spectra appear to collapse, suggesting that the small-scale turbulent cascade is the same in both cases.

We now decompose the flow into a mean and fluctuation: $\boldsymbol{u} = \overline{\boldsymbol{u}} + \boldsymbol{u}'$, where the mean flow $\overline{\boldsymbol{u}}(y,z)$ is computed from an (x,t) average over long time intervals in either the patterned or the uniform state in the Minimal Band Unit. The mean flow in this configuration was studied by Barkley & Tuckerman (2007). The mean flow $\overline{\boldsymbol{u}} = (U(y,z), V(y,z), W(y,z))$ is visualised on figure 3.3c, by showing $U - U_b$ and $\overline{P}$ (colors) and plotting the streamlines of (V,W) (grey lines). (Note that figure 3.3c corrects the erroneous pressure displayed in Barkley & Tuckerman (2007, figure 5).) The flow is centered around the quasi-laminar region, and the total in-plane velocity (V,W) shows a circulation around this region of the flow. $U - U_b$ shows two centro-symmetrically related zones of flow parallel to the band, localised in the upper layer (blue zone) and in the bottom layer (red zone).

The mean flow $\overline{\boldsymbol{u}}$ can also be decomposed into Fourier modes:

$$\overline{\boldsymbol{u}}(y,z) = \overline{\boldsymbol{u}}_0(y) + 2\mathcal{R}\left(\overline{\boldsymbol{u}}_1(y)e^{2\pi i z/L_z}\right) + \overline{\boldsymbol{u}}_{>1}(y,z) \tag{3.5}$$

where $\mathcal{R}$ denotes real part, $\overline{\boldsymbol{u}}_0 \equiv \widehat{\overline{\boldsymbol{u}}}(y, k_z = 0) = (U_0(y), 0, W_0(y))$ is the z-independent (uniform) component of the mean flow, $\overline{\boldsymbol{u}}_1 = \widehat{\overline{\boldsymbol{u}}}(y, k_z = 2\pi/L_z)$ is the Fourier coefficient corresponding to wavelength $\lambda_z = L_z$, and $\overline{\boldsymbol{u}}_{>1} \equiv \sum_{k_z > 2\pi/L_z} \widehat{\overline{\boldsymbol{u}}}(y, k_z)$ is the remainder of the decomposition. (To lighten the notation, we omit the hats on $\overline{\boldsymbol{u}}$ when subscripts 0, 1, or > 1 are used to indicate the corresponding Fourier coefficients.) Most of the mean-flow energy lies in the uniform mode $\overline{\boldsymbol{u}}_0$, with a few percent in the trigonometric component $\overline{\boldsymbol{u}}_1$. The energy in the remaining terms ($\overline{\boldsymbol{u}}_{>1}$) is at least two orders of magnitude lower than that of $\overline{\boldsymbol{u}}_1$ (Barkley & Tuckerman, 2007).

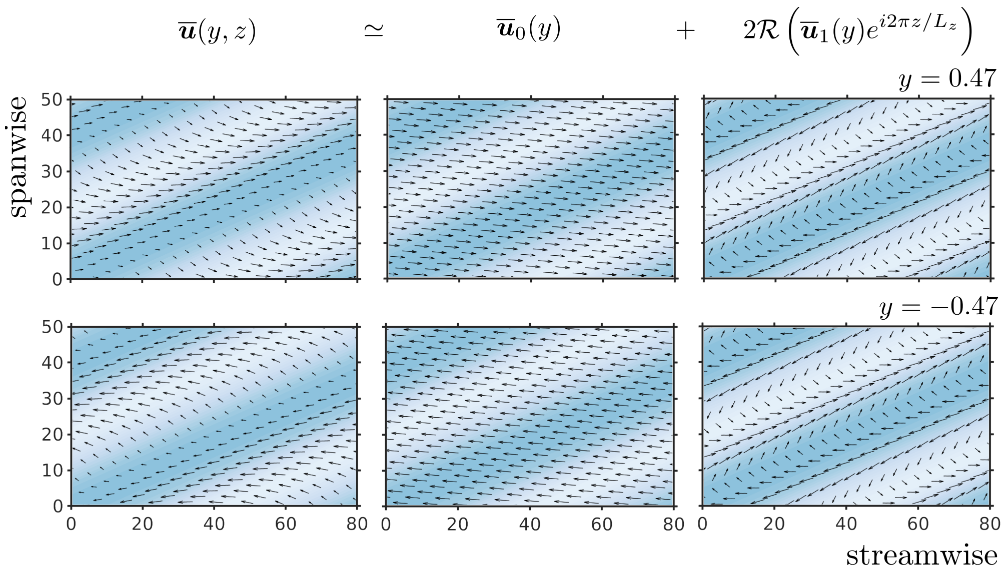

Figure 3.4: mean-flow decomposition in two Fourier modes $\overline{\boldsymbol{u}}_0$ and $\overline{\boldsymbol{u}}_1$ (4.13), visualised in the planes $y = \pm 0.47$. Colors show turbulent kinetic energy $K(y,z)$: turbulent and laminar zones are respectively in blue and white.

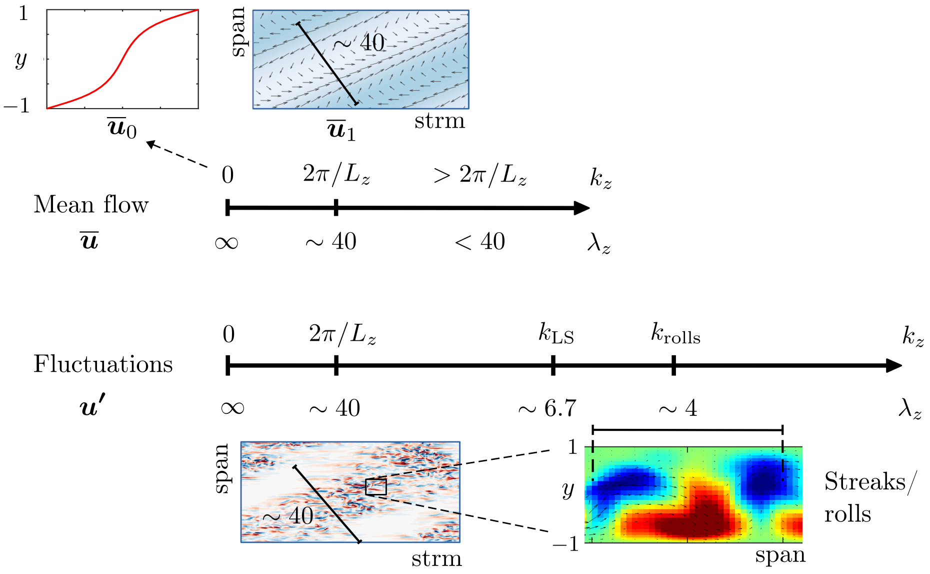

Figure 3.5: Illustration of the most-relevant scales in transitional patterns. The upper part depicts the mean flow: $\overline{\boldsymbol{u}}_0$ is the uniform (z-independent) mean shear, illustrated by the mean streamwise velocity profile, while $\overline{\boldsymbol{u}}_1$ corresponds to scale $\lambda_z \sim 40$ and is dominated by the flow along the laminar-turbulent interfaces as illustrated in the streamwise-spanwise plane. The lower part depicts the fluctuations: scale $\lambda_z \sim 40$ is illustrated by the periodic presence and absence of fluctuating cross-flow velocity. The scale k_{LS} is that below which fluctuations receive energy by non-linear interactions (via $\widehat{T}_{nl}$, eq. (3.14)), and k_{rolls} is the scale of rolls and streaks, illustrated in the spanwise-y plane.

The decomposition of $\overline{\boldsymbol{u}}$ into $\overline{\boldsymbol{u}}_0$ and $\overline{\boldsymbol{u}}_1$ is illustrated in figure 3.4. The mean flow and the turbulent kinetic energy $K(y,z) \equiv \frac{1}{2}\overline{\boldsymbol{u'} \cdot \boldsymbol{u'}}$ are visualised at planes $y = \pm 0.47$. The most relevant scales involved in the mean flow and the fluctuations are illustrated in figure 3.5. Mode $\overline{\boldsymbol{u}}_0$ has a S-shape profile in y with small spanwise component. Mode $\overline{\boldsymbol{u}}_1$ contains the large-scale flow along laminar-turbulent interfaces.

3.4 Physical balance in a Minimal Band Unit

Before turning to the energy balance in spectral space, we first consider the traditional turbulent energy decomposition in the physical-space representation (Pope, 2000), as carried out in transitional pipe flow by Wygnanski & Champagne (1973) and Song *et al.* (2017) and in bent pipe flow by Rinaldi *et al.* (2019). We write the balance equation for the turbulent kinetic energy (TKE), $K(y,z)$, in the physical representation:

$$\frac{\partial K}{\partial t} + \overline{\boldsymbol{u}} \cdot \nabla K = P - \epsilon + T_{nl} + T_p + T_v \tag{3.6}$$

where the production term, dissipation term, and rate of strain are:

$$P \equiv -\overline{u_i' u_j'}\frac{\partial \overline{u}_i}{\partial x_j}, \qquad \epsilon \equiv \frac{2}{Re}\overline{s_{ij}' s_{ij}'}, \qquad s_{ij}' \equiv \frac{1}{2}\left(\frac{\partial u_i'}{\partial x_j} + \frac{\partial u_j'}{\partial x_i}\right). \tag{3.7}$$

Subscripts i and j range over $\{1,2,3\}$ (or equivalently $\{x,y,z\}$) and we use the Einstein summation convention. The transfer terms read:

$$T_{nl} \equiv -\frac{1}{2}\frac{\partial}{\partial x_i}\overline{u_i' u_j' u_j'}, \qquad T_p \equiv -\frac{\partial}{\partial x_i}\overline{u_i' p'}, \qquad T_v \equiv \frac{2}{Re}\frac{\partial}{\partial x_i}\overline{u_j' s_{ij}'} \tag{3.8}$$

which account respectively for non-linear interactions, work by pressure and viscous diffusion. We also introduce the total transfer $T \equiv T_{nl} + T_p + T_v$. This TKE balance is accompanied by the energy balance of the mean flow, $E_{\overline{\boldsymbol{u}}} = \frac{1}{2}\overline{\boldsymbol{u}} \cdot \overline{\boldsymbol{u}} = E - K$ (Pope, 2000, eq. 5.131):

$$\frac{\partial E_{\overline{\boldsymbol{u}}}}{\partial t} + \overline{\boldsymbol{u}} \cdot \nabla E_{\overline{\boldsymbol{u}}} = -P - \overline{\epsilon} + \overline{T}_{nl} + \overline{T}_p + \overline{T}_v \tag{3.9}$$

where

$$\overline{\epsilon} \equiv \frac{2}{Re}\overline{s}_{ij}\overline{s}_{ij}, \qquad \overline{s}_{ij} \equiv \frac{1}{2}\left(\frac{\partial \overline{u}_i}{\partial x_j} + \frac{\partial \overline{u}_j}{\partial x_i}\right) \tag{3.10}$$

and

$$\overline{T}_{nl} \equiv -\frac{\partial}{\partial x_i}\overline{u}_j\overline{u_i' u_j'}, \qquad \overline{T}_p \equiv -\frac{\partial}{\partial x_i}\overline{u}_i\overline{p} \quad \text{and} \quad \overline{T}_v \equiv \frac{2}{Re}\frac{\partial}{\partial x_i}\overline{u}_j\overline{s}_{ij} \tag{3.11}$$

In order to emphasise the derivation of (3.6) and (3.9) from the Navier-Stokes equations, we have retained temporal derivatives, even though these equations described t and x

averaged quantities. Averaging in time is justified by the fact that turbulent-laminar banded patterns are statistically steady in plane Couette flow. There is, in fact, some slight motion of the band position. To gain in precision, we position the pattern at each time based on the phase of the z-trigonometric Fourier coefficient of the along-band flow at the mid-plane: $z_{\mathrm{loc}}(t) = -\phi(t)L_z/2\pi$, where $\phi(t) = \arg \langle \widehat{u}(x, 0, 2\pi/L_z, t)\rangle_x$. Temporal averages are computed with this phase alignment and we consider $\partial K/\partial t = 0$ and $\partial \overline{E}/\partial t = 0$. The results in this section are all presented in a frame centered around the quasi-laminar zone.

In figure 3.6a we represent the streamwise mean flow with arrows and the turbulent kinetic energy $K(y, z)$ by colors. The center of the turbulent region is at $z \pm 20$, while *overhang regions* (Lundbladh & Johansson, 1991; Duguet & Schlatter, 2013) are located around $z \pm 10$, where the along-band large-scale flow is strongest (see figure 3.3c). Figures 3.6b and 3.6c display the energy budgets of equations (3.6) and (3.9). To better relate these results to those from pipe flow, we integrate the energy budgets over the upper half of the domain, where the z component of the mean flow is from left to right. We use the same symbols P, ϵ, etc. to denote these half-height averages. (The lower half can be obtained from the upper half by symmetry and should be compared to pipe flow with the opposite streamwise direction.) All quantities depend strongly on z and it is this dependence on which we will focus.

Figure 3.6b shows the TKE budget. The energy balance is dominated by production and dissipation. Unsurprisingly, production is minimal in the quasi-laminar region where the fluctuations, and hence the Reynolds stresses, are small. The regions where production is larger than and smaller than dissipation are indicated in the figure. There are approximately, but not exactly, centered on peaks and troughs in production. This local disequilibrium between production and dissipation is accounted for by the transfer terms: for $z \in [-10, 0]$ the advective transfer $\overline{\boldsymbol{u}} \cdot \nabla K$ is negative and of larger intensity than the fluctuation transfer terms T, so the net transfer is negative. This is compensated for by a positive transfer that exists in most of the turbulent domain, from $z \simeq 6.5$ to $z \simeq -13$. The spatial flux of energy goes from the turbulent core to the quasi-laminar zone, as schematically indicated by the grey arrows in figure 3.6b. These results are consistent with those in a band in plane Poiseuille flow (Brethouwer *et al.*, 2012, Fig. 5) and in a puff in pipe flow (Song *et al.*, 2017): when entering the turbulent region from upstream to downstream, $P > \epsilon$ first, and then $P < \epsilon$, which signifies a spatial flux of energy from upstream to downstream. (In the upper half of our Couette domain, increasing z corresponds to going downstream in a pipe.)

We now look at the energy budget of the mean flow, presented in figure 3.6c, again centered around the laminar region and integrated over the upper half of the domain. Unlike pressure-driven channel or pipe flows, the energy is injected into the plane Couette flow by the imposed motion of the wall, and this is captured by the viscous diffusion term $\overline{T}_v$ in the mean-flow energy equation. This injection is mostly balanced by dissipation and production which fuels fluctuations by extracting energy from the mean flow). The pressure term $\overline{T}_p$ is very weak and non-linear and advective fluxes are non-uniform. The

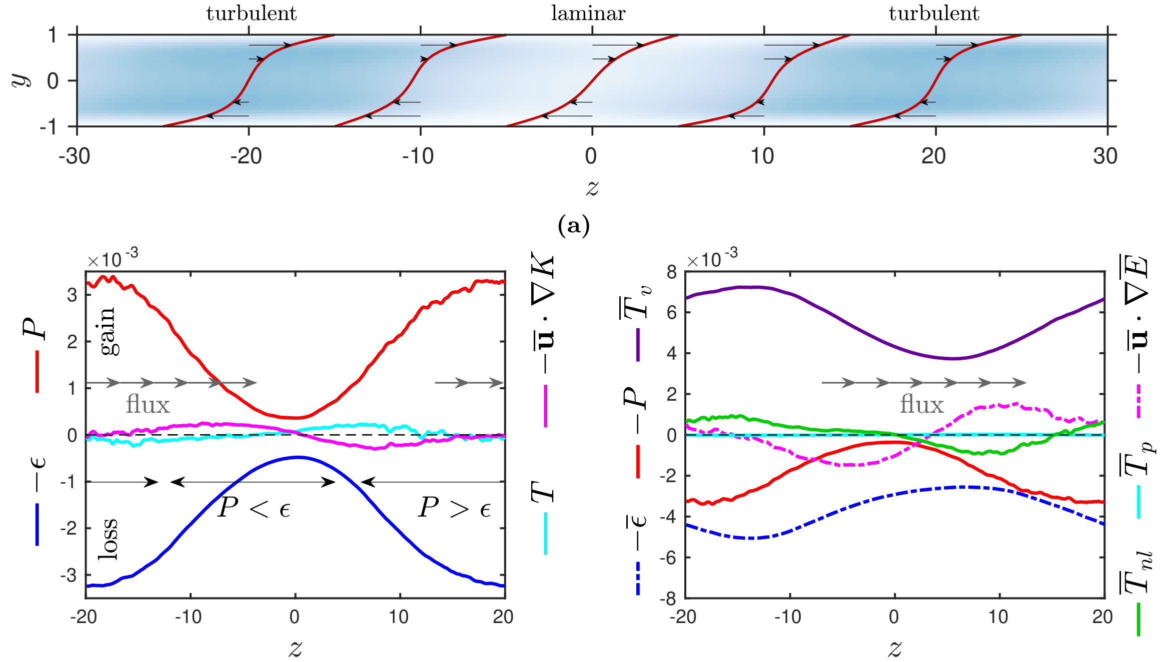

(a)

(b)

(c)

Figure 3.6: (a) Mean-flow profiles (streamwise velocity) and TKE, $K(y, z)$ (white: 0, blue: 0.08), in a turbulent-laminar pattern centered around the laminar gap at $z = 0$. (b) TKE and (c) mean-flow energy budgets for $Re = 400$. Each term is integrated over the upper half of the domain, $y \in [0, 1]$, where advection by the mean flow is towards the right.

advective contribution to the mean flow $\overline{\boldsymbol{u}} \cdot \nabla E_{\overline{\boldsymbol{u}}}$ behaves in the opposite way as the contribution of the Reynolds stress $\overline{T}_{nl}$ This advection term transfers energy of the mean flow from laminar regions, where the production P is small, to turbulent regions, where the production is large.

In the case of pipe flow, Song *et al.* (2017) reported that the peak in TKE dissipation is shifted downstream from the peak in the production. Our data in plane Couette flow does not support a z-shift in the peaks in ϵ and P. Interestingly, we observe a considerable shift between the peaks in mean-flow dissipation $\overline{\epsilon}$ at $z = -15$ and production P at $z = -20$, as shown in figure 3.6c. Recall that these plots show quantities integrated only over the upper half of the domain. The shift in mean-flow peaks is consistent with that between mean flow and turbulent kinetic energy due to the overhang region surrounding localised turbulence, which we illustrated in figure 3.6a: the upper-half mean flow is mostly dissipated in the turbulent-to-laminar overhang region, and not in the center of the turbulent band. In contrast, in the laminar-to-turbulent interface, the mean flow accelerates, as it is energised by an advective transfer from the laminar region.

3.5 Spectral decomposition

We now analyse the spectral balance of kinetic energy. In shear flows at higher Re, this analysis leads to a detailed understanding of the energy sources and transfers within the flow. We refer the reader to Bolotnov *et al.* (2010); Lee & Moser (2015); Mizuno (2016); Cho *et al.* (2018) for studies at higher Re_τ, and to Symon *et al.* (2021) for a minimal channel study at $Re_\tau = 180$. In a similar vein, Lee & Moser (2019) recently computed two-point correlations in channel flow.

3.5.1 Notation and governing equations

We begin by writing the Reynolds-averaged Navier-Stokes equations and the equation for fluctuations from the mean:

$$\frac{\partial \overline{u}_j}{\partial t} + \overline{u}_i \frac{\partial \overline{u}_j}{\partial x_i} + \frac{\partial}{\partial x_i} \overline{u_i' u_j'} = -\frac{\partial \overline{p}}{\partial x_j} + \frac{2}{Re} \frac{\partial \overline{s}_{ij}}{\partial x_i} \tag{3.12}$$

$$\frac{\partial u_j'}{\partial t} + \overline{u}_i \frac{\partial u_j'}{\partial x_i} + u_i' \frac{\partial u_j'}{\partial x_i} = -u_i' \frac{\partial \overline{u}_j}{\partial x_i} + \frac{\partial}{\partial x_i} \overline{u_i' u_j'} - \frac{\partial p'}{\partial x_j} + \frac{2}{Re} \frac{\partial s_{ij}'}{\partial x_i} \tag{3.13}$$

By taking the z Fourier transform of (3.13) and multiplying by $\widehat{u_j'}^{\,*}$, followed by averaging over x and t, we obtain a balance equation for the spectral kinetic energy $\widehat{K}(y, k_z) \equiv$

$\frac{1}{2}\overline{\widehat{\boldsymbol{u'}}^{*} \cdot \widehat{\boldsymbol{u'}}}$:

$$
\begin{aligned}
\underbrace{\frac{\partial \widehat{K}(y,k_z)}{\partial t}}_{0} + \underbrace{\mathcal{R}\left\{\overline{\widehat{u'_j}^{*}\,\widehat{\overline{u}_i \frac{\partial u'_j}{\partial x_i}}}\right\}}_{-\widehat{A}(y,k_z)} = \underbrace{-\mathcal{R}\left\{\overline{\widehat{u'_j}^{*}\,\widehat{u'_i \frac{\partial \overline{u}_j}{\partial x_i}}}\right\}}_{\widehat{\Pi}(y,k_z)} \; \underbrace{-\frac{2}{Re}\overline{\widehat{s'_{ij}}\widehat{s'_{ij}}^{*}}}_{\widehat{D}(y,k_z)} \\
\underbrace{+\frac{2}{Re}\mathcal{R}\left\{\overline{\frac{\partial}{\partial y}(\widehat{u'_j}^{*}\widehat{s'_{yj}})}\right\}}_{\widehat{T}_v(y,k_z)} \; \underbrace{-\mathcal{R}\left\{\overline{\frac{\partial}{\partial y}(\widehat{u'_y}^{*}\widehat{p'})}\right\}}_{\widehat{T}_p(y,k_z)} \; \underbrace{-\mathcal{R}\left\{\overline{\widehat{u'_j}^{*}\,\widehat{u'_i \frac{\partial u'_j}{\partial x_i}}}\right\}}_{\widehat{T}_{nl}(y,k_z)}
\end{aligned}
\tag{3.14}
$$

where we revert from the general partial derivative $\partial/\partial x_i$ or subscript i to the wall-normal coordinate y when this is the only non-zero term.

- $\widehat{A}$ is an interaction between mean velocity and fluctuations, corresponding to the spectral version of the advection term $\overline{\boldsymbol{u}} \cdot \nabla K$;
- $\widehat{\Pi}$ is the spectral production term, which is an interaction between the mean gradient and fluctuations at scale k_z;
- $\widehat{D}$ is the viscous dissipation at mode k_z;
- $\widehat{T}_v$, $\hat{T}_p$ are transfer terms to mode k_z due to strain-velocity and pressure-velocity correlations;
- $\widehat{T}_{nl}$ is an inter-scale transfer to mode k_z and position y due to triad interactions. When summed over k_z and integrated over y, this term is zero.

The forms of the pressure, viscous diffusion, dissipation and triadic terms are the same as they would be if the flow were uniform in z. Only advection and production terms, which contain the inhomogeneous mean flow, do not simplify as in the uniform case, and instead require a convolution over wavenumbers. In the usual analysis of uniform turbulence in a non-tilted box (Bolotnov *et al.*, 2010; Cho *et al.*, 2018; Lee & Moser, 2019), $\overline{\boldsymbol{u}}$ reduces to $(U(y), 0, 0)$ and $\widehat{\overline{\boldsymbol{u}}} = (U(y), 0, 0)$ for $k_z = 0$ and is otherwise 0, which simplifies the spectral balance. In particular, the advection term $\widehat{A}$ vanishes, because in such cases:

$$
\widehat{A}(y,k_z) = -\mathcal{R}\left\{\overline{\widehat{u'_j}^{*} U(y) \frac{\widehat{\partial u'_j}}{\partial x}}\right\} = -\frac{1}{2}\mathcal{R}\left\{\overline{U(y)\frac{\partial}{\partial x}\widehat{u'_j}^{*}\widehat{u'_j}}\right\} = 0 \tag{3.15}
$$

(due to x averaging). This is also true in the case of tilted uniform turbulence $\overline{\boldsymbol{u}} =$

$(U(y), 0, W(y))$:

$$\widehat{A}(y, k_z) = -\mathcal{R}\left\{W(y) i k_z \overline{\widehat{u'_j}^* \widehat{u'_j}}\right\} = 0 \tag{3.16}$$

However, this is not true for a patterned mean flow $\overline{\boldsymbol{u}} = (U(y,z), V(y,z), W(y,z))$ like the one shown in figure 3.3c.

We furthermore introduce the balance equation for the spectral energy of the mean flow $\widehat{E}_{\overline{\boldsymbol{u}}} \equiv \frac{1}{2}\widehat{\overline{\boldsymbol{u}}}^* \cdot \widehat{\overline{\boldsymbol{u}}}$ at wavenumber k_z:

$$\begin{aligned}\underbrace{\frac{\partial \widehat{E}_{\overline{\boldsymbol{u}}}(y,k_z)}{\partial t}}_{0} + \underbrace{\mathcal{R}\left\{\widehat{\overline{u}}_j^* \widehat{\overline{u}_i \frac{\partial \overline{u}_j}{\partial x_i}}\right\}}_{-\widehat{\overline{A}}(y,k_z)} = \underbrace{\mathcal{R}\left\{\frac{\partial \widehat{\overline{u}}_j^*}{\partial x_i} \widehat{\overline{u'_i u'_j}}\right\}}_{-\widehat{\overline{\Pi}}(y,k_z)} - \underbrace{\frac{2}{Re} \widehat{\overline{s}}_{ij} \widehat{\overline{s}}_{ij}^*}_{\widehat{\overline{D}}(y,k_z)} \\ + \underbrace{\frac{2}{Re}\mathcal{R}\left\{\frac{\partial}{\partial y}(\widehat{\overline{u}}_j^* \widehat{\overline{s}}_{yj})\right\}}_{\widehat{\overline{T}}_v(y,k_z)} \underbrace{-\mathcal{R}\left\{\frac{\partial}{\partial y} \widehat{\overline{u}}_y^* \widehat{\overline{p}}\right\}}_{\widehat{\overline{T}}_p(y,k_z)} \underbrace{-\mathcal{R}\left\{\frac{\partial}{\partial y}(\widehat{\overline{u}}_j^* \widehat{\overline{u'_y u'_j}})\right\}}_{\widehat{\overline{T}}_{nl}(y,k_z)}\end{aligned} \tag{3.17}$$

where:

- $\widehat{\overline{A}}$ is a non-linear transfer term for the mean flow. This is a spectral version of the advection term $\overline{\boldsymbol{u}} \cdot \nabla E_{\overline{\boldsymbol{u}}}$ appearing in the mean-flow balance equation (3.9).
- $\widehat{\overline{\Pi}}$ is the interaction between Reynolds stress at scale k_z and the mean gradient at scale k_z, and hence is a form of production term.
- $\widehat{\overline{D}}$ is a dissipation term for the mean flow energy;
- $\widehat{\overline{T}}_v$, $\widehat{\overline{T}}_p$ are transfer terms due to correlations between mean strain and velocity, and mean pressure and velocity;
- $\widehat{\overline{T}}_{nl}$ is a flux term due to the interactions between the Reynolds stress and the mean flow.

In the rest of this section, we will focus on $y-$integrated TKE and mean-flow balance to characterise the spectral distribution of total energy. As the mean flow $\overline{\boldsymbol{u}}$ is dominated by $\overline{\boldsymbol{u}}_0$ and $\overline{\boldsymbol{u}}_1$, we write (3.17) in y-integrated form for $k_z = 0$ and $k_z = 2\pi/L_z$ and obtain:

$$I + \widehat{\overline{A}}_0 - \widehat{\overline{\Pi}}_0 - \widehat{\overline{D}}_0 = 0 \quad \text{and} \quad \widehat{\overline{A}}_1 - \widehat{\overline{\Pi}}_1 - \widehat{\overline{D}}_1 = 0 \tag{3.18}$$

where we have introduced

$$\widehat{\overline{\Pi}}_0 \equiv \int_{-1}^{1} \widehat{\overline{\Pi}}(y, 0)\, \mathrm{d}y \quad \text{and} \quad \widehat{\overline{\Pi}}_1 \equiv \int_{-1}^{1} \widehat{\overline{\Pi}}\left(y, \frac{2\pi}{L_z}\right)\, \mathrm{d}y \tag{3.19}$$

with similar definitions for $\widehat{\overline{A}}_0$, $\widehat{\overline{D}}_0$, $\widehat{\overline{A}}_1$ and $\widehat{\overline{D}}_1$. We have also introduced the total energy injection due to the action of the walls:

$$I = \sum_{k_z} \int_{-1}^{1} \widehat{\overline{\overline{T}}}_v(y, k_z)\ \mathrm{d}y = \frac{2}{Re} \sum_{k_z} \widehat{\overline{u}}_j^*(k_z)\ \widehat{\overline{s}}_{yj}(k_z) \Big|_{-1}^{1} \tag{3.20}$$

This term is non-zero only for mode $k_z = 0$ because the applied wall velocity is uniform, so that

$$I = \frac{2}{Re} \widehat{\overline{u}}_j^*(k_z = 0)\ \widehat{\overline{s}}_{yj}(k_z = 0) \Big|_{-1}^{1} = 2 \frac{u_\tau^2}{U_{\text{wall}}^2} \tag{3.21}$$

Note that $\widehat{\overline{\overline{T}}}_p$ and $\widehat{\overline{\overline{T}}}_{nl}$ integrate to zero, since both $\overline{u}_y$ and the Reynolds stress vanish at the walls.

Two important comments can be made at this stage. The first one starts from a word of caution: all terms in (3.17) are not the Fourier transforms of those in (3.9). (This is a generalisation of the fact that $\widehat{E}(k_z)$ is defined to be $\hat{\boldsymbol{u}}(k_z) \cdot \hat{\boldsymbol{u}}(k_z)/2$ and not $\widehat{\boldsymbol{u} \cdot \boldsymbol{u}}(k_z)/2$.) This means in particular that although energy is injected only in the balance of $\overline{\boldsymbol{u}}_0$ via I, the energy is not injected uniformly within the flow, as $\overline{T}_v$ is not uniform in z (see figure 3.6c). The connection with the physical injection of energy is indeed only through z averaging:

$$I = \frac{1}{L_z} \int_0^{L_z} \int_{-1}^{1} \overline{T}_v(y, z)\ \mathrm{d}y\ \mathrm{d}z \tag{3.22}$$

The second comment is about the way in which this injected energy is communicated to the TKE spectral balance. Contrary to the physical-space version of the energy balance, where the same production P appears in the TKE (3.6) and the mean flow (3.9) equations, the spectral production terms appearing in (3.14) and (3.17), $\widehat{\Pi}$ and $\widehat{\overline{\overline{\Pi}}}$, are different. However, when summed over k_z and integrated over y, these two terms agree, so we can write the total production Π as:

$$\Pi \equiv \sum_{k_z} \int_{-1}^{1} \widehat{\Pi}(y, k_z)\ \mathrm{d}y = \sum_{k_z} \int_{-1}^{1} \widehat{\overline{\overline{\Pi}}}(y, k_z)\ \mathrm{d}y \tag{3.23}$$

Furthermore, in the physical-space representation,

$$\Pi = \frac{1}{L_z} \int_0^{L_z} \int_{-1}^{1} P(y, z)\ \mathrm{d}z\ \mathrm{d}y = \frac{1}{L_z} \int_0^{L_z} \int_{-1}^{1} \epsilon(y, z)\ \mathrm{d}z\ \mathrm{d}y \tag{3.24}$$

where the last equality follows since all transfer terms integrate to zero. The equivalence (3.23) is key to understanding how TKE and mean-flow energy are connected. This will be further developed in section 3.5.2.

3.5.2 Results for the spectral energy balance

a) TKE balance

We examine the spectral balance of the TKE (3.14), integrated over the cross-channel direction. This balance is presented for the patterned state in figure 3.7a ($Re = 400$) and for the uniform state on figure 3.7c ($Re = 500$). The transfer terms $\widehat{T}_v$ and $\widehat{T}_p$ are not shown as they integrate to zero. (The y dependence of energy transfer will be discussed in section 3.7.)

We first focus on the similarities between patterned and uniform states. We observe a peak in the production and dissipation terms near the energy-containing scale k_{rolls}, as we saw for the total energy in figures 3.3a and 3.3b. At this scale, the non-linear transfer $\widehat{T}_{nl}$ is negative and of large amplitude: scale k_{rolls} produces much more than it dissipates, and the remainder is transferred to other k_z. The non-linear transfer becomes positive above a small-scale wavenumber that we denote . ($\simeq 3.6$ in the patterned state at $Re = 400$ and the uniform state at $Re = 500$.) This positive transfer at small scales is indicative of a direct energy cascade to small dissipative scales.

The TKE balance for $k_z < k_{\text{rolls}} \simeq 1.41$ contrasts with that at large k_z. First, production decreases with decreasing k_z and becomes negative for $k_z < 0.5$. This *negative production* at large scales appears in both patterned and uniform states. It corresponds to energy transfer from the fluctuations to the mean flow. The zone of negative production spans from $k_z = 0$ to $k_z \simeq 0.47$ in both the patterned and uniform cases presented here. We note that this unusual sign of part of the production term has been also reported by Symon *et al.* (2021) in spanwise-constant modes of channel flow in a minimal domain. Second, energy in the range $k_z < 0.94$ is fuelled by a positive non-linear transfer $\widehat{T}_{nl}$, which signifies a transfer from small to large scales. This is present in both patterned and uniform states. We denote the (large) scale at which this transfer becomes positive by k_{LS} as seen in figures 3.7a, 3.7d and 3.5. In the part of the spectrum $k_z < k_{LS}$, the influx of energy from smaller scales is mostly balanced by dissipation, while only a relatively small amount of energy is yielded to the mean flow via negative production.

Now considering the differences between the patterned (figure 3.7a) and uniform states (figure 3.7c), the advection term $\widehat{A}$ plays a more significant role in redistributing energy between scales in the patterned state: it is positive for $k_z < 1.1 < k_{\text{rolls}}$, negative near k_{rolls}, and negligible for $k_z > 3$. This role is very similar to that of non-linear transfers $\widehat{T}_{nl}$, but with weaker amplitude. $\widehat{A}$ is nearly zero in the uniform state. This term should vanish when the mean flow is strictly uniform in z, see (3.16). This is not exactly the case here, especially at $k_z \simeq k_{\text{rolls}}$, and this is probably due to the inexact uniformity of the mean flow. Other differences are visible between the uniform and patterned states, especially regarding the shape and intensity of each individual curve: for instance, the behaviour of $\widehat{T}_{nl}$ and $\widehat{D}$ is changed near k_{rolls}: these are almost equal in the uniform case while $\widehat{D}$ exceeds $\widehat{T}_{nl}$ in the patterned case. The comparison between uniform and patterned states

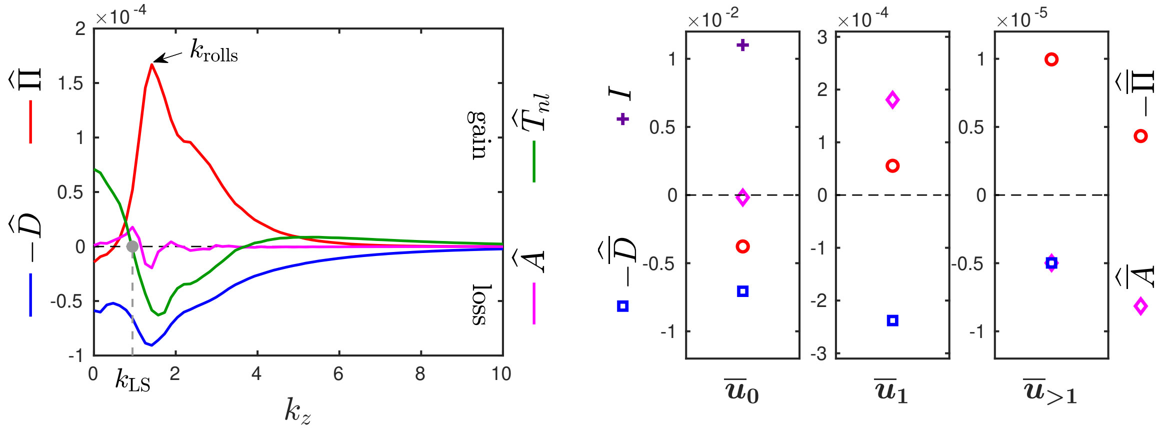

(a) Pattern ($Re = 400$), TKE

(b) Pattern ($Re = 400$), mean flow

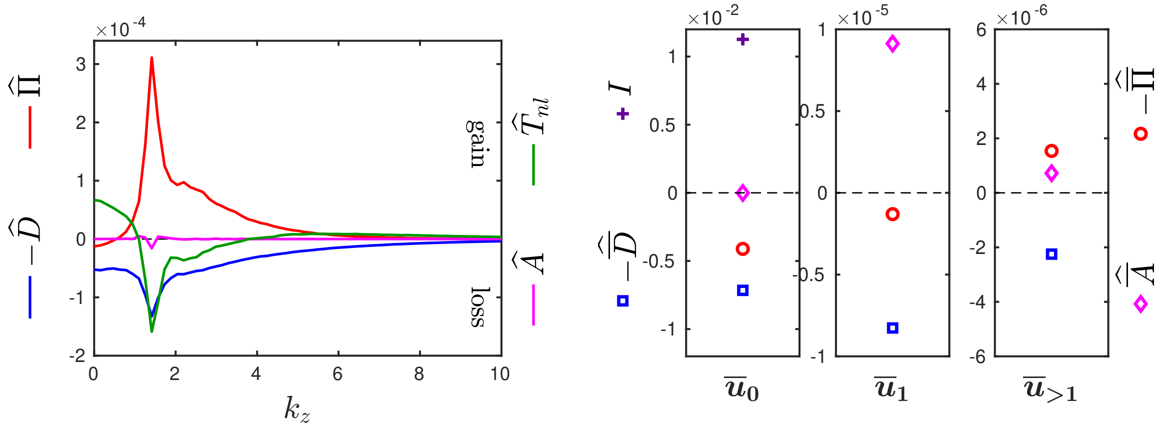

(c) Uniform ($Re = 500$), TKE

(d) Uniform ($Re = 500$), mean flow

Figure 3.7: (a) Spectral energy budget (3.14) for a pattern at $Re = 400$, integrated over $y \in [-1, 1]$. Viscous and pressure transfers are not shown as they integrate to 0. The grey circles indicate k_{LS} and , which delimit the spectral region where transfer $\widehat{T}_{nl}$ is negative. (b) Spectral energy budget of the mean flow (3.17) integrated over $y \in [-1, 1]$, shown for $k_z = 0$, $k_z = 2\pi/L_z$ and summed over $k_z > 2\pi/L_z$. (c, d) show the same as (a, b) for a uniform state at $Re = 500$.

will be discussed further in section 3.6.

b) Mean-flow balance

The spectral energy balance of the mean flow (4.15) is presented in figure 3.7b and 3.7d for both patterned and uniform states. In each case, the three panels correspond, from left to right, to modes $\overline{\boldsymbol{u}}_0$, $\overline{\boldsymbol{u}}_1$ and $\overline{\boldsymbol{u}}_{>1}$. In both patterned and uniform cases, $\overline{\boldsymbol{u}}_0$ is fueled by the mean strain via injection term I (purple cross). This energy is dissipated (blue square) and also transferred to the fluctuations via the production $\widehat{\overline{\Pi}}_0$ (red circle). Note that $\widehat{\overline{\Pi}} > 0$ corresponds to usual positive production and hence a sink of energy with respect to the mean flow: production appears as $-\widehat{\overline{\Pi}}$ in the mean balance equation (3.17).

For $\overline{\boldsymbol{u}}_1$ in the patterned state (middle panel of figure 3.7b), the main source of energy is the advective term $\widehat{\overline{A}}_1$, with some energy coming from the negative production $\widehat{\overline{\Pi}}_1 < 0$. Thus, the $\overline{\boldsymbol{u}}_1$ component of the mean flow is fuelled to some extent by a negative transfer from fluctuations back to mean flow, but the advective contribution dominates. The two sources are balanced by dissipation. For the uniform state (middle panel of figure 3.7d), the terms are more than an order of magnitude smaller than in the patterned state, and the production term has the opposite sign. The remaining scales in the mean spectral balance $k_z > 2\pi/L_z$ (right panels of figures 3.7b and 3.7d) are very weak compared to the first two components.

Our results show that the advection term $\widehat{\overline{A}}$ plays a crucial role in the mean-flow balance in the patterned state. Since this term represents a transfer due to non-linearities, its sum over k_z and y vanishes. At $Re = 400$, we find that $\widehat{\overline{A}}_0 \simeq -9.0 \times 10^{-5}$, $\widehat{\overline{A}}_1 \simeq 9.4 \times 10^{-5}$, and $\sum_{k_z > 2\pi/L_z} \int_{-1}^{1} \widehat{\overline{A}}(y, k_z)\ \mathrm{d}y \simeq -4 \times 10^{-6}$ Hence we have the following approximate equality:

$$\widehat{\overline{A}}_0 \approx -\widehat{\overline{A}}_1. \tag{3.25}$$

Even though the advection is negligible compared with the dominant terms in the $\overline{\boldsymbol{u}}_0$ balance, it is the dominant source of energy at the pattern scale. In the uniform case, $\widehat{\overline{A}}_0 \approx \widehat{\overline{A}}_1 \approx 0$.

c) Connection between TKE and mean flow

We now investigate the connection between the TKE and mean flow, focusing particularly on the spectral production terms $\widehat{\overline{\Pi}}$ and $\widehat{\Pi}$. While these production terms take different forms in the TKE and mean-flow spectral balances (eq. (3.14) and (3.17)), upon integration over y and summation over k_z (equation (3.23)), they give the same total production Π.

State	Re	Π	$\widehat{\widehat{\Pi}}_0$	$\widehat{\widehat{\Pi}}_1$	$\widehat{\Pi}^{>0}$	$\widehat{\Pi}^{<0}$
Pattern	400	3.71×10^{-3}	3.77×10^{-3}	-5.44×10^{-5}	3.76×10^{-3}	-5.34×10^{-5}
Pattern	430	3.82×10^{-3}	3.87×10^{-3}	-4.10×10^{-5}	3.87×10^{-3}	-5.36×10^{-5}
Uniform	430	4.14×10^{-3}	4.14×10^{-3}	$O(10^{-6})$	4.20×10^{-3}	-6.30×10^{-5}
Uniform	500	4.12×10^{-3}	4.11×10^{-3}	$O(10^{-6})$	4.17×10^{-3}	-5.64×10^{-5}

Table 3.2: Production terms appearing in the mean flow (3.17) and the TKE (3.14) balance, as decomposed in (3.26).

We decompose the total production in two ways: first by writing the total TKE production Π as a sum of its positive and negative parts, and second by considering the dominant contributions from $\overline{\boldsymbol{u}}_0$ and $\overline{\boldsymbol{u}}_1$ in the mean-flow production $\widehat{\widehat{\Pi}}$:

$$\Pi = \widehat{\Pi}^{<0} + \widehat{\Pi}^{>0} \simeq \widehat{\widehat{\Pi}}_0 + \widehat{\widehat{\Pi}}_1 \tag{3.26}$$

where:

$$\widehat{\Pi}^{>0} \equiv \sum_{k_z=0}^{\infty} \int_{-1}^{1} \widehat{\Pi}(y,k_z)\,\mathrm{d}y\ \Theta\left(\int_{-1}^{1} \widehat{\Pi}(y,k_z)\,\mathrm{d}y\right) \tag{3.27}$$

$$\text{and}\quad \widehat{\Pi}^{<0} \equiv \sum_{k_z=0}^{\infty} \int_{-1}^{1} \widehat{\Pi}(y,k_z)\,\mathrm{d}y\ \Theta\left(-\int_{-1}^{1} \widehat{\Pi}(k_z)\,\mathrm{d}y\right), \tag{3.28}$$

where Θ is the Heaviside function. We recall that figure 3.7a shows that $\int_{-1}^{1} \widehat{\Pi}(y,k_z)\,\mathrm{d}y < 0$ occurs mostly at large scales. Each term in (3.26) in the patterned and uniform states is displayed in table 3.2 for various values of Re.

We observe that in the patterned case the positive production is very close to $\widehat{\widehat{\Pi}}_0$ and the negative production is very close to $\widehat{\widehat{\Pi}}_1$, *i.e.* $\widehat{\widehat{\Pi}}_0 \simeq \widehat{\Pi}^{>0}$ and $\widehat{\widehat{\Pi}}_1 \simeq \widehat{\Pi}^{<0}$. In the uniform case, $\widehat{\widehat{\Pi}}_1$ is very small and $\widehat{\widehat{\Pi}}_0$ accounts for essentially all the production, so it is the sum of the positive and negative parts. In other words:

$$\widehat{\widehat{\Pi}}_0 \begin{cases} \approx \widehat{\Pi}^{>0} & \text{in patterned state} \\ \approx \widehat{\Pi}^{>0} + \Pi^{<0} & \text{in uniform state} \end{cases} \qquad \widehat{\widehat{\Pi}}_1 \begin{cases} \approx \Pi^{<0} & \text{in patterned state} \\ \ll \Pi^{<0} & \text{in uniform state} \end{cases} \tag{3.29}$$

This supports an essential connection between the TKE and the mean-flow production terms: in the patterned state, almost all negative TKE production goes to $\overline{\boldsymbol{u}}_1$, and almost all positive TKE production comes from $\overline{\boldsymbol{u}}_0$; in the uniform state, the negative TKE production is absorbed by $\overline{\boldsymbol{u}} = \overline{\boldsymbol{u}}_0$. (In all cases, the negative production, $\Pi^{<0}$, represents less than 1.5% of Π: $-\Pi^{<0}/\Pi \simeq 1.46\%$ at $Re = 400$ and 1.37% at $Re = 500$.)

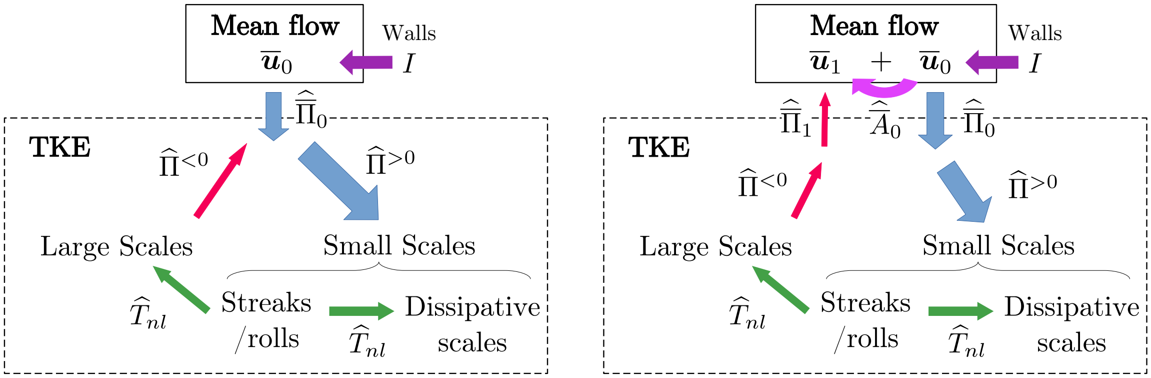

(a) Uniform state (b) Pattern state

Figure 3.8: Illustration of the mean flow - TKE interaction for (a) the uniformly turbulent state and (b) the patterned state. In the uniform state, $\widehat{\widehat{\Pi}}_0 \approx \widehat{\Pi}^{<0} + \widehat{\Pi}^{>0}$, while in the patterned state, $\widehat{\widehat{\Pi}}_0 \approx \widehat{\Pi}^{>0}$ and $\widehat{\widehat{\Pi}}_1 \approx \widehat{\Pi}^{<0}$.

At this stage, we can draw the following conclusions, illustrated in figures 3.8a and 3.8b:

(1) Most of the energy flows into the mean flow and then to TKE according to the usual picture from developed shear flows: energy is injected to $\overline{\boldsymbol{u}}_0$ by viscous stress, and is transferred to fluctuations via positive production. Energy is mostly produced at the scale of the energy-containing eddies (here, streaks and rolls) and is dissipated to the smaller scales through a positive transfer term.

(2) An important modification to this usual picture is the presence of an inverse transfer of some TKE to large scales via triad interactions $\widehat{T}_{nl}$. This energy is not entirely dissipated and instead feeds back to the mean flow via negative production $\widehat{\Pi}^{<0}$.

(3) Although weak compared to total production Π, this negative production $\widehat{\Pi}^{<0}$ fuels $\overline{\boldsymbol{u}}_1$ in the patterned state.

(4) $\widehat{\widehat{A}}_1$ is the main source of energy of $\overline{\boldsymbol{u}}_1$: non-linearities of the mean flow play a stronger role than negative production.

We have defined large scales as those for which the non-linear transfer is negative: $k_z < k_{LS}$ in figures 3.7a and 3.7c. This separates the large and small scales in figure 3.8. Note, however, the scales at which production becomes negative are even larger $k_z \lesssim 0.5 < k_{LS}$ in figures 3.7a and 3.7c. We do not distinguish these distinct notions of large scales in figure 3.8.

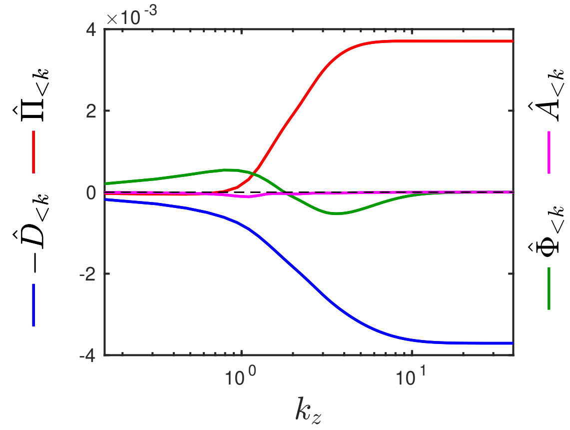

Figure 3.9: Cumulative energy balance (3.30) integrated over $y \in [-1, 1]$ in the patterned case at $Re = 400$.

We extend these considerations of transfers across scales by considering the quantities

$$\widehat{\Pi}_{<k}(k_z) \equiv \sum_{k'_z<k_z} \int_{-1}^{1} \widehat{\Pi}(y,k'_z)\ \mathrm{d}y, \quad \widehat{D}_{<k}(k_z) \equiv \sum_{k'_z<k_z} \int_{-1}^{1} \widehat{D}(y,k'_z)\ \mathrm{d}y$$

$$\widehat{\Phi}_{<k}(k_z) \equiv \sum_{k'_z<k_z} \int_{-1}^{1} \widehat{T}_{nl}(y,k'_z)\ \mathrm{d}y, \quad \widehat{A}_{<k}(k_z) \equiv \sum_{k'_z<k_z} \int_{-1}^{1} \widehat{A}(y,k'_z)\ \mathrm{d}y \qquad (3.30)$$

These scale-to-scale quantities are shown in figure 3.9. $\widehat{\Phi}_{<k}$ is the non-linear energy flux across a wavenumber k_z. This integrated picture conveys the presence of a zone of inverse flux of energy to large scales ($\widehat{\Phi}_{<k} > 0$ for $k_z < 1.88$). For $k_z < O(1)$, this inverse transfer is the dominant source and is mostly balanced by dissipation. Starting at $k_z > O(1)$, production comes into play and eventually is the only source.

We emphasise that this strong inverse transfer does not correspond to an *inverse cascade* per se because it does not lead to an accumulation of energy towards the largest available scale in the system. Indeed, simulations in Large Slender Boxes have emphasized the presence of a small range of energetic large scales, around $\lambda_z \simeq 40$ (figure 3.3a). It is expected that there is a build-up making energy condense around this finite scale.

3.6 Evolution with Reynolds number

We now address the dependence of the global energy balance on Re. Unlike previous studies (Tuckerman & Barkley, 2011; Rolland & Manneville, 2011), we do not focus on an order parameter for the transition between uniform turbulence and patterns, but rather compute the Reynolds decomposition for each of the two states through the transition. Figure 3.10 presents the evolution of several quantities computed in a Minimal Band Unit of $L_z = 40$ for the uniform states at higher Re and for the patterned states at lower Re. For fluctuating bistable cases at intermediate Re (e.g $Re = 430$, as shown in figure 3.2c), conditional averaging has been carried out over selected time windows during which the state is either patterned or uniform. To compare across different values of Re, we will normalise these quantities either by viscous wall units or by global quantities (total injection I or total production Π).

We start with the evolution of energies with Re and consider the following quantities: average energy $\langle E \rangle^+$, relative energy of $\overline{\boldsymbol{u}}_0$ given by $\langle E_{\overline{\boldsymbol{u}}0} \rangle \,/\, \langle E \rangle \equiv \langle \overline{\boldsymbol{u}}_0 \cdot \overline{\boldsymbol{u}}_0 / 2 \rangle \,/\, \langle E \rangle$, average TKE $\langle K \rangle^+$, and average dissipation $\langle \epsilon \rangle^+$. (Here, $\langle \cdot \rangle$ denotes a (y,z) average of the (x,t)-averaged quantities introduced in sections 3.4 and 3.5.) Quantities are defined in terms of wall units (i.e. normalised by $Re\ u_\tau^4 / U_{\text{wall}}^4$). As seen in figure 3.10, all of these quantities change discontinuously when the flow switches from the uniform to the patterned state as Re is decreased.

Next we consider the terms appearing in the mean balance and show their evolution with Re. We normalise all terms by injection rate I except for I itself, which we normalise by wall units and hence plot I^+. The injection, dissipation and advection are discontinuous, with $\widehat{\overline{A}}_1/I$ undergoing an especially dramatic increase, by a factor of nearly ten, when going from uniform turbulence to the patterned state. In contrast, Π/I is approximately continuous through the transition from uniform to patterned states, meaning that at a given Re the transfer of energy between mean flow and TKE is independent of whether the flow is uniformly turbulent or patterned. Interestingly, Π/I decreases with decreasing Re, meaning that relatively less energy is transferred to turbulence when Re is reduced, and hence more energy is retained by the mean flow at lower Re. While Π/I is continuous through the transition, the relative portion of negative production is not continuous: the patterned state shows a smaller $-\widehat{\Pi}^{<0}/\Pi$ than the uniform state. What this means is that, surprisingly, the relative influx of energy from turbulence to the mean flow is lower in the patterned state than in the uniform state.

We now turn to the evolution of transfer terms with Re. For this purpose, we focus only on the non-linear transfers into large scales at $k_z < k_{LS}$, and into small dissipative scales at $k_z >$. (See figure 3.7.) We define the total nonlinear transfer to large scales $\widehat{T}_{LS}$ and to small scales $\widehat{T}_{SS}$ by

$$\widehat{T}_{LS} = \sum_{k_z \leq k_{LS}} \int_{-1}^{1} \widehat{T}_{nl}\ \mathrm{d}y \qquad \widehat{T}_{SS} = \sum_{k_z > k_{SS}} \int_{-1}^{1} \widehat{T}_{nl}\ \mathrm{d}y, \tag{3.31}$$

We plot the ratio $\widehat{T}_{LS}/\widehat{T}_{SS}$ in figure 3.10. For the uniform state, relatively more energy is transferred to large scales as Re decreases. The ratio undergoes a discontinuous drop at the transition to patterns, where relatively less transfer goes to large scales. We find that

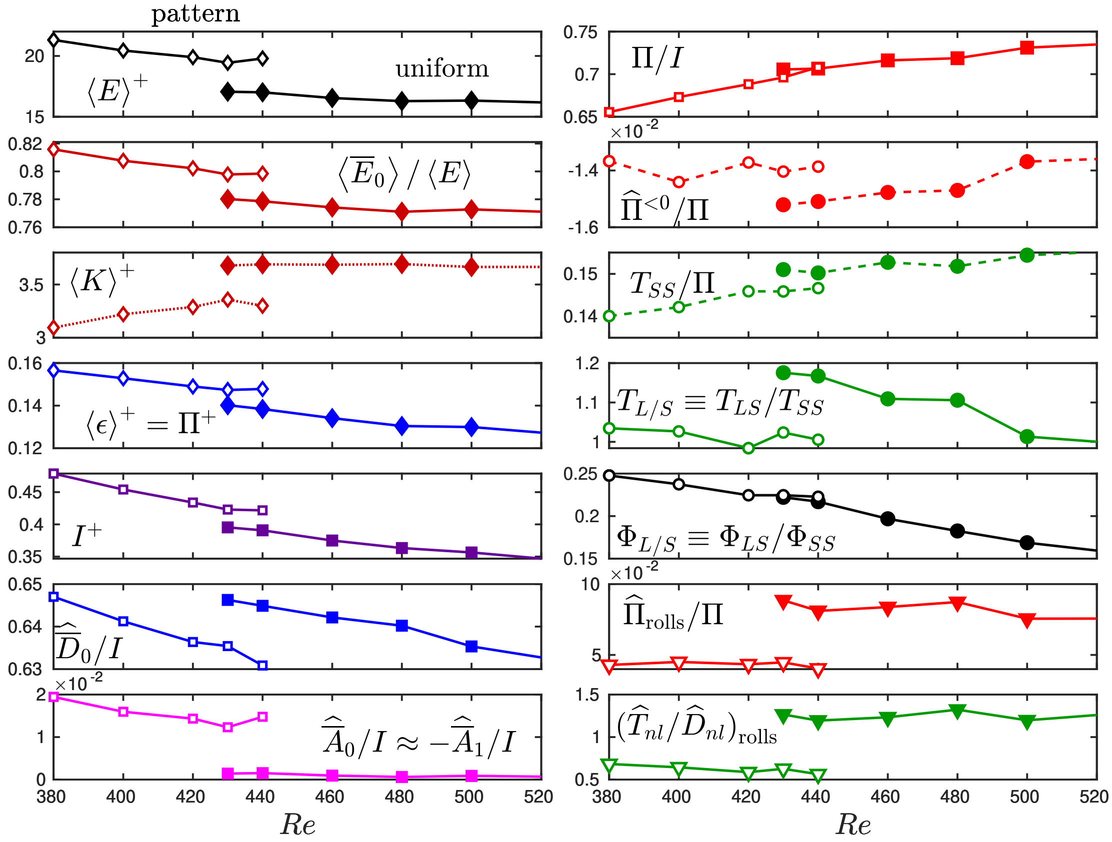

Figure 3.10: Evolution with *Re* of various energetic quantities defined throughout the text (equations (3.20), (4.15), and (3.19)).

$\widehat{T}_{LS}/\widehat{T}_{SS} \sim 1$ in the patterned state.

Lastly, in the two bottom-right plots of figure 3.10 we focus on the streak/roll scale k_{rolls}. We consider three quantities

$$\widehat{\Pi}_{\text{rolls}} = \int_{-1}^{1} \widehat{\Pi}(y, k_{\text{rolls}})\ \mathrm{d}y, \quad \widehat{D}_{\text{rolls}} = \int_{-1}^{1} \widehat{D}(y, k_{\text{rolls}})\ \mathrm{d}y, \quad \widehat{T}_{nl,\text{rolls}} = \int_{-1}^{1} \widehat{T}_{nl}(y, k_{\text{rolls}})\ \mathrm{d}y \tag{3.32}$$

and plot the ratios $\widehat{\Pi}_{\text{rolls}}/\Pi$ and $\widehat{T}_{nl,\text{rolls}}/\widehat{D}_{\text{rolls}}$. We recall that $\widehat{\Pi}_{\text{rolls}}$ is the maximum of $\widehat{\Pi}$ visible in figure 3.7a and 3.7c. We observe that the plotted ratios are approximately constant in each of the uniform and patterned states over the Re range considered, but each ratio exhibits a strong discontinuity at the transition between states. In the uniform case, $\widehat{T}_{nl,\text{rolls}}/\widehat{D}_{\text{rolls}} > 1$, meaning that at the scale k_{rolls}, energy is transferred to other scales more than it is directly dissipated. This relationship is reversed in the patterned state. We note that k_{rolls} is nearly constant with Re in the range under study.

We summarise our findings: First, most quantities are discontinuous through the transition. The notable exception is the relative production, for which the uniform and patterned states at the same Re exhibit the same exchange of energy between mean flow and TKE:

$$\frac{\Pi}{I}\bigg|_{\text{pattern}} \approx \frac{\Pi}{I}\bigg|_{\text{uniform}} \tag{3.33}$$

Moreover, we find that both negative production $\widehat{\Pi}^{<0}$ and inverse transfer to large scales $\widehat{T}_{LS}$ are lower in the patterned state than in the uniform states.

It seems counter-intuitive to associate a stronger mean flow $\overline{\boldsymbol{u}}$ with a reduced fueling of the mean flow by the fluctuations (via negative production $\widehat{\Pi}^{<0}$). This is, however, what we observe in comparing the patterned state to the uniform state at $Re = 430$ and 440. Referring to figure 3.8, the exchange between $\overline{\boldsymbol{u}}$ and TKE is more directional in the patterned state: the negative production is directly transferred to mode $\overline{\boldsymbol{u}}_1$, whereas it is diverted into $\overline{\boldsymbol{u}}_0$ in the uniform state. Furthermore, the patterned state is more balanced

$$\widehat{\Pi}^{<0} \approx \widehat{\widehat{\Pi}}_1, \quad \widehat{\Pi}^{>0} \approx \widehat{\widehat{\Pi}}_0, \quad \widehat{T}_{LS} \approx \widehat{T}_{SS} \tag{3.34}$$

than the uniform state.

The patterned state could be seen as more adapted to an increasingly dissipative environment when Re decreases: as the mean and fluctuations dissipate more their energy, they interact less with each other via the production terms and the fluctuations transfer less of their energy to other scales. Relatively to the amount of injected energy, less energy goes to turbulent fluctuations and the mean flow is therefore stronger in intensity. The patterned state diverts this mean-flow energy from the uniform mean flow $\overline{\boldsymbol{u}}_0$ to the large-scale flow $\overline{\boldsymbol{u}}_1$. Whether these energy processes have a role in the transition from uniform to patterned state is speculative at this stage.

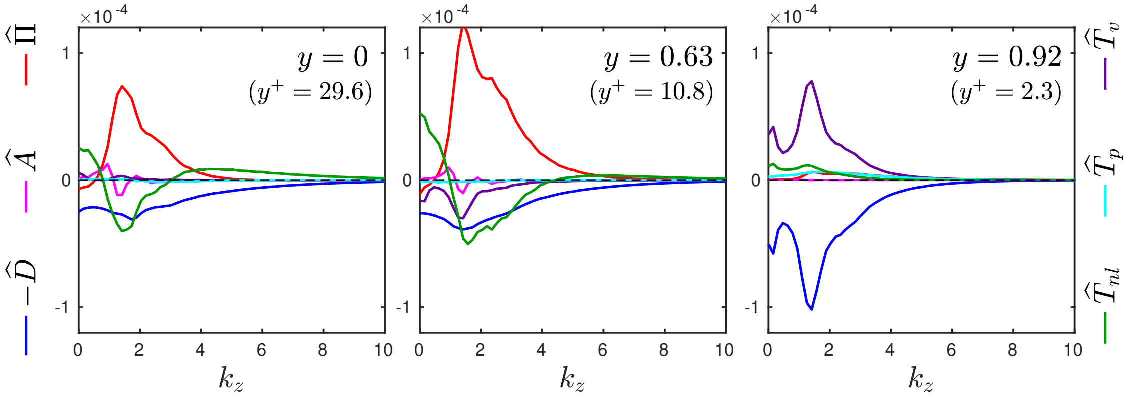

Figure 3.11: TKE spectral balance (3.14) at different y locations (left: mid-plane, $y = 0$; middle: $y = 0.63$; right: near-wall, $y = 0.92$). Shown is a patterned case at $Re = 400$.

3.7 Wall-normal dependence of spectral balance

3.7.1 Energy balance at various y locations

Up to this point, nothing has been said about the location of the energy transfers in the wall-normal direction and no distinction has been made between near-wall and bulk effects on the mean flow and turbulent energies. In this section, we present results on the TKE balance and subsequently the mean-flow balance for the patterned state at $Re = 400$.

Figure 3.11 shows the spectral TKE balance at different y locations: the mid-plane ($y = 0$, $y^+ = 29.6$, left panel), the layer of maximal spectral production $\widehat{\Pi}$ ($y = 0.63$, $y^+ \simeq 11$, middle panel) and the near-wall region ($y = 0.92$, $y^+ \simeq 2.4$, right panel).

The balance in the near-wall region is simple because it is dominated by viscous effects, with injection of energy via the rate-of-strain compensated by dissipation. A small portion of the energy comes from a positive transfer $\widehat{T}_{nl}$. In the plane $y = 0.63$, the production term $\widehat{\Pi}$ is maximal (as will be shown in §3.7.2.). Production peaks at the roll scale k_{rolls}, while the dissipation, viscous diffusion and non-linear transfers are all negative with similar magnitudes near this scale. Production becomes negative and non-linear transfers positive at long length scales (small k_z), similar to what we showed for y-integrated quantities in §3.5.2. The spectral balance at the mid-plane is qualitatively similar to that at the plane $y = 0.63$, with the notable exception that the viscous diffusion $\widehat{T}_v$ vanishes due to reflection symmetry about the midplane. $\widehat{\Pi}$ and T_{nl} are smaller in the mid-plane than in the plane $y = 0.63$, while $\widehat{D}$ and $\widehat{A}$ have nearly the same magnitude in both planes.

The y-dependence of the mean-flow energy balance (3.17) is displayed in figure 3.12. In line with our previous observations on y-integrated quantities (§3.5.2), figure 3.12 reveals different phenomenology depending on the wavenumber ($k_z = 0$, $k_z = 2\pi/L_z$ or $k_z >$

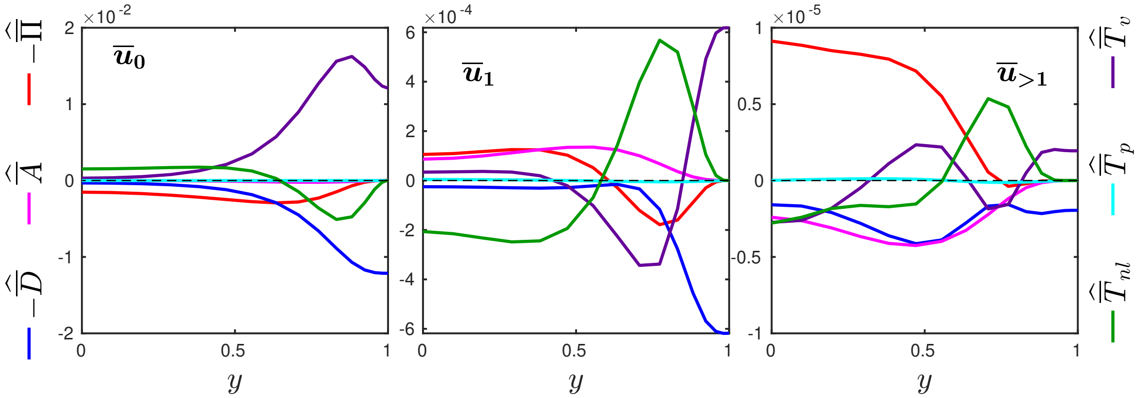

Figure 3.12: Evolution of the mean-flow energy balance (3.17) with y, for $k_z = 0$, $k_z = 2\pi/L_z$, and summed over $k_z > 2\pi/L_z$. (Values for $y < 0$ are obtained by reflection in $y = 0$.) Shown is a patterned case at $Re = 400$.

$2\pi/L_z$). The gain in energy in $\overline{\boldsymbol{u}}_0$ (left panel) due to the viscous transfer term $\widehat{\overline{\overline{T}}}_v$ is large near the wall where energy is injected into the flow, whereas the two terms involving the Reynolds stress, $\widehat{\overline{\overline{\Pi}}}$ and $\widehat{\overline{\overline{T}}}_{nl}$, are dominant and in approximate balance at the mid-plane. Note that while $\widehat{\overline{\overline{T}}}_{nl}$ integrates to zero, it has a local influence: flow above $y = 0.63$ transfers energy to flow below.

The balance of $\overline{\boldsymbol{u}}_1$ (middle panel) presents a complex and interesting behaviour. We know from §3.4 that when integrated over y, the balance for mode $\overline{\boldsymbol{u}}_1$ is such that $\widehat{\overline{\overline{\Pi}}}_1 < 0$ and that this mode extracts energy from TKE. However, the y-dependence of this term shows a change in sign: the production is only negative (i.e. $-\widehat{\overline{\overline{\Pi}}}_1 > 0$) for $-0.6 \lesssim y \lesssim 0.6$. $\widehat{\overline{\overline{T}}}_{nl}$ undergoes a change in sign at approximately the same y value, with similar behaviour, although their y integrals differ (the integral of $\widehat{\overline{\overline{T}}}_{nl}$ vanishes whereas that of $\widehat{\overline{\overline{\Pi}}}$ is negative). $\widehat{\overline{\overline{T}}}_{nl}$ dominates the energy source at $y \simeq 0.8$. At the wall ($y = 1$), the energy balance is between viscous diffusion and dissipation. The advection term $\widehat{\overline{\overline{A}}}$ is always positive.

The situation at $k_z > 2\pi/L_z$ is perhaps of negligible importance because of the small amplitude of the energy at this scale. However, we note that the balance near the wall (i.e. $0.7 \lesssim y \lesssim 1$) is qualitatively similar to that of mode $\overline{\boldsymbol{u}}_1$, dominated by viscous diffusion, dissipation, and triad interaction. In the bulk, energy comes from $\widehat{\overline{\overline{\Pi}}}$ and is diverted towards the other terms

3.7.2 Production and non-linear transfers in the (y, k_z) plane

Figure 3.13 and 3.14 show, respectively, $\widehat{\Pi}^+(y, k_z)$ and $\widehat{T}_{nl}^+(y, k_z)$ (i.e. $\widehat{\Pi}$ and $\widehat{T}_{nl}$ normalised by $Re\, u_\tau^4/U_{\text{wall}}^4$) for different states and Re ranging from 380 to 1000. We focus on these terms because of their unusual signs in the balance at large scales (small k_z). The zone of negative production at large scales is encircled by the dashed contour. We note that negative production spans the range $y \in [0, 0.8]$ at low Re, whereas it is more concentrated between $y = 0.6$ and 0.9 at $Re = 1000$. In viscous units, it approximately spans from $y^+ = 5$ to $y^+ \approx 30$ at all Re.

The triadic interaction term $\widehat{T}_{nl}^+$ is shown on figure 3.14. Inverse transfers are present from $k_z^+ = 0$ up to $k_z^+ \approx 0.07$ in the patterned cases, and $k_z^+ \approx 0.05$ in the uniform case at $Re = 1000$ ($Re_\tau = 66.4$), i.e. scales smaller than that of rolls and streaks ($k_{\text{rolls}} \simeq 1.41$, $k_{\text{rolls}}^+ \simeq 0.04$ for $Re \leq 430$). However, this small-scale part of the inverse transfer is localised only near the wall ($y^+ < 8$), while for $k_z^+ < 0.02$, the inverse transfer concerns the whole y domain.

We see two caveats that prevent further quantitative comparisons to other studies in non-tilted domains, for both transitional and non-transitional regimes. First, the imposition of an angle ($\theta = 24°$) is completely arbitrary for uniform turbulence, and along with the short domain size L_x, the streak spacing is imposed in our numerical domain. In Appendix 3.A, we present results in a non-oblique flow unit $(L_{\text{strm}}, L_{\text{span}}) = (30, 20)$ to confirm our observations in the Minimal Band Unit in the non-transitional case $Re = 1000$ ($Re_\tau = 66.2$). Second, the reduction to one dimension can miss the two-dimensionality of energy transfers: inter-scale transfers can actually be orientational, i.e. they may differ for wavenumbers (k_x, k_z) with the same modulus but different orientations. Therefore, inverse transfers in a one-dimensional spectrum can be misleading as they mix transfers between different orientations and transfers between different scales $|\boldsymbol{k}|$.

3.8 Conclusion

Wall-bounded turbulence at low Reynolds numbers is marked by a strong scale separation between the streak/roll scale of the self-sustaining process that comprises the turbulence, and the large-scale flow associated with oblique laminar-turbulent patterns. In this chapter, we have computed the spectral energy balances for both the mean flow and the turbulent fluctuations in a Minimal Band Unit, thus revealing the energy transfers connecting the different scales in transitional plane Couette flow.

As expected, TKE production is maximal at the scale of streaks and rolls, and a direct cascade sends energy to smaller dissipative scales. However, part of the TKE is also transferred to large scales via non-linear interaction. At large scales, this energy is partly sent to the mean flow, via negative production. Negative production has not received much attention although it has been reported for spanwise-constant modes at $Re_\tau = 180$

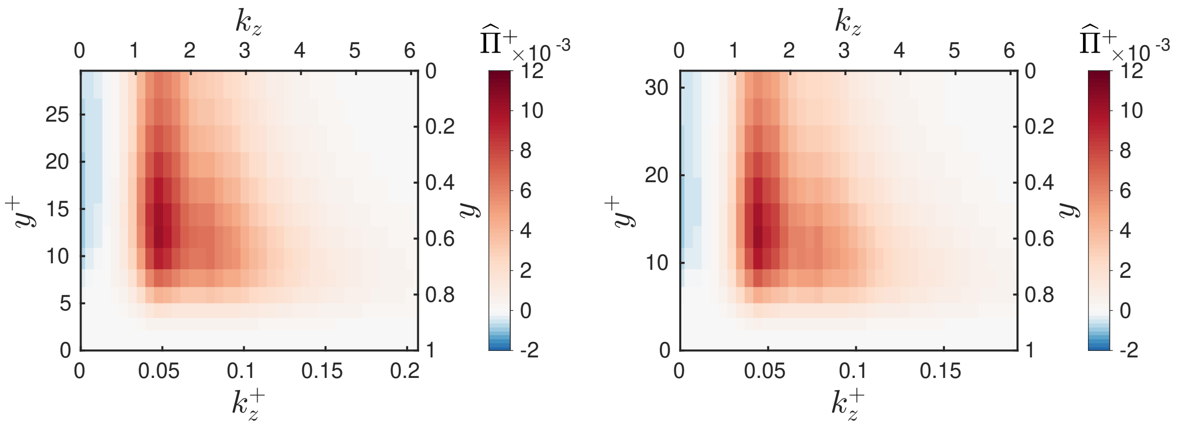

(a) Pattern, $Re = 400$ ($Re_\tau = 29.7$) **(b)** Pattern, $Re = 430$ ($Re_\tau = 31.9$)

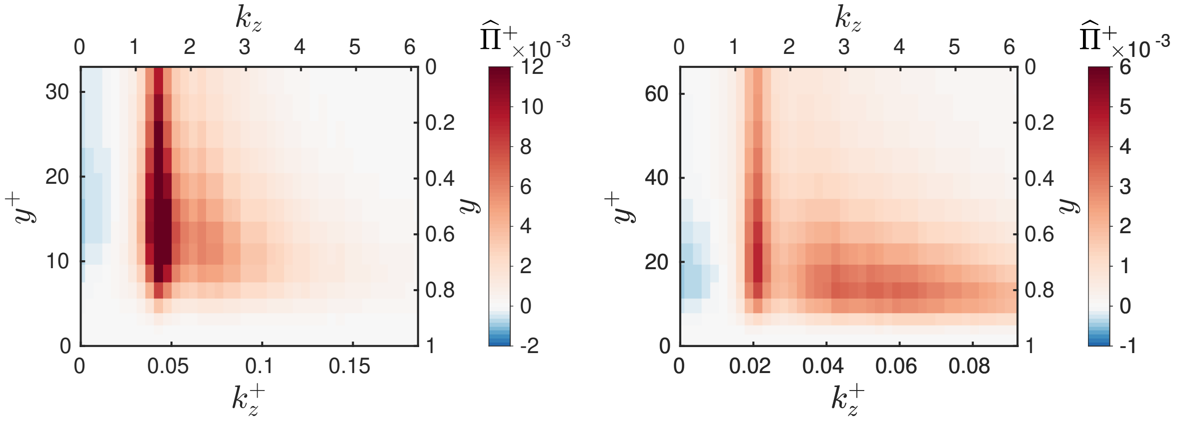

(c) Uniform, $Re = 430$ ($Re_\tau = 33.0$) **(d)** Uniform, $Re = 1000$ ($Re_\tau = 66.4$)

Figure 3.13: Visualisations of production $\widehat{\Pi}^+(y, k_z)$ for different Re and states. The cross-channel range is from the mid-plane ($y = 0$, $y^+ = Re_\tau$, lower axis) to the wall ($y = 1$, $y^+ = 0$, upper axis). Dashed line separates positive from negative value for small k_z.

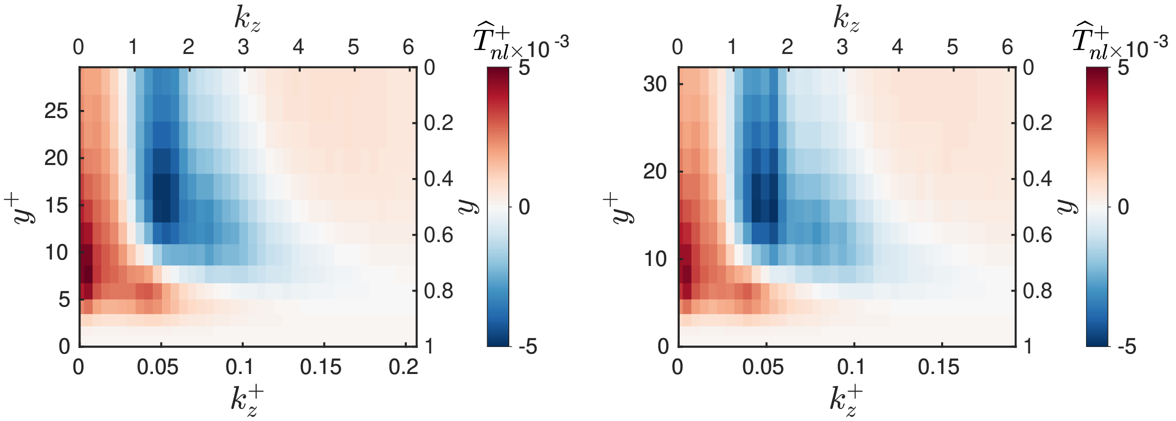

(a) Pattern, $Re = 400$ ($Re_\tau = 29.7$)

(b) Pattern, $Re = 430$ ($Re_\tau = 31.9$)

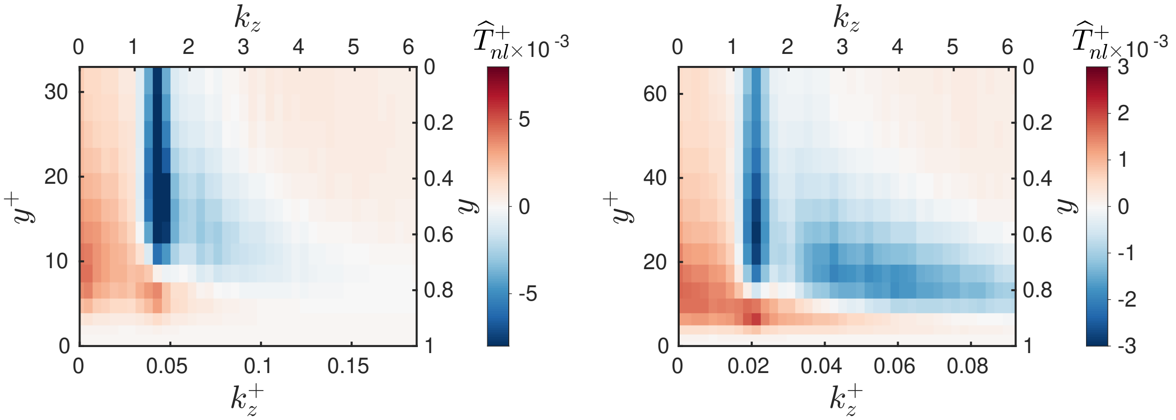

(c) Uniform, $Re = 430$ ($Re_\tau = 33.0$)

(d) Uniform, $Re = 1000$ ($Re_\tau = 66.4$)

Figure 3.14: Visualisations of of non-linear transfer $\widehat{T}_{nl}(y, k_z)$ for different Re and states. The cross-channel range is from the mid-plane ($y = 0$, $y^+ = Re_\tau$, lower axis) to the wall ($y = 1$, $y^+ = 0$, upper axis).

by Symon *et al.* (2021). We have found negative production at large scales for $Re_\tau \lesssim 66$, which, although of weak intensity, plays a role in feeding the inhomogeneous mean flow in transitional patterns.

The intense large-scale flow along laminar-turbulent bands appears in the single trigonometric component of the mean flow $\overline{\boldsymbol{u}}_1$. The main energy source for $\overline{\boldsymbol{u}}_1$ is the non-linear interaction with the uniform component $\overline{\boldsymbol{u}}_0$ (via the term called $\widehat{A}_1$ in this chapter). This interaction is due to the mean advection, which plays a significant role in both spatial and spectral transfers of mean-flow energy. Interestingly, the $\overline{\boldsymbol{u}}_1$ component of the mean flow is also fueled by negative production transferring energy from fluctuations to mean flow. However, this is only a secondary driver of $\overline{\boldsymbol{u}}_1$, as negative production accounts for only approximately 20% of its energy sources (see figure 3.7b).

We have found that the ratio of total TKE dissipation to total energy injection is continuous through the evolution from uniform turbulence to patterns as *Re* decreases. Our results indicate that as the environment becomes more dissipative with decreasing *Re*, the energy is reorganised such as to balance large-scale and small-scale transfers and to direct negative production into large-scale flow $\overline{\boldsymbol{u}}_1$.

The large scales characterising the transitional regime are probably of a different nature than large-scale motions observed in uniform shear flows at higher Re_τ (Jiménez, 1998; Smits *et al.*, 2011; **?**, and references therein), which are typically streamwise-elongated modes dictated by inertial effects far from the wall (in the outer zone). To the extent of our knowledge, large-scale fluctuating motions in fully developed turbulence do not feed the mean flow via negative production. The inverse transfers from small to large scales, which we report here in low-*Re* wall-bounded turbulence, echo those observed at higher *Re* (Cimarelli *et al.*, 2013; Mizuno, 2016; Aulery *et al.*, 2017; Cho *et al.*, 2018; Lee & Moser, 2019; Kawata & Tsukahara, 2021). Understanding the role of these transfers in the autonomous mechanisms governing wall-bounded turbulence is an active research topic. In fully developed turbulence, these inverse transfers are weaker than those reported here in transitional turbulence, and are essentially concentrated near the wall, while we observe inverse transfers over the whole shear layer that dominate the TKE budget at large scales.

Our analysis of energy budgets does not directly invoke a dynamical mechanism, such as the self-sustaining process governing wall-bounded turbulence and related mechanisms describing large scales in developed turbulence (Hwang & Cossu, 2010; Hwang & Bengana, 2016; de Giovanetti *et al.*, 2017; Cho *et al.*, 2018). Further investigations are required to understand whether the strong inverse transfers and the negative production that we observed are connected to the non-linear regeneration of rolls in the self-sustaining process. Note that the energetic imprint of the self-sustaining process in developed wall-bounded turbulence was recently analysed by Cho *et al.* (2018) and Kawata & Tsukahara (2021), the latter emphasising the role of non-linear transfers.

Although the oblique simulation domain is very useful for the study of inter-scale distribution of energy in patterned transitional turbulence, further confirmation via simulations

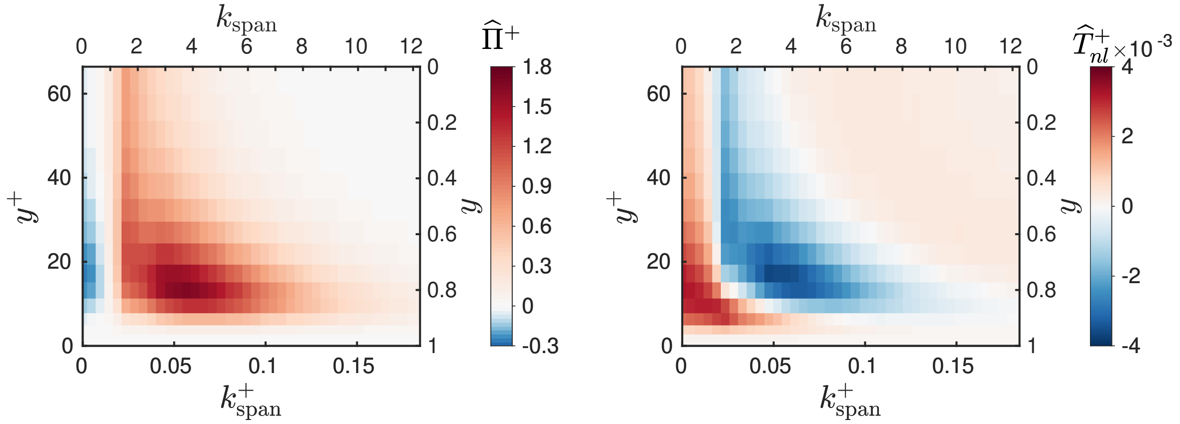

(a) Production **(b)** Non-linear transfer

Figure 3.15: Production and transfer spectra in a non-tilted domain with $(L_{\mathrm{strm}}, L_{\mathrm{span}}) = (30, 20)$ for $Re = 1000$ ($Re_\tau = 66$).

in large streamwise-spanwise domains is also required: our simulation domain restricts the flow in a number of ways, such as imposing an orientation as well as a mean streak spacing due to the restrained short size $L_x = 10$. These features do not seem to alter the robust observations that we have made about mean-turbulent interaction and inverse transfers (see Appendix 3.A). However, it would be beneficial to disentangle the streamwise and spanwise directions in the energy budget and to compute inter-component transfers, so as to better understand the role of the self-sustaining process in the generation of transitional large-scale structures.

In chapter 4, the energy cycle described above will be essential to understand the selection of a finite wavelength of transitional patterns.

3.A Spectral balance in a streamwise-spanwise domain at $Re_\tau = 66$.

The use of a Minimal Band Unit of size $(L_x, L_z) = (10, 40)$ to study Re outside of the transitional regime can be misleading, mainly because the short size and the tilt angle impose a strict spacing for the streaks. This is certainly why the production and transfer spectra shown at $Re = 1000$ (figures 3.13d and 3.14d) present a sharp peak at $k_z = 1.41$ ($k_z^+ = 0.0214$, $\lambda_z^+ = 290$) along with a tenuous maximum around $k_z^+ = 0.05$ ($\lambda_z^+ = 126$, $\lambda^+_{\mathrm{span}} = 138$). In a streamwise-spanwise domain of size $(L_{\mathrm{strm}}, L_{\mathrm{span}}) = (30, 20)$ and number of grid-points $(N_{\mathrm{strm}}, N_{\mathrm{span}}) = (375, 250)$, the streamwise-averaged spectrum is computed as a function of spanwise wavenumber k_{span} on figure 3.15, and presents a peak located around $k^+_{\text{span}} = 0.05$, $\lambda^+_{\text{span}} \simeq 130$, and no peak below. This is also true for the transfer spectrum. However, the features observed in a Minimal Band Unit are still present: negative production for $k^+_{\text{span}} < 0.01$ and inverse transfer occupying the whole shear layer for $k^+_{\text{span}} < 0.02$.

Chapter 4

Nucleation and optimal wavelength for transitional patterns

Low Reynolds number turbulence in wall-bounded shear flows *en route* to laminar flow takes the form of oblique localised turbulent structures. These emerge from uniform turbulence via a spatiotemporal intermittent process in which localised quasi-laminar gaps randomly nucleate and disappear. For slightly lower Reynolds numbers, periodic and approximately stationary laminar-turbulent patterns predominate. The statistics of quasi-laminar regions are analysed in several respects, including the distributions of space and time scales and their Reynolds number dependence. A smooth, but marked transition is observed between uniform turbulence and flow with intermittent quasi-laminar gaps, while the transition from gaps to patterns is more gradual. Wavelength selection in these patterns is analysed via numerical simulations in oblique domains of various sizes. Lifetime measurements in a minimal domain demonstrate the existence of a preferred wavelength. Wavelet transforms are performed on turbulent-laminar patterns, measuring areas and times over which a given wavelength dominates in a large domain. This leads to the quantification of the stability of a pattern as a function of wavelength and Reynolds number. We report that the preferred wavelength maximises the energy and dissipation of the large-scale flow along laminar-turbulent interfaces. This optimal behaviour is primarily due to the advective nature of this large-scale flow, while the role of turbulent fluctuations is secondary in the wavelength selection.

4.1 Introduction

The transition to turbulence in wall-bounded shear flows is characterised by coexisting turbulent and laminar regions. This phenomenon was first described by Coles & van Atta (1966) and by Andereck *et al.* (1986) in Taylor-Couette flow. Later, by constructing

Taylor-Couette and plane Couette experiments with very large aspect ratios, Prigent *et al.* (2002, 2003) showed that these coexisting turbulent and laminar regions spontaneously formed regular patterns with a selected wavelength and orientation that depend systematically on *Re*. These patterns have been simulated numerically and studied intensively in plane Couette flow (Barkley & Tuckerman, 2005, 2007; Duguet *et al.*, 2010; Rolland & Manneville, 2011; Tuckerman & Barkley, 2011), plane Poiseuille flow (Tsukahara *et al.*, 2005*b*; Tuckerman *et al.*, 2014; Shimizu & Manneville, 2019; Kashyap, 2021), and Taylor-Couette flow (Meseguer *et al.*, 2009; Dong, 2009; Wang *et al.*, 2022).

In pipe flow, the other canonical wall-bounded shear flow, only the streamwise direction is long, and transitional turbulence takes the form of *flashes* (Reynolds, 1883) or *puffs* (Wygnanski & Champagne, 1973), which are the one-dimensional analog of bands. In contrast to bands in planar shear flows, experiments and direct numerical simulations show that puffs never form regular spatially periodic patterns (Moxey & Barkley, 2010; Avila & Hof, 2013). Instead, the spacing between them is dictated by short-range interactions (Hof *et al.*, 2010; Samanta *et al.*, 2011). Puffs have been extensively studied, especially in the context of the model derived by **??**Barkley (2016) from the viewpoint of *excitable media*. In this framework, fluctuations from uniform turbulence trigger laminar gaps (i.e. low-energy holes in the turbulent flow) at random instants and locations in the flow, as has been seen in direct numerical simulations (DNS) of pipe flow. The bifurcation scenario giving rise to localised gaps has been investigated by Frishman & Grafke (2022), who called them *anti-puffs*. Interestingly, spatially periodic solutions like those observed in planar shear flows are produced in a centro-symmetric version of the Barkley model (**?**)

In this chapter, we will show that in plane Couette flow, as in pipe flow, short-lived localised gaps emerge randomly from uniform turbulence at the highest Reynolds numbers in the transitional range, which we will see is $Re \approx 470$ in the domain which we will study. The first purpose of this chapter is to investigate these gaps. The emblematic regular oblique large-scale bands appear at slightly lower Reynolds numbers, which we will see is $Re \approx 430$.

If the localised gaps are disregarded, it is natural to associate the bands with a *pattern-forming instability* of the uniform turbulent flow. This was first suggested by Prigent *et al.* (2003) and later investigated by Rolland & Manneville (2011). Manneville (2012) and Kashyap (2021) proposed a Turing mechanism to account for the appearance of patterns by constructing a reaction-diffusion model based on an extension of the Waleffe (1997) model of the streak-roll self-sustaining process. **?** discovered a sequence of bifurcations leading to a large-scale steady state that resembles a skeleton for the banded pattern, arising from tiled copies of the exact Nagata (1990) solutions. The relationship between these pattern-forming frameworks and local nucleation of gaps is unclear.

The adaptation of classic stability concepts to turbulent flows is a major current research topic (see, e.g., Markeviciute & Kerswell (2022)). At the simplest level, it is always formally possible to carry out linear stability analysis of a mean flow as in Barkley (2006);

Bengana *et al.* (2019). The mean flow of uniformly turbulent plane Couette flow has been found to be linearly stable (Tuckerman *et al.*, 2010). However, this procedure makes the drastic simplification of neglecting the Reynolds stress entirely in the stability problem and hence its interpretation is uncertain. The next level of complexity and accuracy is to represent the Reynolds stress via a closure model. However, closure models are designed for high-Reynolds-number fully developped turbulence rather than the weak turbulence of transitional wall-bounded shear flows. Indeed, a study using the (K, Ω) model yielded predictions that are completely incompatible with results from full numerical simulation or experiment (Tuckerman *et al.*, 2010). Another turbulent configuration in which robust large scales emerge are zonal jets, characteristic of geophysical turbulence. For zonal jets, a closure model provided by a cumulant expansion (**?**Tobias & Marston, 2013) has led to a plausible stability analysis (Parker & Krommes, 2013). Other strategies are possible for turbulent flows in general: Kashyap *et al.* (2022) examined the averaged time-dependent response of uniform turbulence to large-wavelength perturbations and provided evidence for a linear instability in plane channel flow. They computed a dispersion relation which is in good agreement with the natural spacing and angle of patterns.

Classic analyses for non-turbulent pattern-forming flows, such as Rayleigh-Bénard convection or Taylor-Couette flow, yield not only a threshold but also a preferred wavelength, as well as existence and stability ranges for other wavelengths through the Eckhaus instability (Busse, 1981; Ahlers *et al.*, 1986; Riecke & Paap, 1986; Tuckerman & Barkley, 1990; Cross & Greenside, 2009). As the control parameter is varied, this instability causes spatially periodic states to make transitions to other periodic states whose wavelength is preferred. Eckhaus instability is also invoked in turbulent zonal jets (Parker & Krommes, 2013).

The second goal of this chapter is to study the regular patterns of transitional plane Couette flow and to determine the wavelengths at which they can exist and thrive. At low enough Reynolds numbers, patterns will be shown to destabilise, acquiring a different wavelength. Using an energy analysis formulated in **?**, we associate the selected wavelength to a maximal dissipation observed for the large-scale flow along the bands.

4.2 Numerical setup

Plane Couette flow consists of two parallel rigid plates moving at different velocities, here equal and opposite velocities $\pm U_{\text{wall}}$. Lengths are nondimensionalised by the half-gap h between the plates and velocities by U_{wall}. The Reynolds number is defined to be $R \equiv U_{\text{wall}} h/\nu$. We will require one further dimensional quantity that appears in the friction coefficient – the horizontal mean shear at the walls, which we denote by U'_{wall}. We will use non-dimensional variables throughout, except when specified. We simulate the

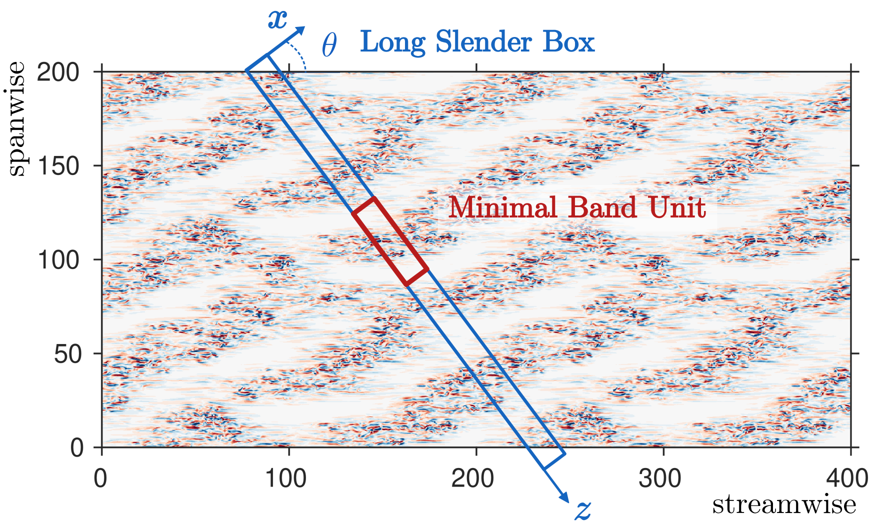

Figure 4.1: Spatial visualization of our numerical domains at $Re = 360$. Colors show v at $y = 0$ (blue: -0.2, white: 0, red: 0.2) in a domain of size $L_{\mathrm{strm}} = 400$, $L_{\mathrm{span}} = 200$. Red and blue boxes respectively show a Minimal Band Unit and a Long Slender Box.

incompressible Navier-Stokes equations

$$\frac{\partial \boldsymbol{u}}{\partial t} + (\boldsymbol{u} \cdot \nabla)\, \boldsymbol{u} = -\nabla p + \frac{1}{Re} \nabla^2 \boldsymbol{u}, \tag{4.1a}$$

$$\nabla \cdot \boldsymbol{u} = 0, \tag{4.1b}$$

using the pseudo-spectral parallel code `Channelflow` (**?**). Since the bands are found to be oriented obliquely with respect to the streamwise direction, we use a doubly periodic numerical domain which is tilted with respect to the streamwise direction of the flow, shown as the oblique rectangle in figure 4.1. This choice was introduced by Barkley & Tuckerman (2005) and has become common in studying turbulent bands (Shi *et al.*, 2013; Lemoult *et al.*, 2016; Paranjape *et al.*, 2020; Tuckerman *et al.*, 2020). The x direction is chosen to be aligned with a typical turbulent band and the z coordinate to be orthogonal to the band. The relationship between streamwise-spanwise coordinates and tilted band-oriented coordinates is:

$$\mathbf{e}_{\mathrm{strm}} = \cos\theta\, \mathbf{e}_x + \sin\theta\, \mathbf{e}_z \tag{4.2a}$$

$$\mathbf{e}_{\mathrm{span}} = -\sin\theta\, \mathbf{e}_x + \cos\theta\, \mathbf{e}_z \tag{4.2b}$$

The usual wall-normal coordinate is denoted by y and the corresponding velocity by v. Thus the boundary conditions are $\boldsymbol{u}(y = \pm 1) = \pm \mathbf{e}_{\mathrm{strm}}$ in y and periodic in x and z, together with a zero-flux constraint on the flow in the x and z directions. The field visualised in figure 4.1 comes from an additional simulation we carried out in a domain of size $(L_{\mathrm{strm}}, L_y, L_{\mathrm{span}}) = (200, 2, 100)$ aligned with the streamwise-spanwise directions. Exploiting the periodic boundary conditions of the simulation, the visualisation shows four copies of the flow instantaneous field.

The tilted box effectively reduces the dimensionality of the system by discarding large-scale variation along the short x direction. The flow in this direction is considered to be statistically homogeneous as it is only dictated by small turbulent scales. In a large non-tilted domain, bands with opposite orientations coexist (Prigent *et al.*, 2003; Duguet *et al.*, 2010; Klotz *et al.*, 2022), but only one orientation is permitted in the tilted box.

We will use two types of numerical domains, with different lengths L_z. Both have fixed resolution $\Delta z = L_z/N_z = 0.08$, along with fixed $L_x = 10$ $(N_x = 120)$ and $\theta = 24°$. These domains are shown in figure 4.1.

(1) **Minimal Band Units**, an example of which is shown as the dark red box in figure 4.1. These domains accommodate a single band-gap pair and so are used to study strictly periodic pattern of imposed wavelength $\lambda = L_z$.

(2) **Long Slender Boxes**, which have a large L_z direction that can accommodate a large and variable number of gaps and bands in the system. The blue box in figure 4.1 is an example of such a domain size with $L_z = 240$, but larger sizes ($L_z = 400$ or $L_z = 800$) will be used in our study.

4.3 Nucleation of laminar gaps

We carry out simulations in a Long Slender Box of size $L_z = 800$ for various Re with the uniform turbulent state from a simulation at $Re = 500$ as an initial condition, a protocol called a quench. Figure 4.2 displays the resulting spatio-temporal dynamics at four Reynolds numbers. Plotted is the (z, t) dependence of the cross-flow energy $(v^2 + u_{\mathrm{span}}^2)/2$ at $(x = L_x/2, y = 0)$. The cross-flow energy is a useful diagnostic because it is zero for laminar flow. The choice $x = L_x/2$ is arbitrary since there is no large-scale variation of the flow field in the short x direction of the simulation.

Figure 4.2 demonstrates strong space-time intermittency and encapsulates the main results of this section: the emergence of patterns out of uniform turbulence is a gradual process. At $Re = 500$, barely discernible low-energy regions appear randomly within the turbulent background. At $Re = 460$ the low-energy regions are more pronounced and begin to constitute localised, quasi-laminar gaps within the turbulent flow. These gaps appear sparsely and are not long lived. At $Re = 440$, clearly demarcated, spatially localised quasi-laminar gaps are seen. As Re is further decreased, these quasi-laminar gaps appear more frequently and persist for longer lifetimes. Eventually, the gaps self-organise into persistent, albeit fluctuating, patterns. The remainder of the section will quantify this transition to patterns.

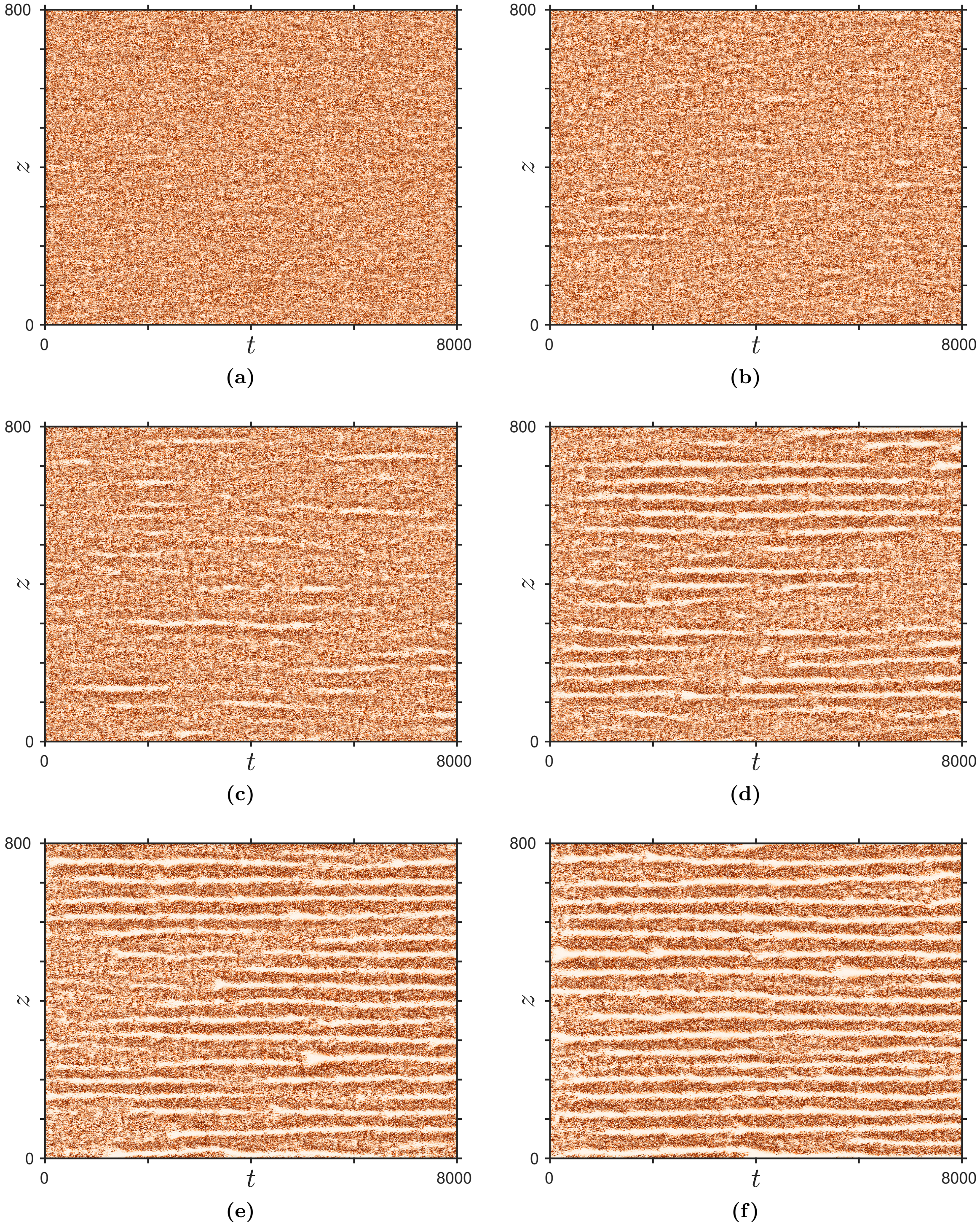

Figure 4.2: Spatio-temporal visualization of pattern formation with $L_z = 800$, for (a) $Re = 500$, (b) $Re = 460$, (c) 440, (d) 420, (e) 400 and (f) $Re = 380$. Flow at $t = 0$ is initiated from uniform turbulence at $Re = 500$. Color shows local cross-flow energy $(v^2 + u^2_{\text{span}})/2$ at $x = L_x/2$, $y = 0$ (white: 0, red: 0.02). At high Re, weak local gaps appear sparsely. When Re is decreased, spatio-temporally intermittent patterns of finite spatial extent emerge. These consist of turbulent cores (dark red) and quasi-laminar gaps (white). For still lower Re, quasi-laminar regions live longer, and patterns are more regular and steady.

We consider the x, y-averaged cross-flow energy

$$e(z,t) \equiv \frac{1}{L_x L_y} \int_{-1}^{1} \int_{0}^{L_x} \frac{1}{2}(v^2 + u_{\text{span}}^2)(x,y,z,t)\ \mathrm{d}x\,\mathrm{d}y \tag{4.3}$$

as a useful diagnostic of quasi-laminar and turbulent zones. The probability density functions (PDFs) of $e(z,t)$ are shown in figure 4.3a for various values of Re. The right tails, corresponding to high-energy events, are broad and exponential for all Re. The left, low-energy portions of the PDFs vary qualitatively with Re, unsurprisingly since these portions correspond to the weak turbulent events comprising the formation of quasi-laminar gaps. For large Re, the PDFs are maximal around $e \simeq 0.007$. As Re is decreased, a low-energy peak emerges at $e \simeq 0.002$, corresponding to the emergence of long-lived, quasi-laminar gaps seen in figure 4.2. The peak at $e \simeq 0.007$ flattens and gradually disappears. An interesting feature is that the distributions broaden with decreasing Re with both low energy and high energy events becoming more likely. This reflects a spatial redistribution of energy that accompanies the formation of quasi-laminar gaps. This is presumably the effect of turbulent bands extracting energy from the quasi-laminar regions and becoming more intense. (See figure 6 of **?**.)

An intuitive way to characterise the intermittent creation of gaps is to define turbulent and quasi-laminar regions by thresholding the values of $e(z,t)$. In the following, a region will be called quasi-laminar if $e(z,t) < e_{\text{turb}}$ and turbulent if $e(z,t) \geq e_{\text{turb}}$. As the PDF of $e(z,t)$ evolves with Re, we define a Re-dependent threshold as a fraction of its average value, $e_{\text{turb}} = 0.75\,\overline{e}$. The thresholding is illustrated in figure 4.3b, which is an enlargement of the flow at $Re = 440$ that shows turbulent and quasi-laminar zones as white and blue areas, respectively. Thresholding within a fluctuating turbulent environment can conflate long-lived quasi-laminar gaps with tiny, short-lived regions where the energy fluctuates below the threshold e_{turb}. These are seen as the numerous small blue spots in figure 4.3b that differ from the wider and longer-lived gaps. This deficiency is addressed by examining the statistics of the spatial and temporal sizes of quasi-laminar gaps.

We present the length distributions of laminar L_{lam} and turbulent zones L_{turb} in figures 4.3c and 4.3d at various Reynolds numbers. These distributions have their maxima at very small lengths, reflecting the large number of small-scale, low-energy regions that arise due to thresholding the fluctuating turbulent field. As Re is decreased, the PDF for L_{lam} begins to develop a peak near $L_{\text{lam}} \simeq 15$, corresponding to the scale of the gaps visible in figure 4.2. The right tails of the distribution are exponential and shift upwards with decreasing Re. The PDF of L_{turb} also varies with Re, but in a somewhat different way. As Re decreases, the likelihood of turbulent length in the range $15 \lesssim L_{\text{turb}} \lesssim 35$ increases above the exponential background, but at least over the range of Re considered, a maximum does not develop. The distributions at large L_{turb} appear to be independent of Re.

It is notable that the laminar-length distributions show the emergence of structure at Re

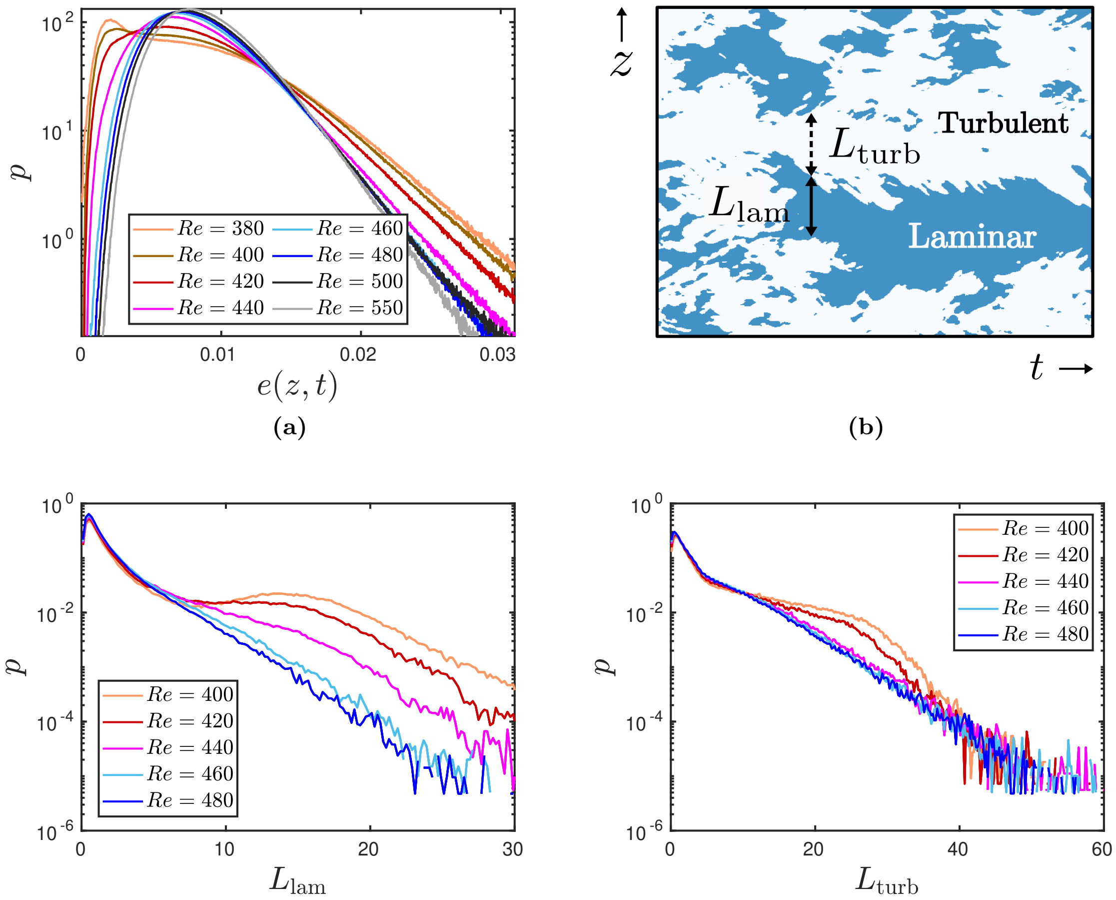

(a) **(b)**

(c) **(d)**

Figure 4.3: (a) PDFs of local cross-flow energy $e(z,t)$ defined in (4.3). Maximum at $e \simeq 0.002$ appears for $Re \leq 420$. (b) Illustration of the thresholding $e(z,t) < e_{\mathrm{turb}}$, of a laminar-turbulent field at $Re = 440$ with turbulent regions, $e(z,t) > e_{\mathrm{turb}}$ in white and quasi-laminar regions in blue. Definitions of laminar and turbulent gaps L_{gap} and L_{turb} are illustrated. (c) PDFs of laminar gap widths L_{lam} showing plateaux near 15 appearing for $Re \leq 440$. (d) PDFs of widths of turbulent regions L_{turb} showing local increase near 20 for $Re \leq 420$.

higher than the turbulent-length distributions. This is particularly visible at $Re = 440$, where the distribution of L_{turb} is indistinguishable from those at higher Re, while the distribution of L_{lam} is substantially altered. This is entirely consistent with impression from the visualisation in figure 4.2c that quasi-laminar gaps are emerging in a uniform turbulent background. Although the distributions of L_{lam} and L_{turb} behave differently, the length scale emerging as Re decreases are of the same order of magnitude for both. This latter aspect is not present in the pipe flow results of Avila & Hof (2013). (See Appendix 4.B for a more detailed comparison.)

Temporal measurements of the gaps are depicted in figure 4.4. Figure 4.4a shows the procedure by which we define the temporal extents t_{gap} of laminar gaps. For each laminar gap, i.e. a connected zone in (z, t) satisfying $e(z, t) < e_{\mathrm{turb}}$, we locate its latest and earliest times and define t_{gap} as the distance between them. Here again, we fix the threshold at $e_{\mathrm{turb}} = 0.75\ \overline{e}$. Figure 4.4b shows the temporal distribution of quasi-laminar gaps, via the survival function of their lifetimes. In a similar vein to the spatial gap lengths, two characteristic behaviours are observed: for small times, many points are distributed near zero (as a result of frequent fluctuations near the threshold e_{turb}), while for large enough times, an exponential regime is seen:

$$P(t_{\mathrm{gap}} > t) \approx e^{-(t-t_0(Re))/\tau_{\mathrm{gap}}(Re)} \text{ for } t > t_0(Re) \tag{4.4}$$

The slope of the exponential tail is extracted at each Re and the resulting characteristic time-scale τ_{gap} is shown in figure 4.4c. The evolution of τ_{gap} with Re displays two regimes, each with nearly exponential dependence on Re, but with very different slopes on the semi-log plot. For $Re \geq 470$, the characteristic lifetimes are $\tau_{\mathrm{gap}} = O(10^2)$ and vary weakly with Re. These timescales correspond to the small white events visible in figure 4.2a and are associated with short-lived, low-energy events on the left tails of the PDFs for $e(z, t)$ in figure 4.3a. Discounting these events, we refer to such states as uniform turbulence. For $Re < 470$, τ_{gap} varies rapidly with Re. The abrupt change in slope seen in figure 4.4c marks the transition between uniform turbulence and the emergence of local gaps as Re is decreased. We denote by $= 470$ the Reynolds number at which this transition occurs. We stress that as far as we have been able to determine, there are no critical phenomenon associated with this change of behaviour. That is, the transition is smooth and lacks a true critical point. It is nevertheless evident that the dynamics of quasi-laminar gaps change significantly in the region of $Re = 470$ and therefore it is useful to define a reference Reynolds number marking this change in behaviour.

Note that typical lifetimes of laminar gaps must become infinite by the threshold $Re \simeq 325$ below which turbulence is no longer sustained (Lemoult *et al.*, 2016). (We believe this to be true even for $Re \lesssim 380$ when the permanent banded regime is attained, although this is not shown here.) For this reason, we have restricted our study of gap lifetimes to $Re \gtrsim 380$ and we have limited our maximal simulation time to $\sim 10^4$.

To quantify the distinction between localized gaps and patterns, we introduce a variable

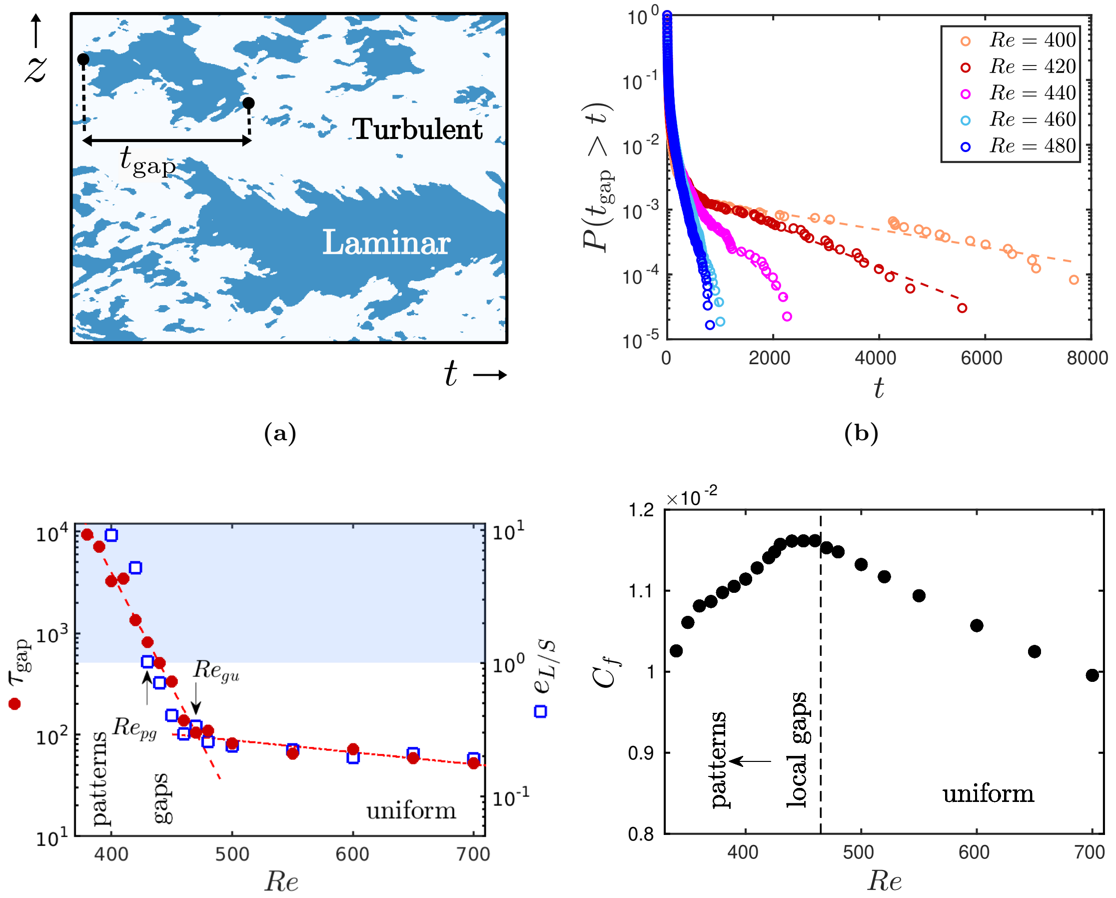

(a) (b) (c) (d)

Figure 4.4: (a) Same as figure 4.3b, but illustrating the definition of lifetimes of quasi-laminar gaps t_{gap}. (b) Survival functions of t_{gap}. After initial steep portions, slopes yield the characteristic times. (c) Evolution with Re of characteristic time τ_{gap} and of ratio of large to small scale energy $e_{L/S}$ defined by (4.7). Both of these quantities present two exponential regimes, with the same slopes and a common crossover. (d) Evolution of friction coefficient C_f with Re, showing three regimes delimited by ≈ 430 and by ≈ 470.

$e_{L/S}$ as follows. Using the Fourier transform in z,

$$\hat{\boldsymbol{u}}(x,y,k_z,t) = \frac{1}{L_z}\int_0^{L_z} \boldsymbol{u}(x,y,z,t)e^{-ik_z z}\,\mathrm{d}z\,, \tag{4.5}$$

we compute the averaged spectral energy

$$\widehat{E}(y,k_z) \equiv \frac{1}{2}\overline{\hat{\boldsymbol{u}}\cdot\hat{\boldsymbol{u}}^*}, \qquad\qquad \widehat{E}(k_z) \equiv \langle \widehat{E}(y,k_z)\rangle_y \tag{4.6}$$

where the overbar designates an average in x and t. This spectral energy was already described in Figure 3.3a. We are interested in the ratio of $\widehat{E}(k_z)$ at large scales (pattern scale) to small scales (roll-streak scale), as it evolves with Re. For this purpose, we define the ratio of large-scale to small-scale maximal energy:

$$e_{L/S} = \frac{\max\limits_{k_z<0.5} \widehat{E}(k_z)}{\max\limits_{k_z\geq 0.5} \widehat{E}(k_z)} \tag{4.7}$$

This quantity is shown as blue squares in figure 4.4c and is highly correlated to τ_{gap}. This correlation is in itself a surprising observation for which we have no explanation.

For $Re \gtrsim 430$, we have $e_{L/S} < 1$, signaling that the dominant peak in the energy spectrum is at the roll-streak scale, while for $Re \lesssim 430$, the large-scale pattern begins to dominate the streaks and rolls, as indicated by $e_{L/S} > 1$ (light blue area on figure 4.4c). Note that $Re = 430$ is also the demarcation between unimodal and bimodal PDFs of $e(z,t)$ in figure 4.3a. The transition from gaps to patterns is smooth. In fact, we do not even observe a qualitative feature sharply distinguishing gaps and patterns. We nevertheless find it useful to define a reference Reynolds number associated to patterns starting to dominate the energy spectrum. This choice has the advantage of yielding a quantitative criterion, which we estimate as ≈ 430.

In addition to the previous quantitative measures, we also extract the friction coefficient. This is defined as the ratio of the mean wall shear stress $\mu U'_{\text{wall}}$ to the dynamic pressure $\rho U_{\text{wall}}^2/2$, which we write in physical units and then non-dimensional forms as:

$$C_f \equiv \frac{\mu U'_{\text{wall}}}{\frac{1}{2}\rho U_{\text{wall}}^2} = \frac{2\nu}{hU_{\text{wall}}}\frac{U'_{\text{wall}}}{U_{\text{wall}}/h} = \frac{2}{Re}\frac{\partial\,\langle u_{\text{strm}}\rangle_{x,z,t}}{\partial y}\bigg|_{\text{wall}} \tag{4.8}$$

In (4.8), the dimensional quantities h, ρ, μ, and ν are the half-height, the density, and dynamic and kinematic viscosities, and U_{wall} and U'_{wall} are the velocity and mean velocity gradient at the wall. We note that the behavior of C_f in the transitional region has been investigated by Shimizu & Manneville (2019) and Kashyap *et al.* (2020*b*). Our measurements of C_f are shown in figure 4.4d. We distinguish three regimes. In the uniform regime $Re >= 470$, C_f increases with decreasing Re. In the patterned regime

$Re <= 430$, C_f decreases with decreasing Re. Between the two, in the localised-gap regime $< Re <$, C_f is approximately constant.

The changes in regimes and the distinction between local gaps and patterns can be further studied by measuring the spatial correlation between quasi-laminar regions within the flow. We define

$$\Theta(z,t) = \begin{cases} 1 & \text{if } e(z,t) < e_{\text{turb}} \text{ (laminar)} \\ 0 & \text{otherwise (turbulent)} \end{cases} \tag{4.9}$$

(this is the quantity shown in blue and white in figures 4.3b and 4.4a.) We then compute its spatial correlation function:

$$C(\delta z) = \frac{\langle \Theta(z)\Theta(z+\delta z)\rangle_{z,t} - \langle \Theta(z)\rangle_{z,t}^2}{\langle \Theta(z)^2\rangle_{z,t} - \langle \Theta(z)\rangle_{z,t}^2}. \tag{4.10}$$

Along with (z,t) averaging, C is also averaged over multiple realisations of the quench experiment. As Θ is a Heaviside function, C can be understood as the average probability of finding quasi-laminar flow at a distance δz from other quasi-laminar flow at position z. The results are presented in figure 4.5a. The comparison between different Re values is enhanced by plotting $\tanh(10\ C)$, shown in figure 4.5b. At long range, C approaches zero with some small fluctuations at $Re = 480$, a noisy periodicity at $Re = 460$, and a nearly periodic behaviour for $Re \leq 420$.

In all cases, C initially decreases from one and reaches a first minimum, due to the minimal possible size of a turbulent zone that suppresses the creation of neighbouring laminar gaps in the range $\delta z \lesssim 30$. C has a prominent local maximum $\delta z_{\max}$ right after the initial decrease of C, at $\delta z_{\max} \simeq 32$ at $Re = 480$, which increases to $\delta z_{\max} \simeq 41$ at $Re = 420$. These maxima, shown as coloured circles in figure 4.5b, indicate that gap nucleation is preferred at distance $\delta z_{\max}$ from an existing gap. The increase in $\delta z_{\max}$ and the subsequent extrema as Re is lowered agrees with the trend of increasing wavelength of turbulent bands as Re is decreased in the fully banded regime at lower Re (Prigent *et al.*, 2003; Barkley & Tuckerman, 2005).

Our observations confirm the absence of large-scale modulation in the uniform regime $Re > 470$ (as defined in figure 4.4c), but emphasise the presence of (weak) gap interaction at a finite distance in this regime. This preference is stronger as Re decreases and multiple gaps appear close to one another. The underlying selection of a finite gap spacing will be investigated in §4.4 and 4.5.

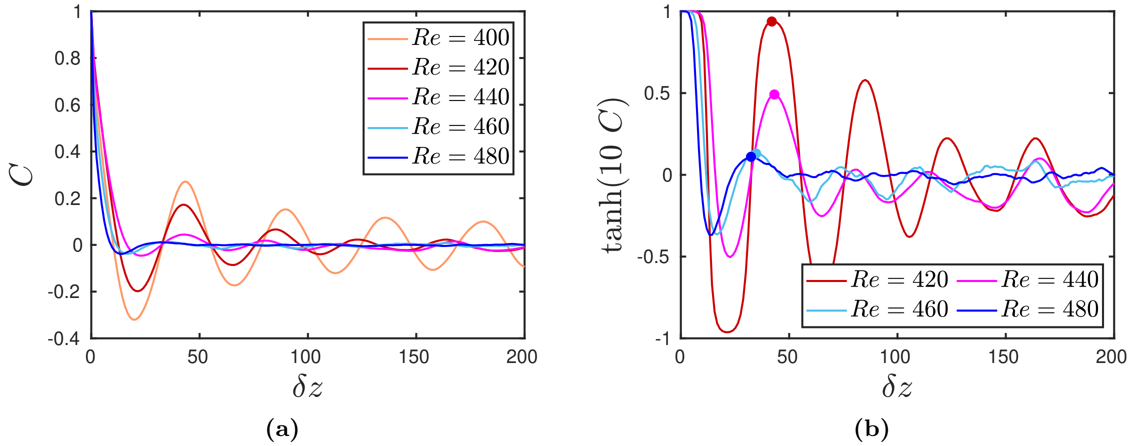

Figure 4.5: (a) Gap-to-gap correlation function $C(\delta z)$ defined by (4.10) for various values of Re. (b) plotting $\tanh(10\ C(\delta z))$ focuses on the short-range behaviour of C. The oscillations at $Re = 420$ are weak at $Re = 460$ and disappear at $Re = 480$. The dots correspond to the first local maximum, indicating the selection of a finite distance between two local gaps.

4.4 Existence and stability of patterns

In this section, we investigate the existence of a preferred pattern wavelength by using as a control parameter the length L_z of the Minimal Band Unit. In a Minimal Band Unit, the system is constrained and the distinction between local gaps and patterns is lost. L_z is chosen such as to accommodate at most a single turbulent zone and a single quasi-laminar zone, which due to imposed periodicity, can be viewed as one period of a perfectly periodic pattern. By varying L_z, we can verify whether a regular pattern of given wavelength L_z can emerge from uniform turbulence, disregarding the effect of scales larger than L_z or of competition with wavelengths close to L_z. We refer to these simulations in Minimal Band Units as *existence* experiments. Indeed, one of the main advantages of the Minimal Band Unit is the ability to create patterns of a given angle and wavelength which may not be stable in a larger domain.

In contrast, in a Long Slender Box, L_z is large enough to accommodate multiple bands and possibly even patterns of different wavelengths. An initial condition consisting of a regular pattern of wavelength λ can be constructed by concatenating bands produced from a Minimal Band Unit of size λ. The *stability* of such a pattern is studied by allowing this initial state to evolve via the non-linear Navier-Stokes equations. Both existence and stability studies can be understood in the framework of the Eckhaus instability (Kramer & Zimmermann, 1985; Ahlers *et al.*, 1986; Tuckerman & Barkley, 1990; Cross & Greenside, 2009).

In previous studies of transitional regimes, Barkley & Tuckerman (2005) studied the evolution of patterns as L_z was increased. In Section 4.4.1, we extend this approach to multiple sizes of the Minimal Band Unit by comparing lifetimes of patterns that naturally arise in this constrained geometry. The stability of regular patterns of various wavelengths will be studied in Long Slender Domains ($L_z = 400$) in Section 4.4.2.

4.4.1 Temporal intermittency of regular patterns in a short-L_z box

Figure 4.6a shows the formation of a typical pattern in a Minimal Band Unit of size $L_z = 40$ and at $Re = 440$. While the system cannot exhibit the spatial intermittency seen in figure 4.2c, temporal intermittency is possible and is seen as alternations between uniform turbulence and patterns. We plot the spanwise velocity at $y = 0$ and $x = L_x/2$. This is a particularly useful measure of the large-scale flow associated with patterns, seen as red and blue zones surrounding a white quasi-laminar region. The patterned state spontaneously emerges from uniform turbulence and remains from $t \simeq 1500$ to $t \simeq 3400$. At $t \simeq 500$, a short-lived quasi-laminar zone appears at $z = 10$, which can be seen as an attempt to form a pattern.

The pattern is characterised quantitatively by computing the wavenumber that instantaneously maximises the energy of the Fourier mode k_z:

$$\widehat{\lambda}_{\max}(t) = \frac{2\pi}{\underset{k_z>0}{\operatorname{argmax}} \, |\langle \widehat{\boldsymbol{u}}(y=0,k_z,t)\rangle_x|^2}, \tag{4.11}$$

where $\langle \widehat{\boldsymbol{u}}(y=0,k_z,t)\rangle_x$ denotes the x average of the z Fourier transform of the mid-plane velocity. The possible values of $\widehat{\lambda}_{\max}$ are integer divisors of L_z, i.e. here 40, 20, 10, etc. Figure 4.6b presents $\widehat{\lambda}_{\max}$ and its short-time average $\langle\widehat{\lambda}_{\max}\rangle_{t_a}$ with $t_a = 30$ as light and dark blue curves, respectively. When turbulence is uniform, $\widehat{\lambda}_{\max}$ varies rapidly between its discrete allowed values, while $\langle\widehat{\lambda}_{\max}\rangle_{t_a}$ fluctuates more gently around 10. The flow state is deemed to be patterned when its dominant mode is $\langle\widehat{\lambda}_{\max}\rangle_{t_a} = L_z$. The long-lived pattern occurring for $1500 \le t \le 3400$ in figure 4.6a is seen as a plateau of $\langle\widehat{\lambda}_{\max}\rangle_{t_a}$ in figure 4.6b. There are other shorter-lived plateaus, notably at for $500 \le t \le 750$. A similar analysis was carried out by Barkley & Tuckerman (2005); Tuckerman & Barkley (2011) using the Fourier component corresponding to wavelength L_z of the spanwise mid-gap velocity.

Figure 4.6c shows the survival function t_{pat} of the pattern lifetimes obtained from $\langle\widehat{\lambda}_{\max}\rangle_{t_a}$ over long simulation times for various Re. This measurement differs from figure 4.4b, which showed lifetimes of *gaps* in a Long Slender Box and not regular *patterns* obtained in a Minimal Band Unit. Here, the spatio-temporal intermittency reduces to a temporal problem, since we consider the flow in the Minimal Band Unit to either contain

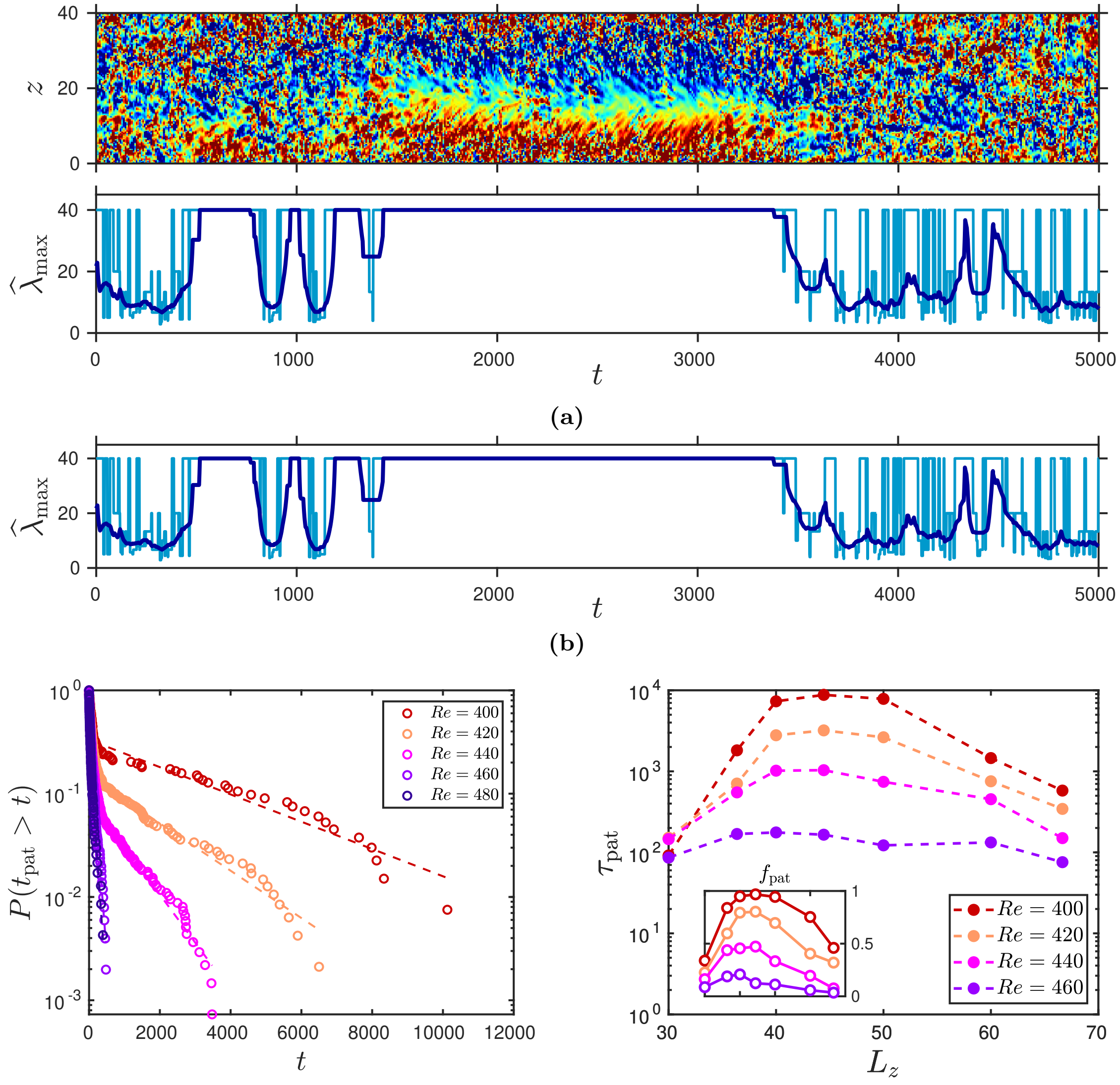

(a)

(b)

(c) **(d)**

Figure 4.6: Pattern lifetimes. (a) Space-time visualization of a metastable pattern in a Minimal Band Unit with $L_z = 40$ at $Re = 440$. Colors show spanwise velocity (blue: -0.1, white: 0, red: 0.1). (b) Values of the dominant wavelength $\widehat{\lambda}_{\max}$ (light blue curve) and of its short-time average $\langle\widehat{\lambda}_{\max}\rangle_{t_a}$ (dark blue curve) are shown; see (4.11). A state is defined to be patterned if $\widehat{\lambda}_{\max} = L_z$. (c) Survival function of lifetimes of laminar-turbulent patterns in a Minimal Band Unit with $L_z = 40$ for various Re. The pattern lifetimes t_{pat} are the lengths of the time intervals during which $\widehat{\lambda}_{\max} = L_z$. (d) Above: characteristic times τ_{pat} extracted from survival functions as a function of L_z and Re. Below: intermittency factor γ_{pat} for the patterned state: the fraction of time spent in the patterned state.

a pattern or not. Nevertheless the picture is qualitatively similar. As with figure 4.4b, in figure 4.6c there are many short-lived patterns due to fluctuations. After $t \simeq 200$, the survival functions enter an approximately exponential regime, from which we extract the characteristic times τ_{pat} by taking the inverse of the slope.

We then vary L_z, staying within the Minimal Box regime $L_z \lesssim 70$ in which only one band can fit. Figure 4.6d (top) shows that τ_{pat} presents a broad maximum in L_z whose strength and position depend on Re: $L_z \simeq 42$ at $Re = 440$ and $L_z \simeq 50$ at $Re = 400$. This wavelength corresponds approximately to the natural spacing observed in a Large Slender Box (figure 4.2). Figure 4.6d (bottom) presents the fraction of time that is spent in a patterned state, denoted γ_{pat}, to reflect that this should be thought of as the intermittency factor for the patterned state. The dependence of γ_{pat} on L_z follows the same trend as τ_{pat}, but less strongly (the scale of the inset is linear, while that for τ_{pat} is logarithmic). For $Re = 480$, the survival function is nearly the same as for 460 and τ_{pat} and γ_{pat} are nearly independent of L_z; this is the situation for uniform turbulence.

These results complement the Ginzburg-Landau description proposed by Prigent *et al.* (2003) and Rolland & Manneville (2011). To quantify the bifurcation from featureless to pattern turbulence, they defined an order parameter and showed that it has a quadratic maximum at an optimal wavenumber. This is consistent to the approximate quadratic maximum that we observe in the logarithmic plot of pattern lifetimes, and in the linear plot of γ_{pat} with regard to L_z.

4.4.2 Pattern stability in a large domain

To study the stability of a pattern of wavelength λ, we prepare an initial condition for a Long Slender Box concatenating repetitions of a single band produced in a Minimal Band Unit. We add small-amplitude noise to this initial pattern so that the repeated bands do not all evolve identically. Figures 4.7a and 4.7b show two examples of such simulations. Depending on the value of Re and of the initial wavelength λ, the pattern destabilises to either another periodic pattern (figure 4.7a for $Re = 400$) or to localised patterns surrounded by patches of featureless turbulence (figure 4.7b for $Re = 430$).

It can be seen that patterns often occupy only part of the domain. For this reason, we turn to the wavelet decomposition (Meneveau, 1991; Farge *et al.*, 1992) to quantify patterns locally. In contrast to a Fourier decomposition, the wavelet decomposition quantifies the signal as a function of space and scale. From this, we are able to define a local dominant wavelength, $\widetilde{\lambda}_{\max}(z,t)$, similar in spirit to $\widehat{\lambda}_{\max}(t)$ in (4.11), but now at each space-time point. (See Appendix 4.A for details.) Figures 4.7c and 4.7d show $\widetilde{\lambda}_{\max}(z,t)$ obtained from wavelet analysis of the simulations visualised in figures 4.7a and 4.7b.

We now use the local wavelength $\widetilde{\lambda}_{\max}(z,t)$ to quantify the stability of an initial wavelength. We use a domain of length $L_z = 400$ and we concatenate $n = 7$ to 13 repetitions of a single band to produce a pattern with initial wavelength $\lambda(n) \equiv 400/n \approx 57, 50, 44 \ldots 31$.

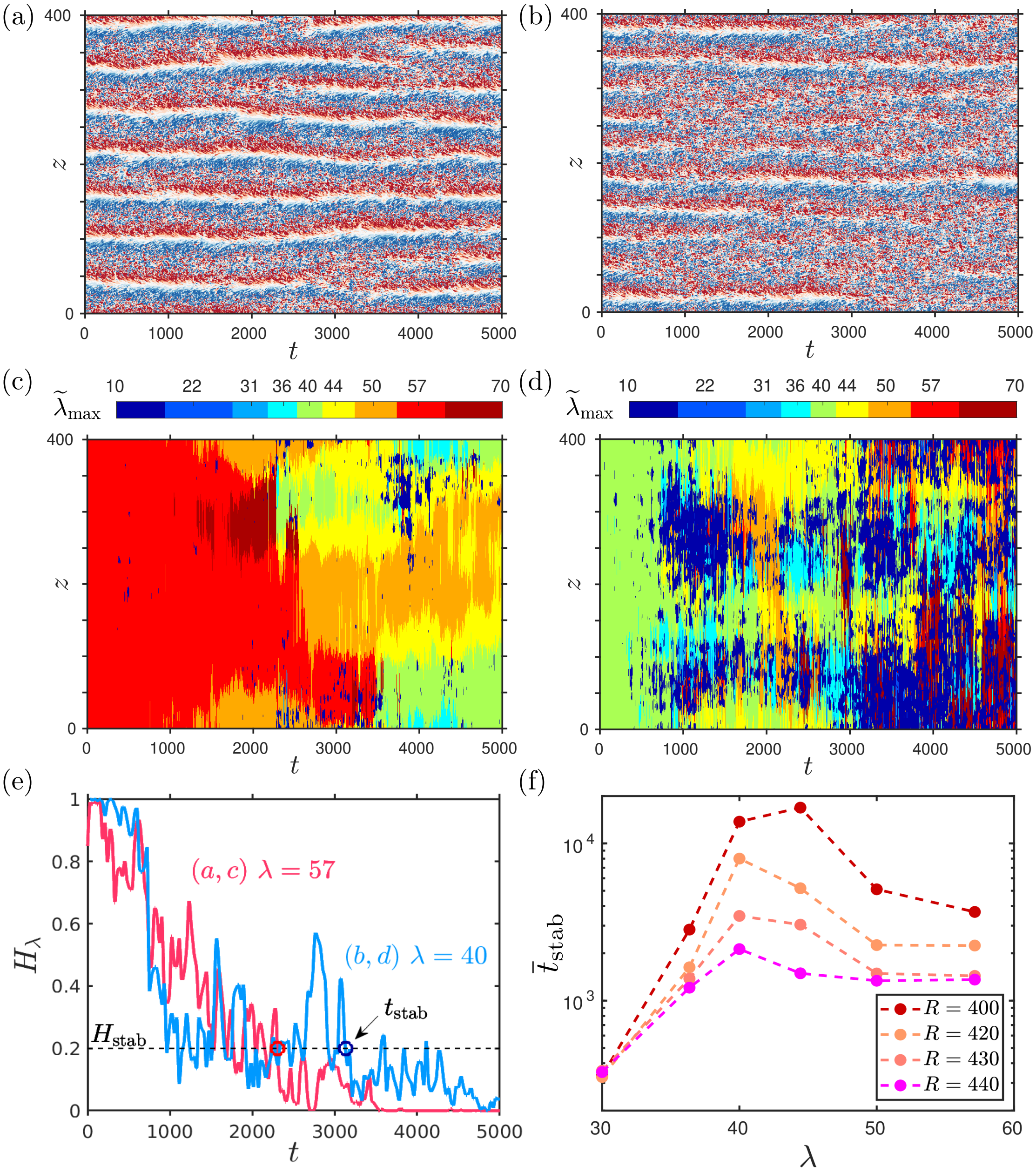

Figure 4.7: Simulation in a Long Slender Box from a noise-perturbed periodic pattern with (a) initial $\lambda = 57$ at $Re = 400$ and (b) initial $\lambda = 40$ at $Re = 430$. Colors show spanwise velocity (red: 0.1, white: 0, blue: -0.1). (c) and (d) show the local dominant wavelength $\widetilde{\lambda}_{\max}(z,t)$ determined by wavelet analysis (see Appendix 4.A) corresponding to the simulations shown in (a) and (b). Color at $t = 0$ shows the wavelength λ of the initial condition. (e) shows the wavelet-defined $H_\lambda(t)$ defined in (4.12), which quantifies the proportion of the domain which retains initial wavelength λ as a function of time for cases (a) and (b). Circles indicate the times for (a) and (b) after which H_λ is below the threshold value H_{stab} for a sufficiently long time. (f) Ensemble-averaged $\bar{t}_{\text{stab}}$ of the decay time of an imposed pattern of wavelength λ for various values of Re. The relative stability of a wavelength, whether localised or not, is measured by $\bar{t}_{\text{stab}}$ via the wavelet analysis.

(We have rounded λ to the nearest integer value here and in what follows.) After adding low-amplitude noise, we run a simulation lasting 5000 time units, compute the wavelet transform and calculate from it the local wavelengths $\widetilde{\lambda}_{\max}(z,t)$. We then compute

$$H_\lambda(t) = \left\langle \frac{1}{L_z} \int_0^{L_z} \Theta\left(\epsilon_\lambda - |\lambda - \widetilde{\lambda}_{\max}(z,t)|\right) \,\mathrm{d}z \right\rangle_{t_a} . \tag{4.12}$$

The short-time average $\langle\cdot\rangle_{t_a}$ is taken over time $t_a = 30$ as before. Θ is the Heaviside function and ϵ_λ is a threshold which selects z-values such that $\widetilde{\lambda}_{\max}$ is closer to $\lambda(n)$ than to its two neighboring values $\lambda(n+1)$ and $\lambda(n-1)$. Thus, H_λ represents the proportion of L_z in which we consider the dominant mode $\widetilde{\lambda}_{\max}$ to be λ. In practice, because patterns in a Long Slender Box still fluctuate in width, a steady pattern may have H_λ somewhat less than 1. If $H_\lambda \ll 1$, a pattern of wavelength λ is present in only a very small part of the flow.

Figure 4.7e shows how wavelet analysis via the Heaviside-like function $H_\lambda(t)$ quantifies the relative stability of the pattern in the examples shown in figures 4.7a and 4.7b. The flow in figure 4.7a at $Re = 400$ begins with $\lambda = 57$, i.e. 7 bands. The red curve in figure 4.7e shows H_λ decaying quickly and roughly monotonically. One additional gap appears at around $t = 2300$ and starting from then, H_λ remains low. This corresponds to the initial wavelength $\lambda = 57$ losing its dominance to $\lambda = 40$, 44 and 50 in the visualisation of $\widetilde{\lambda}_{\max}(z,t)$ in figure 4.7c. By $t = 5000$, the flow shows 9 bands with a local wavenumber λ between 40 and 44.

The flow in figure 4.7b at $Re = 430$ begins with $\lambda = 40$, i.e. 10 bands. The blue curve in figure 4.7e representing H_λ initially decreases and drops fairly suddenly around $t \approx 1000$ as several gaps disappear in figure 4.7b. H_λ then fluctuates around a finite value, which is correlated to the presence of gaps whose local wavelength is the same as the initial λ, visible as zones where $\widetilde{\lambda}_{\max} = 40$ in figure 4.7d. The rest of the flow can be mostly seen as locally featureless turbulence, where the dominant wavelength is small ($\widetilde{\lambda}_{\max} \leq 10$). The local patterns fluctuate in width and strength, and H_λ evolves correspondingly after $t = 1000$. The final state reached in figure 4.7a at $Re = 430$ is characterised by the presence of intermittent local gaps.

The lifetime of an initially imposed pattern wavelength λ is denoted t_{stab} and is defined as follows: We first define a threshold $H_{\mathrm{stab}} \equiv 0.2$ (marked by a horizontal dashed line on figure 4.7e). If $H_\lambda(t)$ is statistically below H_{stab}, the imposed pattern will be considered as unstable. Following this principle, t_{stab} is defined as the first time H_λ is below H_{stab}, with two further conditions to dampen the effect of short-term fluctuations. First, $H_\lambda(t)$ must be below H_{stab} for a period of $\Delta t_1 = 100$ after t_{stab}. This avoids selecting a local minimum of little importance. Second, t_{stab} must obey $\langle H_\lambda(t)\rangle_{t\in[t_{\mathrm{stab}},\, t_{\mathrm{stab}}+\Delta T_2]} < H_{\mathrm{stab}}$, with $\Delta t_2 = 2000$, so as to ensure that the final state is on average below H_{stab}. The corresponding times in case (a) and (b) are marked respectively by a red and a blue circle in figure 4.7e.

Repeating this experiment over multiple realisations of the initial pattern (i.e. different noise realisations) yields an ensemble-averaged $\bar{t}_{\text{stab}}$. This procedure estimates the time for an initially regular and dominant wavelength to disappear from the flow domain, regardless of the way in which it does so and of the final state approached. Figure 4.7f presents the dependence of $\bar{t}_{\text{stab}}$ on λ for different values of Re. We note that a most-stable wavelength emerges from the uniform state, at around $\lambda \simeq 40$ at $Re = 440$, similarly to the results from the *existence* study on figure 4.6d, which showed a preferred wavelength of around 42 at $Re = 440$. Consistently with what was observed in Minimal Band Units of different sizes, the most stable wavelength grows with decreasing Re.

4.4.3 Discussion

Our study of the *existence* and *stability* of large-scale modulations of the turbulent flow is summarised in figure 4.8. This figure resembles the existence and stability diagrams presented for usual (non-turbulent) hydrodynamic instabilities such as Rayleigh-Bénard convection and Taylor-Couette flow (Busse, 1981; Ahlers *et al.*, 1986; Cross & Greenside, 2009). In classic systems, instabilities appear with increasing control parameter, while here gaps and bands emerge from uniform turbulent flow as Re is lowered. Therefore, we plot the vertical axis in figure 4.8 with decreasing upwards Reynolds.

We recall that the existence study of §4.4.1 culminated in the measurement of $\gamma_{\text{pat}}(\lambda, Re)$, the fraction of simulation time that is spent in a patterned state, plotted in figure 4.6d. The parameter values at which $\gamma_{\text{pat}}(\lambda, Re) = 0.45$ (an arbitrary threshold that covers most of our data range) are shown as black circles in figure 4.8. The dashed curve is an interpolation of the iso-γ_{pat} points and separates two regions, with patterns more likely to exist above the curve than below. The minimum of this curve is estimated to be $\lambda \simeq 42$. This is a preferred wavelength at which patterns first statistically emerge as Re is decreased from large values.

The final result of the stability study in section §4.4.2, shown in figure 4.7f, was $\bar{t}_{\text{stab}}(Re, \lambda)$, a typical duration over which a pattern initialised with wavelength λ would persist. The colours in figure 4.8 show $\bar{t}_{\text{stab}}$. This region also has its minimum at $\lambda \approx 42$. The pattern existence and stability zones are similar in shape and in their lack of symmetry with respect to line $\lambda = 42$. The transition seen in figures 4.7a and 4.7c from $\lambda = 57$ to $\lambda = 44$ at $Re = 400$ corresponds to motion from a light blue to a dark blue area in the top row of figure 4.8. This change in pattern wavelength resembles the Eckhaus instability which, in classic hydrodynamics, leads to transitions from unstable wavelengths outside a stability band, to stable wavelengths inside.

An important result of this section is that wavelength 40–44 is preferred, however weakly, up to $Re = 460$, a regime in which no steady patterns are found (see Section 4.3). The presence of a most-probable wavelength confirms the initial results of Prigent *et al.* (2003) and those of Rolland & Manneville (2011). This is also consistent with the

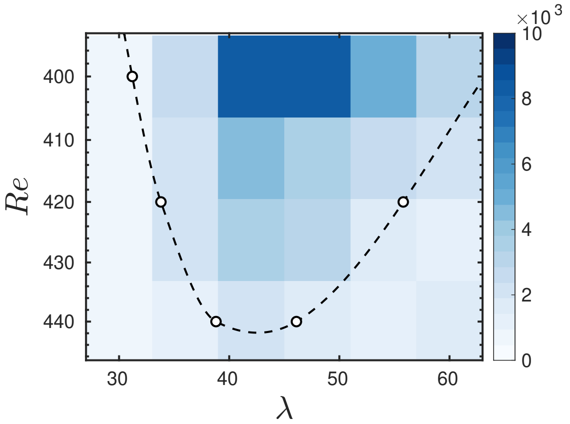

Figure 4.8: Visualisation of the pattern selection in the phase space (λ, Re): black circles are points $\gamma_{\text{pat}}(\lambda, Re) = 0.45$, and colors show the stability times $\bar{t}_{\text{stab}}$. The dashed line is an illustrative interpolation over the data points (black circles).

instability study of Kashyap *et al.* (2022) in plane Poiseuille flow. However, contrary to classic pattern-forming instabilities, the turbulent-laminar pattern does not emerge from an exactly uniform state, but instead from a state in which local gaps are intermittent, as established in Section 4.3. In Section 4.5, we will emphasise the importance of the mean flow in the wavelength selection that we just described.

4.5 Optimisation of the mean flow

This section is devoted to the dependence of various energetic features of the patterned flow on the domain length L_z of a Minimal Band Unit. We fix the Reynolds number at $Re = 400$. In the existence study of §4.4, the wavelength $\lambda \simeq 44$ was found to be selected by patterns. (Recall the upper-most curves corresponding to $Re = 400$ in figure 4.6d.) We will show that this wavelength also extremises quantities in the energy balances of the flow.

4.5.1 Average energies in the patterned state

We first decompose the flow into a mean and fluctuations, $\boldsymbol{u} = \overline{\boldsymbol{u}} + \boldsymbol{u}'$, where the mean is taken over the homogeneous directions x and t. We compute energies of the total flow $\langle E \rangle \equiv \langle \boldsymbol{u} \cdot \boldsymbol{u} \rangle /2$ and of the fluctuations (turbulent kinetic energy) $\langle K \rangle \equiv \langle \boldsymbol{u}' \cdot \boldsymbol{u}' \rangle /2$, where $\langle \cdot \rangle$ is the (x, y, z) average. Figure 4.9a shows these quantities as a function of L_z for the patterned state at $Re = 400$. At $L_z = 44$, $\langle E \rangle$ is maximal and $\langle K \rangle$ is minimal. As a consequence, the mean-flow energy $\frac{1}{2} \langle \overline{\boldsymbol{u}} \cdot \overline{\boldsymbol{u}} \rangle = \langle E \rangle - \langle K \rangle$ is also maximal at $L_z = 44$.

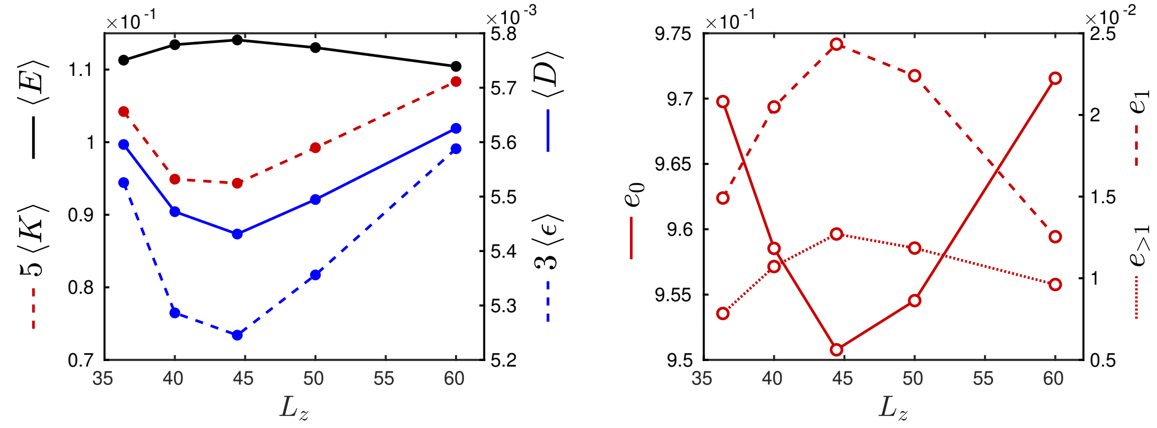

(a) **(b)**

Figure 4.9: Energy analysis for the patterned state at $Re = 400$ as a function of the size L_z of a Miniaml Band Unit. (a) Spatially-averaged total energy $\langle E \rangle$, mean TKE $\langle K \rangle$ ($\times 5$), mean total dissipation $\langle D \rangle$, mean kinetic dissipation $\langle \epsilon \rangle$ ($\times 3$), for the patterned state at $Re = 400$ as a function of L_z. (b) Energy in each of the z-Fourier components of the mean flow (equations (4.13) and (4.14)).

Figure 4.9a additionally shows average dissipation of the total flow $\langle D \rangle \equiv \left\langle |\nabla \times \boldsymbol{u}|^2 \right\rangle / Re$ and average dissipation of turbulent kinetic energy $\langle \epsilon \rangle \equiv \left\langle |\nabla \times \boldsymbol{u}'|^2 \right\rangle / Re$, both of which are minimal at $L_z = 44$.

The mean flow is further analysed by computing the energy of each spectral component of the mean flow. For this, the x and t averaged flow $\overline{\boldsymbol{u}}$ is decomposed into Fourier modes in z:

$$\overline{\boldsymbol{u}}(y,z) = \overline{\boldsymbol{u}}_0(y) + 2\mathcal{R}\left(\overline{\boldsymbol{u}}_1(y) e^{i2\pi z/L_z}\right) + \overline{\boldsymbol{u}}_{>1}(y,z) \tag{4.13}$$

where $\overline{\boldsymbol{u}}_0$ is the uniform component of the mean flow, $\overline{\boldsymbol{u}}_1$ is the trigonometric Fourier coefficient corresponding to $k_z = 2\pi/L_z$ and $\overline{\boldsymbol{u}}_{>1}$ is the remainder of the decomposition, for $k_z > 2\pi/L_z$. (We have omitted the hats on the z Fourier components of $\overline{\boldsymbol{u}}$.) The energies of the spectral components relative to the total mean energy are

$$e_0 = \frac{\langle \overline{\boldsymbol{u}}_0 \cdot \overline{\boldsymbol{u}}_0 \rangle}{\langle \overline{\boldsymbol{u}} \cdot \overline{\boldsymbol{u}} \rangle}, \quad e_1 = \frac{\langle \overline{\boldsymbol{u}}_1 \cdot \overline{\boldsymbol{u}}_1 \rangle}{\langle \overline{\boldsymbol{u}} \cdot \overline{\boldsymbol{u}} \rangle}, \quad e_{>1} = \frac{\langle \overline{\boldsymbol{u}}_{>1} \cdot \overline{\boldsymbol{u}}_{>1} \rangle}{\langle \overline{\boldsymbol{u}} \cdot \overline{\boldsymbol{u}} \rangle} \tag{4.14}$$

These are presented in figure 4.9b. It can be seen that $e_0 \gg e_1 > e_{>1}$ and also that all have an extremum at $L_z = 44$. In particular, $L_z = 44$ minimizes e_0 ($e_0 = 0.95$) while maximizing the trigonometric component ($e_1 = 0.025$) along with the remaining components ($e_{>1} \simeq 0.011$). Note that for a banded state at $Re = 350$, $L_z = 40$, Barkley & Tuckerman (2007) found that $e_0 \approx 0.70$, $e_1 \approx 0.30$ and $e_{>1} \approx 0.004$, consistent with a strengthening of the bands as Re is decreased.

4.5.2 Mean flow spectral balance

We now investigate the spectral contributions to the budget of the mean flow $\overline{\boldsymbol{u}}$, dominated by the mean flow's two main spectral components $\overline{\boldsymbol{u}}_0$ and $\overline{\boldsymbol{u}}_1$. The balances can be expressed as (**?**, Part 1):

$$\widehat{\overline{A}}_0 - \widehat{\overline{\Pi}}_0 - \widehat{\overline{D}}_0 + I = 0 \text{ for } \overline{\boldsymbol{u}}_0 \quad \text{and} \quad \widehat{\overline{A}}_1 - \widehat{\overline{\Pi}}_1 - \widehat{\overline{D}}_1 = 0 \text{ for } \overline{\boldsymbol{u}}_1 \tag{4.15}$$

where I is the rate of energy injection by the viscous shear, and $\widehat{\overline{\Pi}}_0$, $\widehat{\overline{D}}_0$ and $\widehat{\overline{A}}_0$ stand for, respectively, production, dissipation and advection (i.e. non-linear interaction) contributions to the energy balance of mode $\overline{\boldsymbol{u}}_0$ and similarly for $\overline{\boldsymbol{u}}_1$. These are defined by

$$I = \frac{2}{Re}\mathcal{R}\left\{\int_{-1}^{1} \frac{\partial}{\partial y}\left(\widehat{\overline{u}}_j^*(k_z=0)\widehat{\overline{s}}_{yj}(k_z=0)\right)\,\mathrm{d}y\right\} = \frac{1}{Re}\left(\left.\frac{\partial \overline{u}_{\text{strm}}}{\partial y}\right|_{1} + \left.\frac{\partial \overline{u}_{\text{strm}}}{\partial y}\right|_{-1}\right) \tag{4.16a}$$

$$\widehat{\overline{\Pi}}_0 = \mathcal{R}\left\{\int_{-1}^{1} \frac{\partial \widehat{\overline{u}}_j^*}{\partial x_i}(k_z=0)\ \widehat{\overline{u_i' u_j'}}(k_z=0)\ \mathrm{d}y\right\} \tag{4.16b}$$

$$\widehat{\overline{D}}_0 = \frac{2}{Re}\mathcal{R}\left\{\int_{-1}^{1} \widehat{\overline{s}}_{ij}(k_z=0)\ \widehat{\overline{s}}_{ij}^*(k_z=0)\ \mathrm{d}y\right\} \tag{4.16c}$$

$$\widehat{\overline{A}}_0 = -\mathcal{R}\left\{\int_{-1}^{1} \widehat{\overline{u}}_j^*(k_z=0)\ \widehat{\overline{u}_i\frac{\partial \overline{u}_j}{\partial x_i}}(k_z=0)\ \mathrm{d}y\right\} \tag{4.16d}$$

where $\mathcal{R}$ denotes the real part. We define $\widehat{\overline{\Pi}}_1$, $\widehat{\overline{D}}_1$ and $\widehat{\overline{A}}_1$ similarly by replacing $k_z = 0$ by $k_z = 2\pi/L_z$ in (4.16a)-(4.16d).

We recall two main results from chapter 3: first, $\widehat{\overline{A}}_1 \approx -\widehat{\overline{A}}_0$. This term represents the energetic transfer between modes $\overline{\boldsymbol{u}}_0$ and $\overline{\boldsymbol{u}}_1$ via the self-advection of the mean flow (the energetic spectral influx from $(\overline{\boldsymbol{u}}\cdot\nabla)\overline{\boldsymbol{u}}$). Second, $\widehat{\overline{\Pi}}_1 < 0$, and this term approximately balances the negative part of TKE production. This is a feedback from turbulent fluctuations to the component $\overline{\boldsymbol{u}}_1$ of the mean flow.

Each term contributing to the balance of $\overline{\boldsymbol{u}}_0$ and $\overline{\boldsymbol{u}}_1$ is shown as a function of L_z in figures 4.10a and 4.10b. We do not show $\widehat{\overline{A}}_0$ because $\widehat{\overline{A}}_0 \approx -\widehat{\overline{A}}_1$.

We obtain the following results:

(1) Production $\widehat{\overline{\Pi}}_0$, dissipation $\widehat{\overline{D}}_0$ and energy injection I are nearly independent of L_z, varing by no more than 6% over the range shown. These $k_z = 0$ quantities

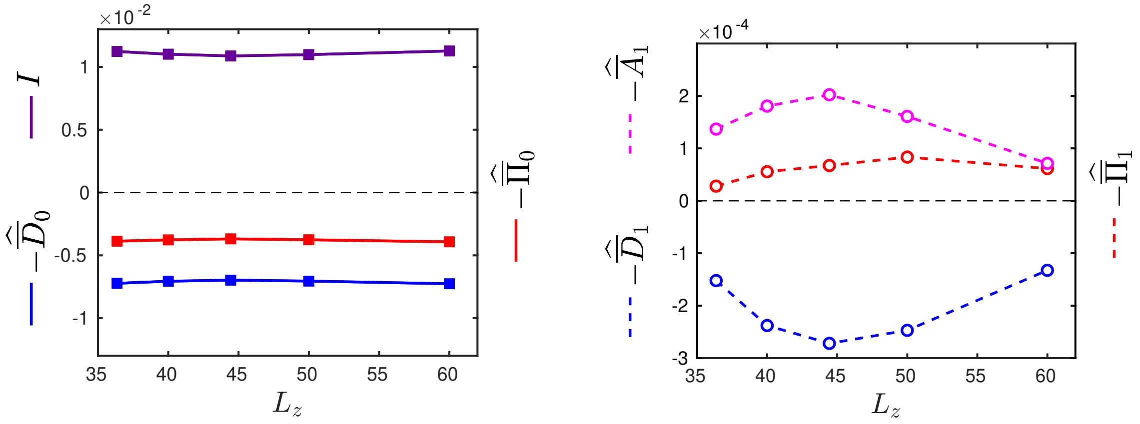

(a) **(b)**

Figure 4.10: Spectral energy balance of the mean flow components (a) $\overline{\boldsymbol{u}}_0$ and (b) $\overline{\boldsymbol{u}}_1$. See equation (4.15).

correspond to uniform fields in z and hence it is unsurprising that they depend very little on L_z.

(2) The non-linear term $\widehat{\overline{A}}_1 \approx -\widehat{\overline{A}}_0$, i.e. the transfer from $\overline{\boldsymbol{u}}_0$ to $\overline{\boldsymbol{u}}_1$ which is the principal source of energy of $\overline{\boldsymbol{u}}_1$, has a maximum at $L_z \simeq 44$. This is the reason for which $\overline{\boldsymbol{u}}_0$ is minimised by $L_z \simeq 44$ (see figure 4.9b): more energy is transferred from $\overline{\boldsymbol{u}}_0$ to $\overline{\boldsymbol{u}}_1$.

(3) Production $\widehat{\overline{\Pi}}_1$ increases with L_z and does not show an extremum at $L_z \simeq 44$ (it instead has a weak maximum at $L_z \simeq 50$). In all cases, $\widehat{\overline{\Pi}}_1 < \widehat{\overline{A}}_1$: the TKE feedback on the mean flow, although present, is not dominant and not selective.

(4) Dissipation $\widehat{\overline{D}}_1$ accounts for the remaining budget and its extremum at $L_z \simeq 44$ corresponds to maximal dissipation.

The turbulent kinetic energy balance is also modified with changing L_z. This is presented in Appendix 4.C. The impact of TKE is however secondary, because the feedback on the mean flow, via $\widehat{\overline{\Pi}}_1$, is not the leading term that fuels $\overline{\boldsymbol{u}}_1$, and does not participate in maximising the energy of $\overline{\boldsymbol{u}}_1$ at the preferred wavelength.

4.6 Conclusion and discussion

We have explored the appearance of patterns from uniform turbulence in plane Couette flow at $Re \leq 500$. We used numerical domains of different sizes to quantify the competition between featureless (or uniform) turbulence and (quasi-) laminar gaps. In Minimal Band Units, intermittency reduces to a random alternation between two states: uniform or patterned. In large slender domains, however, gaps nucleate randomly and locally in space, and the transition to patterns takes place continuously via the regimes presented in Section 4.3: the uniform regime in which gaps are rare and short-lived (above $Re \simeq 470$), and another regime ($Re < 470$) in which gaps are more numerous and long-lived. Below $Re \simeq 430$, the large-scale spacing of these gaps starts to dominate the energy spectrum, which is a possible demarcation of the patterned regime. In this latter regime, with further decreasing in Re, gaps eventually fill the entire flow domain, forming regular patterns. The distinction between these regimes is observed in both gap lifetime and friction factor.

Spatially isolated gaps were already observed by Prigent *et al.* (2003), Barkley & Tuckerman (2005) and Rolland & Manneville (2011). (See also Manneville (2015, 2017) and references therein.) Our results confirm that pattern emergence, mediated by randomly-nucleated gaps, is necessarily more complex than the supercritical Ginzburg-Landau framework initially proposed by Prigent *et al.* (2003) and later developed by Rolland & Manneville (2011). However, this does not preclude linear processes in the appearance of patterns, such as those reported by Kashyap *et al.* (2022) from an ensemble-averaged linear response analysis.

The intermittency between uniform turbulence and gaps that we quantify here in the range $380 \lesssim Re \lesssim 500$ is not comparable to that between laminar flow and bands present for $325 \lesssim Re \lesssim 340$. The latter is a continuous phase transition in which the laminar flow is absorbing: laminar regions cannot spontaneously develop into turbulence and can only become turbulent by contamination from neighbouring turbulent flow. This is connected to the existence of a critical point at which the correlation length diverges with a power-law scaling with Re, as characterised by important past studies (Shi *et al.*, 2013; Chantry *et al.*, 2017; Lemoult *et al.*, 2016) which showed a connection to directed percolation. The emergence of gaps from uniform turbulence is of a different nature. Neither uniform turbulence nor gaps are absorbing states, since gaps can always appear spontaneously and can also disappear, returning the flow locally to a turbulent state. While the lifetimes of quasi-laminar gaps do exhibit an abrupt change in behaviour at $Re = 470$ (figure 4.4c), we observe no evidence of critical phenomena associated with the emergence of quasi-laminar gaps from uniform turbulence. Hence, the change in behaviour appears to be in fact smooth. This is also true in pipe flow where quasi-laminar gaps form, but not patterns (Avila & Hof, 2013; Frishman & Grafke, 2022).

We used the pattern wavelength as a control parameter, via either the domain size or the initial condition, to investigate the existence of a preferred pattern wavelength. We propose that the finite spacing between gaps, visible in both local gaps and patterned regimes, is selected by the preferred size of their associated large-scale flow. Once gaps are sufficiently numerous and patterns are established, their average wavelength increases with decreasing Re, with changes in wavelength in a similar vein to the Eckhaus picture.

The influence of the large-scale flow in wavelength selection is analysed in Section 4.5, where we carried out a spectral analysis like that in chapter 3 for various sizes of the

Minimal Band Unit. In particular, we investigated the roles of the turbulent fluctuations and of the mean flow, which is in turn decomposed into its uniform component $\overline{\boldsymbol{u}}_0$ and trigonometric component $\overline{\boldsymbol{u}}_1$, associated to the large-scale flow along the laminar-turbulent interface. Our results demonstrate a maximisation of the energy of $\overline{\boldsymbol{u}}_1$ by the wavelength naturally preferred by the flow, and this is primarily associated to the advective term $(\overline{\boldsymbol{u}} \cdot \nabla)\overline{\boldsymbol{u}}$ in the mean flow equation. This term redistributes energy between modes $\overline{\boldsymbol{u}}_0$ and $\overline{\boldsymbol{u}}_1$ and is mostly responsible for energising the large-scale along-band flow. Turbulent fluctuations are of secondary importance in driving the large-scale flow and do not play a significant role in the wavelength selection.

This result resonates with certain optimality principles underpinning classical pattern formation and for which Rayleigh-Bénard convection are a canonical example: **?** and Busse (1981) (and references therein) proposed a principle of maximal heat transport, or equivalently maximal dissipation, obeyed by convective turbulent solutions. The maximal dissipation principle, as formulated by Malkus (1956) in shear flows, occurs in other systems such as von Kármán flow (Ozawa *et al.*, 2001; Mihelich *et al.*, 2017). (This principle has been somewhat controversial. Disputed by Reynolds & Tiederman (1967) within the context of stability theory, it was recently revisited with statistical closures by Markeviciute & Kerswell (2022)). In our case, the flow maximises the transport of momentum and the dissipation of the large-scale flow, analogous to the principles mentioned by Malkus (1956) and Busse (1981). Explaining this mere observation from a guiding principle remains a tremendous challenge.

It is essential to understand the creation of the large-scale flow around a randomly emerging laminar hole. The statistics obtained in our tilted configuration must be extended to large streamwise-spanwise domains, in which short-lived and randomly-nucleated holes might align in the streamwise direction (Manneville, 2017, Fig. 5), presumably before the regime of long-lived gaps is attained. Furthermore, a more complete dynamical picture of gap creation is needed. The excitable model of **?** might provide a proper framework, as it accounts for both the emergence of anti-puffs (Frishman & Grafke, 2022) and of periodic solutions (**?**). Connecting this model to the Navier-Stokes equations is, however, a formidable challenge. Our work emphasises the necessity of including the effects of the advective large-scale flow to adapt this model to the establishment of the laminar-turbulent patterns observed in planar shear flows.

4.A Wavelet transform

We introduce the one-dimensional continuous wavelet transform of the velocity $\boldsymbol{u}(z,t)$ taken along the line $(x,y) = (L_x/2, 0)$:

$$\tilde{\boldsymbol{u}}(z,r,t) = C_\psi^{-1/2} r^{-1/2} \int_0^{L_z} \psi^* \left(\frac{z'-z}{r}\right) \boldsymbol{u}(z',t) dz' \qquad (4.17)$$

Here ψ is the Morlet basis function, defined in Fourier space as $\hat{\psi}(k) = \pi^{-1/4}e^{-(k-k_\psi)^2/2}$ for $k > 0$. Its central wavenumber is $k_\psi = 6/\Delta z$, where Δz is the grid spacing. The scale factor r is related to wavelength via $\lambda \simeq 2\pi r/k_\psi$. $C_\psi \equiv \int |k|^{-1}|\hat{\psi}(k)|^2 \mathrm{d}k$ is a normalization constant. Tildes are used to designate wavelet transformed quantities. The inverse transform is:

$$\boldsymbol{u}(z,t) = C_\psi^{-1/2}\int_0^\infty \int_{-\infty}^\infty r^{-1/2}\psi\left(\frac{z-z'}{r}\right)\tilde{\boldsymbol{u}}(z',r,t)\,\frac{dz'\,dr}{r^2} \tag{4.18}$$

The wavelet transform is related to the Fourier transform in z by:

$$\tilde{\boldsymbol{u}}(z,r,t) = \frac{1}{2\pi}C_\psi^{-1/2}r^{1/2}\int_{-\infty}^\infty \widehat{\psi}(r\,k_z)\widehat{\boldsymbol{u}}(k_z,t)e^{ik_z z}\mathrm{d}k_z \tag{4.19}$$

We then define the most energetic instantaneous wavelength as:

$$\widetilde{\lambda}_{\max}(z,t) = \frac{2\pi}{k_\psi}\,\underset{r}{\operatorname{argmax}}\,|\tilde{\boldsymbol{u}}(z,r,t)|^2 \tag{4.20}$$

The characteristic evolution of $\widetilde{\lambda}_{\max}(z,t)$ is illustrated in figure 4.11b for the flow case corresponding to figure 4.11a. Regions in which $\widetilde{\lambda}_{\max}$ is large (> 10) and dominated by a single value correspond to the local patterns observed in figure 4.11a. In contrast, in regions where $\widetilde{\lambda}_{\max}$ is small (< 10) and fluctuating, the turbulence is locally uniform.

This space-time intermittency of the patterns is quantified by measuring

$$f_{L/S} = \left\langle \Theta(\widetilde{\lambda}_{\max}(z,t) - 10)\right\rangle_{z,t} \tag{4.21}$$

and is shown in figure 4.12 as a function of Re.

4.B Laminar and turbulent distributions in pipe vs Couette flows.

From figures 4.3c and 4.3d of the main text, both distributions of laminar or turbulent lengths, L_{lam} and L_{turb}, are exponential for large enough lengths, similarly to pipe (Avila & Hof, 2013). It is however striking that the distributions of L_{lam} and L_{turb} have different shapes for L_{lam} or $L_{\text{turb}} > 10$ in plane Couette flow: L_{lam} shows a sharper distribution, whereas L_{turb} is more broadly distributed. We present on figures 4.13a and 4.13b the cumulative distributions of L_{lam} and L_{turb} for a complementary analysis.

We focus on the characteristic length l^*_{turb} or l^*_{lam} for which $P(L_{\text{lam}} > l^*_{\text{lam}}) = P(L_{\text{turb}} > l^*_{\text{turb}}) = 10^{-2}$: for example, $l^*_{\text{lam}} = 15.5$ and $l^*_{\text{turb}} = 26.5$ at $Re = 440$; $l^*_{\text{lam}} = 23.4$ and $l^*_{\text{turb}} = 30.3$ at $Re = 400$. We see that l^*_{turb} and l^*_{lam} are of the same order of magnitude. This differs from the same measurement in pipe flow, carried out by Avila & Hof (2013, Fig. 2): $l^*_{\text{lam}} = 6$ and $l^*_{\text{turb}} \simeq 50$ at $Re = 2800$; $l^*_{\text{lam}} \simeq 17$ and $l^*_{\text{turb}} \simeq 160$ at $Re = 2500$ (as

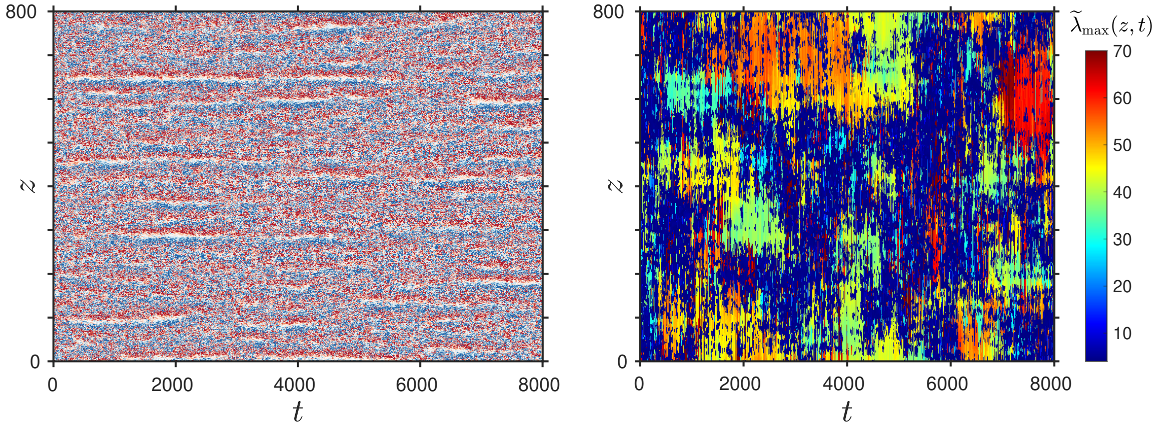

(a) **(b)**

Figure 4.11: Space-time visualisation of a quench experiment at $Re = 430$: (a) spanwise velocity (blue: -0.2, white: 0, red: 0.2), (b) $\widetilde{\lambda}_{\max}(z,t)$ defined by (4.20). $\widetilde{\lambda}_{\max}(z,t)$ (b) quantifies the presence of local large-scale modulations within the flow. Dark blue zones where $\widetilde{\lambda}_{\max}(z,t) < 10$ correspond to locally featureless turbulence in (a). Large-scale modulation of gaps at different wavelengths are visible by the green-to-red spots in (b).

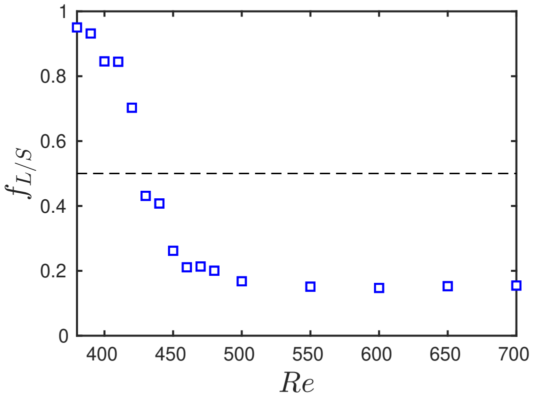

Figure 4.12: Space-time fraction of large to small wavelengths obtained by wavelet transform. $f_{L/S}$ crosses 0.5 at $Re \simeq 427 \simeq$.

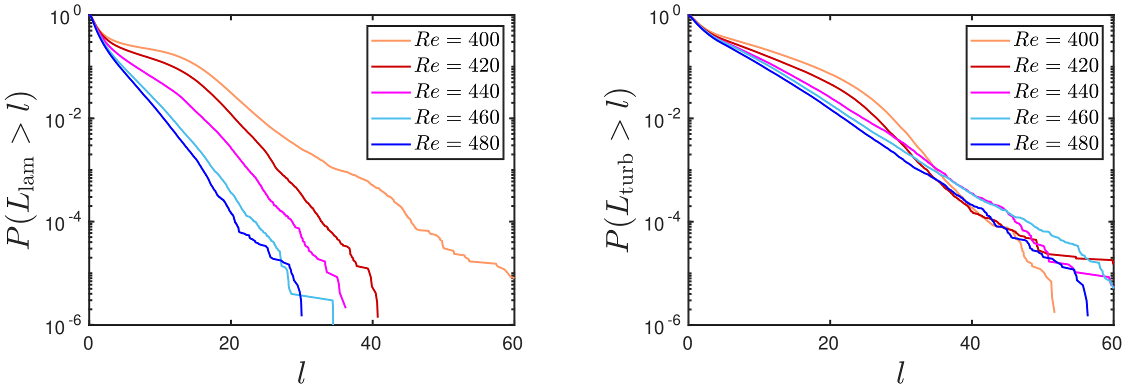

(a) **(b)**

Figure 4.13: Cumulative distribution of (a) laminar gaps and (b) turbulent zones, for various *Re*.

extracted from their figure 2.). This confirms that turbulent and laminar spacings are of the same order of magnitude in plane Couette flow, contrary to pipe flow.

4.C Turbulent kinetic energy balance for various L_z

In this appendix, we address the balance of turbulent kinetic energy $\widehat{K}(k_z)$, written here in a y-integrated form at a specific mode k_z (see equation (5.3) of chapter 3 and the methodology in, e.g., Bolotnov *et al.* (2010); Lee & Moser (2015); Mizuno (2016); Cho *et al.* (2018)):

$$0 = \widehat{\Pi} - \widehat{D} + \widehat{A} + \widehat{T}_{nl} \tag{4.22}$$

where the variables in (4.22) indicate y-integrated quantities:

$$\widehat{\Pi}(k_z) \equiv -\mathcal{R}\left\{\int_{-1}^{1} \overline{\widehat{u'_j}^{*}\,\widehat{\overline{u}_i \frac{\partial u'_j}{\partial x_i}}}\ \mathrm{d}y\right\}, \qquad \widehat{D}(k_z) \equiv \frac{2}{Re}\int_{-1}^{1} \overline{\widehat{s'_{ij}}\,\widehat{s'_{ij}}^{*}}\ \mathrm{d}y,$$

$$\widehat{T}_{nl}(k_z) \equiv -\mathcal{R}\left\{\int_{-1}^{1} \overline{\widehat{u'_j}^{*}\,\widehat{u'_i \frac{\partial u'_j}{\partial x_i}}}\ \mathrm{d}y\right\}, \qquad \widehat{A}(k_z) \equiv -\mathcal{R}\left\{\int_{-1}^{1} \overline{\widehat{u'_j}^{*}\,\widehat{\overline{u}_i \frac{\partial u'_j}{\partial x_i}}}\ \mathrm{d}y\right\} \tag{4.23}$$

respectively standing for production, dissipation, triadic interaction and advection terms. We recall that $\overline{(\cdot)}$ is an average in (x, t). The y evolution of the energy balance was analysed in chapter 3.

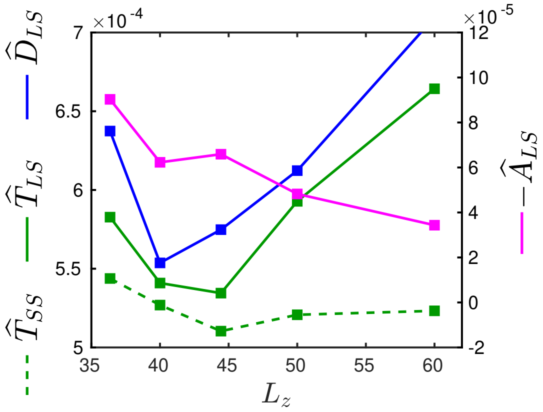

Figure 4.14: Evolution of the large-scale TKE balance with L_z (4.24).

Chapter 3 reported robust negative production at large scales, along with inverse non-linear transfers to large scales. If $k_{\text{rolls}} = 1.41$ denotes the scale of rolls and streaks, this inverse transfer occurs for $k_z < k_{LS} = 0.94$, while a downward transfer occurs for $k_z >= 3.6$ (We refer the reader to the figure 5 of chapter 3). This spectral organization of the energy balance will be quantified by the following transfer terms arising from (4.23):

$$\widehat{T}_{LS} = \sum_{k_z=0}^{k_{LS}} \widehat{T}_{nl}(k_z), \quad \widehat{T}_{SS} = \sum_{k_z=}^{\infty} \widehat{T}_{nl}(k_z), \quad \widehat{D}_{LS} = \sum_{k_z=0}^{k_{LS}} \widehat{D}(k_z), \quad \widehat{A}_{LS} \equiv \sum_{k_z=0}^{k_{LS}} \widehat{A}(k_z) \tag{4.24}$$

$\widehat{T}_{LS}$ quantifies transfer to large scales, $\widehat{T}_{SS}$ the transfer to small scales, $\widehat{D}_{LS}$ the dissipation at large scales, and $\widehat{A}_{LS}$ is a transfer of energy from the mean flow to the large fluctuating scales.

The variables defined in (4.24) are displayed in figure 4.14 as function of L_z. $\widehat{T}_{LS}$ is minimal at $L_z \simeq 44$. $\widehat{D}_{LS}$ is minimal at $L_z \simeq 40$. Contrary to $\widehat{T}_{LS}$, $\widehat{T}_{SS}$ is relatively constant with L_z (green dashed line in figure 4.14), with a variation of around 6%. This demonstrates that transfers to small scales are unchanged with L_z. Large-scale advection decays with increasing L_z and does not play a role in the wavelength preference. Our results confirm that the balance at large-scale is minimised around $L_z \simeq 44$, and that TKE will play a less important role, compared to that of the mean flow whose energy and balance are maximised at $L_z \simeq 44$.

Chapter 5

Transition to turbulence without large-scale flow

In chapters 3 and 4, our focus was on the interconnection between mean flow and pattern emergence in transitional plane shear flows. A large-scale circulation is established as laminar gaps are nucleated out of a uniform turbulent environment. These gaps organise into patterns with a robust preferred wavelength, mode. We linked this non-linear mean flow self-interaction to a principle of maximal dissipation, underpinning wavelength selection. In this chapter, we adopt a different numerical approach to understanding the effect of large-scale circulation on the problem of transition to turbulence.

5.1 Introduction

Landau (1944) pictured the laminar-turbulent transition in shear flows as a first-order transition, driven by the competition of two attractors (a laminar and a turbulent attractor). Later on, Pomeau (1986) connected these two attractors by introducing the notion of moving fronts, by which one phase expands into the other. Pomeau envisioned this process as a second-order phase transition belonging to the universality class of Directed Percolation (Grassberger, 1981; Janssen, 1981), and therefore corrected the initial vision of Landau. This class of phase transition occurs in systems with short-range interactions, between a fluctuating phase and an absorbing phase.

Important experimental surveys confirmed Pomeau's vision in the case of plane Couette flow (Lemoult *et al.*, 2016; Chantry *et al.*, 2017; Klotz *et al.*, 2022). The universal scaling of Directed Percolation is valid in many other wall-bounded flows (Takeda *et al.*, 2020), although deviations can be found in plane channel flow (Shimizu & Manneville, 2019). Apart from wall-bounded flows, Directed Percolation was also validated in the onset of turbulence in linearly-damped 2D Kolmogorov flow (Hiruta & Toh, 2020). Despite its success in describing the universal statistical properties of the spatio-temporal intermittency found in these shear flows, this perspective ignores the details of the turbulent structures, which themselves remain to be fully understood.

Localised turbulent structures in planar shear flows emerge as oblique patterns (Prigent *et al.*, 2003; Barkley & Tuckerman, 2007). When these patterns first appear out of uniform turbulence, their angle is distributed around a specific value of around ±25° in Couette and Poiseuille flows (Duguet *et al.*, 2010; Kashyap *et al.*, 2020*b*). These patterns are marked by robust large-scale circulation going along the laminar-turbulence interface (Coles & van Atta, 1966; Barkley & Tuckerman, 2007; Klotz *et al.*, 2021), which has therefore strong streamwise and spanwise components, along with a coupled circulation bubble in the streamwise/cross-flow plane. It is known that coexisting laminar and turbulent phases automatically induce modulations in the streamwise velocity (Barkley, 2016), but the large-scale circulation found in shear flows is not fully understood. This large-scale flow has an strong advective nature, as was pointed out in previous chapters. When turbulent spots are localised in space, this advective nature has a role in spreading spots throughout the entire flow domain. This was experimentally assessed by Couliou & Monchaux (2016, 2017), who found that the growth due to large-scale advection was comparable to that due to nucleation of streaks.

No laminar-turbulent patterns are present in the case of pipe flow. Nor is there any large-scale circulation like the one observed in previously-mentioned shear flows. In pipe flow, transitional turbulence takes the form of streamwise-localised puffs. The mean flow around a puff is restricted to circulations in the streamwise and wall-normal components, whose shape is toroidal (Wygnanski & Champagne, 1973; Shan *et al.*, 1999; van Doorne & Westerweel, 2009). Recent studies aimed at connecting the two opposite cases of pipe and plane shear flows, with the help of annular pipe or annular Couette flows at different aspect ratios (Ishida *et al.*, 2016, 2017; Kunii *et al.*, 2019; Takeda *et al.*, 2020; Matsukawa & Tsukahara, 2022). These studies discovered a new type of structure, mediating puffs and oblique patterns: helical puffs. Furthermore, by artificially increasing the azimuthal extent of their simulation domain for values larger than 2π, Takeda *et al.* (2020) managed to sustain structures of very small spatial extent, similar to puffs. These puff-like structures were isolated in both streamwise and azimuthal directions and without showing any sign of obliqueness. This experiment gives significant insights on the impact of symmetries and mean flow components on the presence of sustained localised turbulence in the transitional regime. It suggests that a puff does not need periodicity in the azimuthal direction to be sustained.

One different kind of challenge is to design control strategies so as to delay or modify the nature of the transition. Among these strategies, we mention the control of the bluntness of the shear profile (Kühnen *et al.*, 2018; Marensi *et al.*, 2020), the injection of perturbations at specific locations in the flow (Hof *et al.*, 2010), or the introduction of large-scale spanwise oscillations in the flow (Quadrio & Sibilla, 2000). These strategies are important from both practical and theoretical point of views, as they aim at suppressing turbulence and can unravel the fundamental ingredients leading to this suppression.

These various perspectives motivate us to envision another kind of experiment, aiming at directly controlling the mean flow present in transitional shear turbulence. In a numerical simulation of plane Couette flow, we effectively suppress the large-scale circulation along the laminar-turbulent interfaces. The resulting flow will be referred to as Filtered plane Couette flow. We study how laminar-turbulent interfaces survive this control operation, and confirm the role of the circulation on both the appearance of patterns and the phase transition.

5.2 2C-3D Navier-Stokes equations at large scales.

5.2.1 Formulation

We first consider the traditional Navier-Stokes equations describing the motion of an incompressible viscous fluid within two planes moving at $\pm U_{\text{wall}}$, with no-slip boundary conditions at the wall. (x, y, z) denote the usual streamwise, cross-channel and spanwise coordinates. (Note that this differs from our previous usage throughout this thesis, where (x, z) denoted tilted coordinates. This choice of notation is retricted to this chapter and will simplify the discourse.) We introduce the Fourier transform in (x, z),

$$\hat{\boldsymbol{u}}(k_x, y, k_z) = \frac{1}{L_x L_z} \int_0^{L_x} \int_0^{L_z} \boldsymbol{u}(x, y, z) e^{-i(k_x x + k_z z)} \mathrm{d}x \ \mathrm{d}z. \tag{5.1}$$

and write the 3D Navier-Stokes equations in a Fourier form, with non-dimensionalisation of velocity by U_{wall}, space variables by the plane mid-gap, and time by the advective time:

$$\frac{\partial \widehat{u}_j}{\partial t} + \widehat{\nabla}_j \widehat{p} = -\widehat{N}_j + \frac{1}{Re} \widehat{\nabla}^2 \widehat{u}_j \tag{5.2a}$$

$$\widehat{\nabla} \cdot \hat{\boldsymbol{u}} = 0 \tag{5.2b}$$

where $\widehat{\nabla}_j = (ik_x, \partial_y, ik_z)$, $\widehat{N}_j = \widehat{\frac{\partial u_i u_j}{\partial x_i}}$ and $j = (x, y, z)$ (the summation on the i coordinate is implicit). We now modify the 3D Navier-Stokes equations with introducing a pair of cut-off wavenumbers (K_x, K_z). For $k_x < K_x$ and $k_z < K_z$, we introduce the following 2C-3D Navier-Stokes system for the two components (u_x, u_y):

$$\frac{\partial \widehat{u}_j}{\partial t} + \widehat{\nabla}_j \widehat{p} = -\widehat{N}_j + \frac{1}{Re} \widehat{\nabla}^2 \widehat{u}_j \text{ for } j = x, y \tag{5.3a}$$

$$\widehat{\nabla}_{2D} \cdot \hat{\boldsymbol{u}} = 0 \tag{5.3b}$$

$$\widehat{u}_z = 0 \tag{5.3c}$$

with $\widehat{\nabla}_{2D} = (ik_x, \partial_y, 0)$. The spanwise velocity $\widehat{u}_z$ is imposed at 0 and is not treated as a variable for $(k_x, k_z) < (K_x, K_z)$. This treatment is explained in the following section. For $(k_x, k_z) \geq (K_x, K_z)$, the flow will obey 3D Navier-Stokes equations. In this way, the fundamental mechanisms producing wall-bounded turbulence are still present (and especially the turbulent self-sustaining process (Waleffe, 1997), if K_x and K_z are low enough not to alter the dynamics of streaks and rolls).

5.2.2 Numerical set-up

The numerical resolution of 3D Navier-Stokes equations is carried out on ChannelFlow (Gibson, 2012), which uses a semi-implicit pseudo-spectral method on the primitive variables, decomposed in Fourier-Chebychev modes. We shortly explain the underlying numerical principles, derived from Canuto *et al.* (2007). We denote t the current time-step of an implicit time-stepping algorithm. The non-linear term is handled explicitly by the numerical right-hand-side

$$\widehat{\boldsymbol{R}} = \sum_s \frac{\alpha_s}{dt} \hat{\boldsymbol{u}}(s) - \beta_s \widehat{\boldsymbol{N}}(s), \tag{5.4}$$

with s being sum over previous timesteps. α_s and β_s are coefficients depending on the time-stepping method (We use here an implicit backward differentiation method, but the following procedure can be expanded to other implicit methods). In 3D Navier-Stokes, pressure and cross-channel velocity at time-step t are coupled via the following system, issued from Laplace equation $\nabla^2 p = \nabla \cdot \boldsymbol{R}$:

$$\begin{cases} (\partial_y^2 - k_x^2 - k_z^2)\widehat{p}(t) = ik_x\widehat{R}_x + \partial_y\widehat{R}_y + ik_z\widehat{R}_z \\ (\partial_y^2 - \lambda)\widehat{u}_y(t) = \widehat{R}_y - \partial_y p \end{cases} \text{with } \widehat{u}_y(\pm 1) = \partial_y\widehat{u}_y(\pm 1) = 0 \tag{5.5}$$

with $\lambda = 2/dt + \nu(k_x^2 + k_z^2)$ accounting for the implicit treatment of the Laplace operator. This coupled Helmholtz problem is solved via an influence-matrix method. The two remaining components $\widehat{u}_x, \widehat{u}_z$ are solved by:

$$(\partial_y^2 - \lambda)\widehat{u}_x(t) = \widehat{R}_x - ik_x\widehat{p}, \tag{5.6}$$

$$(\partial_y^2 - \lambda)\widehat{u}_z(t) = \widehat{R}_z - ik_z\widehat{p} \tag{5.7}$$

We now turn to our large-scale 2C-3D problem (5.3). With this numerical set-up, imposing $\widehat{u}_z(k_x, k_z) = 0$ for $(k_x, k_z) < (K_x, K_z)$ at the beginning of each time-step is not sufficient for suppressing spanwise velocity. There is indeed a complication in Fourier space, which comes from the fact that $\widehat{N}_z(k_x, k_z)$ is not meant to cancel if triad interactions act on spanwise velocity at wavenumbers $(k_x, k_z) < (K_x, K_z)$. We need to effectively cancel out this effect on the spanwise evolution equation (5.7). For this, we add to the right-hand side of (5.7) an instantaneous force to compensate the pressure gradient at all time. This defines a new right-hand side

$$\widehat{R}'_z = \widehat{R}_z + F = ik_z\widehat{p} \tag{5.8}$$

and results in a new equation for $\widehat{u}_z$, in place of (5.7)

$$(\partial_y^2 - \lambda)\widehat{u}_z(t) = \widehat{R}'_z - ik_z\widehat{p} = 0 \tag{5.9}$$

which yields $\widehat{u}_z(t) = 0$ (since we will initialise $\widehat{u}_z$ at 0). Taking into account the new right-hand side (5.8), the pressure equation in (5.5) now writes:

$$(\partial_y^2 - k_x^2)\widehat{p}(t) = ik_x\widehat{R}_x + \partial_y\widehat{R}_y \tag{5.10}$$

This is equivalent to solving $\nabla_{2D}^2\ p = \nabla_{2D} \cdot \boldsymbol{R}$. The influence matrix must be modified accordingly to solve the coupled Helmholtz problem $(\widehat{p}, \widehat{u}_y)$ with the boundary conditions on $\widehat{u}_y$ and $\partial_y\widehat{u}_y$. We note that a related strategy was used by Jiménez & Pinelli (1999); Jimenez (2022), so as to study the cyclic mechanisms in the turbulence production in wall-bounded flows.

5.3 Preliminary results in a large streamwise-spanwise domain

We first present visualisations of the filtered flow in a domain of size $(L_x = 400, L_z = 200)$, with a number of grid points of $(N_x = 3336, N_z = 1668)$. The filtration window used here is $(K_x, K_z) = (0.24, 0.47)$. The corresponding wavelengths are $(\Lambda_x, \Lambda_z) = (26, 13)$. The filtration window is therefore smaller than the typical pattern wavelength in plane Couette flow, $(\lambda_x, \lambda_z) \simeq (100, 44)$ (Prigent *et al.*, 2003). The resulting flow is illustrated on Figure 5.1b and compares to plane Couette flow on Figure 5.1a. The large-scale flow at plane $y = 0$ is extracted by a Fourier filter and shown by arrows.

The large-scale flow in plane Couette flow is oriented obliquely with the streamwise direction, aligning with turbulent bands. As a result of the large-scale control on the spanwise velocity in the filtered case, the obliqueness of the laminar-turbulent structures is modified. The large-scale flow is still strong at the interface, with only variations of the streamwise velocity. The left interface of a turbulent zone presents a negative large-scale streamwise velocity, while that in the right interface is positive.

We extend this observation by presenting multiple instantaneous snapshots in Figure 5.2, at various values of Re. The values of Re are $Re = 390$ (a), 380 (b) and 360 (c), but their absolute meaning is of secondary importance. Filtering the large-scale flow indeed modifies the total dissipation in an unclear manner, and Re can be shifted compared to

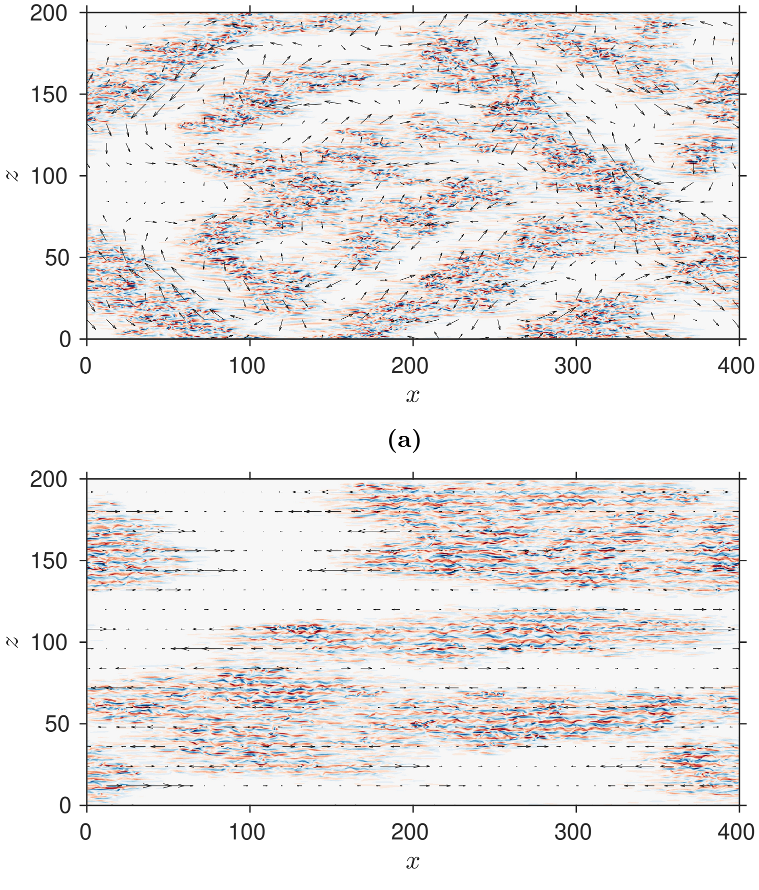

(a)

(b)

Figure 5.1: Visualizations of (a) plane Couette flow and (b) Filtered plane Couette flow in the transitional regime ($Re = 360$). Colors and arrows respectively show cross-channel velocity v and in-plane velocity (u, w) at $y = 0$ (blue: -0.2, white: 0, red: 0.2).

the natural Couette case. We think that the value of Re in itself, and the comparison with Re in Couette flow, is not important in understanding the main physical impact of filtration. A more relevant parameter is instead the relative distance to some critical Reynolds number Re_c, below which turbulence is not statistically sustained. It might be relevant to study the effect of the filtration window on possibly shifting Re_c downwards or upwards, but this is beyond the scope of this primary analysis.

On Figure 5.2, we see that laminar gaps take the form of streamwise-elongated structures. For low enough Re, the laminar gaps extend and leave room to localised structures, one of them being elongated in the streamwise direction (Fig. 5.2c, t=1900). The laminar-turbulent interface does not show any preferred angle aside from 0, contrary to the natural Couette case.

5.4 Quenches in a long oblique domain.

We now describe some other qualitative differences between plane Couette flow and Filtered plane Couette flow. These differences are important to better understand the effect of large-scale filtration on localised turbulence in the transitional regime. For this we use a slender simulation domain, oblique with the streamwise direction, as introduced by Barkley & Tuckerman (2005). The angle of such a domain is denoted θ. Many studies already used such a geometry (Shi *et al.*, 2013; Lemoult *et al.*, 2016), because it simplifies the complex two-dimensional intermittent behaviour of plane Couette flow by reducing it into a quasi one-dimensional problem.

However, if localised turbulent structures are known to favour a non-zero angle in plane Couette flow, this is not true in the filtered case. This is worth an important cautionary statement: imposing an angulation to the filtered system is fundamentally irrelevant (as shown on Figure 5.2). However, the oblique configuration can be used for two reasons: first, it is a reduced system with simplified dynamics, in which simple arguments can be made. Second, one can draw comparisons with plane Couette bands at the same imposed angle.

We therefore introduce tilted directions, x' and z', related to x and z by the following trigonometric transformation:

$$\mathbf{e}_x = \cos\theta\,\mathbf{e}_{x'} + \sin\theta\,\mathbf{e}_{z'} \tag{5.11a}$$

$$\mathbf{e}_z = -\sin\theta\,\mathbf{e}_{x'} + \cos\theta\,\mathbf{e}_{z'} \tag{5.11b}$$

The angle of the domain with the streamwise direction is fixed at $\theta = 24°$, the domain size is $L_{x'}, L_{z'} = (10, 800)$ and the resolution $N_{x'}, N_{z'} = (84, 6667)$. The strategy to filter the large-scale spanwise velocity is comparable to that introduced in Section 5.2.2, with some specificities due to the trigonometric transformation, which are exposed in Appendix 5.A. The filtration window is $(K_{x'}, K_{z'}) = (0, 0.24)$. The corresponding wavelength is

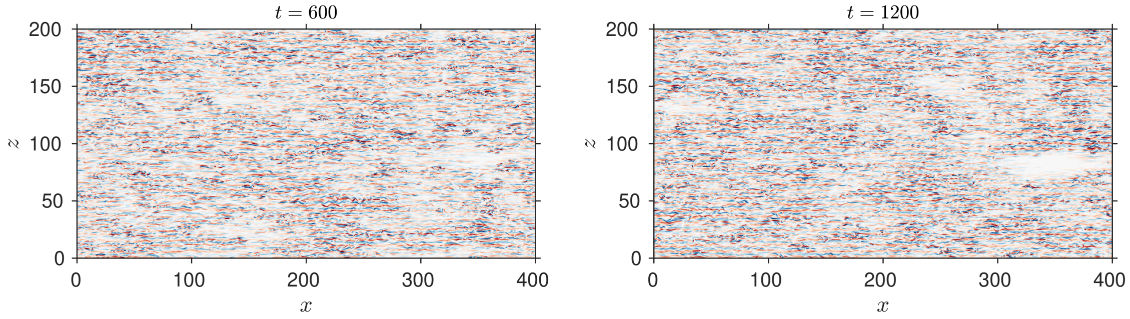

(a) $Re = 390$

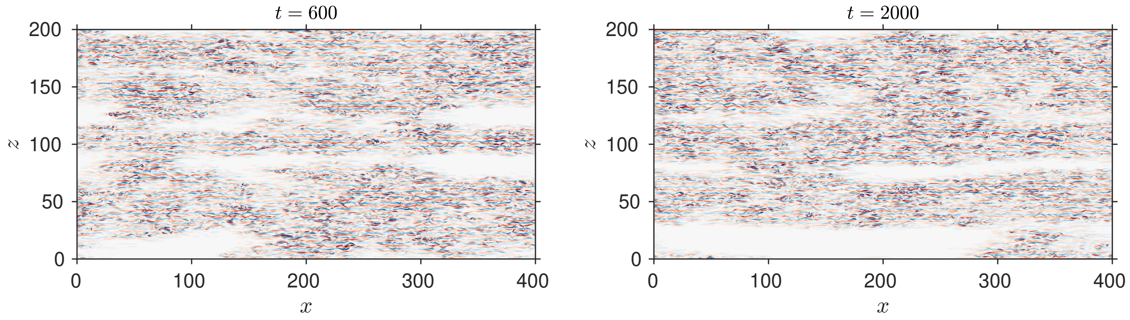

(b) $Re = 380$

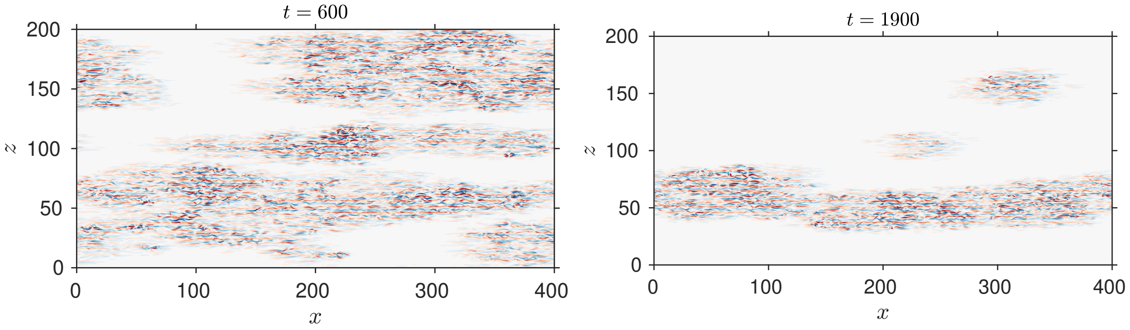

(c) $Re = 360$

Figure 5.2: Instantaneous visualisations of Filtered plane Couette flow in a streamwise-spanwise domain of $(L_x, L_z) = (400, 200)$. Shown is cross-flow velocity v (blue: -0.2, white: 0, red: 0.2). Three values of Re are considered.

lower than that of natural transitional patterns (of around 40). Choosing a filtration window which compares to that in the non-tilted case of Section 5.3 is complex, because of the obliqueness of the filtration grid and the discrete values of possible wavenumbers. Therefore, exact comparisons in terms of Re are difficult to make. The specific values of Re are however not necessary to understand the physical processes induced by filtration.

We initiate the simulations with a uniformly turbulent flow field, which originates from a simulation at $Re = 500$. The Reynolds number is then changed to some desired value. In plane Couette flow, the uniform flow is known to be unstable for $Re < 460$, with intermittent laminar gaps emerging, and self-organising into turbulent-laminar patterns once Re is decreased. For $Re < 340$, these patterns live room to isolated turbulent bands, surrounded by laminar flow. This process is illustrated on the left column of Figure 5.3. Around $Re = Re_c \simeq 325$, the laminar-turbulent intermittency is known to enter the Directed Percolation class of continuous phase transitions (Lemoult *et al.*, 2016; Klotz *et al.*, 2022). Below Re_c, turbulent bands will preferentially decay, even after a very long time, while for $325 < Re < 340$, bands will essentially spread into the laminar zone via a specific process called splitting (Shi *et al.*, 2013): a second band is nucleated from a mother band, in a self-replicating process.

The right column of Figure 5.3 illustrates the different regimes present in the case of Filtered plane Couette flow, with varying Re. At high Re ($Re \simeq 380$), uniform turbulence is destabilised by local nucleations of gaps. When Re is decreased, these gaps are more numerous and get wider. They give birth to localised turbulent structures. These structures live up to a point ($Re = 360$) where they eventually decay.

This process is extremely different from that of plane Couette flow:

(1) We do not observe traces of pattern formation with suppressed spanwise large-scale flow;
(2) The widths of turbulent zones seem widely distributed as compared to plane Couette bands;
(3) We do not observe band splitting;
(4) The transition from uniform turbulence to laminar flow happens in a shorter range in Re compared to plane Couette flow.

5.5 Slugs and splitting

We now carry out a second experiment, which is the counterpart of the quench experiment described in Section 5.4. Once a local turbulent band is created (e.g, by imposing a perturbation of finite amplitude), it is known to either expand (via *slugs*), split, or decay (Barkley, 2016). We present the results of such a procedure in Figure 5.4, in both plane Couette flow (a, c, e) and Filtered plane Couette flow (b, d, f).

In the plane Couette case, isolated bands will statistically decay for $Re < Re_c \simeq 325$

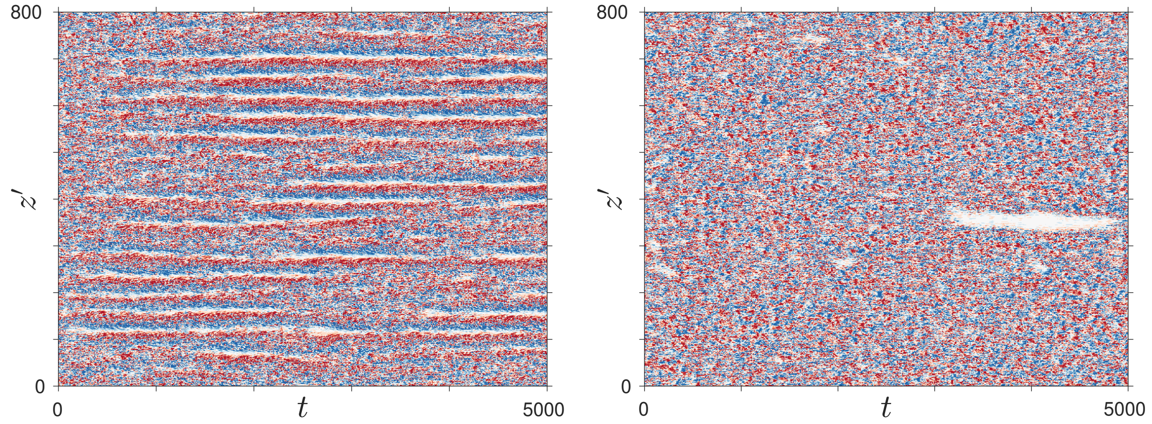

(a) $Re = 420$ **(b)** $Re = 380$

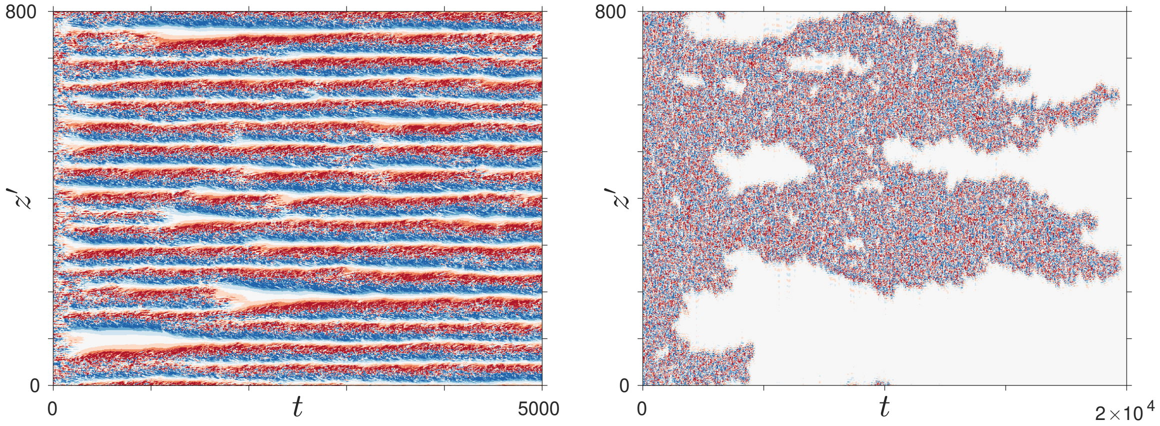

(c) $Re = 350$ **(d)** $Re = 370$

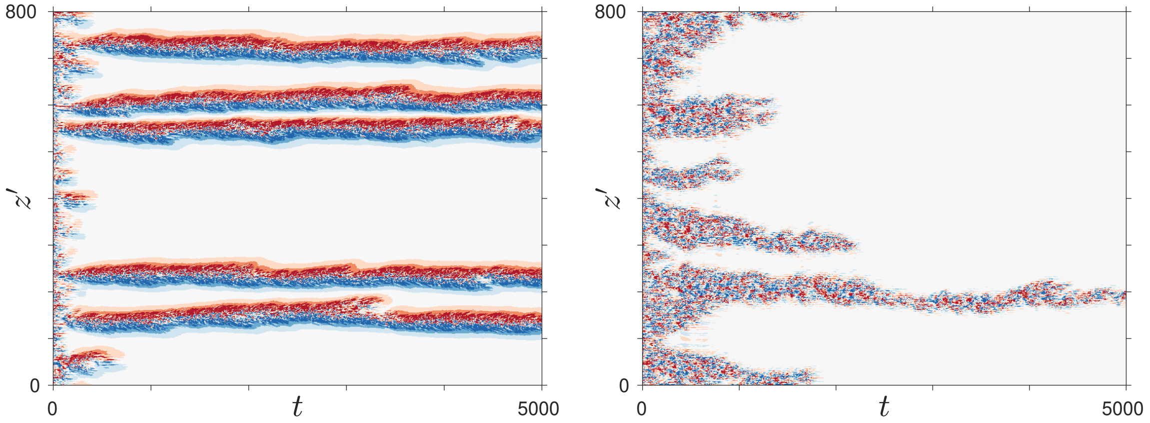

(e) $Re = 320$ **(f)** $Re = 350$

Figure 5.3: Space-time visualization of laminar-turbulent intermittency in an oblique domain of size $(L_{x'} = 10, L_{z'} = 800)$ and tilt angle $\theta = 24°$. Left column: plane Couette flow; right column: Filtered plane Couette flow $(K_{x'} = 0, K_{z'} = 0.24)$. Different Reynolds number are shown in each case. Flow at $t = 0$ is initiated from uniform turbulence at $Re = 500$. Colors show local spanwise velocity $u_{z'}(z, t)$ at $x' = L_{x'}/2$, $y = 0$ (blue: -0.1, red: 0.1).

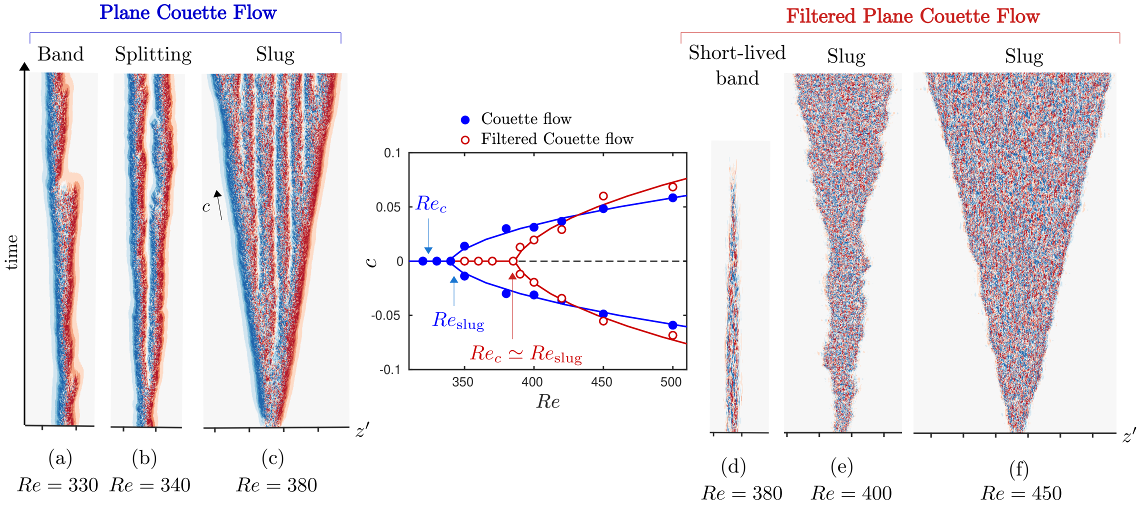

Figure 5.4: Space-time visualizations of bands and slugs in an oblique slender domain of plane Couette flow (a, b, c) and Filtered plane Couette flow (d, e, f) ($K_{z'} = 0.24$). Flow at $t = 0$ is initiated from a localised turbulent patch. Colors show local spanwise velocity $u_z(z', t)$ at $x' = L_{x'}/2$ and $y = 0$ (blue: -0.1, red: 0.1). Center plot: Front velocity as a function of Re, in plane Couette (blue points) and Filtered plane Couette flows (red points). Solid lines are square-root interpolations of the data points.

(Shi *et al.*, 2013; Lemoult *et al.*, 2016). Around $Re_c \simeq 325$, an isolated band is long-lived (see Fig. 5.4a at $Re = 330$). Above Re_c, bands can proliferate via self-replication, as shown in Fig. 5.4b at $Re = 340$. For $Re \gtrsim 350$, slugs start to appear: the localised turbulent patch expands towards positive and negative z', by fronts moving at opposite velocities. This value of Re is denoted Re_{slug}. The slug phase is illustrated on Fig. 5.4c at $Re = 380$. Note that up to $Re \simeq 440$, the slug phase contains laminar-turbulent patterns, as was already observed by Shi *et al.* (2013).

The case of Filtered Couette flow shows a different succession of regimes. Isolated bands do not survive a long time even at $Re = 380$ (Fig. 5.4d), and localised turbulence starts to propagate via moving fronts for $Re \gtrsim Re_{\text{slug}} \simeq 385$, as shown in Fig. 5.4e and f at $Re = 400$ and 450. Near Re_{slug}, the individual bands do not spread via self-replication. They only propagate via front motion.

The average front speed c is presented on the center graph of Figure 5.4 as a function of Re. Front velocities at the two ends of the turbulent region are symmetric on average. They are null in the regime where only individual bands exist, for $Re < Re_{\text{slug}}$. The trend $c = f(Re)$ in Filtered Couette flow contrasts with that of Couette flow: the graph is shifted towards larger Re as an effect of filtration. Furthermore, the values of the velocities differ, slightly: when viewed as a function of $Re - Re_{\mathrm{slug}}$, the front velocity is larger in the filtered case. We can approximate both cases with a square-root trend: $c \propto (Re - Re_c)^{1/2}$, which is consistent with generic bifurcation theory (Pomeau, 1986).

Without the advection of large-scale flow, the mechanism responsible for the velocity of the front is only the nucleation or annihilation of streaks and rolls at the interface. Our results suggest that the large-scale circulation along the interface has a tendency to dampen the front velocity.

Let us once more emphasise that the one-dimensional nature of front motion in this configuration is idealised. Here, the large-scale circulation is orthogonal to the front motion, so it is expected that it does not contribute much to the front advection. In real experiments and simulations in large streamwise-spanwise domains, localised turbulent spots grow in the two directions, and are associated to quadrupolar-shaped large-scale flow (Kashyap *et al.*, 2020*a*). In their experimental study, Couliou & Monchaux (2015) compared the effect of advection by this large-scale flow to that of streak/rolls nucleation. They found that large-scale advection stands for a large part of front motion, but this is because the large-scale flow is two-dimensional, contrary to our simplified case.

5.6 Symmetries of the mean flow

The absence of long-standing isolated bands and self-replication can be explained by the shape of the mean flow in the filtered configuration. We visualise on Figure 5.5 the mean flow around a band in both plane Couette and Filtered plane Couette flows. In a tilted geometry (x', z') (we recall that z' is the long direction of the oblique domain), the mean flow $\overline{\boldsymbol{u}}$ is computed from an average in (x', t) over individual bands, during periods when the turbulent structure is stationary. This computation is carried out at a value of Re where turbulent structures are localised and not propagating ($Re = 330$ in Couette flow and $Re = 380$ in Filtered Couette flow).

The mean flow is shown on Figure 5.5 by red and blue colors, representing the along-band velocity relative to the base flow, $\overline{u}_{x'} - U_{b,x'}$. ($U_b$ stands for the laminar profile and $U_{b,x'}$ its along-band component). Streamlines in the plane (z', y) represent the circulation around the laminar region. We also compute the turbulent kinetic energy $E_{\mathrm{turb}} = \frac{1}{2}\left\langle \overline{\boldsymbol{u'} \cdot \boldsymbol{u'}} \right\rangle_{y \in [0\ 1]}$, where $\boldsymbol{u'} = \boldsymbol{u} - \overline{\boldsymbol{u}}$, and the average is taken on the upper layer (blue line). The mean streamwise velocity at $y = 0.5$, $\overline{U}_{0.5}$, is also presented as a red solid line, with having previously subtracted it from the laminar velocity at this plane, 1/2. (this is done so as to better visualise the shift between E_{turb} and $\overline{U}_{0.5}$.

In both cases, the mean flow is centro-symmetric around the band center $z' = 0$. But in plane Couette flow, there is no reflection symmetry along planes $z' = 0$ or $y = 0$. The mean flow in the upper layer is shifted from that in the lower layer. This creates what Duguet & Schlatter (2013) coined *overhang regions*: in the boundaries of the turbulent

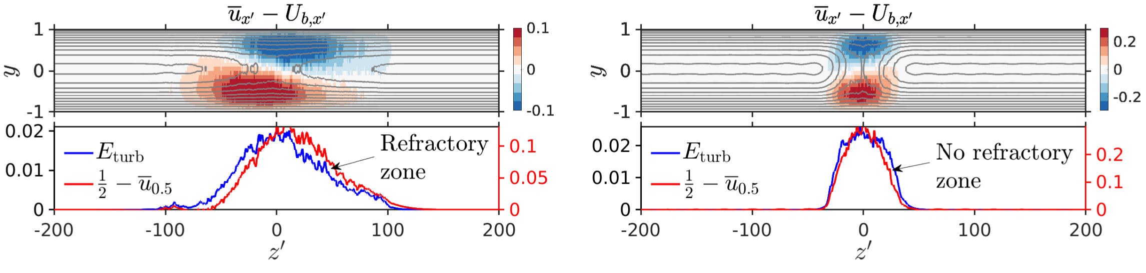

(a) **(b)**

Figure 5.5: Visualisation of the mean flow (top row) in an oblique domain in (a) plane Couette flow and (b) Filtered plane Couette flow. Colors show the velocity along the band, $\overline{U'} - U_b'$ and solid grey lines correspond to streamlines. The bottow row shows corresponding turbulent kinetic energy E_{turb} and $(U_b - \overline{U})_{y=0.5} = 1/2 - \overline{U}_{0.5}$.

zone (e.g. $z' = -80$), the turbulent region in the lower layer faces a quasi-laminar flow in the upper layer. In this region, the mean profile is non-symmetric along plane $y = 0$. These overhang regions are connected to the large-scale spanwise circulation, as follows from incompressibility (Duguet & Schlatter, 2013).

Furthermore, the mean flow in the upper layer is shifted with regard to the kinetic energy E_{turb}: from low to high z', E_{turb} first increases, by extracting energy from the laminar flow. As a consequence of this production of turbulent eddies, the total mean flow decreases in intensity ($1/2 - \overline{U}_{0.5}$ increases from 0). As a result, turbulent eddies are not strongly fuelled, compared to the injection from laminar flow, and they start decaying in energy. Subsequently, the mean flow restores its laminar shape, with some spatial shift. This latter decaying region is called a *refractory region*. In this zone, turbulent production is lower than dissipation (Song *et al.*, 2017).

Contrary to Couette flow, Filtered Couette flow seems to render approximately two reflection symmetries: along the $y = 0$ plane, and the $z = 0$ (band center) plane. The two regions of positive and negative velocities oppose one another, unlike in plane Couette flow. This approximately restores the reflection symmetry along plane $y = 0$ and prohibits overhang regions. The approximate symmetry along $z = 0$ is visible when looking at E_{turb} and $\overline{u}_{0.5}$ as a function of z'. Unlike in Couette flow, there is no robust delay between the two signals. At the laminar-turbulent interface, $\overline{u}_{0.5}$ even increases before E_{turb} decreases. As a consequence, there is no refractory zone in the filtered case, and the disequilibrium between mean flow and turbulent energy is not the same.

The absence of refractory zone explains the absence of long-lived isolated structures and of band splitting in Filtered Couette flow. The refractory tail indeed creates an effective buffer zone surrounding each individual band. Neighbouring interaction between closely-spaced bands happen via this buffer zone (Hof *et al.*, 2010; Barkley, 2016). When eddies move across the refractory tail, they have a high probability to decay due to the absence of energy fueling from fresh laminar flow. In some regimes, these eddies survive the refractory zone and leave it. Then, once energised by fresh laminar flow, they create a new band, via splitting.

In the filtered case, there is no refractory zone preventing the localised structure from expanding downstream. As a consequence, no long-lived isolated band can be sustained: turbulence will eventually either expand or retract. Moreover, there is no need to overcome the refractory tail via splitting. In the absence of sustained isolated bands and bands self-replication in the Filtered Couette case, there is a direct connection to the primary vision of Pomeau (1986): he envisioned two equilibria, a metastable turbulent state and a stable laminar state. When Re is sufficiently low, the stable state invades the metastable state via a laminar-turbulent front. The velocity of such front inverts at the critical point, above which turbulence contaminates the laminar regions. This picture is only a simplification of what happens in transitional shear flows (Barkley, 2016), as the situation near the critical point is more intricate: localised structures are sustained, and can decay or split. However, the vision of Pomeau (1986) essentially captures our observations in Filtered plane Couette flow.

We wish to verify the continuous nature of the phase transition in the Filtered Couette case, by measuring turbulent fraction at equilibrium, denoted F_t. Results in an oblique domain of size $L_{z'} = 800$ are presented on Figure 5.6 and can be compared to those of Lemoult *et al.* (2016). We find a critical Reynolds number $Re_c \simeq 383$ below which $F_t = 0$. This value of Re nearly coincides with $Re_{\text{slug}} \simeq 385$ above which the turbulent state starts to contaminate the laminar state (Fig. 5.4). This points out again a crucial difference with plane Couette flow, where $Re_c \neq Re_{\text{slug}}$ ($Re_c \simeq 325$ and $Re_{\text{slug}} \simeq 350$).

These results are preliminary and not yet conclusive in properly characterising the nature of the phase transition.

5.7 Discussion

We demonstrate an essential connection between large-scale circulation and the presence of oblique patterns in transitional shear flows. Annihilating large-scale circulation prevents a wavelength from being selected in the flow. This is in agreement with the role of along-band circulation in the selection of a specific wavelength, developed in previous chapters. This is also in line with the results of Tuckerman & Barkley (2011) and Duguet *et al.* (2011), who used a long spanwise, short streamwise simulation domain of plane Couette flow, which prevents large-scale circulation along the laminar-turbulent interface, and where this interface can only grow or shrink, without forming patterns. Duguet *et al.* (2011) analysed this process as a time-continuous random walk, with two competing events: the propagation or retraction of the front. In this system, the average front velocity balances near $Re \simeq 325$, surprisingly close to the threshold of Directed Percolation (Lemoult *et al.*,

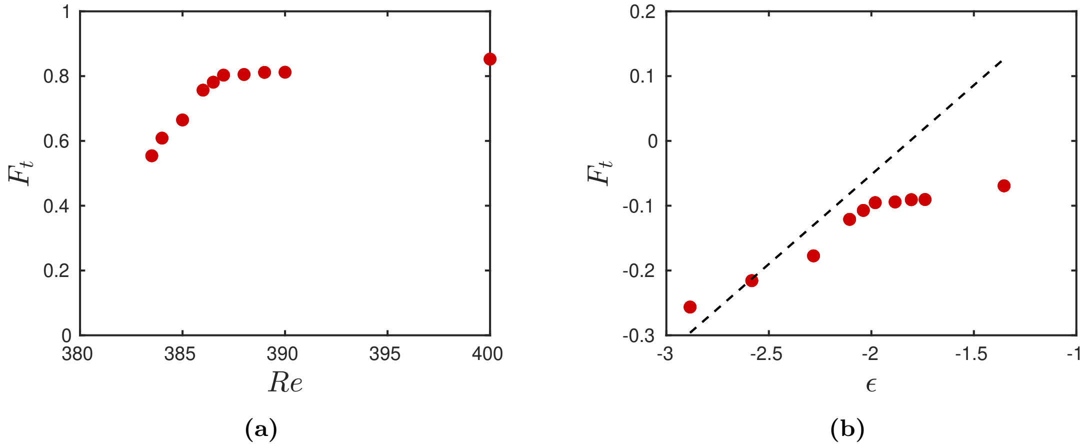

(a) (b)

Figure 5.6: Evolution of equilibrium turbulent fraction F_t with Re in Filtered plane Couette flow in (a) linear-linear axes and (b) log-log axes ($\epsilon \equiv \frac{Re-Re_c}{Re_c}$). The dashed line shows the theoretical 1D-DP scaling $F_t \sim \epsilon^\beta$ with $\beta = 0.276$. Note that convergence is not achieved yet and the results are inconclusive for proving the obedience to DP.

2016).

Suppressing the large-scale circulation strongly reduces the lifetime of individual localised turbulent structures. Our control experiment has therefore altered the efficiency of energy extraction from surrounding laminar flow, and this is due to the shape of the mean flow resulting from filtration. However, the fundamental mechanisms underlying the problem of transition to turbulence are not totally altered by this operation. Turbulence is still spatially and temporally intermittent, with possible expansion of turbulent zones via slug phases, without the need of large-scale circulation. A crucial difference lies in the absence of self-replication (splitting) of localised turbulent bands. In plane Couette flow, this process was essential near the laminar-turbulent critical point ($Re \simeq 325$), as the slug phase does not exist in this regime. We therefore confirm the role of the energy refractory zone in preventing slugs and promoting splitting near the critical Re, and its connection to large-scale circulation. The second-order nature of the phase transition seems preserved in our filtered system, in agreement with Pomeau (1986, 2015), but more conclusive results are needed.

Two seemingly different phenomena, the formation of patterns and the presence of long-lived isolated turbulence, were suppressed by the filtration experiment. It might be possible to suppress only one of these phenomena, perhaps by imposing a certain shape of the large-scale streamwise or wall-normal flow. Furthermore, the filtration scale (K_x, K_z) is a direct parameter delaying and modifying the transition. It is possible that intermediate regimes would be found when the filtration length is close to the natural wavelength of patterns.

Our filtered system is strikingly similar to the case of bent pipe flow. When curving a pipe, Rinaldi *et al.* (2019) demonstrated the presence of only slugs and puffs, without any trace of puff splitting. The effect of bending the pipe could be to induce a secondary flow (Dean, 1927) responsible for an assymmetry in the localisation of turbulent energy within puffs.

Although for now only numerical, our control strategy echoes with various experiments on annular pipe or Couette flow, in which a variety of states, patterned or isolated, were found (Ishida *et al.*, 2016, 2017; Kunii *et al.*, 2019; Takeda *et al.*, 2020; Matsukawa & Tsukahara, 2022). In such experiments, or also in the case of stratified or magnetised shear flows (Brethouwer *et al.*, 2012), multiple physical effects are at play, and could impact large-scale circulation and pattern formation. It would be interesting to find cases of planar shear flows in which these physical effects counter-balance this large-scale circulation. Inspired by curved pipe flow, a possible strategy could be to slightly incline the two planes in Couette or Poiseuille flow, which would result in a secondary flow interacting with the large-scale flow.

5.A Filtration strategy in an oblique numerical domain

In the main text, we have exposed a strategy for filtering Navier-Stokes equations in a streamwise-spanwise domain. This method has to be adapted in an oblique domain. This requires using trigonometric prefactors so as to suppress spanwise large-scale flow in a (x', z') coordinate system. There is however a strong caveat of the initial procedure exposed in Section 5.2.2: the influence matrix resulting from the coupled variables $(\widehat{p}, \widehat{u}_y)$ in the two-component system is not invertible. This is a peculiar case for which we could not find any reliable solution. We therefore adopt a different strategy. This time, the new RHS $\widehat{R}'_z$ will be forced to zero, instead of forcing it to balance the pressure gradient:

$$\widehat{R}'_z = \widehat{R}_z + F = 0 \tag{5.12}$$

The equation for $\widehat{u}_z$, in place of (5.9), writes:

$$(\partial_y^2 - \lambda)\widehat{u}_z(t) = \widehat{R}'_z - ik_z\widehat{p} = -ik_z\widehat{p} \tag{5.13}$$

and pressure is solved by $\nabla^2 p = \nabla \cdot \boldsymbol{R}'$. This method effectively reduces the large-scale spanwise flow (it is of order $\sim 10^{-6}$ in the filtered case, compared to $\sim 10^{-1}$ in plane Couette flow), without exactly imposing it to be 0. There might be however some small inconsistencies between the two filtering strategies used in the tilted and non-tilted geometries. But these do not alter the fundamental differences in the phenomenology of the transition between Couette and Filtered Couette flow, as presented in the main text.

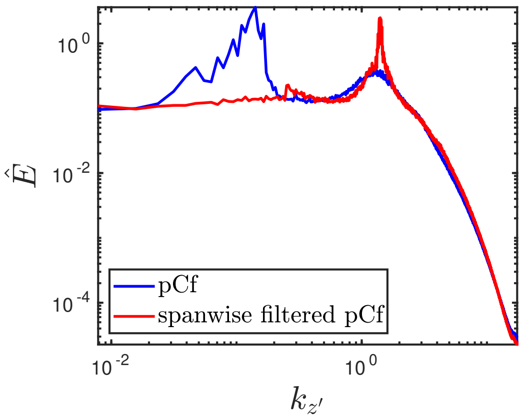

(a)

Figure 5.7: Spectral energy $\hat{E}(k_z) = \frac{1}{2}\overline{\widehat{\boldsymbol{u}}) \cdot \widehat{\boldsymbol{u}}}$ along band-orthogonal wavenumber $k_{z'}$. Average is taken over (x', t). Spectra are shown at $y = 0$. Blue line: plane Couette flow at $Re = 360$; red line: filtered plane Couette flow at $Re = 360$.

5.B Spectral impact of the filtration

In a tilted numerical domain, we compute the mean energy spectrum $\frac{1}{2}\langle \hat{\boldsymbol{u}} \cdot \hat{\boldsymbol{u}} \rangle_{x',t}$, with $\hat{\boldsymbol{u}}$ the z'-Fourier transform of total velocity $\boldsymbol{u}$. This is presented on Figure 5.7, in plane Couette flow and Filtered Couette flow, both at $Re = 360$. The characteristic large-scale motions in Couette flow are damped out to a constant energy distribution in the filtered case. As a consequence of filtration, the energy at small scales is increased.

Conclusion and perspectives

Understanding how chaotic motions emerge out of quiescent flows is a long and adventurous path. But this path is nothing but vain. And this is not because the destination was somehow achieved, but because the route one takes is more important than the destination. I hope that this thesis has illustrated how fruitful this route is. I tried to apply various methods and concepts issued from other areas of Physics or Mathematics to the following question: how does turbulence rise in shear flows, and, more specifically, why does it spontaneously take the form of isolated oblique structures, coexisting with laminar flow? This thesis is only a small step in some of the many possible pathways that one could follow when addressing such a important and fascinating problem.

In Chapters 1 and 2, we used numerical simulations of a planar shear flow in a reduced system effectively imposing the angulation of turbulent bands. This led to a statistical description of the onset of turbulence, and to a super-exponential scaling of the lifetime of turbulent structures in the case of plane channel flow. In Chapter 2, a rare-event strategy was successfully applied to enhance this statistical description, and try to pave the infinitely large phase space describing our turbulent system. Our methodology was inherited from statistical mechanics, and precisely from the study of stochastic processes. Its application to rare transitions in deterministic hydrodynamical systems is important, both for practical applications and fundamental understandings.

With this toolbox, we could build a probabilistic description of localised shear turbulence, based on the extreme value principle. This led to a quantitative understanding of the interplay between the distribution within a chaotic attractor, and the probability of the system to escape this chaotic attractor. This description relies on condensing the infinite degrees of freedom of a turbulent system onto a single, one-dimensional, observable. This required a coarse-grained description of ”microscopic” turbulent fluctuations, that we obtained by measuring the spatial extension of an isolated turbulent band.

In this thesis, we viewed each localised turbulent zone as an individual object, subject to seemingly random fluctuations, and which is constantly fuelled by its environment (the laminar flow) via energy transfers. This is a mesoscopic description, which averages out small-scale turbulent interactions. This description was completed in Chapter 3. We quantified the interactions between small turbulent eddies and the strong large-scale circulation along laminar-turbulent interfaces. This was carried out in a spectral sense, with a particular focus on the establishment of patterns out of uniform turbulence. A cyclic mechanism fueling turbulent-laminar patterns was unravelled.

In Chapter 4, this cycle helped us understand the emergence of a selected wavelength from a turbulent environment. We found an empirical principle of maximal dissipation, obeyed by the large-scale flow along laminar-turbulent interfaces. Laminar gaps arise intermittently and locally in the flow, and create such a large-scale flow by which they interact, and form patterns as a result of this interaction. To some extent, this is similar to a jamming process. The crucial role of this large-scale flow in selecting a preferred angulation was better understood in Chapter 5.

This approach is a small step in understanding the physical principles behind the emergence of some order out of turbulent motion, when dissipation is too strong for wall-bounded turbulence to sustain homogeneously. The advection by the large-scale flow is key in optimally distributing the energy within the flow. An important achievement could be to treat incoherent turbulent fluctuations like thermal fluctuations in near-equilibrium thermodynamics, potentially with help of the large-deviation theory, and to connect it to the effective free energy minimised by turbulent-laminar patterns, as the one disclosed in Chapter 4. But at this stage, this view is purely speculative.

There is another fundamental gap that is not yet bridged: the connection between this intermediate viewpoint at the scale of puffs or bands, and the macroscopic description of phase transition, which accurately describes the collective behaviour of localised turbulent structures. One presumably needs another toolkit, maybe issued from statistical mechanics, so as to connect all these levels of description, from microscopic (streaks and rolls in wall-bounded turbulence) to macroscopic scales (phase transition), going through intermediate scales (puffs and bands).

Bibliography

Ahlers, Guenter, Cannell, David S, Dominguez-Lerma, Marco A & Heinrichs, Richard 1986 Wavenumber selection and Eckhaus instability in Couette-Taylor flow. *Physica D: Nonlinear Phenomena* **23** (1-3), 202–219.

Andereck, C David, Liu, SS & Swinney, Harry L 1986 Flow regimes in a circular Couette system with independently rotating cylinders. *J. Fluid Mech.* **164**, 155–183.

Aulery, Frederic, Dupuy, Dorian, Toutant, Adrien, Bataille, Françoise & Zhou, Ye 2017 Spectral analysis of turbulence in anisothermal channel flows. *Computers & Fluids* **151**, 115–131.

Avila, Kerstin, Moxey, David, de Lozar, Alberto, Avila, Marc, Barkley, Dwight & Hof, Björn 2011 The onset of turbulence in pipe flow. *Science* **333** (6039), 192–196.

Avila, Marc & Hof, Björn 2013 Nature of laminar-turbulence intermittency in shear flows. *Physical Review E* **87** (6), 063012.

Avila, Marc, Willis, Ashley P & Hof, Björn 2010 On the transient nature of localized pipe flow turbulence. *J. Fluid Mech.* **646**, 127–136.

Barkley, Dwight 1990 Theory and predictions for finite-amplitude waves in two-dimensional plane Poiseuille flow. *Phys. Fluids A* **2** (6), 955–970.

Barkley, Dwight 2006 Linear analysis of the cylinder wake mean flow. *EPL (Europhysics Letters)* **75** (5), 750.

Barkley, Dwight 2011 Simplifying the complexity of pipe flow. *Phys. Rev. E* **84** (1), 016309.

Barkley, Dwight 2016 Theoretical perspective on the route to turbulence in a pipe. *J. Fluid Mech.* **803**, P1.

Barkley, Dwight, Song, Baofang, Mukund, Vasudevan, Lemoult, Grégoire, Avila, Marc & Hof, Björn 2015 The rise of fully turbulent flow. *Nature* **526** (7574), 550–553.

Barkley, Dwight & Tuckerman, Laurette S 2005 Computational study of turbulent-laminar patterns in Couette flow. *Phys. Rev. Lett.* **94** (1), 014502.

Barkley, Dwight & Tuckerman, Laurette S 2007 Mean flow of turbulent–laminar patterns in plane Couette flow. *J. Fluid Mech.* **576**, 109–137.

Bengana, Y, Loiseau, J-Ch, Robinet, J-Ch & Tuckerman, LS 2019 Bifurcation analysis and frequency prediction in shear-driven cavity flow. *Journal of Fluid Mechanics* **875**, 725–757.

Berghout, Pieter, Dingemans, Rick J, Zhu, Xiaojue, Verzicco, Roberto, Stevens, Richard JAM, van Saarloos, Wim & Lohse, Detlef 2020 Direct numerical simulations of spiral Taylor-Couette turbulence. *J. Fluid Mech.* **887**.

Bolotnov, Igor A, Lahey Jr, Richard T, Drew, Donald A, Jansen, Kenneth E & Oberai, Assad A 2010 Spectral analysis of turbulence based on the dns of a channel flow. *Computers & fluids* **39** (4), 640–655.

Bottin, Sabine & Chaté, Hugues 1998 Statistical analysis of the transition to turbulence in plane Couette flow. *Eur. Phys. J. B* **6** (1), 143–155.

Bottin, Sabine, Daviaud, Francois, Manneville, Paul & Dauchot, Olivier 1998 Discontinuous transition to spatiotemporal intermittency in plane Couette flow. *Europhys. Lett.* **43** (2), 171.

Bouchet, Freddy, Rolland, Joran & Simonnet, Eric 2019 Rare event algorithm links transitions in turbulent flows with activated nucleations. *Phys. Rev. Lett.* **122**, 074502.

Brand, Evan & Gibson, John F 2014 A doubly localized equilibrium solution of plane Couette flow. *J. Fluid Mech.* **750**, R3.

Bréhier, Charles-Edouard, Gazeau, Maxime, Goudenège, Ludovic, Lelièvre, Tony, Rousset, Mathias & others 2016 Unbiasedness of some generalized adaptive multilevel splitting algorithms. *Ann. Appl. Probab.* **26** (6), 3559–3601.

Brethouwer, G., Duguet, Y. & Schlatter, P. 2012 Turbulent-laminar coexistence in wall flows with Coriolis, buoyancy or Lorentz forces. *J. Fluid Mech.* **704**, 137–172.

Busse, Friedrich H 1981 Transition to turbulence in rayleigh-beénard convection. In *Hydrodynamic instabilities and the transition to turbulence*, pp. 97–137. Springer.

Butler, Kathryn M & Farrell, Brian F 1992 Three-dimensional optimal perturbations in viscous shear flow. *Physics of Fluids A: Fluid Dynamics* **4** (8), 1637–1650.

Canuto, Claudio, Hussaini, M Yousuff, Quarteroni, Alfio & Zang, Thomas A 2007 *Spectral methods: fundamentals in single domains*. Springer Science & Business Media.

Cérou, Frédéric & Guyader, Arnaud 2007 Adaptive multilevel splitting for rare event analysis. *Stochastic Analysis and Applications* **25** (2), 417–443.

Cérou, Frédéric, Guyader, Arnaud, Lelievre, Tony & Malrieu, Florent 2013 On the length of one-dimensional reactive paths. *ALEA, Lat. Am. J. Probab. Math. Stat.* **10**, 359–389.

Cérou, Frédéric, Guyader, Arnaud, Lelievre, Tony & Pommier, David 2011 A multiple replica approach to simulate reactive trajectories. *J. Chem. Phys.* **134** (5), 054108.

Cérou, Frédéric, Guyader, Arnaud & Rousset, Mathias 2019 Adaptive multilevel splitting: Historical perspective and recent results. *Chaos* **29** (4), 043108.

Chantry, Matthew 2020 private communication.

Chantry, Matthew & Schneider, Tobias M 2014 Studying edge geometry in transiently turbulent shear flows. *J. Fluid Mech.* **747**, 506–517.

Chantry, Matthew, Tuckerman, Laurette S & Barkley, Dwight 2016 Turbulent–laminar patterns in shear flows without walls. *J. Fluid Mech.* **791**, R8.

Chantry, Matthew, Tuckerman, Laurette S & Barkley, Dwight 2017 Universal continuous transition to turbulence in a planar shear flow. *J. Fluid Mech.* **824**, R1.

Chaté, Hugues & Manneville, Paul 1987 Transition to turbulence via spatio-temporal intermittency. *Physical review letters* **58** (2), 112.

Cho, Minjeong, Hwang, Yongyun & Choi, Haecheon 2018 Scale interactions and spectral energy transfer in turbulent channel flow. *Journal of Fluid Mechanics* **854**, 474–504.

Cimarelli, A, De Angelis, E & Casciola, CM 2013 Paths of energy in turbulent channel flows. *Journal of Fluid Mechanics* **715**, 436–451.

Coles, Donald 1965 Transition in circular Couette flow. *Journal of Fluid Mechanics* **21** (3), 385–425.

Coles, Donald & van Atta, Charles 1966 Progress report on a digital experiment in spiral turbulence. *AIAA Journal* **4** (11), 1969–1971.

Couliou, M & Monchaux, Romain 2015 Large-scale flows in transitional plane Couette flow: a key ingredient of the spot growth mechanism. *Physics of Fluids* **27** (3), 034101.

Couliou, Marie & Monchaux, Romain 2016 Spreading of turbulence in plane Couette flow. *Physical Review E* **93** (1), 013108.

Couliou, Marie & Monchaux, Romain 2017 Growth dynamics of turbulent spots in plane Couette flow. *Journal of Fluid Mechanics* **819**, 1–20.

Cross, Michael & Greenside, Henry 2009 *Pattern formation and dynamics in nonequilibrium systems*. Cambridge University Press.

Darbyshire, AG & Mullin, T 1995 Transition to turbulence in constant-mass-flux pipe flow. *J. Fluid Mech.* **289**, 83–114.

Dean, Wo R 1927 Xvi. note on the motion of fluid in a curved pipe. *The London, Edinburgh, and Dublin Philosophical Magazine and Journal of Science* **4** (20), 208–223.

Dematteis, Giovanni, Grafke, Tobias, Onorato, Miguel & Vanden-Eijnden, Eric 2019 Experimental evidence of hydrodynamic instantons: the universal route to rogue waves. *Phys. Rev. X* **9** (4), 041057.

Domaradzki, J Andrzej, Liu, Wei, Härtel, Carlos & Kleiser, Leonhard 1994 Energy transfer in numerically simulated wall-bounded turbulent flows. *Physics of Fluids* **6** (4), 1583–1599.

Dong, S 2009 Evidence for internal structures of spiral turbulence **80** (6), 067301.

van Doorne, Casimir WH & Westerweel, Jerry 2009 The flow structure of a puff. *Phil. Trans. R. Soc. A* **367** (1888), 489–507.

Duguet, Yohann, Le Maitre, Olivier & Schlatter, Philipp 2011 Stochastic and deterministic motion of a laminar-turbulent front in a spanwisely extended Couette flow. *Physical Review E* **84** (6), 066315.

Duguet, Yohann & Schlatter, Philipp 2013 Oblique laminar-turbulent interfaces in plane shear flows. *Physical review letters* **110** (3), 034502.

Duguet, Yohann, Schlatter, Philipp & Henningson, Dan S 2010 Formation of turbulent patterns near the onset of transition in plane Couette flow. *J. Fluid Mech.* **650**, 119–129.

Duguet, Yohann, Willis, Ashley P & Kerswell, Rich R 2008 Transition in pipe flow: the saddle structure on the boundary of turbulence. *J. Fluid Mech.* **613**, 255–274.

Eckhardt, Bruno, Schneider, Tobias M, Hof, Bjorn & Westerweel, Jerry 2007 Turbulence transition in pipe flow. *Annu. Rev. Fluid Mech.* **39**, 447–468.

Faisst, Holger & Eckhardt, Bruno 2004 Sensitive dependence on initial conditions in transition to turbulence in pipe flow. *J. Fluid Mech.* **504**, 343–352.

Faranda, Davide, Lucarini, Valerio, Manneville, Paul & Wouters, Jeroen 2014 On using extreme values to detect global stability thresholds in multi-stable systems: The case of transitional plane Couette flow. *Chaos, Solitons, Fractals* **64**, 26–35.

Farge, Marie & others 1992 Wavelet transforms and their applications to turbulence. *Annual review of fluid mechanics* **24** (1), 395–458.

Feigenbaum, Mitchell J 1978 Quantitative universality for a class of nonlinear transformations. *Journal of statistical physics* **19** (1), 25–52.

Fisher, R. A. & Tippett, L. H. C. 1928 Limiting forms of the frequency distribution of the largest or smallest member of a sample. *Math. Proc. Camb. Philos. Soc.* **24** (2), 180–190.

Frishman, Anna & Grafke, Tobias 2022 Dynamical landscape of transitional pipe flow. *Phys. Rev. E* **105**, 045108.

Fukudome, Koji & Iida, Oaki 2012 Large-scale flow structure in turbulent Poiseuille flows at low-Reynolds numbers. *J. Fluid Sci. Tech.* **7** (1), 181–195.

Gibson, J. F. 2012 Channelflow: A Spectral Navier-Stokes Simulator in C++. *Tech. Rep.*. University of New Hampshire, see Channelflow.org.

de Giovanetti, Matteo, Sung, Hyung Jin & Hwang, Yongyun 2017 Streak instability in turbulent channel flow: the seeding mechanism of large-scale motions. *J. Fluid Mech.* **832**, 483–513.

Goldenfeld, Nigel 2018 *Lectures on phase transitions and the renormalization group*. CRC Press.

Goldenfeld, Nigel, Guttenberg, Nicholas & Gioia, Gustavo 2010 Extreme fluctuations and the finite lifetime of the turbulent state. *Phys. Rev. E* **81** (3), 035304(R).

Goldenfeld, Nigel & Shih, Hong-Yan 2017 Turbulence as a problem in non-equilibrium statistical mechanics. *Journal of Statistical Physics* **167** (3), 575–594.

Gollub, Jerry P & Swinney, Harry L 1975 Onset of turbulence in a rotating fluid. *Physical Review Letters* **35** (14), 927.

Gomé, Sébastien, Tuckerman, Laurette S & Barkley, Dwight 2020 Statistical transition to turbulence in plane channel flow. *Phys. Rev. Fluids* **5** (8), 083905.

Gomé, Sébastien, Tuckerman, Laurette S & Barkley, Dwight 2022 Extreme events in transitional turbulence. *Philosophical Transactions of the Royal Society A* **380** (2226), 20210036.

Grafke, Tobias, Grauer, Rainer & Schäfer, Tobias 2013 Instanton filtering for the stochastic Burgers equation. *Journal of Physics A: Mathematical and Theoretical* **46** (6), 062002.

Grafke, Tobias, Grauer, Rainer & Schäfer, Tobias 2015 The instanton method and its numerical implementation in fluid mechanics. *J. Phys. A Math.* **48** (33), 333001.

Grafke, Tobias & Vanden-Eijnden, Eric 2019 Numerical computation of rare events via large deviation theory. *Chaos* **29** (6), 063118.

Graham, Michael D. & Floryan, Daniel 2021 Exact coherent states and the nonlinear dynamics of wall-bounded turbulent flows. *Annu. Rev. Fluid Mech.* **53** (1), 227–253, arXiv: https://doi.org/10.1146/annurev-fluid-051820-020223.

Grassberger, Peter 1981 On phase transitions in schlögl's second model. In *Nonlinear Phenomena in Chemical Dynamics*, pp. 262–262. Springer.

Hamilton, James M, Kim, John & Waleffe, Fabian 1995 Regeneration mechanisms of near-wall turbulence structures. *J. Fluid Mech.* **287**, 317–348.

Henkel, Malte, Hinrichsen, Haye, Lübeck, Sven & Pleimling, Michel 2008 *Non-equilibrium phase transitions*, , vol. 1. Springer.

Hinrichsen, Haye 2000 Non-equilibrium critical phenomena and phase transitions into absorbing states. *Advances in physics* **49** (7), 815–958.

Hiruta, Yoshiki & Toh, Sadayoshi 2020 Subcritical laminar–turbulent transition as nonequilibrium phase transition in two-dimensional kolmogorov flow. *Journal of the Physical Society of Japan* **89** (4), 044402.

Hof, Björn, De Lozar, Alberto, Avila, Marc, Tu, Xiaoyun & Schneider, Tobias M 2010 Eliminating turbulence in spatially intermittent flows. *Science* **327** (5972), 1491–1494.

Hof, Björn, De Lozar, Alberto, Kuik, Dirk Jan & Westerweel, Jerry 2008 Repeller or attractor? selecting the dynamical model for the onset of turbulence in pipe flow. *Phys. Rev. Lett.* **101** (21), 214501.

Hof, Björn, Westerweel, Jerry, Schneider, Tobias M & Eckhardt, Bruno 2006 Finite lifetime of turbulence in shear flows. *Nature* **443** (7107), 59–62.

Hwang, Yongyun & Bengana, Yacine 2016 Self-sustaining process of minimal attached eddies in turbulent channel flow. *J. Fluid Mech.* **795**, 708–738.

Hwang, Yongyun & Cossu, Carlo 2010 Self-sustained process at large scales in turbulent channel flow. *Physical review letters* **105** (4), 044505.

Ishida, Takahiro, Duguet, Yohann & Tsukahara, Takahiro 2016 Transitional structures in annular Poiseuille flow depending on radius ratio. *J. Fluid Mech.* **794**, R2.

Ishida, Takahiro, Duguet, Yohann & Tsukahara, Takahiro 2017 Turbulent bifurcations in intermittent shear flows: From puffs to oblique stripes. *Phys. Rev. Fluids* **2** (7), 073902.

Janssen, Hans-Karl 1981 On the nonequilibrium phase transition in reaction-diffusion systems with an absorbing stationary state. *Zeitschrift für Physik B Condensed Matter* **42** (2), 151–154.

Jiménez, Javier 1998 The largest scales of turbulent wall flows. *CTR Annual Research Briefs* **137**, 54.

Jimenez, Javier 2022 Streak-less wall-bounded turbulence. *arXiv preprint arXiv:2202.09814* .

Jiménez, Javier & Pinelli, Alfredo 1999 The autonomous cycle of near-wall turbulence. *Journal of Fluid Mechanics* **389**, 335–359.

Kanazawa, Takahiro 2018 Lifetime and growing process of localized turbulence in plane channel flow. PhD thesis, Osaka University.

Kaneko, Kunihiko 1985 Spatiotemporal intermittency in coupled map lattices. *Progress of Theoretical Physics* **74** (5), 1033–1044.

Kashyap, Pavan 2021 Subcritical transition to turbulence in wall-bounded shear flows: spots, pattern formation and low-order modelling. PhD thesis, Université Paris-Saclay.

Kashyap, Pavan V, Duguet, Yohann & Chantry, Matthew 2020*a* Far field of turbulent spots. *Physical Review Fluids* **5** (10), 103902.

Kashyap, Pavan V, Duguet, Yohann & Dauchot, Olivier 2020*b* Flow statistics in the transitional regime of plane channel flow. *Entropy* **22** (9), 1001.

Kashyap, Pavan V, Duguet, Yohann & Dauchot, Olivier 2022 Linear instability of turbulent channel flow. *arXiv preprint arXiv:2205.05652* .

Kawahara, Genta, Uhlmann, Markus & Van Veen, Lennaert 2012 The significance of simple invariant solutions in turbulent flows. *Annu. Rev. Fluid Mech.* **44**, 203–225.

Kawata, Takuya & Tsukahara, Takahiro 2021 Scale interactions in turbulent plane Couette flows in minimal domains. *Journal of Fluid Mechanics* **911**.

Kerswell, RR 2005 Recent progress in understanding the transition to turbulence in a pipe. *Nonlinearity* **18** (6), R17.

Kim, John, Moin, Parviz & Moser, Robert 1987 Turbulence statistics in fully developed channel flow at low Reynolds number. *J. Fluid Mech.* **177**, 133–166.

Klotz, Lukasz, Lemoult, Grégoire, Avila, Kerstin & Hof, Björn 2022 Phase transition to turbulence in spatially extended shear flows. *Phys. Rev. Lett.* **128** (1), 014502.

Klotz, Lukasz, Lemoult, Grégoire, Frontczak, Idalia, Tuckerman, Laurette S & Wesfreid, José Eduardo 2017 Couette-Poiseuille flow experiment with zero mean advection velocity: Subcritical transition to turbulence. *Phys. Rev. Fluids* **2** (4), 043904.

Klotz, Lukasz, Pavlenko, AM & Wesfreid, JE 2021 Experimental measurements in plane Couette–poiseuille flow: dynamics of the large-and small-scale flow. *Journal of Fluid Mechanics* **912**.

Klotz, L., Pavlenko, A.M. & Wesfreid, José Eduardo 2020 Experimental measurements in plane Couette-Poiseuille flow: dynamics of the large and small scale flow. preprint.

Komminaho, Jukka, Lundbladh, Anders & Johansson, Arne V 1996 Very large structures in plane turbulent Couette flow. *Journal of Fluid Mechanics* **320**, 259–285.

Kramer, Lorenz & Zimmermann, Walter 1985 On the Eckhaus instability for spatially periodic patterns. *Physica D: Nonlinear Phenomena* **16** (2), 221–232.

Kubo, Ryogo, Toda, Morikazu & Hashitsume, Natsuki 2012 *Statistical physics II: nonequilibrium statistical mechanics*, , vol. 31. Springer Science & Business Media.

Kühnen, Jakob, Scarselli, Davide, Schaner, Markus & Hof, Björn 2018 Relaminarization by steady modification of the streamwise velocity profile in a pipe. *Flow, turbulence and combustion* **100** (4), 919–943.

Kunii, Kohei, Ishida, Takahiro, Duguet, Yohann & Tsukahara, Takahiro 2019 Laminar–turbulent coexistence in annular Couette flow. *Journal of Fluid Mechanics* **879**, 579–603.

Landau, Lev D 1944 On the problem of turbulence. In *Dokl. Akad. Nauk USSR*, , vol. 44, p. 311.

Lawless, J. F. 2002 *Statistical Models and Methods for Lifetime Data, Second Edition*. John Wiley & Sons, Inc.

Lee, Myoungkyu & Moser, Robert D 2015 Direct numerical simulation of turbulent channel flow up to. *Journal of fluid mechanics* **774**, 395–415.

Lee, Myoungkyu & Moser, Robert D 2019 Spectral analysis of the budget equation in turbulent channel flows at high reynolds number. *Journal of Fluid Mechanics* **860**, 886–938.

Lemoult, Grégoire, Gumowski, Konrad, Aider, Jean-Luc & Wesfreid, José Eduardo 2014 Turbulent spots in channel flow: an experimental study. *Eur. Phys. J. E* **37** (4), 25.

Lemoult, Grégoire, Shi, Liang, Avila, Kerstin, Jalikop, Shreyas V, Avila, Marc & Hof, Björn 2016 Directed percolation phase transition to sustained turbulence in Couette flow. *Nature Physics* **12** (3), 254.

Lestang, Thibault, Bouchet, Freddy & Lévêque, Emmanuel 2020 Numerical study of extreme mechanical force exerted by a turbulent flow on a bluff body by direct and rare-event sampling techniques. *J. Fluid Mech.* **895**.

Lestang, Thibault, Ragone, Francesco, Bréhier, Charles-Edouard, Herbert, Corentin & Bouchet, Freddy 2018 Computing return times or return periods with rare event algorithms. *J. Stat. Mech.: Theory Exp.* **2018** (4), 043213.

Liu, T., Semin, B., Klotz, L., Godoy-Diana, R., Wesfreid, J.E. & Mullin, T. 2020 Anisotropic decay of turbulence in plane Couette-Poiseuille flow. *arXiv:2008.08851* .

Liu, T., Semin, B., Klotz, L., Godoy-Diana, R., Wesfreid, J.E. & Mullin, T. 2021 Decay of streaks and rolls in plane Couette–Poiseuille flow. *J. Fluid Mech.* **915**, A65.

Lu, Jianzhou, Tao, Jianjun, Zhou, Weitao & Xiong, Xiangming 2019 Threshold and decay properties of transient isolated turbulent band in plane Couette flow. *Applied Mathematics and Mechanics* **40** (10), 1449–1456.

Lumley, JL 1964 Spectral energy budget in wall turbulence. *The Physics of Fluids* **7** (2), 190–196.

Lundbladh, Anders & Johansson, Arne V 1991 Direct simulation of turbulent spots in plane couette flow. *J. Fluid Mech.* **229**, 499–516.

Malkus, WVR 1956 Outline of a theory of turbulent shear flow. *Journal of Fluid Mechanics* **1** (5), 521–539.

Manneville, Paul 2011 On the decay of turbulence in plane Couette flow. *Fluid Dynamics Research* **43** (6), 065501.

Manneville, Paul 2012 Turbulent patterns in wall-bounded flows: A turing instability? *EPL (Europhysics Letters)* **98** (6), 64001.

MANNEVILLE, PAUL 2015 On the transition to turbulence of wall-bounded flows in general, and plane Couette flow in particular. *European Journal of Mechanics-B/Fluids* **49**, 345–362.

MANNEVILLE, PAUL 2017 Laminar-turbulent patterning in transitional flows. *Entropy* **19** (7), 316.

MARENSI, ELENA, DING, ZIJING, WILLIS, ASHLEY P & KERSWELL, RICH R 2020 Designing a minimal baffle to destabilise turbulence in pipe flows. *Journal of Fluid Mechanics* **900**.

MARKEVICIUTE, VILDA K & KERSWELL, RICH R 2022 Improved assessment of the statistical stability of turbulent flows using extended orr-sommerfeld stability analysis. *arXiv preprint arXiv:2201.01540* .

MARXEN, OLAF & ZAKI, TAMER A 2019 Turbulence in intermittent transitional boundary layers and in turbulence spots. *J. Fluid Mech.* **860**, 350–383.

MATSUKAWA, YUKI & TSUKAHARA, TAKAHIRO 2022 Subcritical transition of taylor-Couette-poiseuille flow at high radius ratio. *Physics of Fluids* .

MENEVEAU, CHARLES 1991 Analysis of turbulence in the orthonormal wavelet representation. *Journal of Fluid Mechanics* **232**, 469–520.

MESEGUER, ALVARO, MELLIBOVSKY, FERNANDO, AVILA, MARC & MARQUES, FRANCISCO 2009 Instability mechanisms and transition scenarios of spiral turbulence in Taylor-Couette flow **80** (4), 046315.

MESEGUER, A & TREFETHEN, LLOYD N 2003 Linearized pipe flow to reynolds number 107. *Journal of Computational Physics* **186** (1), 178–197.

MIHELICH, MARTIN, FARANDA, DAVIDE, PAILLARD, DIDIER & DUBRULLE, BÉRENGÈRE 2017 Is turbulence a state of maximum energy dissipation? *Entropy* **19** (4), 154.

MIZUNO, YOSHINORI 2016 Spectra of energy transport in turbulent channel flows for moderate reynolds numbers. *Journal of Fluid Mechanics* **805**, 171–187.

MOXEY, DAVID & BARKLEY, DWIGHT 2010 Distinct large-scale turbulent-laminar states in transitional pipe flow. *Proceedings of the National Academy of Sciences* **107** (18), 8091–8096.

NAGATA, MASATO 1990 Three-dimensional finite-amplitude solutions in plane Couette flow: bifurcation from infinity. *J. Fluid Mech.* **217**, 519–527.

NEMOTO, TAKAHIRO & ALEXAKIS, ALEXANDROS 2018 Method to measure efficiently rare fluctuations of turbulence intensity for turbulent-laminar transitions in pipe flows. *Phys. Rev. E* **97** (2), 022207.

NEMOTO, TAKAHIRO & ALEXAKIS, ALEXANDROS 2021 Do extreme events trigger turbulence decay?–a numerical study of turbulence decay time in pipe flows. *J. Fluid Mech.* **912**.

NISHI, MINA, ÜNSAL, BÜLENT, DURST, FRANZ & BISWAS, GAUTAM 2008 Laminar-to-turbulent transition of pipe flows through puffs and slugs. *J. Fluid Mech.* **614**, 425–446.

OBUKHOV, SP 1980 The problem of directed percolation. *Physica A: Statistical Mechanics and its Applications* **101** (1), 145–155.

OZAWA, HISASHI, SHIMOKAWA, SHINYA & SAKUMA, HIROFUMI 2001 Thermodynamics of fluid turbulence: A unified approach to the maximum transport properties. *Physical Review E* **64** (2), 026303.

PARANJAPE, CHAITANYA S, DUGUET, YOHANN & HOF, BJÖRN 2020 Oblique stripe solutions of channel flow. *J. Fluid Mech.* **897**, A7.

PARK, JAE SUNG & GRAHAM, MICHAEL D. 2015 Exact coherent states and connections to turbulent dynamics in minimal channel flow. *Journal of Fluid Mechanics* **782**, 430–454.

PARKER, JEFFREY B & KROMMES, JOHN A 2013 Zonal flow as pattern formation. *Physics of Plasmas* **20** (10), 100703.

PEIXINHO, JORGE & MULLIN, TOM 2006 Decay of turbulence in pipe flow. *Phys. Rev. Lett.* **96** (9), 094501.

POMEAU, YVES 1986 Front motion, metastability and subcritical bifurcations in hydrodynamics. *Physica D* **23, 3**.

POMEAU, YVES 2015 The transition to turbulence in parallel flows: a personal view. *Comptes Rendus Mécanique* **343** (3), 210–218.

POMEAU, YVES & MANNEVILLE, PAUL 1989 Intermittent transition to turbulence in dissipative dynamical systems. In *Universality in Chaos*, pp. 327–335. Routledge.

POPE, STEPHEN B 2000 *Turbulent flows*. Cambridge university press.

PRIGENT, ARNAUD, GRÉGOIRE, GUILLAUME, CHATÉ, HUGUES & DAUCHOT, OLIVIER 2003 Long-wavelength modulation of turbulent shear flows. *Physica D* **174** (1-4), 100–113.

PRIGENT, ARNAUD, GRÉGOIRE, GUILLAUME, CHATÉ, HUGUES, DAUCHOT, OLIVIER & VAN SAARLOOS, WIM 2002 Large-scale finite-wavelength modulation within turbulent shear flows. *Phys. Rev. Lett.* **89** (1), 014501.

Pugh, JD & Saffman, PG 1988 Two-dimensional superharmonic stability of finite-amplitude waves in plane Poiseuille flow. *J. Fluid Mech.* **194**, 295–307.

Quadrio, Maurizio & Sibilla, Stefano 2000 Numerical simulation of turbulent flow in a pipe oscillating around its axis. *Journal of Fluid Mechanics* **424**, 217–241.

Reetz, Florian, Kreilos, Tobias & Schneider, Tobias M 2019 Invariant solution underlying oblique stripe patterns in plane Couette flow. *Nat. Comm.* **10**, 2277.

Reynolds, Osborne 1883 An experimental investigation of the circumstances which determine whether the motion of water shall be direct or sinuous, and of the law of resistance in parallel channels. *Phil. Trans. R. Soc. Lond.* **174**, 935—982.

Reynolds, WC & Tiederman, WG 1967 Stability of turbulent channel flow, with application to malkus's theory. *J. Fluid Mech.* **27** (2), 253–272.

Riecke, Hermann & Paap, Hans-Georg 1986 Stability and wave-vector restriction of axisymmetric taylor vortex flow. *Physical Review A* **33** (1), 547.

Rinaldi, Enrico, Canton, Jacopo & Schlatter, Philipp 2019 The vanishing of strong turbulent fronts in bent pipes. *Journal of Fluid Mechanics* **866**, 487–502.

Ritter, Paul, Zammert, Stefan, Song, Baofang, Eckhardt, Bruno & Avila, Marc 2018 Analysis and modeling of localized invariant solutions in pipe flow. *Physical Review Fluids* **3** (1), 013901.

Rolland, Joran 2018 Extremely rare collapse and build-up of turbulence in stochastic models of transitional wall flows. *Phys. Rev. E* **97** (2), 023109.

Rolland, Joran 2022 Collapse of transitional wall turbulence captured using a rare events algorithm. *J. Fluid Mech.* **931**, A22.

Rolland, Joran, Bouchet, Freddy & Simonnet, Eric 2016 Computing transition rates for the 1-D stochastic Ginzburg–Landau–Allen–Cahn equation for finite-amplitude noise with a rare event algorithm. *J. Stat. Phys.* **162** (2), 277–311.

Rolland, Joran & Manneville, Paul 2011 Ginzburg–Landau description of laminar-turbulent oblique band formation in transitional plane Couette flow. *The European Physical Journal B* **80** (4), 529–544.

Rolland, Joran & Simonnet, Eric 2015 Statistical behaviour of adaptive multilevel splitting algorithms in simple models. *J. Comput. Phys.* **283**, 541–558.

Ruelle, David & Takens, Floris 1971 On the nature of turbulence. *Les rencontres physiciens-mathématiciens de Strasbourg-RCP25* **12**, 1–44.

Samanta, Devranjan, De Lozar, Alberto & Hof, Björn 2011 Experimental investigation of laminar turbulent intermittency in pipe flow. *J. Fluid Mech.* **681**, 193–204.

Schneider, Tobias M, Eckhardt, Bruno & Yorke, James A 2007 Turbulence transition and the edge of chaos in pipe flow. *Phys. Rev. Lett.* **99** (3), 034502.

Schorlepp, Timo, Grafke, Tobias, May, Sandra & Grauer, Rainer 2021 Spontaneous symmetry breaking for extreme vorticity and strain in the 3d Navier-Stokes equations. *arXiv:2107.06153* .

Shan, H, Ma, B, Zhang, Z & Nieuwstadt, FTM 1999 Direct numerical simulation of a puff and a slug in transitional cylindrical pipe flow. *Journal of Fluid Mechanics* **387**, 39–60.

Shi, Liang, Avila, Marc & Hof, Björn 2013 Scale invariance at the onset of turbulence in Couette flow. *Phys. Rev. Lett.* **110** (20), 204502.

Shih, Hong-Yan 2017 Spatial-temporal patterns in evolutionary ecology and fluid turbulence. PhD thesis, University of Illinois at Urbana-Champaign.

Shimizu, Masaki, Kanazawa, Takahiro & Kawahara, Genta 2019 Exponential growth of lifetime of localized turbulence with its extent in channel flow. *Fluid Dyn. Res.* **51** (1), 011404.

Shimizu, Masaki & Manneville, Paul 2019 Bifurcations to turbulence in transitional channel flow. *Phys. Rev. Fluids* **4**, 113903.

Shimizu, Masaki, Manneville, Paul, Duguet, Yohann & Kawahara, Genta 2014 Splitting of a turbulent puff in pipe flow. *Fluid Dyn. Res.* **46** (6), 061403.

Simonnet, Eric, Rolland, Joran & Bouchet, Freddy 2021 Multistability and rare spontaneous transitions in barotropic β-plane turbulence. *J. Atm. Sci.* **78** (6), 1889–1911.

Smits, Alexander J, McKeon, Beverley J & Marusic, Ivan 2011 High–reynolds number wall turbulence. *Annu. Rev. Fluid Mecha.* **43**, 353–375.

Song, Baofang, Barkley, Dwight, Hof, Björn & Avila, Marc 2017 Speed and structure of turbulent fronts in pipe flow. *J. Fluid Mech.* **813**, 1045–1059.

Stuart, John Trevor 1958 On the non-linear mechanics of hydrodynamic stability. *Journal of Fluid Mechanics* **4** (1), 1–21.

Symon, Sean, Illingworth, Simon J & Marusic, Ivan 2021 Energy transfer in turbulent channel flows and implications for resolvent modelling. *Journal of Fluid Mechanics* **911**.

Takeda, Kazuki, Duguet, Yohann & Tsukahara, Takahiro 2020 Intermittency and critical scaling in annular Couette flow. *Entropy* **22** (9), 988.

Takeishi, Keisuke, Kawahara, Genta, Wakabayashi, Hiroki, Uhlmann, Markus & Pinelli, Alfredo 2015 Localized turbulence structures in transitional rectangular-duct flow **782**, 368–379.

Tao, J.J., Eckhardt, Bruno & Xiong, X.M. 2018 Extended localized structures and the onset of turbulence in channel flow. *Physical Review Fluids* **3** (1), 011902.

Täuber, Uwe C 2014 *Critical dynamics: a field theory approach to equilibrium and non-equilibrium scaling behavior*. Cambridge University Press.

Taylor, Geoffrey Ingram 1923 Viii. stability of a viscous liquid contained between two rotating cylinders. *Philosophical Transactions of the Royal Society of London. Series A, Containing Papers of a Mathematical or Physical Character* **223** (605-615), 289–343.

Tobias, SM & Marston, JB 2013 Direct statistical simulation of out-of-equilibrium jets. *Phys. Rev. Lett.* **110** (10), 104502.

Touchette, Hugo 2011 A basic introduction to large deviations: Theory, applications, simulations. *arXiv:1106.4146* .

Trefethen, Lloyd N, Trefethen, Anne E, Reddy, Satish C & Driscoll, Tobin A 1993 Hydrodynamic stability without eigenvalues. *Science* **261** (5121), 578–584.

Tsukahara, Takahiro, Kawamura, Hiroshi & Shingai, Kenji 2006 DNS of turbulent Couette flow with emphasis on the large-scale structure in the core region. *Journal of Turbulence* **7**, N19.

Tsukahara, Takahiro, Seki, Yohji, Kawamura, Hiroshi & Tochio, Daisuke 2005*a* DNS of turbulent channel flow at very low Reynolds numbers. In *Proc. 4th Int. Symp. on Turbulence and Shear Flow Phenomena*, pp. 935–940. ArXiv:1406.0248.

Tsukahara, Takahiro, Seki, Yohji, Kawamura, Hiroshi & Tochio, Daisuke 2005*b* Dns of turbulent channel flow at very low reynolds numbers. In *Fourth International Symposium on Turbulence and Shear Flow Phenomena*. Begel House Inc.

Tuckerman, Laurette S & Barkley, Dwight 1990 Bifurcation analysis of the Eckhaus instability. *Physica D: Nonlinear Phenomena* **46** (1), 57–86.

Tuckerman, Laurette S & Barkley, Dwight 2011 Patterns and dynamics in transitional plane Couette flow. *Phys. Fluids* **23** (4), 041301.

Tuckerman, Laurette S, Barkley, Dwight & Dauchot, Olivier 2010 Instability of uniform turbulent plane Couette flow: Spectra, probability distribution functions and k–Ω closure model. In *Seventh IUTAM Symposium on Laminar-Turbulent Transition*, pp. 59–66. Springer.

Tuckerman, Laurette S, Chantry, Matthew & Barkley, Dwight 2020 Patterns in wall-bounded shear flows. *Annu. Rev. Fluid Mech.* **52**, 343.

Tuckerman, Laurette S, Kreilos, Tobias, Schrobsdorff, Hecke, Schneider, Tobias M & Gibson, John F 2014 Turbulent-laminar patterns in plane Poiseuille flow. *Phys. Fluids* **26** (11), 114103.

Van Atta, Charles 1966 Exploratory measurements in spiral turbulence. *Journal of Fluid Mechanics* **25** (3), 495–512.

Vanden-Eijnden, Eric & others 2006 Towards a theory of transition paths. *Journal of statistical physics* **123** (3), 503–523.

Waleffe, Fabian 1997 On a self-sustaining process in shear flows. *Phys. Fluids* **9** (4), 883–900.

Wang, B., Ayats, R., Deguchi, K., Mellibovsky, F. & Meseguer, A. 2022 Self-sustainment of coherent structures in counter-rotating Taylor–Couette flow. *J. Fluid Mech.* **951**, A21.

Willis, Ashley P & Kerswell, Rich R 2007 Critical behavior in the relaminarization of localized turbulence in pipe flow. *Phys. Rev. Lett.* **98** (1), 014501.

Woillez, Eric & Bouchet, Freddy 2020 Instantons for the destabilization of the inner solar system. *Phys. Rev. Lett.* **125** (2), 021101.

Wouters, Jeroen & Bouchet, Freddy 2016 Rare event computation in deterministic chaotic systems using genealogical particle analysis. *J. Phys. A Math.* **49** (37), 374002.

Wygnanski, I, Sokolov, Mo & Friedman, D 1975 On transition in a pipe. Part 2. The equilibrium puff. *Journal of Fluid Mechanics* **69** (2), 283–304.

Wygnanski, Israel J & Champagne, FH 1973 On transition in a pipe. Part 1. The origin of puffs and slugs and the flow in a turbulent slug. *Journal of Fluid Mechanics* **59** (2), 281–335.

Xiao, Xiangkai & Song, Baofang 2020 The growth mechanism of turbulent bands in channel flow at low Reynolds numbers. *J. Fluid Mech.* **883**, R1.

Xiong, Xiangming, Tao, Jianjun, Chen, Shiyi & Brandt, Luca 2015 Turbulent bands in plane-Poiseuille flow at moderate Reynolds numbers **27** (4), 041702.

Yeomans, Julia M 1992 *Statistical mechanics of phase transitions*. Clarendon Press.

Zammert, Stefan & Eckhardt, Bruno 2014 Streamwise and doubly-localised periodic orbits in plane Poiseuille flow. *J. Fluid Mech.* **761**, 348–359.

Zammert, Stefan & Eckhardt, Bruno 2016 Streamwise decay of localized states in channel flow. *Phys. Rev. E* **94** (4), 041101(R).

Abstract

In planar shear flows, the route to turbulence is paved by coexisting laminar and turbulent structures. These transitional structures either decay to the absorbing laminar state or self-replicate via splitting, depending on the Reynolds number. The average passage times from one state to the other depend super-exponentially on the Reynolds number and lead to a crossing Reynolds number above which proliferation is more likely than decay. We apply a rare event algorithm, the Adaptative Multilevel Splitting (AMS), to the deterministic Navier-Stokes equations to study transition paths and estimate large passage times in channel flow, more efficiently than with direct simulations. We build a probabilistic description of the decay or split of localised turbulence, connected to extreme value theory. In transitioning from one state to another, the flow visits a regime that is self-similar with the Reynolds number. Our description connects the super-exponential variation of the passage times to the Reynolds-number dependence of the parameters of an extreme value distribution, which quantifies the fluctuations of an isolated structure around its averaged state.

We furthermore focus on the spontaneous emergence of laminar-turbulent patterns from uniform plane Couette flow. These patterns are associated to a strong mean flow, whose energisation mechanisms are unravelled. This large-scale circulation is partly fuelled by small-scale turbulence, but also extracts energy from the mean shear, via a non-linear interaction due to mean advection. This energy cycle clarifies the way in which a specific wavelength is preferred in the flow. Via simulations in domains of various finite sizes, we associate this preferred wavelength to a stronger energy of the mean circulation, and to maximised advection and dissipation. In large domains, the uniform turbulent state leaves room to a regime punctuated by randomly-nucleated isolated laminar gaps. These laminar gaps eventually form patterns because of their associated large-scale flow, which is best energised at the preferred wavelength. The effect of this circulation is confirmed by a filtration experiment, where the large-scale flow is controlled: as a consequence, regular patterns disappear and the transition scenario is altered.

Résumé

Dans les écoulements parallèles cisaillés, la turbulence apparait sous forme de bandes localisées, entourées de zones laminaires. Ces structures turbulentes disparaissent (elles atteignent l'état laminaire absorbant) ou se multiplient en fonction du nombre de Reynolds. Dans l'écoulement de Poiseuille plan, les temps de passage moyen d'un état à l'autre dépendent super-exponentiellement du nombre de Reynolds. Ils permettent de définir un nombre de Reynolds critique à partir duquel la prolifération des bandes est plus probable que leur disparition. Un algorithme d'événements rares, l'Adaptative Multilevel Splitting (AMS), est utilisé pour étudier les chemins de transition et estimer les longs temps de passage d'une manière plus efficace que la simulation directe. Nous établissons une connexion avec la théories des valeurs extrêmes. La variation super-exponentielle des temps de passage avec le nombre de Reynolds est liée aux paramètres de ces distributions extrêmes, qui quantifient les fluctuations des bandes turbulentes autour de leur état moyen.

Nous étudions en outre l'émergence de motifs laminaire-turbulents obliques à partir d'une turbulence uniforme. Ces motifs sont associés à un champ moyen intense, qui est énergisé par un cycle que nous décrivons. Cet écoulement à large-échelle absorbe une partie de l'énergie turbulente, mais est aussi nourri par le cisaillement moyen, en raison d'une interaction non-linéaire liée à l'advection moyenne. Ce cycle est étudié en faisant varier la longueur d'onde du motif, grâce à des simulations numériques dans des domaines de taille variable. L'énergie de la circulation moyenne, et le terme d'advection qui l'alimente majoritairement, sont maximisés par la longueur d'onde préferentielle du motif, correspondant à un principe de dissipation maximale du champ moyen. Dans un domaine très large, des trous laminaires apparaissent aléatoirement de manière intermittente, et quand le nombre de Reynolds est diminué, s'organisent en des motifs réguliers qui maximisent le champ moyen associé aux trous. L'effet de cette grande circulation est confirmé par une expérience de filtration de l'écoulement à grande échelle: les motifs réguliers sont ainsi supprimés et le processus de transition vers la turbulence est altéré.